COLD WORK EMBRITTLEMENT OF INTERSTITIAL-FREE SHEET STEEL

By

KEVIN PATRICK BOYLE

A Thesis

Submitted to the School of Graduate Studies

In Partial Fulfillment of the Requirements

For the Degree

Doctor of Philosophy

McMaster University

COLD WORK EMBRITTLEMENT OF

INTERSTITIAL-FREE SHEET STEEL

DOCTOR OF PHILOSOPHY (2001) McMASTER UNIVERSITY

(Materials Science and Engineering) Hamilton, Ontario, Canada

TITLE: Cold Work Embrittlement of Interstitial-Free Sheet Steel

AUTHOR: Kevin Patrick Boyle, B. Eng. (McMaster University)

SUPERVISOR: Professor J. D. Embury (McMaster University)

Professor D. D. Perovic (University of Toronto)

NUMBER OF PAGES: xix, 178

ABSTRACT

The occurrence of brittle intergranular fracture during sheet metal forming operations or during in-service use in low carbon steels is often termed cold work embrittlement (CWE). Interstitial-free steels are especially susceptible to brittle intergranular fracture, as there is little free carbon in solid solution left to segregate to the grain boundaries, where its presence is thought to intrinsically strengthen the grain boundaries and indirectly strengthen the grain boundaries by impeding the segregation of deleterious elements such as phosphorus and tin. These embrittled grain boundaries, coupled with an increased flow stress from cold working, result in intergranular fracture, especially after deep drawing, with cracks propagating in the drawing direction. The purpose of the present work was to identify the key microstructural parameters controlling cold work embrittlement.

Tensile tests performed on well-characterized undeformed and predeformed IF steel sheet indicated that the grain shape was a key microstructural parameter. A strain path dependent fracture criterion was developed and used to predict the occurrence of cold work embrittlement for forming operations from the evolution of the resulting intergranular fracture surface and the yield surface with deformation. A series of experiments on deep drawn cups were used to test the key predictions of the model. The role of grain shape, amount of deep drawing, segregation levels, macroscopic residual stresses, strain rate, and surface condition were further clarified. Although a fracture path investigation indicated that low angle boundaries were resistant to fracture, the density of these boundaries were insufficient to affect the bulk macroscopic fracture properties.

The potency and amount of segregant at the grain boundary controls the cohesive strength of the grain boundary. Quantitative analytical electron microscopy detected higher levels of phosphorus segregation for batch annealed steel as opposed to continuously annealed steel. The higher level of segregation resulted in a greater susceptibility to CWE especially for severe deep drawing. The process of phosphorus segregation during recrystallization annealing was modeled by accounting for the migrating grain boundary.

ACKNOWLEDGMENTS

I wish to express my sincere appreciation towards my academic supervisors, Prof. J. D. Embury and Prof. D. D. Perovic. Their support and understanding throughout the course of this work made its completion possible. As well, I am especially grateful to my industrial advisors, Mr. J. E. Hood (now retired) and Mr. J. G. Thomson (now manager of the McMaster Steel Research Center). Constant dialogue with, and support from them had a direct influence on my research. Finally, I would like to acknowledge Materials and Manufacturing Ontario and Stelco Inc. for financial support of this work.

Various researchers have also influenced the course of this work with advice and fruitful discussions. Accordingly, I would like to thank Prof. Yves Bréchet, Dr. Pierre Martin, Prof. Gary Purdy, Prof. George Weatherly, Prof. David Wilkinson, and Dr. Aleksandra Perovic. I am also very grateful to have had the opportunity to discuss my research with many internationally renowned visiting researchers including Dr. M. Guttmann, Prof. G.D.W. Smith, Prof. A. J. Garratt-Reed, Prof. M. Militzer, Prof. M. Hillert, Prof. H.R. Piehler, Prof. R.G. Hoagland, Prof. P. Guyot, Dr. W. R. Tyson, Prof. J. J. Jonas, Prof. S. Saimoto, Prof. G. Saada, and Prof. L. M. Brown.

The analysis of the local grain boundary composition was performed in collaboration with Dr. Aleksandra Perovic. The bulk X-ray texture analysis was performed by Dr. Carl Necker at Los Alamos National Laboratories (LANL). I am also indebted to Prof. Mateusz Sklad for loan of the strain analysis system.

A great deal of research would be impeded without the excellent technical personnel available here at McMaster. In particular, I would like to thank Jim Garret, Andy Duft, Ed McCaffery, Tom Bryner, John Hudak, Chris Butcher, Dave Schick, Sal Boccia (at University of Toronto) and Fred Pearson for their advice, help and general technical excellence over the years.

Finally, I would like to thank the students and researchers, whom over the years contributed to the A206 atmosphere including (in somewhat chronological order only) Joël, Denis, Kelly, Rosaura, Peter, Ben, Colin, Eric, James, Chad, John, Kutty, Justin, Tony, Hatem, Christine, Jaydeep, Stephane, Kevin, Jinichiro and Josie. Many friendships also developed with visiting international students whose tenure here was often far too short, including Stefan, Muriel, Frederic, Vladimir and Naoki.

TABLE OF CONTENTS

5.2.2 Flow Behaviour · · · 108

5.2.3 Results of Modeling · · · 109

5.2.4 Extension of Model to Include Transgranular Fracture · · · 117

5.3 Intergranular Delamination · · · 118

5.4 Influence of Draw Ratio on Cold Work Embrittlement · · · 121

5.5 Recrystallization Annealing, Grain Boundary Segregation Level · · · 123

5.6 Macroscopic Residual Stresses · · · 124

5.7 The Influence of Strain Rate · · · 128

5.8 Galvannealed Coating · · · 131

5.9 Grain Boundary Structure and Intergranular Fracture · · · 132

5.10 Kinetics of Grain Boundary Segregation During Recrystallization Annealing · · · 134

5.10.1 Solute Drag · · · 134

5.10.2 Procedure and Assumptions · · · 136

5.10.3 Kinetics of Grain Boundary Segregation During Recrystallization · · · 140

5.10.4 Implications of Modeling Kinetics of Segregation for Moving Grain Boundary · 149

5.11 Suggestions for Reducing Impact of Cold Work Embrittlement · · · 155

6.0 CONCLUSIONS · · · 159

6.1 Future Work · · · 161

APPENDIX · · · 163

A Physical Metallurgy of Interstitial-Free Steels · · · 163

B Circumferential Strain Rate During Cup Expansion Test · · · 165

C Bending During Cup Drawing · · · 166

REFERENCES · · · 168

LIST OF FIGURES

Figure 3.11 - Geometry used to estimate interaction volume to calculate the absolute amount of segregant. · · · 52

Figure 4.1 - Optical micrographs and grain area section distributions for RP CA material in the three orthogonal directions of the sheet. · · · 56

Figure 4.2 - Optical micrographs and grain area section distributions for RP BA material in the three orthogonal directions of the sheet. · · · 56

Figure 4.3 - Through-thickness microstructure of RP BA steel etched with 5% Nital. · · · 57

Figure 4.4 - Variation of sectional grain area as a function of through-thickness position in the RP CA material. · · · 57

Figure 4.5 - X-ray energy dispersive spectrum from fine niobium carbide precipitates found in rephosphorized IF sheet steel. · · · 58

Figure 4.6 - Micrograph and the associated XEDS spectrum of typical manganese sulphide precipitates found in RP CA steel. · · · 58

Figure 4.7 - Uniaxial flow properties of RP CA light gage tested in rolling, diagonal, and transverse directions. · · · 59

Figure 4.8 - Work hardening properties of the as-received RP CA light gage tested in rolling, diagonal, and transverse directions. · · · 60

Figure 4.9 - Flow behaviour to fracture for RP CA material in rolling direction. Bridgeman correction not made. · · · 60

Figure 4.10 - Progression of necking from diffuse to localized for the continuously annealed light gage grade tested in uniaxial tension in the rolling direction. · · · 60

Figure 4.11 - Flow curves for a) RP CA and b) RP BA steels as a function of temperature. · · · 61

Figure 4.12 - Yield and tensile stress with temperature for the continuously and batch annealed steels. · · · 61

Figure 4.13 - Work hardening plots for RP BA at 25°C, -78° C, and -187°C. · · · 61

Figure 4.14 -Yield stress as a function of temperature for continuously annealed material predeformed by cold rolling to $\varepsilon_t \approx 0.35$, 0.65 and 0.90. · · · 62

Figure 4.15 - Flow behaviour of predeformed RP CA grade tested parallel to the subsequent cold rolling direction as a function of temperature compared to the flow behaviour for the undeformed material. · · · 63

Figure 4.16 - Percent fracture mode for RP CA and RP BA tested in tension as a function of temperature. · · · 63

Figure 4.17 - Ductile fracture by microvoid coalescence. Batch annealed material tested at 25°C. · · · 64

Figure 4.18 - a) Partial delamination crevice for continuously annealed material tested at -75°C b) Inside delamination crevice, batch annealed material tested at -40°C. · · · 64

Figure 4.19 - Delamination and intergranular separations for continuously annealed material tested at -140°C. · · · 65

Figure 4.20 - Elongated grain bridging intergranular delamination crevice, batch annealed tested at -75°C. b) Delaminated grains are not as elongated for batch anneal material tested at -165°C. · · · 65

Figure 4.21 - Intergranular delamination in through-thickness direction and width direction in batch annealed material tested at -75°C. · · · 66

Figure 4.22 - Micrographs of batch annealed sample pulled at -184°C a) Intergranular fracture mixed with microvoid coalescence, fractograph from middle width of sample b) Intergranular fracture showing elongated grains, fractograph from outer width of sample. · · · 66

Figure 4.23 - Intergranular fracture observed after uniaxial plastic deformation, continuously annealed material tested at -187°C. · · · 67

Figure 4.24 - Intergranular fracture in a) continuously annealed material and b) batch annealed material tested at -196°C. · · · 67

Figure 4.25 - Intergranular fracture of continuously annealed steel tested in tension at -196°C. At high magnifications slip bands are not visible on the intergranular facets due to their absence or due to limiting depth resolution of SEM. · · · 67

Figure 4.26 - Cold rolled 35%, tested in transverse direction at -196°C, b) cold rolled 90%, tested in transverse direction at -196°C. · · · 68

Figure 4.27 - Continuously annealed material cold rolled a) 65% and b) 90% and tested in the rolling direction at -196°C. · · · 68

Figure 4.28 - Cup wall height of deep drawn cups as a function of radial position and draw ratio 0.8 mm gage steel. · · · 70

Figure 4.29 - Height and thickness variation as a function of radial position along top of lathed deep drawn cup for a draw ratio of 2.2. · · · 70

Figure 4.30 - Progression of earing for cylindrical flat-bottomed deep drawn cups, 0.8 mm gage continuously annealed material, as a function of draw ratio. · · · 70

Figure 4.31 - Load versus stroke data during cup drawing as a function of a) draw ratio and b) sheet thickness. · · · 71

Figure 4.32 - Load versus stroke data during cup drawing comparing different die geometries. · · · 71

Figure 4.33 - a) Strain in drawing direction, ε_1, and b) circumferential direction, ε_2, along RD as a function of cup wall height for different draw ratios. · · · 72

Figure 4.34 - Principal strain in drawing direction in RD, TD and 45° and b) effective strain, $\bar{\varepsilon}$, in RD for a draw ratio of 1.65,1.8,2.2 and 2.4 for the 0.8mm gage material. · · · 73

Figure 4.35 - Principal strains ε_1, ε_2 and ε_3 along RD and b) Principal strains in RD for partially drawn cup with flange left on compared to DRs of 1.65 and 1.8. · · · 73

Figure 4.36 - Vickers microhardness as a function of cup wall height for different DRs (in RD). · · · 74

Figure 4.77 - Discrete plot of θ / *l* stereographic projection for a) uncracked and b) cracked.grain boundaries from batch annealed deep drawn sample. · · · · · · · · · · · · · · · · · · · 91

Figure 4.78 - STEM micrographs and the associated XEDS spectra for the continuously annealed grade. · 93

Figure 4.79 - Example of EELS spectrum used to determine the foil thickness. · · · · · · · · · · · · 94

Figure 4.80 - Grain boundary composition for carbon, boron, phosphorus as a function of position across a grain boundary in a low P IF sheet steel determined using a 3-dimensional atom probe combined with field ion microscopy (Seto et al., 1999). · · · · · · · · · · · · · · · · · · · 95

Figure 4.81 - STEM micrographs and the associated XEDS spectra for the batch annealed grade. · 95

Figure 4.82 - Solute enrichment factor versus solute solubility (Hondros and Seah 1983). · · · · · · 97

Figure 4.83 - Error in the corrected grain boundary concentration as a function of foil thickness for phosphorus in α-iron, an accelerating voltage of 200 kV, and a grain boundary width of $3a_o$. · 97

Figure 4.84 -Crystal and sample orientation distributions for batch and continuously annealed as-received material. · 98

Figure 4.85 - Crystal and sample orientation distributions for batch and continuously annealed deep drawn material. · 99

Figure 4.86 - Inverse texture plot from EBSD data for batch annealed material. · · · · · · · · · · 100

Figure 5.1 - Davidenkov diagram depicting the DBTT for undeformed material a). For the DBTT to remain constant with cold work the IGF stress must increase the same amount as the flow stress b). For a downward shift in the DBTT the IGF stress must increase more than the flow stress c). · 104

Figure 5.2 - a) An initiated crack in an infinite isotropic elastic medium b) Two orientations were used to model the initial geometry of the hexagonal grains. · 107

Figure 5. 3 - a) Deep drawn cup of rephosphorized IF steel sheet b) Idealized microstructure for two different levels of strain and c) the associated optical micrographs of the microstructure (1 and 2 are the directions of major and minor strains respectively in the plane of the sheet, and 3 is the through-thickness direction). · 107

Figure 5.4 - Predominantly intergranular fracture in a continuously annealed rephosphorized IF sheet steel tested in uniaxial tension in liquid nitrogen (-196°C). · · · · · · · · · · · · · · · · · · · 109

Figure 5.5 - Fracture maps for the undeformed microstructure for grain orientation 1, grain orientation 2, the minimum and average fracture envelopes. · 110

Figure 5.6 - Intergranular fracture criteria and the effect of hydrostatic pressure on the IGF stress. · 111

Figure 5.7 - Forming limit diagram for a RP IF steel. The IGF stress, expressed as an equivalent strain, increases in the direction of the major applied strain for all strain paths · · · · · 112

Figure 5.8 - Buckling of batch annealed rephosphorized IF sheet steel during deep drawing (drawing ratio=2.2) leading to an intergranular crack down the cup wall and b) the associated micrograph of the fracture surface. · · · 112

Figure 5.9 - Uniaxial tensile test data for continuously annealed IF sheet steel tested at -187°C and the predicted evolution of the IGF stress, and the associated scanning electron micrograph of the fracture surface. · · · 113

Figure 5.10 - Evolution of the intergranular fracture and yield surface in the plane of the sheet for a) pure drawing and b) plane strain rolling deformation c) uniaxial tension and d) pure biaxial stretching. · · · 114

Figure 5.11 - Evolution of IGF stress and flow stress with primary and secondary forming operations. · · · 115

Figure 5.12 - The FLD is roughly divided into two areas: 1) the material is susceptible to IGF in the prior compressive direction, 2) the material is susceptible to IGF in the plane of the sheet. · · 115

Figure 5.13 - Change in IGF stress with strain for a pure drawing operation and an applied tensile stress in direction 2 as the secondary operation for different assumed initial fracture stresses (average k_I criteria). · · · 116

Figure 5.14 - a) Grain size dependence of the IGF stress based on the Griffith fracture stress (equations and), and the consequence of changes in segregation levels, grain shape and crack size. · · · 117

Figure 5.15 - Modeling competition between TGF and IGF by using a statistical approach. · · · · 118

Figure 5.16 - Probability of IGF in the prior compressive direction with deep drawing strain for fully brittle material with different initial values of the IGF stress normalized by the TGF stress. · · · 118

Figure 5.17- Intergranular delamination during uniaxial tension at –78 °C for a) an optical micrograph of the 1-3 plane, b) a scanning electron micrograph of the fracture surface (2-3 plane), and c) the highly flattened and elongated grains (near plane strain deformation) inside the intergranular delamination crevice. · · · 119

Figure 5.18 - Maximum through-thickness stress as a function of the uncorrected flow stress for different measured flow stresses and notch acuities. · · · 120

Figure 5.19 - Example of notch profile sectioned from the middle of the width for batch annealed uniaxial tensile specimen tested at -40°C. · · · 120

Figure 5.20 - Measured and predicted transition temperatures as a function of true effective strain. · · · 121

Figure 5.21 - Davidenkov diagram illustrating the evolution of the transition temperature with deep drawing for three different steel chemistries. · · · 122

Figure 5.22 - Cold work embrittlement transition temperature versus draw ratio for different grades of low carbon and interstitial-free steels (Oka and Takechi 1987). · · · 123

Figure 5.23 - Predicted evolution of the transition temperature with deep drawing deformation for three different grades of sheet steel. · · · 123

Figure 5.41 - Isoconcentration lines comparing the kinetics of grain boundary segregation for a static grain boundary to a moving grain boundary, for P in -iron, for different driving pressures for recrystallization. 144

Figure 5.42 - Isoconcentration contours for static and moving grain boundary for concentrations of a) 0.01 and b) 0.06 wt% P and a 10 MPa driving pressure. 144

Figure 5.43 - a) Isoconcentration contours for a bulk concentration of 0.01wt% P and a driving pressure of 15 MPa and b) the dynamic equilibrium concentration as a function of temperature for the same conditions. 145

Figure 5.44 - Isoconcentration contours for static grain boundary for an assumed initial grain boundary concentration of 0.06 wt.% and 6.0 wt.%. 145

Figure 5.45 - Simulation of segregation kinetics for continuous annealing recrystallization heat treatment, 820°C for 40s, heating rate of 50°C/s and a driving pressure of 2 MPa. 146

Figure 5.46 - Simulation of segregation kinetics for continuous annealing recrystallization heat treatment, 805°C for 40s, heating rate of 50°C/s and a driving pressure of 2 MPa. 146

Figure 5.47 - Simulation of segregation kinetics for continuous annealing recrystallization heat treatment, 790°C for 40s, heating rate of 50°C/s and a driving pressure of 2 MPa. 147

Figure 5.48 - Simulation of segregation kinetics for continuous annealing recrystallization heat treatment, 820°C for 40s, heating rate 200°C/s and a driving pressure of 2 MPa. 148

Figure 5.49 - Simulation of segregation kinetics for continuous annealing recrystallization heat treatment, 820°C for 40s, heating rate 15°C/s and a driving pressure of 2 MPa. 148

Figure 5.50 - Simulation of segregation kinetics for comparing industrial batch annealing with industrial continuous annealing heat treatment for both dynamic and static analysis. 149

Figure 5.51 - Recrystallization behaviour as a function of phosphorus content in cold rolled high purity iron at 550°C (Inagaki 1988). 150

Figure 5.52 - Geometry for an incident electron beam penetrating a grain boundary with a triangular or square concentration profile of width δ 152

Figure 5.53- Modified potential well for different grain boundary structures. 154

Figure 5.54 - Transition temperature as a function of draw ratio for a change in grain size for rephosphorized unprotected grade of IF sheet steel. 157

Figure 5.55 - Smooth and jagged grains (Sadosvsky, Bogacheva and Umova 1972). 158

Figure 5.56 - Variation of transition temperature as a function of Fe content in the galvannealed coating of Ti-Nb stabilized low phosphorus IF sheet steel (Lau, De Cooman and Vermeulen 1998) 158

Figure A.1- Classification of drawing quality according to r-value and total elongation. 164

Figure B.1- Schematic of geometry used to derive the circumferential strain rate for a given ram velocity in the cup expansion test. 165

Figure C.1- Coordinate system and notation for analysis of bending. 166

LIST OF TABLES

1.0 INTRODUCTION

Steel sheet is an important class of structural material; of the 242 million metric tons of steel exported worldwide, 48 million metric tons were steel sheet products (International Iron and Steel Institute 2000). The primary consumer of cold rolled sheet is the automotive industry. Therefore, the requirement of sheet steel as a structural material in the automobile has driven many of the improvements in formability. Steel sheet presently accounts for roughly one half to two-thirds of the total steel material used in the average automobile. The need for steel sheet with excellent functional properties, including improved formability, shape stability (little elastic springback), good surface appearance, weldability, energy absorption, corrosion resistance, and fatigue strength, has been intensified by direct competition from lightweight aluminum alloys and from reinforced plastics.

The ability to produce complex shapes, in a reduced number of stampings, with increased strength to reduce vehicle weight, has required a great deal of research into the variables that influence the forming and post-formed properties. The main parameters that influence the cold formability of steel sheet are related to i) intrinsic properties of the material, ii) microstructure, which, for a given chemistry, is determined by the thermo-mechanical processing and the strain path, iii) tool geometry and lubrication, iv) stress state, both local and global, and iv) heterogeneities present including surface defects or inclusions. These factors are not independent; for instance, damage by growth and coalescence of voids, which depends on the size and distribution of second phase particles, is a function of the stress state and strain path. These in turn are influenced by the interaction between the lubrication, tooling and workpiece.

Removing the interstitial elements, such as carbon and nitrogen, from ferrous solid solution improves the response needed for severe forming operations. This approach has lead to the development of interstitial-free (IF) sheet steels in which titanium and/or niobium are added to the steel to form carbides and nitrides with the interstitial carbon and nitrogen atoms. Interstitial-free steels were first patented in the 1970s by Armco Steel Corporation (now AK Steel) but did not come into wide scale production commercially until advances in vacuum degassing and continuous annealing technologies were developed. Presently, ultra low carbon steels (ULC), steels with a carbon content less than 50 parts per million, are used to make IF sheet steels, but the same technology is being applied to develop high strength (HS) IF steels, stainless IF steels, and bake hardening steels. These ULC IF steels have extraordinary cold formability and resistance to strain aging and are therefore used mainly for automotive applications where excellent formability and stringent quality control are required.

Although interstitial-free sheet steels exhibit excellent cold formability, the occurrence of brittle fracture can limit their usefulness. The brittle fracture is primarily intergranular in character and is in competition with plastic flow during the primary or secondary forming operations or during in-service use. This phenomenon has been called cold work embrittlement (CWE), secondary work embrittlement (SWE), strain induced embrittlement, or 'longitudinal cracking' (Tsujimura et al. 1974), as the cracks usually propagate in the drawing direction. Interstitial-free steels are especially susceptible to intergranular fracture, as there is little free carbon in solid solution left to segregate to the grain boundaries, where it is thought to compete for sites at the grain boundary with impurity elements (or equivalently directly repel impurity atoms) and/or directly strengthen the grain boundary (Suzuki et al. 1983). In the absence of free carbon, grain boundary segregation of impurities or alloying elements, such as P, Sn, Si, S and As (especially group IVB to VIB elements) is increased, which then further weakens the grain boundaries. The lack of carbon and increased segregated impurity elements at the grain boundaries coupled with an increase in the flow stress from cold working results in intergranular fracture especially in the direction of the prior compressive strain.

Cold work embrittlement has been recognized as a significant industrial problem and has been extensively investigated over the past 10 years as there is potential for failure during fabrication and in the post-formed component, (Oka and Takechi 1987, Bhat et al. 1994, Bleck and Heßling 2000). Automobile manufacturers, such as General Motors, have recently set standards for resistance to CWE. To help clarify this situation, the steel industry has conducted round-robin testing to standardize the most common test used to evaluate for susceptibility to CWE, the cup expansion test. The need for improved forming characteristics, and increased strength, necessary for weight reduction and dent resistance, has lead to the continuing development of HS IF steels such as rephosphorized (RP) IF sheet steel. These HS IF have good forming characteristics and strength. However, with an increase in strength there is usually a tendency towards more brittle behaviour. As well, increased scrap metal is being used during the steelmaking process. This leads to a higher concentration of embrittling tramp elements, such as As and Sn in the steel, which then leads to decreased resistance to CWE (CRM Annual R&D Report 1995, Neutjens, Mathy and Herman 1997).

The main objective of this research was to investigate the occurrence of intergranular fracture in IF steel sheet. The work set out to define the basic mechanical and microstructural factors which control CWE. There are various areas in the field that have been studied extensively and are well accepted and understood; refer to the reviews by Yan and Gupta (1998) of Inland Steel, Lewis et. al. (1998) of British Steel (now Corus Steel) and Li, Heßling and Bleck (1999) of Aachen University. There are also other areas that need to be clarified in order to obtain a better understanding of CWE. The current work was undertaken to primarily focus on these less well understood issues. This research attempts to relate the thermal history and mechanical processing to the susceptibility to grain boundary fracture by considering the bulk properties derived from the tensile test and the cup expansion test, and to relate the local grain boundary chemistry and structure to the propensity for grain boundary fracture.

On a macroscopic scale it is worth developing and testing criteria that can be used to predict the occurrence of intergranular fracture in formed parts. For these criteria to have predictive capabilities the bulk mechanical properties, such as the fracture and flow behaviour, must be accurately characterized. The fracture properties were characterized by measuring transition temperatures and the intergranular fracture stress from uniaxial tension tests on annealed and predeformed material, and by measuring the transition temperatures on well-characterized deep drawn cups using the cup expansion test. This test involves expanding the deep drawn cup over a conical punch, for a variety of thermo-mechanical conditions. The flow behaviour was characterized by measuring the flow curves as a function of temperature, the strain rate sensitivity, the r-value, the grain size, and the bulk crystallographic texture.

Grain boundary fracture can be studied on a mesoscopic scale, as the grain boundary structure varies with position throughout the microstructure. This was accomplished by investigating the relationship between grain boundary structure, grain boundary segregation, and grain boundary fracture. Local grain boundary chemistry and the inherent connection to the local grain boundary structure is pivotal as to whether intergranular fracture occurs. Analytical electron microscopy, with a field emission gun (FEG) transmission electron microscope (TEM), coupled with X-ray energy dispersive spectroscopy (XEDS), allowed grain boundary segregation levels to be quantified. The relationship between the grain boundary structure and intergranular fracture was then studied by analyzing the intergranular fracture path with an automated electron back-scatter diffraction (EBSD) with a FEG scanning electron microscope (SEM).

The thesis is organized as follows. Chapter 2 is a literature review and is divided into three pertinent subsections - the first a review of cold work embrittlement, the second a critical appraisal on the mechanics and mechanisms of intergranular fracture, and the third a summary of the thermodynamics and kinetics of grain boundary segregation. The experimental methods used are described in Chapter 3. Chapter 4 presents the experimental results. Chapter 5 is divided into two sections, both of which provide a basic scientific framework to understand and evaluate the CWE in terms of both the current results and examples taken from the literature. In order to do so, two models were developed; one predicts the occurrence of CWE for various forming operations by considering the key microstructural parameters in the competition between brittle fracture and plastic flow, the other predicts the extent of segregation during recrystallization annealing and hence the associated level of embrittlement. Finally, Chapter 6 contains a summary of the salient features extracted from the experimental results and modeling, and gives suggestions for future work.

2.0 LITERATURE REVIEW

The literature review is divided into three sections. The first is a current review of status of cold work embrittlement, the second is a critical appraisal on the mechanics and mechanisms of intergranular fracture, and the third a summary of the thermodynamics, kinetics and structural aspects of grain boundary segregation. Different alloy chemistries, thermo-mechanical processing and coatings are used for IF sheet steels. These in turn influence the steel's susceptibility to cold work embrittlement. Therefore, to familiarize the reader with the terminology of IF sheet steels, a brief review of the physical metallurgy of IF sheet steels is given in Appendix A.

2.1 Cold Work Embrittlement

The occurrence of brittle primarily intergranular fracture during or after cold forming low carbon or IF steels forms the impetus for the present research. The terminology describing this phenomenon (e.g. CWE, secondary work embrittlement, and strain-induced embrittlement) offers insight into the conditions that promote this mode of failure. Fracture most readily occurs during secondary cold working. The fracture process is always associated with some proportion of brittle intergranular fracture. Fracture entirely associated with a transgranular fracture process is not cold work embrittlement and is taken as a baseline. Therefore, the study of CWE focuses on the study of intergranular fracture and the conditions which promote this form of fracture through thermo-mechanical processing and subsequent forming. Cold work embrittlement can be viewed as a competition between plastic flow and brittle fracture. Conditions that promote brittle fracture by increasing the flow stress include cold work, a decrease in temperature or an increase in strain rate, while conditions that promote brittle fracture by decreasing the fracture stress include grain boundary segregation of embrittling elements and an increase in grain size. Cold work embrittlement usually occurs after deep drawing, with cracking occurring in the drawing direction. Deep drawing of the steel serves to raise the flow stress and aligns the grains of the steel is such a way that aids the fracture path in following the grain boundaries.

2.1.1 Historical Development

It is well established that the removal of interstitial elements from solid solution in relatively pure iron can result in a change in fracture mode from transgranular to intergranular. Low and Feustel (1953), after decarburizing a low carbon rimmed steel in wet hydrogen, found a transition from transgranular fracture to intergranular fracture when tested at -195°C. Subsequently, a recarburization treatment restored the fracture mode to transgranular. Teshima and Shimizu (1965), while working on recrystallization of decarburized low carbon steel, were the first to show increased embrittlement in the prior compressive direction after a critical

drawing ratio during the secondary working stage, and in doing so pioneered the use of the cup expansion test (CET) (Figure 2.10). As IF steels came into commercial production in the late 1970s, the first papers documenting CWE were published (Konishi, Nishida and Onashi 1974) (Konishi, Kohara and Tanaka 1977) (Matsudo et al. 1977) (Gupta and Scime 1979). A number of papers, many published in Tetsu-to-Hagane, appeared over the course of the 1980s, while by the end of the decade and during the 1990s an increasing number of papers dedicated to or mentioning CWE were published, mostly in conference proceedings devoted to IF sheet steels.

As a class of steels, IF sheet steels are inherently prone to grain boundary embrittlement since little carbon is left to segregate to the grain boundaries. Carbon is thought to a) directly strengthen the grain boundary and b) indirectly strengthen the grain boundary by reducing the amount of embrittling elements through site competition and/or repulsive interaction. Without free carbon, grain boundary segregation of impurities elements such as P, S, As, Sn, Sb and Si (generally group IVB to VIB elements) is promoted which then weakens the grain boundaries leading to embrittlement. IF steels are not the only steels reported to be susceptible to CWE. Charpentier and Piehler (1980) have noted increased susceptibility to IGF in the prior compressive direction for a low carbon AK and a V-N HSLA steel with increased levels of deep drawing (Figure 2.1). As well, CWE has been observed in a batch annealed phosphorized low carbon steels (Gupta and Scime 1979) and also in aluminum-killed steels which have been heavily redrawn (Lewis 1998, 31). Sudo, Tsukatani and Shibata (1982) have observed mixed intergranular and transgranular fracture for a batch annealed AK dual phase steel (ferritic and martensitic) with high phosphorus levels by using a ring expansion test on specimens cut from deep drawn cups. Interstitial-free based ferritic stainless steels have also been shown to be susceptible to CWE (Takahashi and Sumitomo 1998).

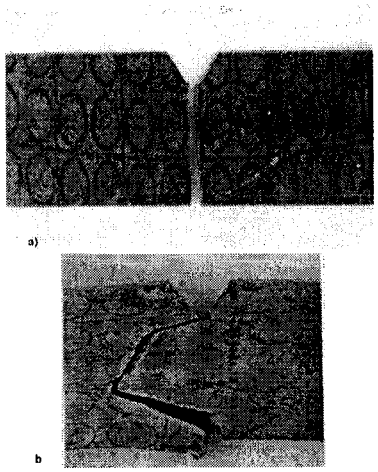

Figure 2.1 - Fractured Charpy specimens taken from the flange of a deep draw cup (Charpentier 1981, 176) and fractured in drawing direction and perpendicular to drawing direction. Energy absorbed was lower in sample a).

2.1.2 Examples of CWE - Occurrence of CWE in Service

Although there have been few documented cases of CWE in service in the automotive industry, there have been many cases of CWE during press forming. One noted example of an in-service failure was reported by Volkswagen. They attributed the failure of a door hinge to CWE (Hood 1998), however to the authors knowledge, no automobile manufacturers have systematically inspected parts made of IF sheet steel after failure during press forming or after in-service impact for brittle intergranular fracture. Therefore, the question remains as to the real extent of IGF during in-service failures. Steel makers have generally conceded that the

industrial test to probe susceptibility to CWE (which will be described shortly) has not been linked to in-service performance (Lewis et al. 1998). Attempts to determine in-service performance have involved dropping weights on manufactured parts formed out of IF steel in a cold room. For instance, Stelco have tested rephosphorized (RP) IF steel formed into a structural automobile bumper by dropping a 45.4 kg weight from a height of 5 meters at a temperature of -20°C (Hood 1998). The part failed by IGF in areas that were not necessarily the most severely deep drawn. British Steel (Lewis 1998) has performed similar tests, dropping a 16 kg weight from a height of 10 meters on a structural member of a RP Ti IF grade maintained at -30°C, which had previously failed a laboratory test at room temperature. After impact, a small intergranular crack of 40 mm was observed on the flange radius.

On the other hand, IF sheet steels have been heavily used by the automotive industry without any *major* problems for some time now. But the likelihood of CWE increases as the need for increasing shape complexity and strength required for greater production efficiency and vehicle weight reduction is met by more severe deformations and stronger materials. Also, an increase in the amount of scrap due to the recycling of steel can lead to an increase in tramp elements such as tin and arsenic. This is a concern, as tin is a more potent embrittling element than phosphorus (Neutjens, Herman and Leroy 1998). Therefore, a desire for increased severity of deformation, and increased strength, and a possible increase in embrittling elements, points to the need for a fundamental and comprehensive understanding of CWE.

2.1.3 Industrial Measurement of CWE

Several tests have been developed to evaluate the susceptibility of sheet steel to CWE, but as of yet, there are no industry wide standards. The most commonly used test to evaluate a steel's likelihood for CWE is the cup expansion test (CET), although a bending and unbending test, a cup side crushing test, Charpy tests, uniaxial tensile tests, and a biaxial stretching test (Lewis 1998) have also been used. Test methods can be divided into tests where a deep drawing process is applied before the sample is tested, which is the case for tests involving cup drawing, or tests without pre-deformation or with pre-deformation that is not classified as deep drawing, which is the case for Charpy tests, uniaxial tension tests, biaxial tension tests and unbend-bend tests. The material's susceptibility to CWE is evaluated by determining a ductile-to-brittle transition (DBT) as a function of temperature (at constant strain rate and draw ratio), draw ratio (at constant temperature and strain rate) or strain rate (at constant temperature and draw ratio).

The tests have been found to produce widely varying results, ensuing from differences in test procedure, specimen geometry, the amount and method of applying the primary strain, the way the secondary working process is applied and the evaluation criteria used. It is therefore recognized that CWE test results are strongly dependent on the specific test procedure and caution has to be exercised in applying the laboratory test results to practical situations.

2.1.3.1 Cup Drawing Tests

Because deep drawn material is the most vulnerable to CWE, cup drawing is used to simulate the primary working process. For a review of the cup drawing process see Backhofen (1966) or the ASM Handbook on Forming and Forging (1988). Cups are deep drawn using for instance, either a Swift round or flat bottomed punch. Redrawing has been used to obtain draw ratios greater than 2.4 (Takahashi et al. 1982). The secondary working process is then simulated by expanding the mouth of the cup over a cylindrical punch, as in the cup expansion test (CET), or by crushing the cup on its side, as in the side crushing test. Both of these secondary processes result in an applied primarily tensile stress in the circumferential direction of the cup. The load can be applied statically, using a universal testing load frame, or dynamically, via a drop weight; the strain rates attained are generally between 0.0001 s^{-1} and 100 s^{-1}. The CET is by far the most commonly used test and has recently been used in round robin testing by a group of North American steel producers (Yan and Gupta 1998). Temperature is usually the independent variable, although draw ratio has also been used. A ductile-to-brittle transition plot is then constructed by plotting the chosen evaluation criterion, which include a pass/fail, percent brittle crack length or energy absorbed, versus the independent variable.

There are many variables which can have a significant influence on the results. These can be divided into cup drawing variables (draw ratio, amount of ironing, the die profile radius and die clearance, gage of the sheet), cup expansion test variables (edge condition, the effective strain rate of the expanded cup, the geometry of the punch used to expand the cup, whether the cups are immersed in the cooling bath) and material parameters (type and extent of segregation, grain size, strain rate sensitivity, work hardening characteristics, distribution of grain boundary structures, anisotropy of the yield and hardening) which are heavily influenced by the material chemistry and thermo-mechanical processing. These variables are not entirely independent, for instance, the punch geometry will affect the applied strain rate, but the material's strain rate sensitivity will provide the response to that variable.

2.1.3.2 Bend-Unbend Test

The bend-unbend test, developed at Armco Inc. by Henning (1992) involves bending a rectangular blank to a 0t radius, cooling the sample to the desired test temperature, and then unbending the sample. The sample is given a pass rating if metal/metal contact is maintained near the original bend and a fail rating is given if the piece cracks at the original bend. This process is conducted at a variety of temperatures until a transition temperature is found. The advantages of this test include ease of execution and low cost. However, the test has not gained favour in industry since the results are not reproducible (Thomson 1996) due to the manual bending and unbending procedure. Yan and Gupta (1996) have shown that the strains developed in the inner bend radius for a 0t bend are similar to those in deep drawn cups. Plane strain conditions prevail on the inner surface of the 0t bend specimens and are comparable to the stain levels to a drawn cup with a draw ratio of 2.4. On the inner bend radius, the grains are flattened in the plane of the sheet, like in cold rolling. Unbending allows a

tensile stress to act against the flattened grains. The transition temperatures obtained by comparing the bend-unbend test and the cup expansion test with the same material are comparable (Yan and Gupta 1996) (Henning 1992).

2.1.3.3 Charpy Tests

The Charpy test has often been used to evaluate the DBTT of materials. It is the preferred method of evaluating hot rolled materials and is usually performed on undeformed specimens. Sub-size Charpy specimens have also been cut out of the cup walls (Matsudo et. al. 1977) (Martin et al. 2000) and flange (Charpentier 1981) of deep drawn specimens in both radial and longitudinal directions.

2.1.4 Influence of Chemistry and Thermo-Mechanical Processing on CWE

The effect of material chemistry and thermo-mechanical processing is by far the most studied aspect of CWE. Many, if not most, studies on CWE compare different steel chemistries for their susceptibility to CWE by varying the bulk content of P, the free C and B additions. The steel chemistry affects the embrittlement phenomena by influencing the grain boundary cohesive strength and the flow strength. Grain boundary strength is affected by the amount and potency of the embrittling agent (such a P or Sn) and the amount of beneficial strengthening elements (C or B) at the grain boundary. Carbon and boron compete with impurity elements for sites at the grain boundary and also directly strengthen the grain boundary. The amount and type of elements at the grain boundary also exert a drag force on the grains during recrystallization annealing and, along with the fine dispersion of precipitates, controls the size of the grains. The grain size influence on the fracture and flow stress will be discussed in section 2.2.

2.1.4.1 Influence of Annealing Cycle on CWE

Recrystallization heat treatments, applied to the cold rolled sheet, have a significant effect on CWE. Pradhan (1994) has provided evidence showing that, for a wide range of steel chemistries - including steels with different levels of excess Ti, residual P levels, and added P or Mn for solid solution strengthening - batch annealed steel is more brittle than continuously annealed steel. The CET test was used with a draw ratio of 2.1 with cups trimmed to a height of 40 mm, and expanded over a cone with an apex of 60° at 25mm/hr. Yan (2000) reports a 60 °C (20 °C compared to -40 °C) increase for a batch annealed grade compared to a continuously annealed ELC-IF grade (CET, DR 2.4, impact). Meyer, Bleck and Muschenborn (1994) have also studied the effect of the annealing treatment on CWE for a range of compositions (Figure 2.2). In all cases batch annealing leads to higher transition temperatures. Batch annealing (longer times, lower temperatures) generally promotes more complete segregation of P in IF steels compared to continuous annealing (shorter times, higher temperatures).

2.1.4.2 *Influence of Chemistry on CWE*

The vast majority of work on CWE has been aimed at showing the embrittling effect of P, and the anti-embrittling effects of boron and carbon. Generally, P increases the DBTT, while boron and free carbon lower the DBTT. Phosphorus, present as a residual impurity element, is also added to steel as it is the most efficient (in terms of the increase in strength per wt.%) and economical solid solution strengthener, and has the least adverse affect on formability, compared to Mn or Si.

Takahashi et al. (1982) studied the effect of P and B additions on CWE in a Ti stabilized ULC IF steel. The CET was used with cups of different draw ratios tested at 0 °C. The critical draw ratio decreased with increasing P content, while the addition of 60 ppm B to the 0.06 and 0.1 P wt% grades significantly increased the critical draw ratio (Figure 2.3). Rege (1997) has studied Ti and Ti-Nb stabilized IF sheet steels with and without P additions. The addition of P increases the transition temperature substantially (Figure 2.4). Mega et al. (1996) and Pradhan (1994) come to the same conclusion, P increases the susceptibility to CWE (Figure 2.5). Phosphorus additions increase the likelihood of intergranular fracture and can significantly increase the transition temperature even when boron is added. For example, a change in fracture mode from transgranular to intergranular was reported when the phosphorus content was changed from 0.01 to 0.15 wt% P in a grade with 20 ppm B present (Yasuhara et al. 1994) (Figure 2.6).

The amount of carbon in solid solution, and therefore the amount of carbon free to segregate to the grain boundary, has a large effect on the steels susceptibility to CWE. Various methods are used to adjust the amount of carbon in solid solution. Irie et al. (1982) controlled the aging index, a measurement of the amount of free carbon, by varying the annealing temperature between 800°C and 920°C under a heating rate of 35°C/s and

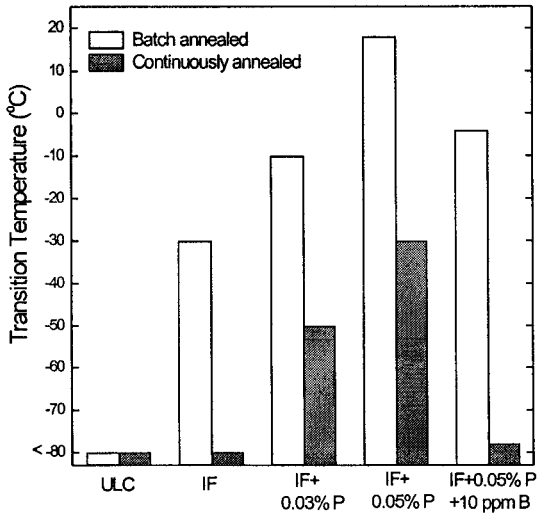

Figure 2.2 - Effect of annealing treatment on the DBTT, CET, DR 2.1, impact (Meyer, Bleck and Muschenborn 1994).

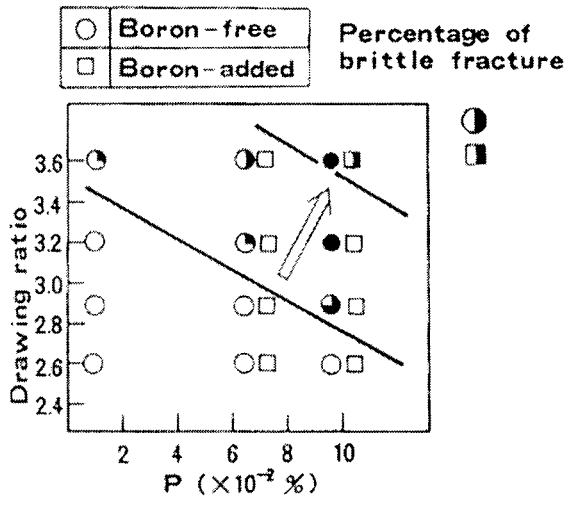

Figure 2.3 - Influence of boron and phosphorus additions on the ductile-to-brittle draw ratio (Takahashi et al. 1982).

cooling of 70°C/s for a ULC 100C-1100Mn-720P-280Ti CA IF steel. The transition temperature decreased with increased aging index as seen in Figure 2.7. Steels with different bulk P content also had the aging index changed by varying the annealing temperature and cooling rates after soaking (1°C/s to about 2000°C/s). Deep drawn cups were tested at 0 °C using the side crush test. The results indicate that free carbon suppresses brittle behaviour, while increased P in the bulk, which would lead to increased P at the grain boundary, encourages brittle behaviour (Figure 2.8). Neutjens et al. (1998) investigated a stabilized, partially stabilized and under-stabilized continuously annealed grade of IF sheet steel with and without P additions. The solute carbon was adjusted by varying the stabilizing (Ti+Nb)/C ratio. Solute carbon provided an effective way to increase the resistance to CWE for both the P added and low P grades as seen in Figure 2.9. Kitamura, Tsukatani and

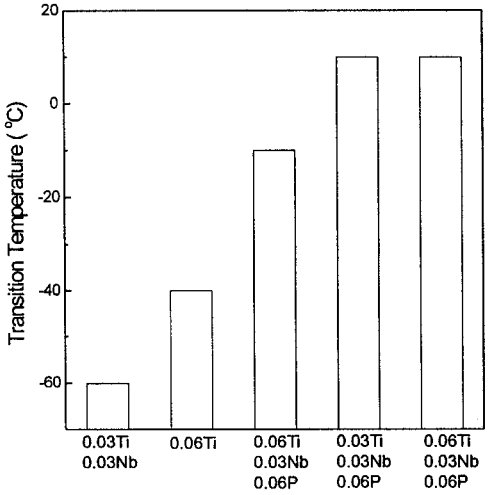

Figure 2.4 - Ductile-to-brittle transition temperature measured by using the CET with a draw ratio of 2.0, trimmed and impact tested (Rege 1997).

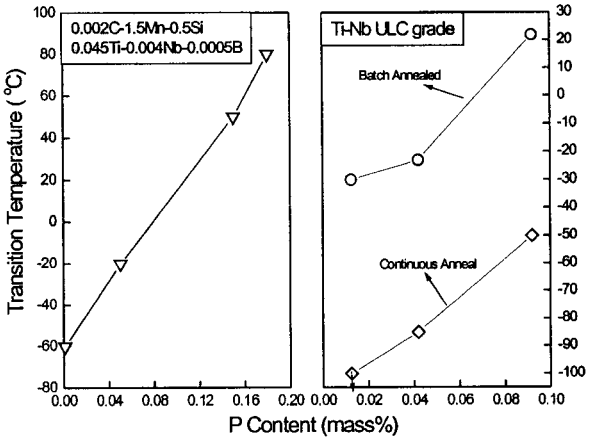

Figure 2.5 - Ductile-to-brittle transition temperature as a function of bulk P content (Mega et al. 1996, and Pradhan 1994).

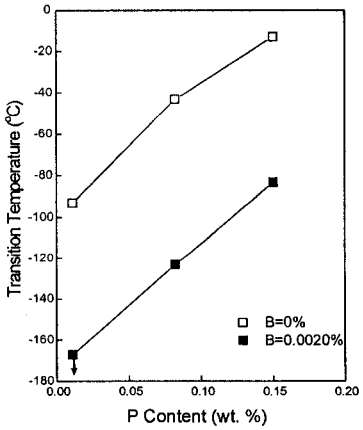

Figure 2.6 - Relation between the transition temperature and P content for a drawing ratio of 1.8 (Yasuhara et al. 1994).

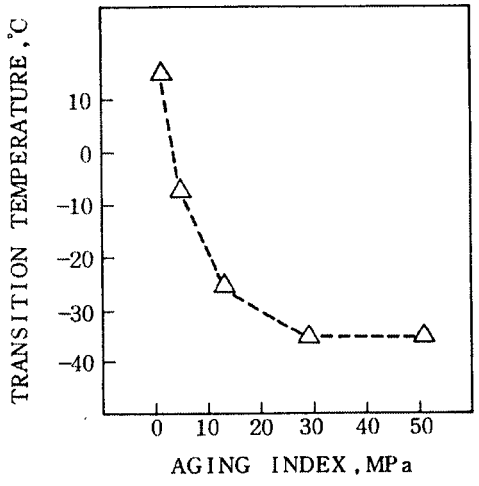

Figure 2.7 - Ductile-to-brittle transition temperature as a function of the aging index (Irie et al. 1982).

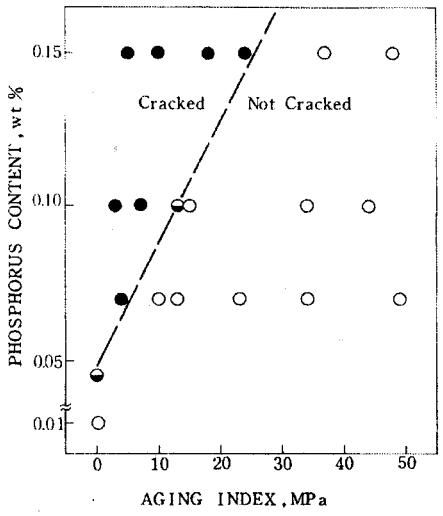

Figure 2.8 - Brittle behaviour of deep drawn cups tested at 0 °C for different phosphorus levels and aging indexes (Irie et al. 1982).

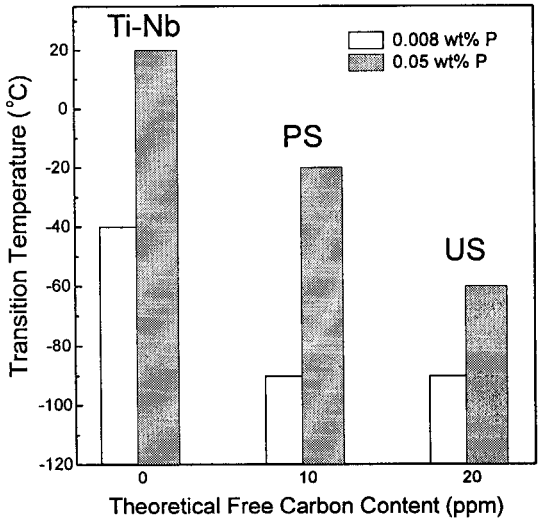

Figure 2.9 - Effect of free carbon on the DBTT for a low P and high P IF steel (Neutjens et al. 1998). Cup expansion test with draw ratio of 2.0, ears trimmed, and impact tested from a height of 1 meter.

Inoue (1994) used a novel technique to investigate the effect of solute carbon on the DBTT. A cold rolled RP Ti ULC steel, annealed in a H_2-N_2 gas containing 3 vol.% carbon monoxide gas, was compared to the same grade annealed in the H_2-N_2 gas without carbon monoxide. The transition temperature was shifted by 35°C, from -63°C for the conventional grade to -98°C for the recarburized grade.

The addition of boron reduces a steel's susceptibility to CWE (Figures 2.2 and 2.6). The addition of up to 12 ppm B reduces the transition temperature by segregating to the grain boundary and impeding segregation of embrittling segregants and by directly strengthening the grain boundary. Boron additions greater than 60 ppm have been reported to reduce the transition temperature in Ti-stabilized grades. In this case, boron preferentially combines with nitrogen forming BN, leaving extra Ti to form precipitates with P, thereby lowering the free P levels and reducing embrittlement. Takahashi et al. (1982) used the CET with cups of draw ratio 2.1 to investigate the effect of boron additions on the DBTT of an ULC Ti-stabilized CA IF sheet steel. The addition of up to 15 ppm resulted in a 20°C drop in the transition temperature; greater additions did not affect the transition temperature. Auger electron microscopy was used with the same steel fractured in situ exposing the intergranular facets. The boron concentration was seen to reach the maximum level in the range of 10 ppm, and remained unchanged for greater amounts. The phosphorus concentration at the grain boundary did not decline until boron levels of 25 ppm which suggests boron can prevent intergranular fracture by directly strengthening the grain boundaries.

2.1.5 Influence of Draw Ratio on CWE

A fundamental aspect of CWE is the increased brittleness with deep drawing. The question must be asked as to why deep drawing increases the susceptibility to CWE more than other modes of deformation. Although deep

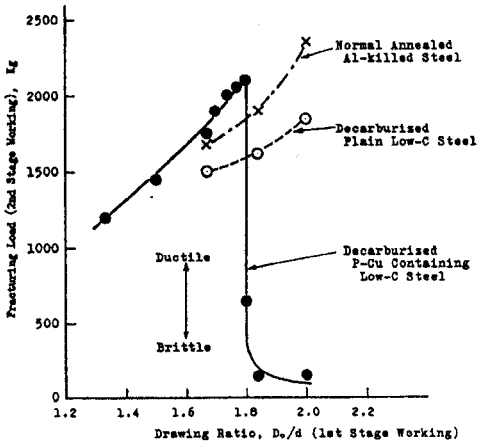

Figure 2.10 - Ductile-to-brittle transition temperature as a function of draw ratio (Teshima and Shimizu 1965).

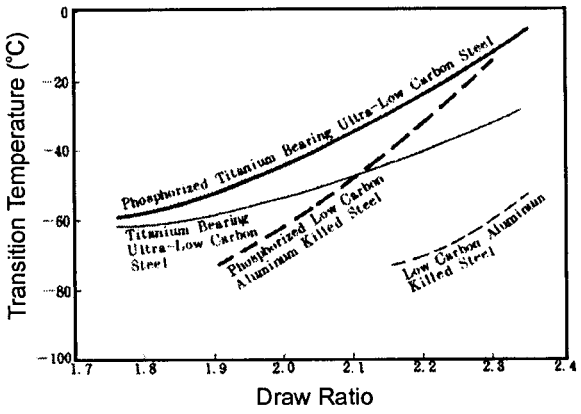

Figure 2.11 - Transition temperature as a function of draw ratio for different grades of steel (Oka and Takechi 1995).

drawing work hardens the materials, raising the flow stress, it also severely elongates the grains parallel to the draw axis. These elongated grains, tested in tension when the cup is crushed or expanded, have been suspected to be the cause of the increased susceptibility to IGF (Gupta and Scime 1977, 266) (Konishi, Ohashi and Yoshida 1974) (Bhat et al. 1994). In fact, the transition from ductile-to- brittle behaviour has often been determined by a critical draw ratio as seen in Figure 2.10. Although the influence of deep drawing is very fundamental to the nature of the embrittlement, it has been relatively ignored compared to the influence of material chemistry and thermo-mechanical processing. Oka and Takechi (1989, reference 29) cite unpublished research showing the variation in transition temperature with draw ratio for different grades of formable sheet steel (see Figure 2.11). The increase in transition temperature with draw ratio depends on the steel chemistry. The draw ratio was found to be the most significant variable in an informal round robin testing

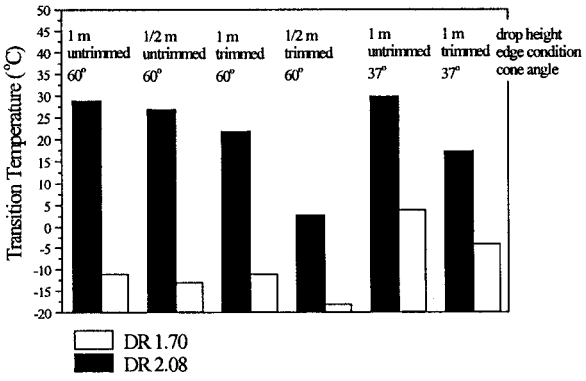

Figure 2.12 - Effect of draw ratio on DBTT with drop height, cone angle, and edge condition as variables (Lewis et al. 1998).

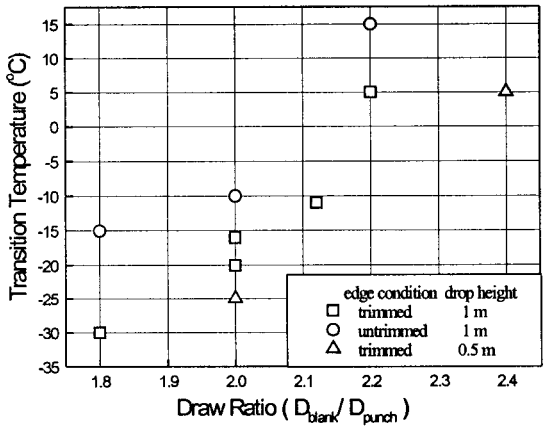

Figure 2.13 - Ductile-to-brittle transition temperature as a function of draw ratio from results of informal round robin testing of North American steel producers (Yan and Gupta 1998).

of the CET (Yan and Gupta 1998). One grade, a Ti ULC BA steel (52C-1800Mn-80P-780Ti), was tested by each company using their existing test conditions. The transition temperatures obtained are plotted as a function of draw ratio in Figure 2.13. Lewis et al. (1998) compared draw ratios of 1.7 and 2.08 for a 41C-5300Mn-460P-680Ti CA IF steel, using the CET with a variety of testing conditions including the drop height, edge condition, and cone angle. An increase of 40°C is reported for most tests (Figure 2.12). Bleck and Heßling (2000) report data for three grades (CA IF Ti ULC, CA IF Ti-Nb ULC, CA IF Ti-Nb ULC P B added, and SULC) of IF steels with draw ratios of 2.0 and 2.4 tested at a strain rate of 70 s^{-1}. The draw ratio had a large influence on the transition temperature, increasing the transition temperature by 41°C, 47°C and 87°C respectively.

2.1.6 Influence of Edge Conditions on CWE

During the CET, fracture initiates at the top of the cup, where it is first expanded and, therefore, the conditions at the top edge of the deep drawn cup are critical. In general, three cases are commonly encountered: a flanged cup, a trimmed cup, and an untrimmed cup. Due to planar anisotropy, ears are formed on nearly all deep drawn cups; these can be trimmed off (usually with a lathe) before testing. Any defects present at the edge of the cup, including ears, wrinkles, or cracks act as stress concentrators and also induce plastic constraint. Trimming the cup removes the ears, material, cracks, defects or burs. It is generally found that leaving the ears on raises the transition temperature by at approximately 10°C or more. Lewis (1998) has shown that the effect of ears are more pronounced at higher draw ratios. The average decrease for the trimmed cups was 4°C for a draw ratio of 1.7, and 15°C for a draw ratio of 2.08 for a 41C-5300Mn-460P-680Ti CA IF steel. Tests conducted at LTV Steel (1996) have shown a 10°C increase in transition temperature for cups with the ears left on. The transition temperature increased from -30°C, -20°C, and 0°C for draw ratios of 1.8, 2.0, and 2.2 respectively (impact 1 m, 50C-2000Mn-100P-820Ti CA IF uncoated). Bhat et al. (1994) noted a 35°C decrease in the DBTT, for a BA Ti ULC steel, when the ears were trimmed off (impact loaded at a draw ratio of 2.41). Wrinkling at the top of the cup presents a more severe defect than earing and can lead to IGF during deep drawing (Boyle et al. 2000). In practice, commercial pressings commonly have the flange left on, although they can be trimmed or punched off. When a flange is left on the most severe deep drawn material is removed from the edge, which generally leads to less brittle conditions. Therefore tests have been done to compare cups not fully drawn (i.e. with the flange left on) to fully drawn cups of the same height. Bhat et al. (1995) found a 35°C decrease in transition temperature between a fully drawn cup (DR 2.03), and a cup of the same height with the flange left on (BA Ti ULC static test).

2.1.7 Strain Rate Effects on CWE

A range of loading rates have been used when expanding the deep drawn cups with typical values between 0.001 mm s^{-1} and 4500 mm s^{-1}. Cups are loaded quasi-statically using a servo-hydraulic load frame and dynamically using a weight dropped from a specified height. The loading rate will specify a strain rate

depending on the cone geometry. Equations used to convert the ram speed into a circumferential strain rate have been provided by Lewis et al. (1998) and Bleck and Heßling (2000), as,

$$\dot{\varepsilon} = \frac{v \sin \theta}{D_p} \tag{2.1a}$$

$$\dot{\varepsilon} = \frac{2v \tan \theta/2}{D_p} \tag{2.1b}$$

where v is the velocity at impact, θ is the apex angle of the cone, and D_p is the punch diameter. The loading rate influences the DBTT through the effect of strain rate hardening, as the intergranular fracture stress is unaffected by the strain rate (Nakamura and Sakaki 1970).

Bleck and Heßling (2000) tested four grades of sheet steel (CA IF Ti ULC, CA IF Ti-Nb ULC, CA IF Ti-Nb ULC P B added, and SULC) comparing a tangential strain rate of 0.04 s^{-1} to 70 s^{-1} for a draw ratio of 2.0. The DBTT increased by about 40°C with strain rate and the percentage of intergranular fracture was found to be independent of strain rate. Bhat et al. (1994) compared dynamic loading (42 s^{-1}) with static loading (0.01s^{-1}) for a BA Ti stabilized ULC steel with draw ratio of 2.41. Dynamic loading increased the DBTT by about 30°C. Li et al. (1999) showed that the DBTT was changed from -87°C to -60°C, for a Ti stabilized IF grade with a DR of 2.0, for a change in tangential strain rate of 0.04 to 2.6 s^{-1}. Figure 2.14 summarizes the results concerning the effect of strain rate on the DBTT. Data was added to the plot of Bleck and Heßling (2000), who made no justification for assuming a linear-log relationship.

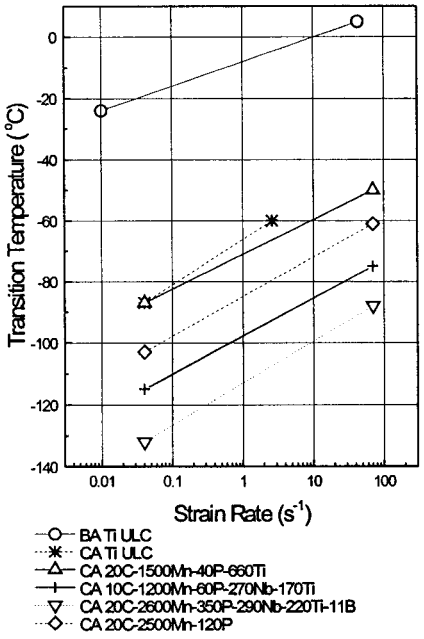

Figure 2.14 - Effect of strain rate on the DBTT. Data adapted from Bleck and Heßling (2000).

2.1.8 Influence of Coating on CWE

Few studies have analyzed the effect of coating on CWE. As mentioned in the processing review section, IF steels are often hot dip galvanized or galvannealed, or electro-galvanized for added corrosion resistance, especially for exposed parts. A comprehensive study was undertaken by Kase et al. (1993) to examine the effect of coating on CWE for four grades of IF steel and one unstabilized grade. The chemistries are given in Figure 2.15. Each grade was evaluated with the CET in the uncoated (CR), galvanized (GI), and galvannealed (GA) state. The B added and unstabilized grades, which are relatively resistant to CWE, show little variation

in transition temperature with coating. The transition temperature of the other three grades of IF steel increased slightly with galvanizing, and increased significantly with galvannealing (see Figure 2.15). Lewis (1998) investigated the effect of galvannealed coating for a 56C-5900Mn-560P-750Ti CA IF sheet steel using the CET with cups of draw ratio 1.7 and impact tested from a height of 1m. The coating was removed prior to and after cup drawing using a concentrated 50% HCl acid solution. No change was found whether the coating was removed prior to or after cup drawing, and a difference in transition temperature of 10°C was found between the galvannealed and stripped cups, -55°C and -65°C respectively.

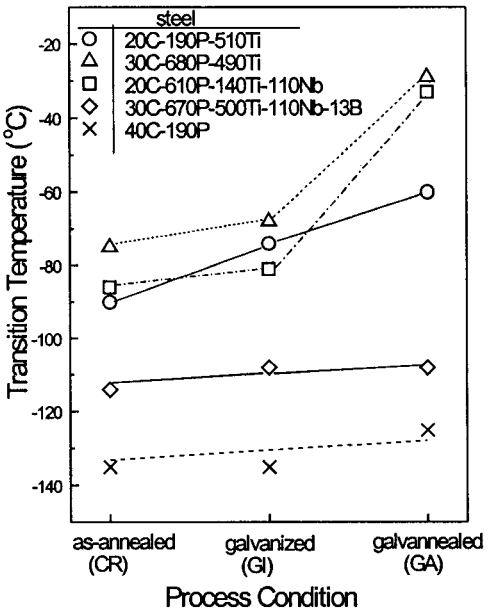

Figure 2.15 - Effect of coating on the transition temperature for trimmed cups with a draw ratio 2.3,and initial sheet thickness of 0.8mm. (Kase et al. 1993)

Lau, DeCooman and Vermeulen (1998) compared an uncoated and a galvannealed Ti-Nb ULC IF RP B added steel. Using the CET they showed that the galvannealed coating, with a nominal Fe content of 10 wt%, increased the transition temperature by about 35°C (from -40°C to -5°C). By varying the Al content of the zinc bath and the galvannealing temperatures a Ti Nb ULC IF grade was produced with varying iron content (1-10%) in the galvannealed coating. The transition temperature was found to depend on the composition of the coating, embrittlement was most pronounced when the coating contained 4% Fe. It was thought that more crack deflection would occur along the substrate-coating interface as the brittle Γ layer more fully developed. This result was corroborated by the work of Tokunaga (1986) who observed that cracks originated from the galvannealed layer tend to propagate in the layer parallel to the steel substrate and cause powdering. The surface of an uncoated steel after drawing is compared to the surface of a galvannealed steel with the coating removed with a HCl acid solution and Fe inhibitor in Figure 2.16. Cracks, due to the galvannealed coating are clearly observed to have propagated into the ferrite substrate. As well, the

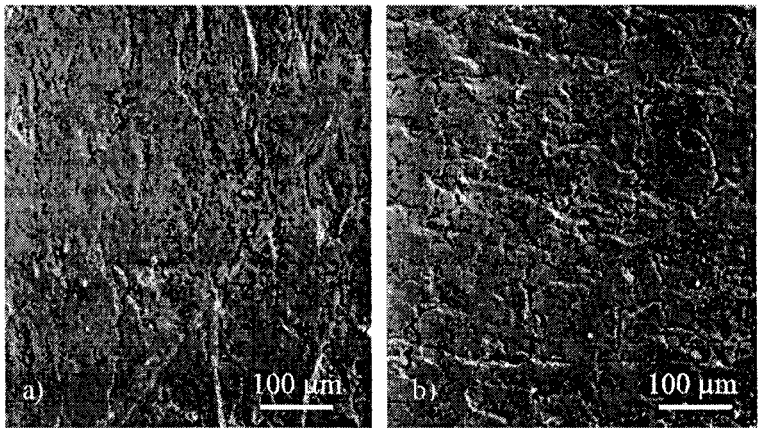

Figure 2.16 - Micrographs of deep drawn cups for an a) uncoated steel and b) coating removed after deep drawing (Lau, DeCooman and Vermeulen 1998).

percentage of intergranular fracture was higher for two to three grain diameters next to the galvannealed layer. Martin et al. (2000) have examined cracking in galvannealed coatings for two Ti-Nb IF RP steels. Although cracking leading to delamination between the coating/substrate layer was most common, cracks from the coating did penetrate from one to several grain diameters along ferrite grain boundaries (Figure 2.17).

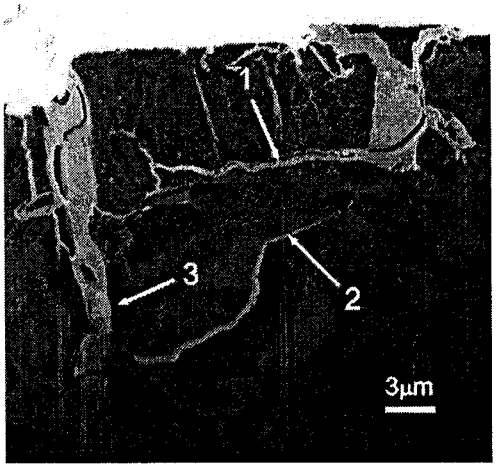

Figure 2.17 - Cross section adjacent to a CWE crack showing (1) delamination of the coating/ substrate interface, and (2) intergranular and (3) transgranular crack paths (Martin et al. 2000).

Hot Rolled Steels

Hot rolled IF sheet steels have been shown to be susceptible to CWE. Most studies have used Charpy tests to characterize the steel's susceptibility to CWE, as hot-rolled steels are usually 3-4 mm thick and not amenable to cup drawing. Exceptions are the work of Sakata et al. (1988) and Higashino et al. (1987) who use the CET with deep drawn large size compressor shells with a draw ratio of 3.45. The deleterious effect of P and beneficial effect of free C and B is the same in hot rolled steels as in cold rolled steels. The amount of carbon in solution can be increased by lowering the coiling temperature after hot-rolling, although free carbon obtained in this manner does not necessarily stay in solution after cold rolling and recrystallization annealing (Neutjens, Herman and Leroy 1998).

Sakata et al. (1988) use a low coiling temperature after hot rolling and low sulphur levels in a Ti-stabilized grade of IF steel to produce a hot rolled grade resistant to CWE. Lowered sulphur levels lead to residual solute carbon (deduced by an increased aging index) which effectively increased the resistance to CWE (Figure 2.18). Neutjens, Herman and Leroy (1998) compared a partially stabilized, with less stabilizing elements added, and a fully stabilized Ti-Nb high phosphorus grade. The partially stabilized grade had a yield point, and a lower P/Fe peak as measured by Auger spectroscopy. The ductile-to-brittle transition temperature decreased from 0°C to -80°C and the fracture mode changed from fully intergranular to transgranular. The transition temperature of a hot rolled Ti-stabilized phosphorus added grade was improved by lowering the coiling temperature beneath that which full stabilization occurred. Lowering the coiling temperature

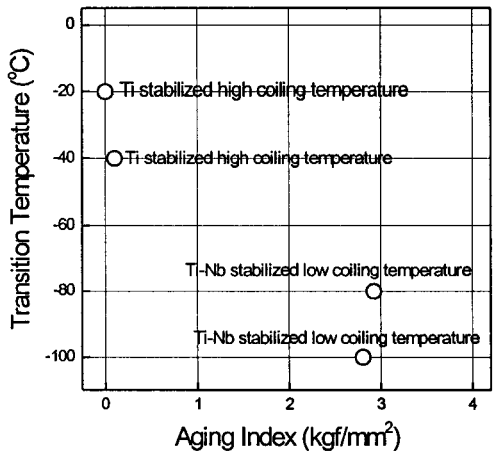

Figure 2.18 - Effect of aging index on the DBTT of hot rolled IF sheet steel (Sakata et al. 1988).

from 660°C to 550°C changed the carbon precipitation from full to incomplete and decreased the transition temperature from -0°C to -100°C (Neutjens, Herman and Leroy 1998).

Neutjens, Herman and Leroy (1998) have investigated the effect of tin on the transition temperature of hot rolled ULC-Ti steels using Charpy tests. Increasing amounts of Sn (0.0, 0.011 and 0.049wt.% Sn) in the 3.0 mm hot rolled sheet lead to increased transition temperatures (-100, -30 and -10°C respectively). Girina and Bhattacharya (2000) investigated the influence of coiling temperature and boron additions on the transition temperature of a hot rolled Ti-Nb stabilized IF steel. Charpy tests were used; lowering the coiling temperature from 700°C to 650°C in steel without boron additions enhanced the resistance to CWE, whereas boron additions to steel coiled at 700°C prevented brittle fracture down to -90°C, the lowest test temperature used.

2.0

2.2 Brittle Intergranular Fracture

Intergranular fracture is a decohesion process occurring between grains of the same phase in a polycrystalline material; this decohesion process can be either brittle or ductile in nature. Ductile intergranular fracture, a localized process of microvoid coalescence, is caused by, for instance, a soft precipitate-free zone on either side of the grain boundary plane, and is not relevant to the present work. Brittle intergranular fracture (IGF) is a cleavage fracture process that follows the grain boundary plane. In a quasi-brittle metal such as α-iron significant plastic energy can be dissipated during the cracking process due to dislocation emission around the crack tip. The fracture surface reveals grain boundary facets that are relatively smooth in appearance (Figure 2.). When significant plasticity occurs before the brittle decohesion process, the grain boundary facets can have a non-smooth appearance due to intersecting slip bands.

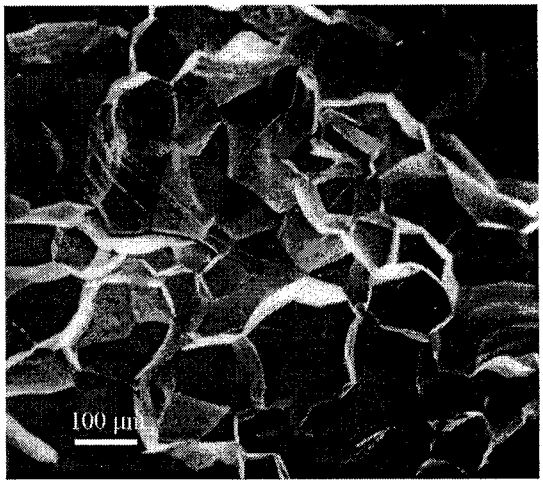

Figure 2.19 - Micrograph of IGF surface for decarburized NPL iron. 100x (Timbres 1970)

Brittle IGF occurs in wide variety of metals and alloys, and is usually associated with grain boundaries that have been weakened by deleterious grain boundary segregants. One striking example of an impurity causing IGF is Bi in Cu; Cu, a normally ductile metal, fails by brittle IGF with the addition of a few ppm Bi (Joshi and Stein 1971). Other selected examples in metals include P in W (Joshi and Stein 1970), and S in Ni (Floreen and Westbrook 1969). Elements known to embrittle iron, the most studied material with respect to IGF, are shown in the form of a periodic table adapted from McMahon, Briant and Banerji (1978) (Figure 2.20). For a general review of intergranular embrittlement see Hondros and Seah (1983).

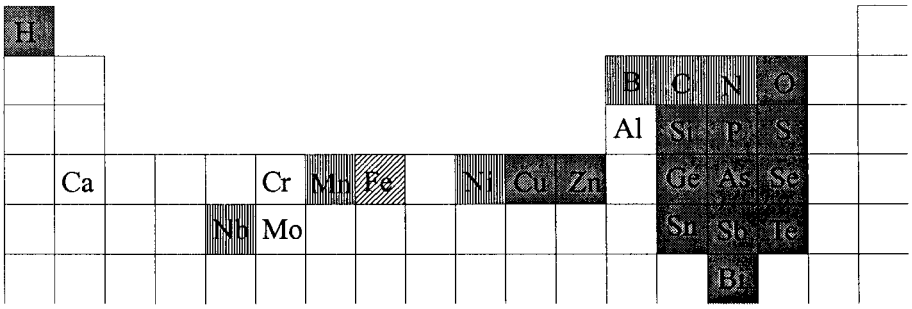

Figure 2.20 - Elements known to segregate to grain boundaries in iron are filled, while those known to embrittle grain boundaries are evenly shaded.

2.2.1 Fracture Propagation and Nucleation

Fracture is controlled by the most difficult step in the fracture process, whether this be the nucleation stage or the propagation stage (Tetelman and McEvily 1967). After the critical step has been reached the crack propagates in an unstable manner causing catastrophic failure. The measured fracture stress will therefore be the nominal stress at which the most difficult stage is overcome.

2.2.2 Propagation Controlled Fracture

Propagation controlled fracture is based on the presumption of a crack, inherent or nucleated, and on a Griffith energy balance. The Griffith criterion states that crack extension can occur when the driving force for crack growth, G, the energy release rate, is sufficient to overcome the materials resistance, R. The resistance to transgranular crack propagation, R_{TGF}, for an ideal brittle solid is $2\gamma_S$, the surface energy per unit area of the fractured surface (typically the {100} planes in α- iron). For resistance term for ideal elastic IGF, R_{GB}^{EL}, is modified to take into account the surface energy of the grain boundary, which is consumed during the fracture process, and the differences in surface energies between the exposed upper and lower grain boundary surfaces,

$$R_{GB}^{EL} = \gamma_{up} + \gamma_{low} - \gamma_{GB} = \gamma^{EL} \tag{2.2}$$

Each of the energy terms will depend on the grain boundary structure and chemistry. The driving force, G, is related to the effective stress intensity, K^*, by,

$$G = \frac{K^{*2}}{A_1} \tag{2.3}$$

and therefore,

$$K^* = \sqrt{GA_1} = \sqrt{R_{GB} A_1} \tag{2.4}$$

where the elastic modulus, A_1, is $A_1 = \frac{E}{1-\nu^2}$ for an isotropic solid in plane strain and is,

$$A_1 = \left\{ \left(\frac{b_{11} b_{22}}{2} \right)^{1/2} \left[\left(\frac{b_{22}}{b_{11}} \right)^{1/2} + \frac{2b_{12} + b_{66}}{2b_{11}} \right]^{1/2} \right\}^{-1} \tag{2.5}$$

for an anisotropic solid (Sih and Liebowitz 1968). The b_{ij}s are with reference to the crack tip coordinate system and are related to the elastic compliance, s_{ij}s, by the following relations,

$$b_{ij} = s_{ij} - \frac{s_{i3}s_{j3}}{s_{33}} \tag{2.6}$$

As the elastic response depends on the grain orientation for anisotropic materials, the effective elastic compliance, A_1^*, can be taken to be the average of the upper and lower grains and is given as,

$$A_1^* = \left[\frac{1}{2}\left(\frac{1}{A_{1up}} + \frac{1}{A_{1low}}\right)\right]^{-1} \tag{2.7}$$

The elastic anisotropy and the misorientation at the grain boundary can lead to elastic and plastic compatibility stresses (Sutton and Balluffi 1995, 704-710) which can affect the form of the stress intensity relations in the vicinity of the crack tip. Saada (1998, 1995) presents an approach to calculate the stress fields at interfaces based on the stress field of dislocation arrays.

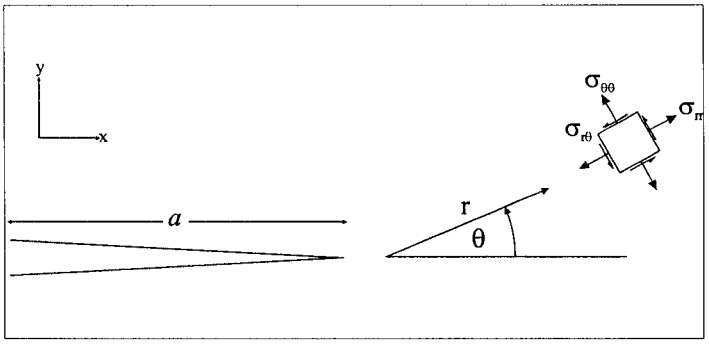

Figure 2.21 - Crack tip coordinate system.

The stress intensity relations (for a review see Irwin, 1958) describe the stress field around the crack tip and are given in polar coordinates (Figure 2.21) by,

$$\sigma_{rr} = a_{11}\frac{K_I}{\sqrt{2\pi r}} + a_{12}\frac{K_{II}}{\sqrt{2\pi r}} \tag{2.8a}$$

$$\sigma_{\theta\theta} = a_{21}\frac{K_I}{\sqrt{2\pi r}} + a_{22}\frac{K_{II}}{\sqrt{2\pi r}} \tag{2.8b}$$

$$\sigma_{r\theta} = a_{31}\frac{K_I}{\sqrt{2\pi r}} + a_{32}\frac{K_{II}}{\sqrt{2\pi r}} \tag{2.8c}$$

where $K_{I,\ II}$ are the mode I (tensile) and mode II (shear) applied stress intensity factors resolved into the coordinate system of the incipient crack, r is the distance from the crack tip, the angular coefficients, a_{ij}, are given by (Lawn 1993, 25),

$$a_{11} = \frac{5}{4}\cos\frac{\theta}{2} - \frac{1}{4}\cos\frac{3\theta}{2} \qquad a_{12} = -\frac{5}{4}\sin\frac{\theta}{2} + \frac{3}{4}\sin\frac{3\theta}{2} \tag{2.9a}$$

$$a_{21} = \frac{3}{4}\cos\frac{\theta}{2} + \frac{1}{4}\cos\frac{3\theta}{2} \qquad a_{22} = -\frac{3}{4}\sin\frac{\theta}{2} - \frac{3}{4}\sin\frac{3\theta}{2} \tag{2.9b}$$

$$a_{31} = -\frac{1}{4}\sin\frac{\theta}{2} + \frac{1}{4}\sin\frac{3\theta}{2} \qquad a_{32} = \frac{1}{4}\cos\frac{\theta}{2} + \frac{3}{4}\cos\frac{3\theta}{2} \tag{2.9c}$$

The fracture process is usually considered to be pure mode I loading with crack extension in the plane of the crack, e.g. $\theta = 0$. The normal stress in this case is given by,

$$\sigma_{\theta\theta} = \frac{K_I}{\sqrt{2\pi r}} \tag{2.10}$$

At fracture the local normal stress acting on the grain boundary must reach the cohesive stress of the grain boundary, σ_c, over some distance, r^*.

$$\sigma_c\sqrt{2\pi r^*} = \sigma_f\sqrt{\pi d/2} \tag{2.11}$$

where the crack size, $2a$, is taken to be one facet length (approximately equal to $0.5d$, where d is the grain diameter) and the applied mode I stress intensity is given by $K_1 = Y\sigma_{yy}\sqrt{\pi a}$. The geometric factor, Y, is equal to one for a through-thickness crack and $2/\pi$ for a penny shaped crack. The local critical mode I stress intensity for propagation controlled fracture can be defined by, $k_f^p = \sigma_c\sqrt{2\pi r^*}$, and therefore,

$$\sigma_f = \frac{k_f^p}{\sqrt{\pi 0.5d/2}} \tag{2.12}$$

for $Y = 1$. By inserting equation 2.3, the Griffith fracture stress is obtained as,

$$\sigma_f = \sqrt{\frac{2}{\pi}\frac{A_1\gamma^*}{d/2}} \tag{2.13}$$

for a through-thickness crack or,

$$\sigma_f = \sqrt{\frac{\pi}{2}\frac{A_1\gamma^*}{d/2}} \tag{2.14}$$

for a penny shaped crack where γ^* is a modified surface energy term that accounts for plastic energy dissipation per unit area of crack extension as discussed in section 2.2.3.

2.2.3 Plasticity During IGF

Crack tip dislocation emission has traditionally been viewed by considering the competition between crack blunting and bond breaking as exclusive processes (Kelly, Tyson and Cottrell 1967) (Rice and Thomson 1973); for instance, dislocation emission blunts the crack tip by creating ledges and decreases the stress intensity at the crack tip, further inhibiting brittle fracture. Although this approach has been successful at investigating the intrinsic nature of fracture, the measured fracture surface energies are much larger than those predicted and measured based on thermodynamic considerations. For instance, the reported energy of the {100} transgranular cleavage plane in α-iron is 1.92 J/m^2 (Inman and Tippler 1963), whereas the measured energy dissipated during transgranular fracture is ~ 10 times this value (Hahn 1984, 948) (Cottrell 1983). To reconcile this difference, a modification is made to the resistance term for quasi-brittle materials such as α-iron, to take into account the plastic energy dissipated per unit area of surface, γ_{GB}^{PL}, during the cracking process (Irwin 1948) (Orowan 1948),

$$R_{GB}^{PL} = 2\gamma_{GBS} - \gamma_{GB} + \gamma_{GB}^{PL} = \gamma^* \tag{2.15}$$

where $\gamma_{GBS} = (\gamma_{up} + \gamma_{low})/2$. Models have been developed which considered dislocation emission and bond breaking as concomitant processes (Jokl Vitek and McMahon 1980) (Freund and Hutchinson 1985).

Embrittling elements lower the elastic resistance term, R_{GB}^{EL}, but also significantly lower the plastic energy dissipated during fracture (Knott 1977). One explanation is to consider that the ability of dislocations to be unlocked and emitted from the grain boundary can be altered by the presence of the segregant (this will be more fully discussed in section 2.2.7). An alternate explanation recognizes that the stress that can be sustained at the crack tip depends on $2\gamma_S$, which is the same stress responsible for the generation of dislocations and hence γ_{GB}^{PL} (Rice 1966) (McMahon and Vitek 1979). A measurement of the dislocation density next to the intergranular fracture surface has found the density of dislocations to decrease with increased grain boundary segregation (Kameda and McMahon 1980) (Kumar and Eyre 1980) and increased potency of segregant at the grain boundary (Kameda and McMahon 1980). Generally, IGF propagates with less plastic energy dissipation due to the lower fracture stress as compared to TGF.

Although the major influence on the work to fracture is from plastic energy dissipation, the fracture stress for propagation controlled fracture is not dependent (or has a small) dependence on temperature. This has

been found by measuring the fracture stress as function of temperature, or from examining k_f, which shows no change with temperature (Nakamura and Sakaki 1970). Knott (1983) has rationalized this temperature independence by categorizing two modes of plastic relaxation:

"One mode is the operation of sources, at relatively low stress at a distances remote form the crack tip: the other is the generation of dislocations from the tip (at a stress of 0.1μ) and their propagation through the steep stress gradient. The former process may depend strongly on temperature and crack-tip velocity (strain rate: the later in its early stage, may be virtually athermal, because thermal fluctuations at low temperature are not sufficient to significantly affect the local stress required to generate dislocations from the tip. It should be noted that the two modes of relaxation are somewhat analogous to those treated by Cottrell (1963) in his analysis of the interpretation of k during Luders band propagation." (Knott 1983)

Knott's extension of Cottrell's theory is further corroborated by the temperature independence of k_y in mild steels for most cases (Timbres 1970, 86, 94) (Conrad and Schoek 1960) (Petch 1958) (Heslop and Petch 1956). Knott (1977,1983) has also estimated the plastic energy dissipated at the front of a moving crack in iron, by considering two dislocations on each side of the crack moving three Burgers vectors. The work done was estimated to be $0.24Eb$ (~12 Jm^{-2}), a five fold increase compared to the elastic cleavage surface energy of $0.05Eb$ (~2 Jm^{-2}).

2.2.4 Nucleation Controlled Fracture

A nucleation controlled fracture process entails that the crack propagates catastrophically during the nucleation process without blunting in the initial growth stage and subsequent propagation. Slip and twinning are responsible for the nucleation of brittle fracture in quasi-brittle metals. The basic mechanism for slip initiated crack nucleation was first described by Zener (1948) and Stroh (1954). Under the influence of an applied stress, dislocations, slip bands or concentrated shear bands are thought to be blocked at a microstructural barrier. This pile-up acts like a pure mode II crack (Hirth and Lothe 1982) and the associated stress concentration leads to the initiation of a crack at the barrier (the barrier might be for instance, an inclusion, a precipitate, a hard second phase, a grain boundary facet, or any other interface). (see Figure 2.22).

The local normal stress acting on the barrier (in this case a grain boundary), is given by equation 2.8b. None of the mode I applied stress is transferred; the crack is in pure mode II loading, where $K_{II} = Y\sigma_{r\theta}\sqrt{\pi a}$. The applied stress, resolved onto the slip band, is opposed by the friction stress, σ_o, therefore equation 2.8b reduces to,

$$\sigma_{\theta\theta} = a_{22}\left(f_2\sigma_{yy} - \sigma_o\right)\left(\frac{\sqrt{\pi d/2}}{\sqrt{2\pi r}}\right) \qquad (2.16)$$

At fracture the local normal stress across the grain boundary must reach the cohesive stress of the grain boundary, σ_c, over some distance, r^*.

$$\sigma_c\sqrt{2\pi r^*} = a_{12}\left(f_2\sigma_f - \sigma_o\right)\sqrt{\pi d/2} \tag{2.17}$$

Again a local critical stress intensity, k_f, may be defined as the criterion for fracture. The condition obtained for nucleation controlled fracture follows a Hall-Petch type relation (Tetelman and McEvily 1967) (Knott 1973),

$$\sigma_f = \frac{\sigma_o}{f_2} + \frac{k_f}{f_2 a_{12}\sqrt{d/2}} \tag{2.18}$$

Fracture is more likely to initiated by twinning (Hull 1963, 424) as opposed to slip as temperature decreases, or strain rate and grain size increase (Tetelman and McEvily 1967, 157). The stress concentration due to a blocked twin band can be used to derive the fracture stress for twin controlled fracture in a similar manner (Priestner 1964) (Armstrong 1964).

$$\sigma_f = \frac{\sigma_o^{tw}}{f_2} + \frac{k_f}{f_2 a_{12}\sqrt{d/2}} \tag{2.19}$$

2.2.5 Transmission of Slip, Competition Between Plastic Relaxation and Fracture

The stress concentration due to a crack or slip band impingement can be relaxed by the transmission of slip; a competition between plasticity and brittle fracture exists at the grain boundary and is local in nature. The condition for the transmission of slip due to the stress concentration can be examined by resolving the shear stress due to the stress concentration onto the slip systems ahead of the crack or pile-up. The same approach can be used for a mode I, mode II or a mixed mode crack. The resulting shear stress for a pure mode II crack is given by,

$$\sigma_{r\theta} = a_{32}\left(f_2\sigma_{yy} - \sigma_o\right)\left(\frac{\sqrt{\pi d/2}}{\sqrt{2\pi r}}\right) \tag{2.20}$$

For the transmission of slip, a dislocation source must be activated in the next grain, or the grain boundary must act as a dislocation source. Therefore, a critical shear stress, $\sigma_{r\theta}^{CR}$, must be reached over some distance, r^*, ahead of the stress concentration,

$$\sigma_{r\theta}^{CR}\sqrt{2\pi r^*} = a_{32}\left(f_2\sigma_{slip} - \sigma_o\right)\sqrt{\pi d/2} \tag{2.21}$$

In the two dimensional simplification shown in Figure 2.22, one possible slip system accessible to the crack, for a bcc metal, is shown ({121}[111] system). The approach developed by Rice and coworkers (Beltz and Rice 1991) (Rice 1992) can be used to define a critical stress intensity for dislocation emission, k_{II}^{em} where

$k_{II}^{em} = \sqrt{A_2 \gamma_{US}}$. This local condition must be met on the relevant slip system ahead of the crack. Rice defined k_{II}^{em} in terms of the unstable stacking fault energy, γ_{US}, where the shear modulus is given by $A_2 = \frac{2\mu}{1-\nu}$ for an isotropic solid and is given by,

$$A_2 = \left\{ \frac{b_{11}}{\sqrt{2}} \left[\left(\frac{b_{22}}{b_{11}} \right)^{1/2} + \frac{2b_{12} + b_{66}}{2b_{11}} \right]^{1/2} \right\}^{-1} \tag{2.22}$$

for an anisotropic solid (Sih and Liebowitz 1968). It was shown that for pure mode II loading the condition for nucleation of a pure edge dislocation, on a slip plane parallel to the crack plane is given by γ_{US}. The unstable stacking fault is defined as the integral of the shear stress curve from zero displacement to the unstable equilibrium position at which the shear stress next vanishes and represents a maximum energy barrier when two blocks are sheared relative to one another. This formalism follows the nucleation of a dislocation up to the point where it can be released from the crack tip, which for simple lattices is given by $b/2$, where b is the Burgers vector. Therefore, the local condition for slip transmission can then be written as,

$$\sigma_{slip} = \frac{\sigma_o}{f_2} + \frac{k_{II}^{em}}{f_2 a_{32} \sqrt{d/2}} = \frac{\sigma_o}{f_2} + \frac{\sqrt{A_2 \gamma_{US}}}{f_2 a_{32} \sqrt{d/2}} \tag{2.23}$$

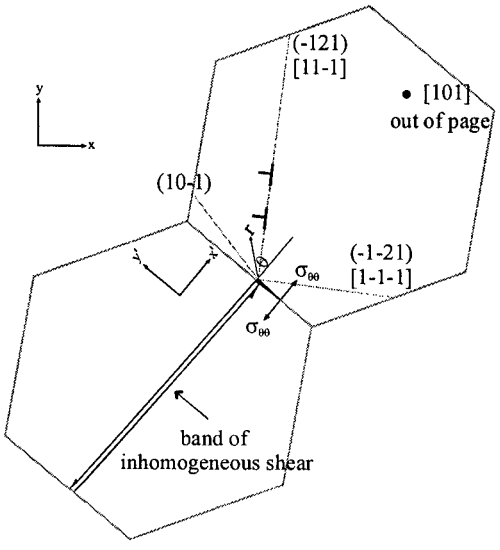

Figure 2.22 - Concentrated shear stress leading to i) crack formation at a grain boundary, or to ii) transmission of slip across grain boundary into the adjacent

For loading other than pure mode II, a ledge is expected to form when the dislocation is emitted from the crack, or the grain boundary is expected to be structurally rearranged. Therefore, the proper energy term is γ_{US}^{*}, the unstable stacking fault energy plus the required additional energies. When the approach followed in this section is applied globally by using averaged values, the Hall-Petch equation for yielding is obtained as,

$$\sigma_y = M \cdot \sigma_o + \frac{M \cdot k_y}{a_{32} \sqrt{d/2}} = M \cdot \sigma_o + \frac{k_y^{'}}{\sqrt{d}} \tag{2.24}$$

where $1/f_2$ is replaced by the the Taylor factor, M (Armstrong 1964).

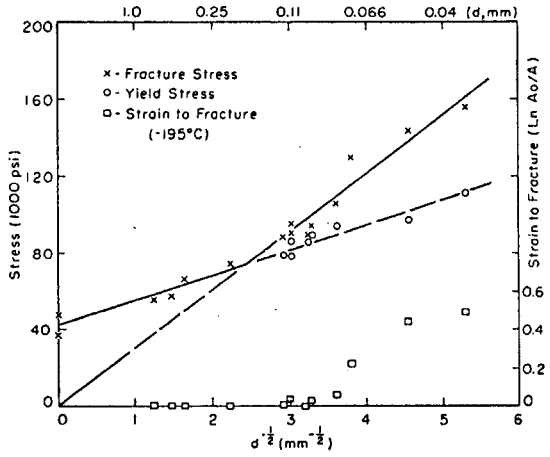

Figure 2.23 - The yield and fracture stresses at -196 °C as a function of grain size for a low carbon steel. Single crystal cleavage stresses are plotted at $d^{1/2}=0$.

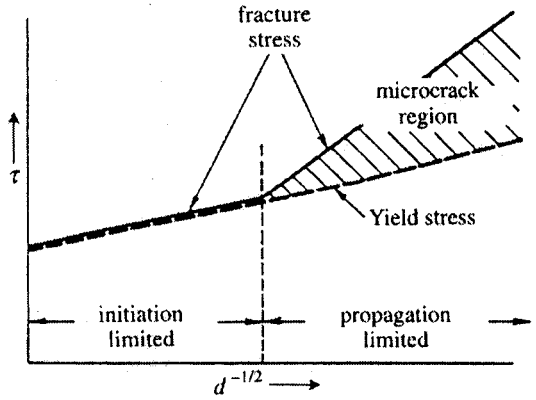

Figure 2.24 -The fracture and yield stress as a function of grain size - the standard interpretation of the data in Figure 2.23.

2.2.6 Discussion on Propagation and Nucleation Controlled Intergranular Fracture

From equations 2.13 and 2.17 it can be seen that the IGF stress scales with the inverse square root of the grain size, whether fracture is nucleation or propagation controlled. The competition between brittle fracture and plastic flow has often been explained based on the classic experimental results of Low (1954). The results for transgranular fracture on a low carbon steel (see Figure 2.23) showed that above a critical grain size, d*, the fracture stress in tension was equal to the yield stress in compression. Below this critical grain size, the fracture occurred after some plastic strain. This suggested that the brittle fracture stress was linked to the yield stress in

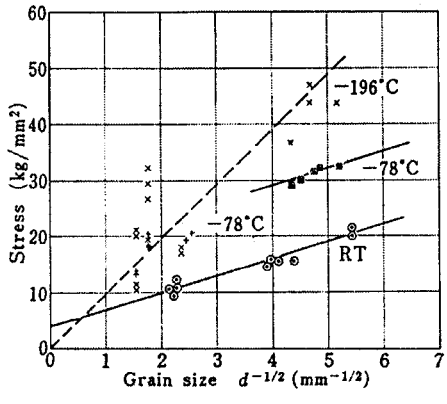

Tensile speed was 0.3 mm/min.
⊙ Lower yield stress at 23°C
⊡ Lower yield stress at −78°C
\+ Intergranular brittle fracture stress at −78°C
× Intergranular brittle fracture stress at −196°C

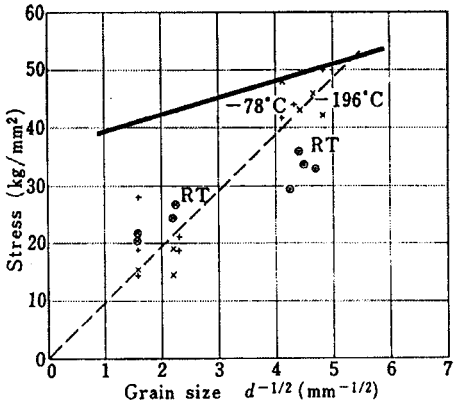

Tensile speed was 2.3×10^3 mm/min.
⊙ Lower yield stress at 23°C
⊗ Intergranular brittle fracture stress at 23°C
\+ Intergranular brittle fracture stress at −78°C
× Intergranular brittle fracture stress at −196°C

Figure 2.25 - The lower yield stress and brittle IGF stress of iron as function of grain diameter and testing temperature for a tensile speed of 0.3 mm/min and $2.3\text{x}10^3$ mm/min.

tension. From this work it has been generally accepted that yield is coincident with or precedes brittle fracture in quasi-brittle metals. The explanation of these results (Figure 2.24) (Gilman 1958) is that for nucleation controlled fracture, the stress intensities arising from the mode II crack are large enough to drive the crack across other obstacles. For propagation controlled fracture, the stress intensities are not large enough to drive the nucleated crack across any barriers, and therefore additional applied stress is necessary for propagation.

The IGF stress versus grain size for electron beam melted iron at different temperatures and strain rates is shown in Figure 2.25 (Nakamura and Sakaki 1970). The results indicated that the fracture stress is not a function of temperature or strain rate, and follows a Griffith relation, suggesting propagation controlled fracture. Upon first observation, it is not clear if a transition occurs from propagation controlled to nucleation controlled fracture at a critical grain size. Upon closer inspection, it can be seen that a propagation controlled mechanism dominates, even as the grain size increases, as it is clear that the brittle fracture stress at a test temperature of -78°C does not fit the expected yield curve at -78°C. The expected yield curve that would be obtained at -78°C for a crosshead speed of 2.3×10^3 mm/min has been superimposed on the original data by assuming the same strain rate sensitivity at -78°C as that for room temperature.

In general, a temperature dependent or strain rate dependent IGF stress is not observed experimentally. This indicates propagation controlled fracture is the dominant mechanism as a temperature and strain rate dependent fracture stress is expected for nucleation controlled fracture due to the temperature and strain rate dependence of the friction stress. For propagation controlled fracture it is often assumed that general yield must be reached before IGF, but this assumption is not observed experimentally. The error in this assumption can be shown by depicting the competition between yield and brittle IGF using a Davidenkov diagram (Davidenkov 1936); a plot of the fracture and yield stress as a function of temperature for a constant grain size (see Figure 2.26). Below the transition temperature, defined by the intersection of the yield and fracture curve, the extrapolated yield stress continues to increase exponentially above the fracture stress. The fact that the yield stress can be appreciably above the fracture stress, but the initiation mechanism is still based on yield can be rationalized by observing that friction stress (or micro-yield stress) can still be activated at temperatures below the transition temperature.

A reinterpretation of Figure 2.23 can be made to rationalize the experimental observations by plotting the Griffith fracture stress, the

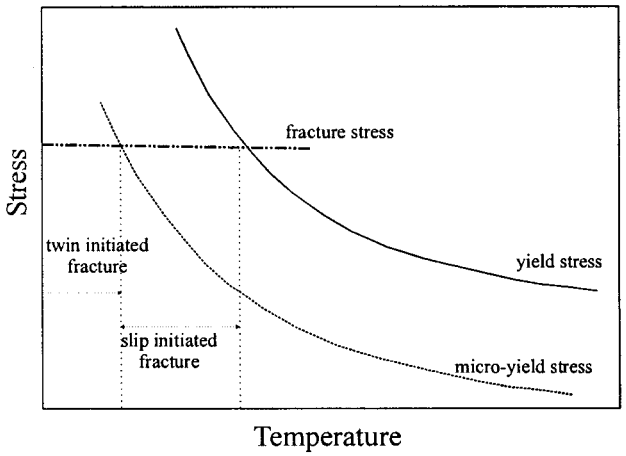

Figure 2.26 - Davidenkov diagram showing the transition from twin initiated fracture to slip initiated fracture when the microyield stress is no longer able to

nucleation fracture stress and the yield stress, equations 2.13, 2.17, and 2.23 (Figure 2.27). The intercepts for the nucleation controlled fracture stress and the yield stress are nominally the same according to equations 2.17 and 2.23, and therefore it appears that yield is coincident with fracture, when in fact, the fracture mechanism is nucleation controlled. In the nucleation controlled regime, crack nucleation is the limiting step as there is enough driving force to propagate the crack once nucleated. With decreasing grain size, the propagation limited regime is encountered: note the bulk yield stress has not been reached. The range of propagation controlled fracture extends beyond the intersection of the yield and Griffith curves, as general yield is possible before brittle intergranular fracture, but not necessary. Above this region, general yield, followed by ductile fracture is encountered. There is much experimental evidence to support propagation based IGF occurring before general yield; for instance, for the coarsest grain tested (250 μm), IGF occurred at 177 MPa at -196° C, which is lower than the friction stress of at least 539 MPa at this temperature (Nakamura and Sakaki 1970), although in this case twinning was thought to be responsible for crack nucleation.

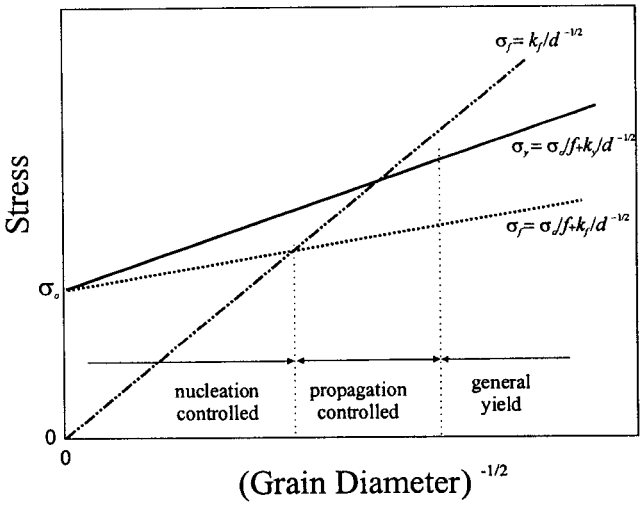

Figure 2.27 - Modified stress versus grain size schematic explaining the competition between yield and fracture.

2.2.7 *Effect of Segregation on* k_f^p, k_f^n, k_y

Embrittling segregants lower the cohesiveness of the grain boundary, thereby changing critical stress intensity necessary for fracture, mainly by affecting the surface energy term as discussed in section 2.3. Of course, the effect will be greater for smaller grained material. Grain boundary segregation also changes the grain boundaries' ability to transmit slip or to emit dislocations. Although there is a dearth of information in this area, experimental evidence has suggested that grain boundary segregation can result in a change in the Hall-Petch slope indicating segregation affects the transmission of slip across or from the relevant barrier. Wilson (1967) obtained $k_y = 0.725 MNm^{-3/2}$ for a low carbon steel annealed at 700°C and then slowly cooled, while $k_y = 0.315 MNm^{-3/2}$ was obtained for annealed then quenched specimens. Aging returned the higher value of k_y. Mintz, Ke and Smith (1992) repeated the experiments on a low carbon steel with similar chemistry, and measured the grain boundary carbon content with an field ion atom probe. The observed true interstitial content at the boundary was equal to 17.64 at.% for the furnace cooled steel, and was equal to 3.15 at.% for the quenched steel. A reasonable agreement was found between a calculated Hall-Petch slope based on the interstitial content at the grain boundary and those measured by Wilson (1967).

2.2.8 Criteria for Intergranular Fracture

The criterion most often used for transgranular cleavage fracture is a critical stress criterion; fracture occurs at a maximum tensile critical stress (Knott 1977). This is equivalent to assuming a propagation mechanism with self similar crack extension and pure mode I loading, as was done to derive the Griffith equation (equation 2.13). This equation is also most often used to model IGF (Nakamura and Sakaki 1970, Murr 1975, Kanditis, Marini and Pineau 1994, Reidel 1995). Experiments exploring the possibility of different criteria for IGF are much more scarce.

Zok (1988) has tested an embrittled copper alloy (Cu-0.02wt.%Bi) over a range of superimposed hydrostatic pressures (0-690 MPa). The measured intergranular fracture stress increased linearly with hydrostatic pressure (up to 250 MPa) with a slope nearly equal to one (Figure 2.28). Above 250 MPa, the samples thinned to a chisel point. It was concluded that IGF occurs at a critical stress and is controlled by crack propagation. Zok (1988) also interrupted samples tested to a true strain of 0.23 and 1.45 under a hydrostatic pressure of 690 MPa before they failed and then retested these samples under atmospheric pressure. The sample predeformed to $\varepsilon = 0.23$ exhibited no additional plastic flow and fractured by an intergranular mode at a stress of 140 Mpa (~50% greater that the brittle fracture stress of the undeformed material). The sample predeformed to $\varepsilon = 1.45$ fractured with an additional plastic strain of 0.76 at a tensile stress of 650 Mpa and also was intergranular. It was concluded that the grain shape contributes to the increased fracture stress and that the fractional area coverage of solute at the grain boundary decreases as the grain boundary area is increased with plastic deformation.

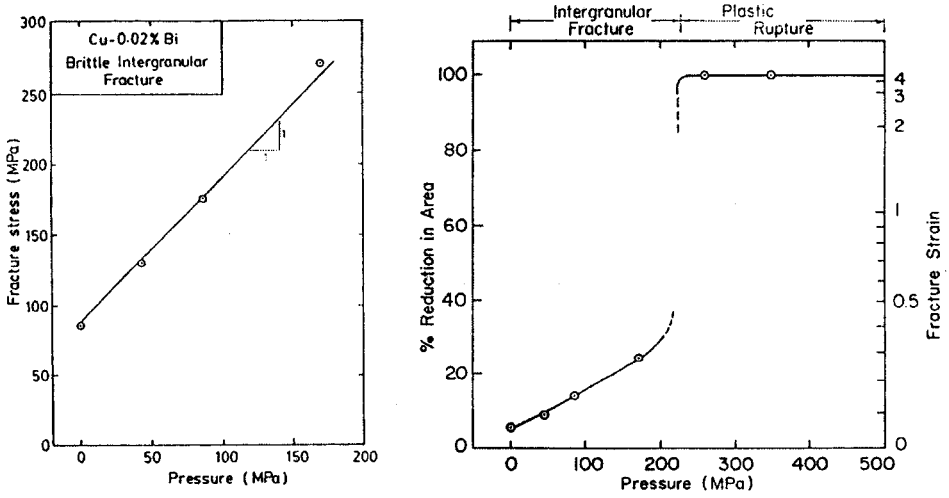

Figure 2.28 - Intergranular fracture stress as a function of superimposed hydrostatic pressure for a Cu-0.02wt.%Bi alloy and the associated strain to fracture (Zok 1988).

2.2.9 Transgranular versus Intergranular Fracture, Intrinsic Nature of Fracture

It is commonly assumed that grain boundaries are intrinsically stronger than the lattice, except when weakened by impurities. It is actually surprising that the grain boundaries are not always the preferred method of brittle fracture. The ratio of the intergranular fracture resistance for clean grain boundaries, R^o_{GB}, to transgranular fracture resistance, is given by,

$$\frac{R^o_{GB}}{R_{TGF}} = \frac{2\gamma^o_{GBS} - \gamma^o_{GB}}{2\gamma_{TGFS}} \tag{2.25}$$

where the average surface energy for the exposed upper and lower grain boundary facets for a high angle boundary is given by γ_{GBS}. The surface energy of a clean high angle grain boundary can be estimated by assuming the surface exposed would be atomically rough and thus the surface energy would be near maximum. The transgranular cleavage crack takes the path of the lowest energy and therefore the cleaved plane would have a minimum surface energy. Data obtained for the maximum and minimum surface energies of various metals near the melting point (McLean 1971) was extrapolated to room temperature by Cottrell (1989) and the value obtained for most metals was ≈1.2. It has been reported that for most metals $\gamma^o_{GB} \approx 1/3\,\gamma^o_{GBS}$ (Hondros and McLean 1976). Therefore equation 2.25 reduces to a value near one; neither intergranular fracture nor transgranular fracture is a preferred mode of fracture. Cottrell (1989) has taken a slightly different approach, by considering a transition from transgranular to intergranular fracture at a critical value of μ/K, where μ is the average shear modulus and K is the bulk modulus. Rhodium, Ir, Mo, W and Cr were considered to have intrinsic intergranular weakness, whereas Fe was a borderline case, it was predicted to be marginally ductile.

Clean grain boundaries are more an exception than a rule, the grain boundary structure and the amount of grain boundary segregation affects the surface energies as discussed in section 2.3.5. As well, only half of the equation has been considered; the change in driving force as a function of the microstructure with respect to the applied stress must be considered. Therefore the variation in the motive force $g = G - R$ must be considered for the microstructure under consideration (Lawn 1993). Generally, the fracture will be intergranular in nature if the grain boundary is sufficiently weak to compensate for the extra energy consumed due to the more tortuous path.

The question of whether of not the grain boundary is intrinsically stronger than the lattice is difficult to answer experimentally; atomistic simulation are pointing the way in this regard (Hoagland 1997) (deCelis Argon and Yip 1983). Experimental results on polycrystalline iron (Matsui et al. 1978) of 99.999% and higher purity did not fracture in an intergranular manner even at 4.2 K. Less pure iron, 99.99% purity, fractured in an IGF mode. It was concluded that IGF was not inherent in iron but caused by impurities. Fifteen years later the experiments were repeated (Ohfuji et al. 1992), but the importance of the grain boundary structure on the mechanical

properties was realized. Iron of 99.999% or higher purity was tested and it was found that IGF did occur for samples that contained ~90% high angle boundaries while samples that had ~ 20% high angle boundaries failed in a transgranular manner. Therefore, it was concluded that the mechanical strength of the grain boundary is controlled by the associated structure and impurity content.

2.0

2.3 Segregation to Grain Boundaries

The entrapment of solute atoms at grain boundaries during thermal processing of metals has been called grain boundary segregation. In many systems, the local grain boundary chemistry determines the grain boundary strength, and therefore the propensity for intergranular fracture. It is therefore necessary to understand the process of grain boundary segregation in order to understand the causes of intergranular fracture. Grain boundary segregation involves diffusion of atomic species to the grain boundary, and therefore it is a thermally activated process.

Two classes of grain boundary segregation have been defined, equilibrium segregation and non-equilibrium segregation. Non-equilibrium segregation is, in a general sense, a consequence of kinetic processes and does not represent a true equilibrium; the segregation will dissipate with a sufficient combination of thermal energy and time. Non-equilibrium grain boundary segregation is usually the result of a frozen-in vacancy concentration that forms complexes with segregant atoms. Grains boundaries act as a sink for the vacancies, the diffusion of the vacancy-segregant complexes allow solute profiles to develop (Aust et al. 1967). Equilibrium segregation represents a drive towards true equilibrium and is a reversible process. It is generally thought that heterogeneity of equilibrium segregation occurs over a much smaller length scale than non-equilibrium segregation, on the order of a few nanometers compared to hundreds of nanometers respectively.

The driving force for grain boundary segregation can be separated into a chemical driving force, which includes electronic interactions between the solute and solvent, and a mechanical driving force, in which the elastic strain energies are reduced with segregation. As well, complex re-arrangements can occur at the grain boundary due to segregation; these include two-dimensional phase transformations, faceting, grain boundary migration, and precipitation. These complexities have been the focus of much theoretical (Guttmann 1977, Guttmann and McLean 1979, Militzer and Wieting 1987) and experimental work (Ference and Balluffi 1988). In general the same rules, the Hume-Rothery rules, that govern the solid solubility of a species, determine the driving force for segregation. The driving force is a balance between the species desire to reside at a matrix site compared to a grain boundary site. Interactions between grain boundaries and solute atoms can be short or long-range. This distinction is not independent as short-range attraction of solute to the grain boundary will establish a long-range concentration gradient during the segregation process.

2.3.1 Thermodynamics of Grain Boundary Segregation

The grain boundary may be considered to be a separate phase (Defay and Prigogine 1951) (Guggenheim 1933) whose mean properties can be described as excess properties compared to the bulk phase. The fundamental

equation for the internal energy, U, in terms of the volume, V, the entropy, S, and the amount, n_i, of each species i, is given in terms of the grain boundary excess quantities as,

$$dU^{XS} = TdS^{XS} + PdV^{XS} + \sum_{i=1}^{1} \mu_i dN_i^{XS} + \gamma dA \tag{2.26}$$

where γ is the specific grain boundary energy and represents the reversible internal energy necessary to create a unit surface area of boundary at constant entropy and volume for a closed system, and T is the temperature, P is the pressure and μ is the chemical potential. Equivalent descriptions can be made in terms of the Gibbs free energy, G, the Helmholtz free energy, F, and the grand canonical potential, Ω (Cahn 1979). Therefore γ corresponds to,

$$\gamma = \left[\frac{\partial U}{\partial A}\right]_{S,V,n_i} = \left[\frac{\partial G}{\partial A}\right]_{T,P,n_i} = \left[\frac{\partial F}{\partial A}\right]_{T,V,n_i} = \left[\frac{\partial \Omega}{\partial A}\right]_{T,V,\mu_i} \tag{2.27}$$

Applying the Gibbs-Duhem relation to equation 2.26 and dividing by the area, the Gibbs adsorption isotherm (Gibbs 1948), at constant temperature and pressure (where the pressure though the thickness is assumed to be zero), is obtained as,

$$d\gamma = -\sum_{i=1}^{i} \Gamma_i d\mu_i \tag{2.28}$$

where $\Gamma_i = n_i^{XS}/A$ is the excess concentration of solute i per unit area at the grain boundary. For a binary system,

$$d\gamma = -\left(\Gamma_2 - \frac{X_2}{X_1}\Gamma_1\right) d\mu_2 \tag{2.29}$$

For interstitial solute as the segregating element, $\Gamma_1 = 0$, and for a dilute solution obeying Henry's law, the excess solute at the grain boundary is given by,

$$\Gamma_2 = -\frac{1}{RT}\left(\frac{\partial \gamma}{\partial \ln X_2}\right)_T \tag{2.30}$$

Similarly for a substitutional solution, $\Gamma_1 = -\Gamma_2$, and therefore,

$$\Gamma_2 = -\frac{X_1}{RT}\left(\frac{\partial \gamma}{\partial \ln X_2}\right)_T \tag{2.30}$$

For the excess segregation to be positive, the interfacial energy must be decreased by the segregant. For a pure metal at equilibrium, it is found that an increase in temperature decreases the interfacial energy.

2.3.2 Equilibrium Segregation Isotherms

Both a classical solution thermodynamics and a statistical mechanics approach have been used to derive the interfacial composition in terms of the temperature and the bulk composition allowing a more direct comparison with experimental evidence. The basic formalism used to derive the equilibrium grain boundary concentration, in terms of the bulk concentration and temperature, considers the grain boundary to be a two-dimensional phase (Defay and Prigogine 1951) (Guttmann and McLean 1979) where all the classical thermodynamic function can be defined analogous to the bulk phase. The thermodynamic equilibrium, in terms of the chemical potentials, μ, of solute *i*, and the solvent 1, at the grain boundary (ϕ) and the bulk (B) where the exchange of atoms is substitutional (Hillert 1998) (Du Plessis and van Wyk 1988), is given by,

$$\mu_i^{\phi} - \mu_i^{B} = \mu_1^{\phi} - \mu_1^{B} \tag{2.32}$$

The chemical potential of species *i* is $\mu_i = \mu_i^o + RT \ln a_i$, where R is the universal gas constant, T is the temperature, and a_i is the activity. The McLean-Langmuir isotherm (Langmuir 1918) (McLean 1957), is derived by substituting the chemical potentials into the condition for thermodynamic equilibrium and by assuming an ideal binary alloy, and is given as,

$$\frac{X_i^{\phi}}{X_1^{\phi}} = \frac{X_i^{B}}{X_1^{B}} \exp\left[-\Delta G_i^s / RT\right] \tag{2.33}$$

where ΔG_i^s is the molar free energy of segregation of species *i*. The conservation equation,

$$\sum_{i=1}^{n} X_i^{\phi} = \sum_{i=1}^{n} X_i^{B} = 1 \tag{2.34}$$

for sublattice saturation can then be used to obtain the segregation isotherm for a binary system,

$$\frac{X_2^{\phi}}{1-X_2^{\phi}} = \frac{X_2^{B}}{1-X_2^{B}} \exp\left[-\Delta G_i^s / RT\right] \tag{2.35}$$

where X_2 is the mole fraction of the segregating solute. For a dilute solution, $X_2^B << 1$, and equation 2.35 reduces to,

$$\frac{X_i^{\phi}}{1-X_2^{\phi}} = X_i^{B} \exp\left[-\Delta G_i^s / RT\right] \tag{2.36}$$

or equivalently,

$$X_2^{\phi} = \frac{X_2^{\mathrm{B}} \exp\left[-\Delta G_i^s / RT\right]}{1 + X_2^{B} \exp\left[-\Delta G_i^s / RT\right]} \tag{2.37}$$

For a dilute solution, $X_2^B << 1$, and low levels of segregation,

$$X_2^{\phi} = X_2^{\mathrm{B}} \exp\left[-\Delta G_i^s / RT\right] \tag{2.38}$$

the Boltzmann isotherm is obtained. This last isotherm is approximately valid for dilute solutions at high homologous temperatures. For a ternary system, two separate cases can be considered, one where both species compete for the same sites, the other where the species are segregating to separate sub-lattices at the grain boundary. The segregation in a ternary system with site competition is given as (Guttmann and McLean 1979) (Guttmann 1975),

$$\frac{X_2^{\phi}}{1 - X_1^{\phi} - X_2^{\phi}} = \frac{X_2^{\mathrm{B}}}{1 - X_1^{B} - X_2^{\mathrm{B}}} \exp\left[-\Delta G_s / RT\right] \tag{2.39}$$

For a non-ideal solution, $a_i = f_i X_i$, and the free energy of segregation is described by,

$$\Delta G_s = \Delta G_s^o + \Delta G_s^{XS} \tag{2.40}$$

This excess free energy of segregation can be derived by assuming regular solution behaviour (Guttmann 1975); the chemical interactions between the nearest neighbours are described by constant pair interaction energies. When the interaction coefficients in the bulk and grain boundary were assumed to be approximately the same and in the dilute solution approximation the free energy of segregation simplifies to,

$$\Delta G_i^s = \left(\Delta \mathrm{H}_i^o + T\Delta S_i^o\right) - 2\alpha_{ii} X_i^{\phi} + \alpha_{ij} X_j^{\phi} \tag{2.41}$$

where $\alpha_{ii}s$ and $\alpha_{ij}s$ are the interaction coefficients. The second term of equation 2.41 is recognized as the Fowler (Fowler and Guggenheim 1965) term and describes self-interaction, while the third term in equation 2.41 described the interaction between unlike solutes.

One of the basic assumptions made in the models presented thus far was that each site has the same potential for segregation. This assumption can be dealt with by assuming a distribution of site potentials (White and Coghlan 1977, White and Stein 1978) where a fraction, F_{ix}, of the total sites have a segregation energy, ΔG_{ix}^s. In terms of the Langmuir-McLean isotherm, the mole fraction, X_{ix}, of type x grain boundary sites occupied by solute atoms is given as,

$$X_{ix}^{\phi} = \frac{X_i^{B} \exp\left[-\Delta G_{ix}^{s}/RT\right]}{1 - X_i^{B} \exp\left[-\Delta G_{ix}^{s}/RT\right]} \tag{2.42}$$

The overall atom fraction of solute at the grain boundary, X_{2x}^{ϕ}, is the weighted average summed over all of the grain boundary sites, $X_2^{\phi} = \sum F_{ix} X_{2x}^{\phi}$.

2.3.3 Kinetics of Segregation

An analytical expression for the kinetics of grain boundary segregation was derived by McLean (1957) based on the application of Fick's Laws and the assumption of a local equilibrium and a constant grain boundary enrichment factor, $\beta = X_2^{\phi} / X_2^{B} = \exp \Delta G_s / RT$. McLean showed that,

$$X = 1 - \exp(s^2) erfc(s) \tag{2.43}$$

where $$X = \left[X_2^{\phi}(t) - X_2^{\phi}(0)\right] / \left[X_2^{\phi}(\infty) - X_2^{\phi}(0)\right] \tag{2.44}$$

represents the progress towards equilibrium, and

$$s = \sqrt{D_2 t} / \left[\beta(\delta / 2)\right] \tag{2.45}$$

is a time variable, where t is the time, D_2 is the diffusion coefficient of the solute in the bulk and δ is the grain boundary thickness. As discussed the assumption of a constant enrichment factor is applicable only in the limiting case of dilute binary alloy with low equilibrium segregation. A numerical approach (Tyson 1978) is required to properly model high segregation levels, solute-solute interactions, and competition for grain boundary sites.

3.0 EXPERIMENTAL METHODS

3.1 Introduction

Much of the previous research on CWE has focused on comparing IF steels of different chemistries. General trends have been found, but the ability to predict the ductile-to-brittle transition temperature for a given grade of sheet steel is not yet possible. This stems from the need to define the key issues surrounding CWE; some of which include the hardening behaviour, the role of grain shape on intergranular fracture and the possible effect of residual stresses. This section describes the material used in the current work, the microstructural characterization, and mechanical testing done to elucidate the phenomenon of CWE.

3.2 Material Chosen for Study

A rephosphorized (RP) ultra-low carbon IF sheet steel was chosen because of the high phosphorus content which would a) facilitate the detection of P segregation with analytical techniques such as transmission electron microscopy (TEM) and b) promote IGF and hence CWE. The RP IF steel is in a sense a model material, as there is little free carbon and no boron added to prevent CWE, therefore IGF and CWE are accentuated. The material was chosen for all testing in order to eliminate the variables which different chemistries introduce.

The basic processing route for this grade of steel can be summarized as follows. Hot metal from the blast furnace with scrap metal added in a ratio of 3:1, is refined in the basic oxygen furnace. The steel is then vacuum degassed, alloyed, continuously cast and hot rolled. Hot rolled steel 3.25 mm thick is cold rolled to 0.8 mm for thin gage steel and 1.5 mm for thicker gage steel. The cold rolled steel is then continuously annealed, galvannealed and temper rolled. The continuously annealed steel was galvannealed by dipping the sheet steel through a zinc pot with further annealing for 6 s at 530°C. A coil of the RP IF thin gage steel was industrially

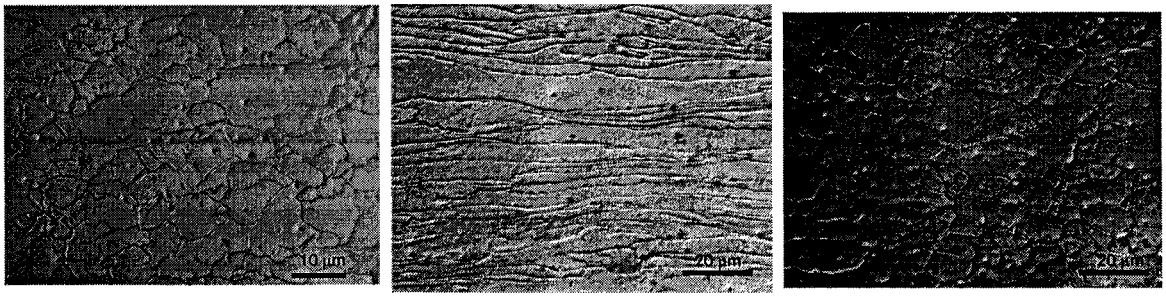

a) hot rolled *b) full hard* *c) annealed*

Figure 3.1 - Optical micrographs of a) hot rolled, b) cold rolled (full hard) and c) cold rolled and annealed microstructures of RPCA 0.8 mm IF sheet steel (Marshall's reagent).

Table III-I Chemistries of RP IF sheet steel in wt.%

Grade	C	P	Mn	S	Si	Cu	Ni	Cr	Mo	ASA	N	Ti	Nb
RPCA 0.8 mm	.0045	.069	.24	.015	.006	.037	.014	.034	.002	.054	.0034	.003	.039
RPBA 0.8 mm	.0040	.065	.24	.014	.008	.023	.008	.037	.004	.061	.0034	.003	.037
RPCA 1.5 mm	.0020	.070	.26	.009	.010	.025	.017	.021	.005	.070	.0020	.002	.041

Table III-II Thermo-mechanical processing

Grade	Hot Rolling FDT*	CT†	Cold Reduction	Annealing	Galvannealing
RPCA 0.8 mm	915°C	730°C	75%	820°Cx40s:-10°C	530°Cx6s
RPBA 0.8 mm	915°C	730°C	75%	18°C/hr:690°Cx12hr:-18°C/hr‡	none
RPCA 1.5 mm	915°C	730°C	55%	820°Cx40s:-10°C	530°Cx6s

*finishing delivery temperature, †coiling temperature, ‡done in an atmosphere of 95% H_2 and 5% N_2

batch annealed as an experimental grade and was not coated. Both the batch annealed and continuously annealed grades have been used in the current work. The composition and thermo-mechanical treatments are given in Tables III-I and III-II.

3.3 Metallography

3.3.1 Basic Sample Preparation for Optical Microscopy, Electron-Back Scatter Diffraction, and Micro-Hardness Testing

Samples for metallographic examination and hardness testing were cold mounted in epoxy. Samples for electron back-scatter diffraction were mounted on copper blocks with Crystalbond 509† or double sided tape. The mounted samples were then ground successively with 220, 300, 400, 600 grit SiC paper with water as the washing lubricant, and then mechanically polished with 15μm, 6μm and 1μm diamond paste impregnated cloths using kerosene as the lubricant. Colloidal silica, in the form of a 0.01 μm suspension, was used with a soft nap cloth for final polishing before etching. Grain boundaries were delineated with Marshall's etchant which consists of 8g of oxalic acid, 5 ml of sulfuric acid, 100 ml of distilled water and 100 ml hydrogen peroxide(30% by volume). Nital, 5 vol.%, was used to expose precipitates for chemical analysis using energy dispersive spectroscopy. This etchant results in preferential attack of certain grain orientations and causes significant surface relief (see Figure 4.3). Some specimens were also chemically thinned prior to mechanical testing. The chemical thinning solution (34% nitric acid, 32% hydrogen peroxide, 17% acetic acid, and 17%

† Thermoplastic polymer removable adhesive

water by volume) was diluted with varying amounts of distilled water to control the rate of thinning and the evolution of heat during thinning.

Samples used for electron back-scatter diffraction were electro-polished to ensure the removal of surface deformation introduced during polishing. The electrolytic polishing solution comprised 78 ml perchloric acid, 120 ml distilled water, 700 ml ethanol and 100 ml butylcellusolve. Consistent polishing was obtained with 40 V for 8 s for a 2 cm^2 surface area.

3.3.2 Grain Size and Shape Measurement

Optical microscopy was used with image analysis software (ImageTool v.2.3) to analyze the grain size and shape. Grain sectional area distributions were measured in the three orthogonal directions of the sheet. The grain boundaries were traced with a fine marker. This trace was then thresholded and used for analysis. The size of the grains was characterized by an average sectional area, $\overline{A}_A$, the number of grains per unit area, N_A, and grain boundary surface area per unit volume, S_V, and the ASTM metric grain size number, G_m. The average sectional area was converted into an equivalent grain diameter by assuming spherical grains,

$$\overline{D}_{eq} = \frac{4}{\pi}\left(\frac{4}{\pi}\overline{A}_A\right)^{1/2} \tag{3.1}$$

Grain shape was measured by using the mean intercept method to measure an effective grain diameter as a function of radial orientation in the place of the section. The standard equation,

$$\overline{D} = \frac{3L_t}{2P_A M} \tag{3.2}$$

was used to convert number of intercepts into a grain size number, where $\overline{D}$ is the grain diameter, L_t is the total length of the test line, M is the magnification and P is the number of intercepts the test line makes with the grain boundaries.

3.4 Uniaxial Tensile Testing

3.4.1 Load Frame and Testing System

Uniaxial tensile tests were performed on a Materials Testing System (MTS) model 810 servo-hydraulic universal testing frame. The system was controlled and data was acquired with a computer and the MTS TestStar II Controlling System. The servo-loop for length and force control were tuned for the most sensitive response. A load cell, with a maximum capacity of 100 kN and a resolution of 3.5 N, was used to collect force data. The noise in the collected load data varied between ±10 to ±20 N. Displacement, measured with an LVDT in the actuator piston, was used as the controlling channel. Axial displacement of the specimen was

measured with an axial extensometer. The extensometer, MTS model 632.13E-21, is designed for low temperature use and can be used submersed in electrically non-conducting fluids between -268 °C and 65 °C. The extensometer gauge length with the zeroing pin is 12.7 mm and the travel is ±1.905 mm. The extensometer was calibrated with a Mitotuyo traveling micrometer set up as a calibrating block at room temperature and in liquid nitrogen. The extensometer and load cell were checked for linearity over 80% of their range before each test by performing a shunt calibration. Prior to each test, the force channel was zeroed without tightening the sample, while the extensometer was zeroed with the zeroing pin. Grips were designed for low temperature testing of flat specimens (Figure 3.3).

3.4.2 Tensile Tests

Tensile specimens, for characterizing the room temperature uniaxial flow behaviour, were cut in the rolling direction and at 45°(diagonal direction) and 90°(transverse direction) to the rolling direction. The dimensions of the tensile specimens followed ASTM standard E345.3. The crosshead speed used was 0.01 mm/s which gives a strain rate of 0.0005 s^{-1}. The strain rate sensitivity index, m, was determined from continuous measurements, as opposed to the jump test.

Tensile tests, over a range of temperatures, were used to document the transition from ductile-to-brittle behaviour. The test setup used to obtain the necessary range of temperatures is described in section 3.4.3. Specimens for low temperature testing were cut in the rolling direction. The effect of predeformation on the DBTT was documented by cold rolling RP CA IF sheet in the prior rolling direction. A small scale rolling mill was used to deform the as-received sheet to a true thickness strain of 0.35, 0.65 and 0.90 in plane strain. The samples were then cut in the rolling direction and transverse to the rolling direction. Samples were cut from cross-rolled sheet, e.g. one pass in the rolling direction, the next pass in the transverse direction, to the same true thickness strains.

3.4.3 Low Temperature System

Low temperature tensile testing and cup expansion testing was carried out with the specimens and grips submersed in baths held in an insulated container and maintained at constant temperature. Bath temperature was monitored with a thermometer and a K-type thermocouple. The temperature ranges for the various combinations used for the baths are given in Table III-III. A suitable and safe liquid for bath temperatures in the

Table III-III Baths used for low temperature testing

Bath	Temperature (°C)
$N_{2\,(l)}$	-196
sprayed $N_{2\,(l)}$	-150 →-190
99.999% ethanol, dry ice, $N_{2\,(l)}$	-78 →-120
99.999% ethanol, dry ice	0 →-78
water, ice	0
air	20 →25
vegetable oil, immersion heater	30 →140

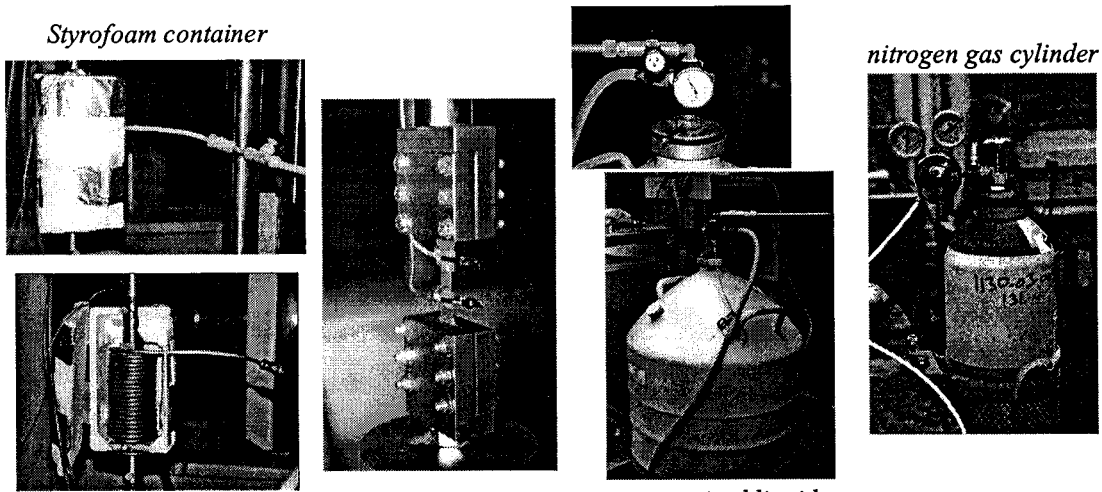

Figure 3.3 - Low temperature liquid nitrogen spray system used to test material between -140°C and -190°C.

range of -120°C to -196°C could not be found. Therefore, a liquid nitrogen spray system (see Figure 3.3) was designed to maintain the selected temperature in this temperature range. A copper coil was wound around the tensile grips and specimen, and 0.5 mm holes where drilled on the inside of the winding. A sealed liquid nitrogen Dewar, maintained at constant pressure with gaseous nitrogen, was used to spray liquid nitrogen on the sample. The rate of spraying was adjusted to achieve different temperatures. The grips and specimens were enclosed in a Styrofoam container, and two thermocouples were attached to the specimen gage to monitor temperature.

3.5 Deep Drawing Cylindrical Flat-Bottomed Cups

Circular blanks of the appropriate diameter were machined from the as-received industrially annealed materials. The galvanized coating on the continuously annealed material was removed with a 10% hydrochloric acid by volume and distilled water solution. Square grids, 1.0 mm in length, were electro-etched on the specimens as outlined in section 3.6 and used for strain measurement.

Cylindrical flat-bottomed cups were deep drawn using two different methods; a Swift flat-bottomed die and punch assembly and a tractrix die (Keeler 1969) and punch assembly. The different die geometries

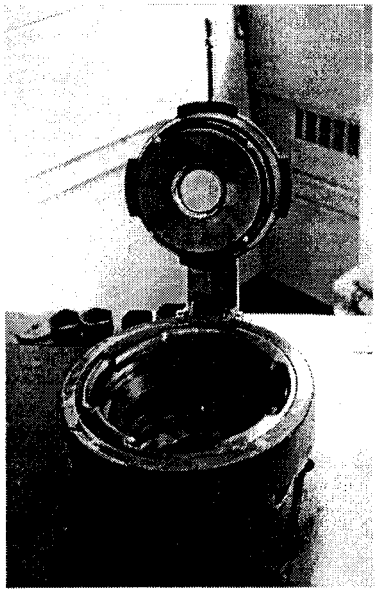

Figure 3.2 - Hille double-action inverted hydraulic press.

were used to investigate the influence of die geometry and residual stresses on CWE.

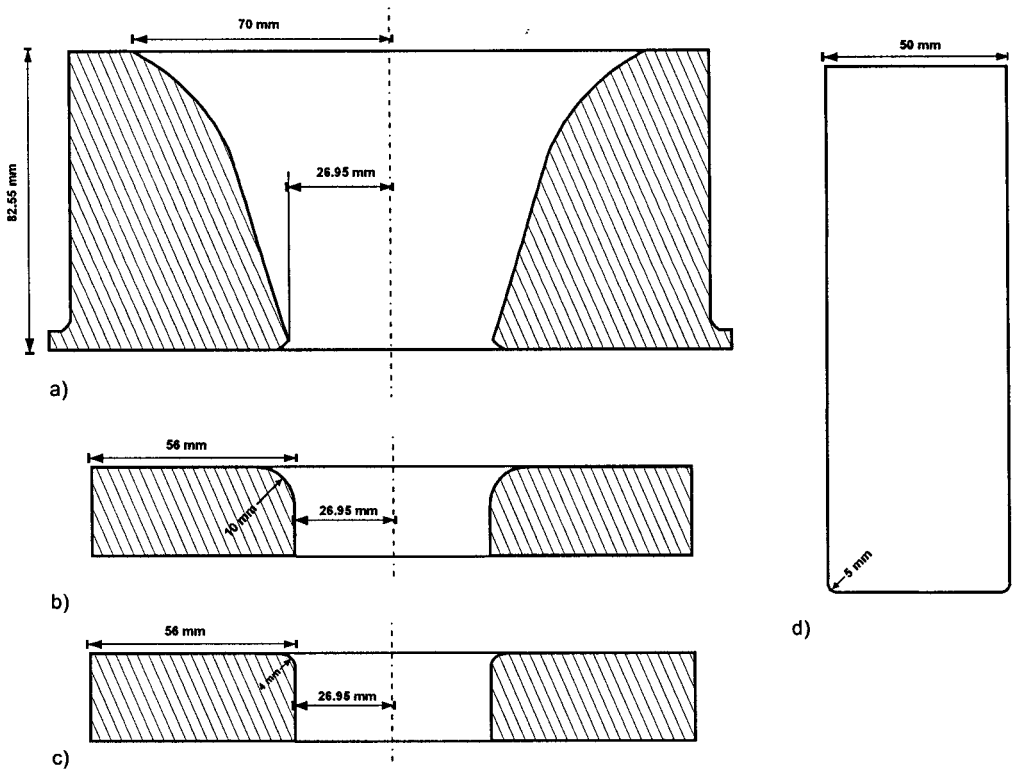

Figure 3.4 - Dies and punch geometries for cup drawing a) tractrix die b) die configuration 1 c) die configuration 2 and d) punch.

Table III-IV Geometry of drawing dies, punch and blankholder

TOOL	DIE/NOSE RADIUS	DIE/PUNCH CLEARANCE
DIE 1	R10 mm	1.95 mm
DIE 2	R4 mm	1.95 mm
TRACTRIX DIE	tractrix profile	1.95 mm
PUNCH	R5 mm	---

Table III-V Trimmed cup height

DRAW RATIO	1.5	1.65	1.8	2.0	2.2	2.4
HEIGHT	15	20	26	34	43	54

Swift flat-bottomed cups were drawn using a Hille inverted die double-action hydraulic press (Figure 3.2) with a 50 mm diameter punch. A hydraulic cylinder supplied a nearly constant blank holder force with the hold-down pressure adjusted to prevent wrinkling. Two dies with different radii (10 mm and 4 mm) were used. The die and punch geometries are shown in Figure 3.4, with the relevant information summarized in Table III-IV. This die and punch geometry gives a clearance of 1.3t for the thicker gage steel, and 2.44t for the thinner gage steel where t is the sheet thickness. The drawing force is minimal with a clearance of 1.15t - 1.20t, while a clearance of 1.07t - 1.15t is usual. A punch speed of 90 mm/min was used for all cups. The blanks were lubricated with a non-petroleum based synthetic drawing compound (Drawsol 260), mixed with water in the ratio 1:1. Load and punch stroke data was acquired with a calibrated load cell and linear variable displacement transducer (LVDT).

Cylindrical cups were also drawn using a single action tractrix assembly on an MTS universal load frame. The stroke speed was of 12 mm/min and Drawsol 260 diluted with water was used as the lubricant (1:1 ratio). The geometry of the tractrix die is summarized in Figure 3.4 and Table III-IV. The tractrix (or Hugyen) die assembly was patented May (1938). A tractrix curve has the property that any tangent to the curve and a fixed straight line is of constant length. This line is the generator of the circular punch in the drawing operation. The tractrix die is considered to minimize redundant plastic work. The need for hold-down pressure is eliminated with the use of a tractrix die. However, without a hold-down force, the likelihood of failure by wrinkling is increased. When cup drawing without a hold-down force, the ratio of the supported length to the sheet thickness must be within a certain limit or the blank will wrinkle. Therefore, although the advantages of deep drawing with a tractrix die include i) lower cupping loads, ii) lower die wear, iii) greater dimensional accuracy, iv) greater drawing ratios (Oehler 1963), and v) the ability to use a single action press, a certain sheet thickness must be employed to prevent wrinkling.

After drawing, the cups ears were cut using a lathe with a sharpened and polished tool steel bit using WD 40 as the cutting lubricant. The minimum amount of material was removed at each draw ratio, so that the height of all cups for a given drawing ratio was the same (Table III-V).

3.6 Nodal Strain Measurement Using Square Grid Analysis

Nodal strain measurement suing square grid analysis was used to measure the plastic deformation of deep drawn cups. The square grids, 1.00 mm in length, were electro-etched onto the surface of the flat specimen. An example of the etched grids, before and after deformation, is shown in Figure 3.5. Strains were measured with FMTI Systems Square Grid Analysis (SGA) software version 2.2 (Sklad 1990). A traveling micrometer stage, with a CCD camera fixed on a vertical traveling arm, were used to capture the grid elements as a function of position on the deep drawn cups. For a review of experimental nodal strain measurement using square grids see Sowerby (1985) and Sowerby, Chu and Duncan (1982).

Pure homogeneous proportional deformation is assumed. The principle strains, assuming incompressibility, are,

$$d\varepsilon_1 \qquad d\varepsilon_2 = \alpha d\varepsilon_1 \qquad d\varepsilon_3 = -(1+\alpha)d\varepsilon_1 \tag{3.3}$$

Where α is a constant and the principal direction, 3, is normal to the sheet. The measured strain in the plane of the sheet can be used to calculate an effective strain. To so do, a yield criterion must be chosen. Interstitial-free sheet steels are not isotropic, they exhibit significant normal anisotropy and to a lesser extent planar anisotropy. Therefore, a yield criterion must be chosen that models the material behaviour accounting for the anisotropy. Hill's 1950 criterion was chosen (Hill 1950). This is a planar isotropic yield criterion, it is assumed that the normal anisotropy coefficient, *r*, is constant in the plane of the sheet and remains constant throughout the deformation process. The RP IF sheet steel investigated exhibits planar anisotropy, but the assumption of planar isotropy greatly simplifies the strain analysis and does not change the magnitude of the effective strains or the shape of the yield surface significantly (when compared to the equivalent planar anisotropic case). Hill (1950) proposed the symmetric yield function,

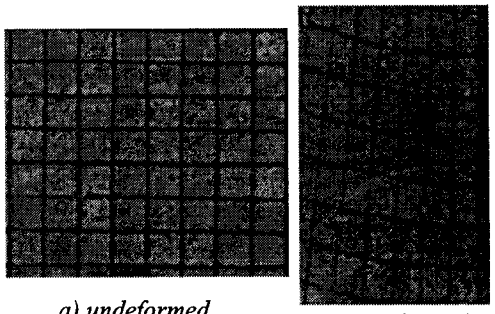

a) undeformed *b) deformed*

Figure 3.5 - Electro-etched 1.00 mm square grids, undeformed and after deep drawing.

$$\bar{\sigma}^2 = \sigma_1^2 + \frac{2r}{1+r}\sigma_1\sigma_2 + \sigma_2^2 \tag{3.4}$$

This leads to an effective stress, $\bar{\sigma}$, and strain, $\bar{\varepsilon}$, given by,

$$\bar{\sigma} = \left(1 - \frac{2r}{1+r}\beta + \beta^2\right)^{1/2}\sigma_1 \tag{3.5}$$

$$\bar{\varepsilon} = \left(\frac{1+r}{\sqrt{1+2r}}\right)\left(1 + \frac{2r}{1+r}\alpha + \alpha^2\right)^{1/2}\varepsilon_1 \tag{3.6}$$

$$\beta = \frac{(1+r)\alpha + r}{\alpha r + (1+r)} \tag{3.7}$$

3.7 Microhardness Tests

Vickers microhardness indents were used to determine the hardness of the steel as a function of deformation. The LECO M-400-H2 hardness testing machine was used with a 200g load and a 20 s dwell time. Industrially annealed material was compared to deep drawn cups, sectioned to expose the rolling direction. This sectioning allowed hardness test to be performed around the bend and up the cup wall height. The Vickers hardness, H_v, can be related to the flow stress by the simple relation (Shaw 1966),

$$H_v = 3 \cdot \bar{\sigma}(kgf/mm^2) \tag{3.8}$$

The flow stress is therefore,

$$\bar{\sigma} = 3.269 \cdot H_v(MPa) \tag{3.9}$$

This relation is derived by assuming a plastic-rigid material; as such, it is most applicable for low strain hardening or highly cold worked materials.

3.8 Residual Stress Measurement

Macroscopic residual stresses were measured using a separation technique (Hatfield and Thirkell 1919, Sachs and Espey 1942, Siebel and Muhlhauser 1954). Electro-discharge machining was used to cut cylindrical rings from the deep drawn cups and to slice them for the macroscopic circumferential residual stress, and to cut longitudinal tongues for the macroscopic longitudinal residual stresses. Measurement of the curvature before and after opening gives an approximation of the maximum macroscopic residual stress on the outside surface.

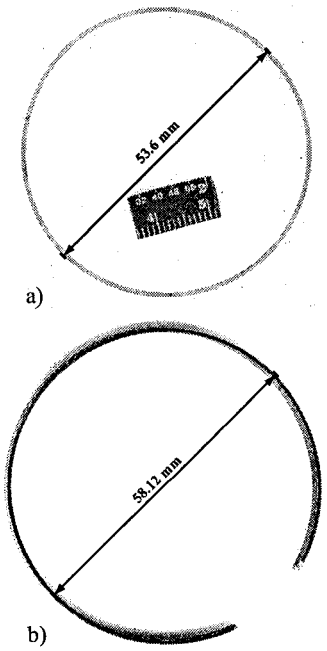

Figure 3.6 - Example of ring cut from deep drawn cup, a) before and b) after opening.

A simple analysis, used by Davidenkov (1932), Siebel and Muhlhauser (1954) and Sachs and Espey (1941) and more recently by Ragab and Orban (2000) is the standard approach taken to obtain the magnitude of the macroscopic residual stresses. Residual stresses are assumed to vary linearly through the thickness with the same magnitude, but of opposite sign, on the outside and inside surfaces. Residual stresses originate from the bending and unbending over the die radius during deep drawing (Saito and Shimahashi 1978). The elastic bending moment released during the opening flexure is used to derive the maximum unbending residual stress (for details see Appendix C). A comparison of the initial curvature , $\frac{1}{r_o}$, to the curvature after opening,

$\frac{1}{r_1}$, gives the elastic unbending strain at the outer surface and therefore the maximum unbending stress is given by,

$$\sigma = \frac{E \cdot t}{2}\left(\frac{r_1 - r_o}{r_1 r_o}\right) \tag{3.10}$$

An example of a ring cut from a deep drawn cup (RP BA DR 2.2), before and after opening, is shown in Figure 3.6. The curvature of the longitudinal tongues was calculated by differentiating a fifth order polynomial fit to the profile of the tongue before and after slitting (equation C.8).

Rings were cut from cups with draw ratios of 1.65 (die 1, die 2 and tractrix die), 1.8, 2.2 (thin gage sheet for die 1, die 2, heat treated at 550°C for 1 hr before and after, heat treated at 820°C for 60s and thick gage sheet for die 1 and the tractrix die) and 2.4. The width of the rings varied down the length of the cup; the first five rings, starting from the top of the cup, were 3 mm wide, the next three rings were 4 mm wide, while the last rings were 6 mm wide. Longitudinal residual stresses were measured on the 0.8 mm gage material, for a draw ratio of 2.2.

3.9 Cup Expansion Test

The cup expansion test was used to test the steel's susceptibility to CWE. A conical punch and a ram were used to circumferentially expand the deep drawn cups. This was done over a range of temperatures to obtain a ductile-to-brittle transition temperature. The experimental setup and geometry of the conical punch are shown in Figure 3.7. Cups were tested submersed in the low temperature baths (section 3.4.3). Bath temperature was monitored with a thermometer and a K-type thermocouple. The temperature of the cup was also monitored with a K-type thermocouple. An MTS universal testing frame, using a constant ram speed of 5 mm/s, was used for testing. For most tests a minimum of 15 cups were used to obtain the transition temperature. Higher ram speeds, greater than 50 mm/s, were achieved by using a guided ram weighing 10.43 kg and dropped from various heights.

The DBTT was determined by observing the percent brittle crack length along the cup height as a function of temperature. The nature

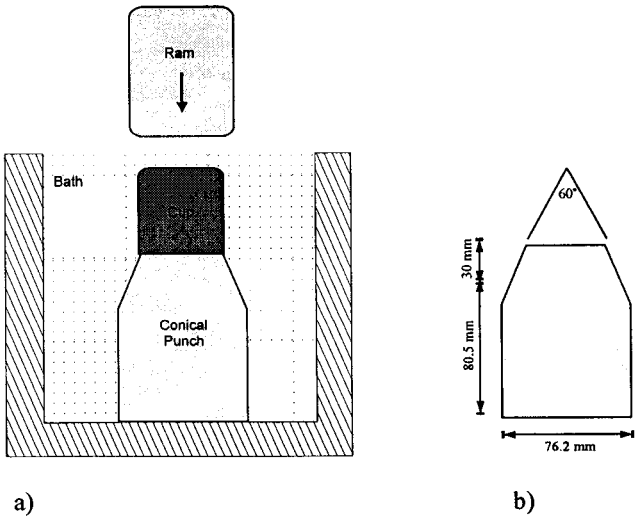

Figure 3.7 - a) Cup expansion test setup and b) geometry of conical punch.

of fracture along the cup height in terms of brittle versus ductile behaviour was distinguished optically and verified by SEM analysis. The DBTT was defined as the temperature when 50% brittle crack length occurs.

A series of cup expansion tests were performed to assess different test conditions. The baseline test uses 0.8 mm thick sheet, a ram speed of 5 mm/s, and cups drawn with die 1.

Industrial Annealing Treatment: The light gage RP, 0.8 mm, was compared in the batch and continuously annealed state for a DR of 2.2.

Draw ratio: Circular blanks of different diameters (75 mm, 82.5 mm, 90 mm, 100 mm, 110 mm, 120 mm, 125 mm, 130 mm) were machined out of the RP CA 0.80 mm sheet, giving draw ratios of 1.5, 1.65, 1.8, 1.9, 2.0, 2.2, 2.4, 2.5, and 2.6. The limiting draw ratio (LDR), the ratio of the largest blank that can be successfully drawn over the punch diameter, was found to be 2.4. Cups, with a DR of 2.4, were also lathed down to the same height as cups with a DR of 2.2 and cups with a DR of 1.8.

Thickness: The 1.5 mm gage RP CA was compared to 0.8 mm gage RP CA for DRs of 2.2 and 1.65.

Die geometry: Die 1, die 2 and the tractrix die were compared for a DR of 1.65 with 0.8 mm gage material. The limiting draw ratio for this gage of steel using the tractrix die was 1.65, therefore the 1.5 mm gage was used to compare die 1 with the tractrix die for draw ratios of 1.65 and 2.2.

Coating: Cups of DRs 1.65 and 2.2 were formed and tested with the galvannealed coating left on and compared to cups tested with the coating removed with 10% HCl prior to forming. To ensure the removal of surface cracks, blanks 110 and 82.5 mm in diameter were chemically thinned 50 μm on each side after removing the galvannealed coating and prior to deep drawing. These blanks were then deep drawn into cups and tested.

Edge conditions: Blanks of 120 mm diameter were partially deep drawn. The resulting cups had the flange left on and had a height of 30 mm. The results were compared to cups with a draw ratio of 1.8, which have roughly the same height.

Rate of expanding the drawn cup: Cups of CA and BA materials with DRs of 2.2, tested using a ram speed of 5 mm/s, were compared to cups of CA and BA, DR 2.2, tested using a weight of 10.43 kg dropped from a height of 1 m. As well, the RP CA DR 2.2 was tested at a ram speed of 0.01 mm/s, which gives the same strain rate as that used in the tensile tests. The ductile-to-brittle was also determined as a function of strain rate, at constant temperature (25°C) and draw ratio (2.2).

Post forming annealing treatment: A series of deep drawn cups, RP CA DR 2.2, were annealed in a salt bath at 550 °C for 1 hour. Another series of blanks were annealed at 550 °C for 1 hour prior to drawing. The intention

of these heat treatments was to relieve the residual stresses without appreciably changing the flow stress. Two recrystallization heat treatments were also performed on the deep drawn cups. One series was heat treated at 820 °C for 60 s. This was sufficient to fully recrystallize the material. The other recrystallization was performed at 820 °C for 5 minutes. A third series was recrystallized at 820 °C for 60 s, then heat treated at 550 °C for 1hr. The oxide was removed from the cups with a solution consisting of 225 ml water, 275 ml HCl acid and 1/2 gram of methenamine.

A quantitative fractographic analysis was performed for all the different conditions used in the cup expansion experiments to determine the percentage of intergranular fracture.

3.10 Bulk X-ray Crystallogr aphic Texture

Crystallographic texture was measured on a Scintag 5-axis pole figure goniometer, with 2mm oscillation, a 4mm diffracted beam slit, a 0.8mm circularly collimated monochromated Fe radiation beam, and with a counting time of 1 second per position. Batch and continuously annealed materials were compared in the cold rolled and annealed state (as-received) and after deep drawing. Samples were taken from the top of the deep drawn cup in the prior rolling direction (a height of about 35 mm). The samples were two centimeters square. Texture data was analyzed with popLA software (Kallend et al. 1991). Raw data was corrected for background, defocused and normalized. Data was slightly rotated to force symmetry, correcting for slight sample misalignments in the goniometer. Data was analyzed using a harmonics algorithm to produce FUL pole figures, and then run though the WIMV algorithm to produce sample orientation distributions (SOD). Crystallographic orientation distributions (COD) and inverse pole figures were calculated from the SOD.

3.11 Scanning Electron Microscopy

Fractographic analysis of tensile specimens and expanded deep drawn cups was performed on a Philips 515 scanning electron microscope (SEM) with a LaB_6 cathode. Secondary electron mode with an accelerating voltage of 20 KeV was used for imaging. The percent fracture mode was determined on the tensile fractures and on the fractured deep drawn cups by using a grid counting method. The Philips 515 SEM was coupled with X-ray energy dispersive spectroscopy (XEDS) (Link QX2000 Energy Dispersive X- RAY Analyzer) to identify the chemical composition of precipitates. The precipitate analysis was not rigorous, no attempt was made to quantify the chemistry or the volume distribution of the precipitates. Precipitates were exposed with a deep 5% nital etch. The smaller precipitates, typically niobium carbides, were analyzed using the transmission electron microscope with XEDS.

3.12 Electron Back-Scatter Diffraction

Electron back-scatter diffraction (EBSD) was used to examine the relationship between grain boundary structure and the propensity for IGF. The geometrical nature of the grain boundary can be described by five

macroscopic degrees of freedom; these five parameters are needed to describe the misorientation between grains and the orientation of the grain boundary plane. Three microscopic degrees of freedom describe the relative translations at the grain boundary of one grain with respect to the other. A review of the different methods of characterizing the geometrical nature of grain boundaries can be gained by referring to Wolf (1989)(1992), Sutton and Balluffi (1987), and Randle (1992). Excellent reviews of the EBSD technique have been provided by Randle (1992), Randle and Engler (2000) and Schwarzer (1993).

A Hitachi S-4500 cold field emission gun (cFEG) SEM was equipped with TexSEM Laboratories' (TSL) Orientation Imaging Microscopy (OIM) system. The electron back-scatter patterns (EBSP) are captured with a low-light CCD camera. The operating conditions for EBSD runs were an accelerating voltage of 20 KeV, an emission current of 20 μA, and a working distance of 15 mm. The cathode stabilizes 1.5 to 2 hours after flashing, therefore scans of 14 hours were possible as the cathode must be flashed every 16 hours. Samples (preparation described in 3.3.1) were mounted on a small stub with silver paste to provide good conduction to prevent charging. The stubs were inserted in a holder designed for EBSD work; a stage with a surface inclined 70° to the incident electron beam. The EBSD scans were run in low magnification mode so the strong magnetic field of the objective lens would not distort the Kikuchi maps. A permalloy shielding aperture was also available; this was attached to the EBSD holder above the specimen for runs in high magnification mode. The EBSD system was calibrated for the pattern center by using the camera method and by using the Si single crystal method (Randle 1992, 38-46). The pattern center could be consistently determined within 1-2° with the objective lens off and 5° with the objective lens on. This error is taken as an inherent error in determining the absolute orientation. Additional errors in determining the absolute orientation arise, as in bulk texture measurements, from errors placing the sample in the reference orientation. The errors in determining the absolute orientation do not affect the determination of the misorientation, as the error in the absolute orientation will be the same for both grains. Errors in misorientation arise due to errors in indexing the EBSPs; the error in the automated indexing are not necessarily shifted in the same direction for each grain. The error in relative orientation has been reported to be 0.5° (Randle 1992), but a more realistic (conservative) value was estimated from a random sampling of indexed patterns to be 1°. Improvements in spatial resolution always compete with a degradation in pattern intensity. The spatial resolution depends on the accelerating voltage, the emission current, and working distance, the tilt angle, and the atomic number of the sample. It is also non-symmetric, as the electron beam smears in the longitudinal direction. The lateral and longitudinal spatial resolution has been reported to be between 150-200 nm and 300-450 nm respectively for a nickel sample under similar operating conditions (30 KeV,

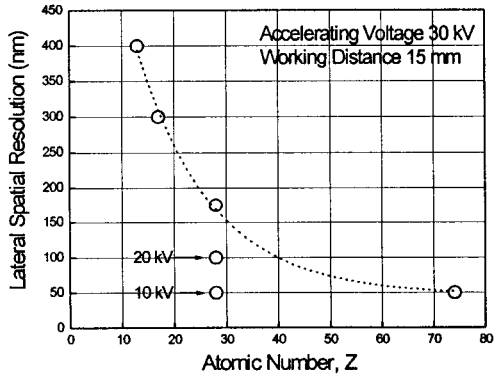

Figure 3.8 - Lateral spatial resolution as a function of atomic number for a FEGSEM EBSD system (Isabell and Dravid 1997).

15 mm WD, 70° tilt, Hitachi S-4500 II FEGSEM)(Isabell and Dravid 1997). The lateral spatial resolution for Fe can estimated from Figure 3.8 to be 190 nm at 30kVand 100 nm at 20 kV. The sectional grain area distributions of the RP IF steel warranted a step size of 0.8 μm. A square grid was used for the scan. Indexing was done using a Hough transform for the undeformed patterns, while both the Hough and Burns algorithms were used with band width determination for the deformed samples. The number of video frames over which the diffraction pattern was integrated was set to 32 for deformed samples, as opposed to 16 for undeformed samples. These different conditions used for the deformed samples increased their indexing ability. An example of an indexed Kikuchi map in shown in Figure 3.10.

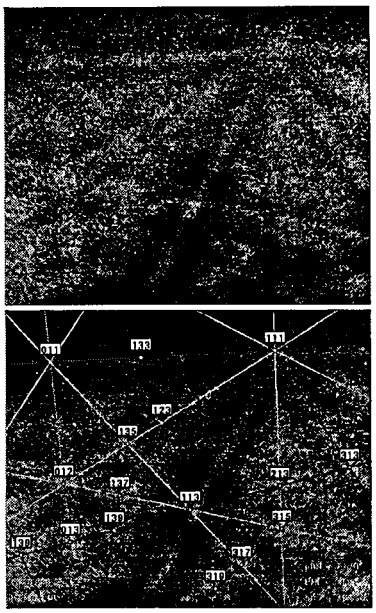

Figure 3.10 - a) Un-indexed and b) indexed Kikuchi map taken from highly deep drawn RP CA IF steel ($\bar{\varepsilon} = 0.5$) using EBSD system and conditions

Raw data obtained from the EBSD runs include the spatial position of the EBSD pattern, the three Euler angles describing the misorientation, Δg, the image quality (IQ), a parameter measuring the Kikuchi pattern quality, and the confidence index (CI), a parameter measuring the confidence in the automated indexing of the Kikuchi pattern. For a more complete description of these terms, see Orientation Imaging Microscopy - User Manual (1996). The orientation of the grain boundary plane was not obtained in the present fracture path study.

The intergranular fracture path was characterized for grain boundary structure using EBSD to determine if a correlation between grain boundary structure and the probability of intergranular fracture exists. A new approach for characterizing fracture paths was developed. Automated EBSD runs were performed prior to fracture at the tip of an arrested crack for the deep drawn material and at the tip of an electro-machined notch for the undeformed material. The notches were electro-discharge machined into the specimens and had a 45 μm radius. The samples were then bent in liquid nitrogen, with fracture initiating at the pre-existing flaw and running through the analyzed area. The specimens were approximately one centimeter in width and five centimeters in length. A three point bend apparatus was used for bending; the nominal stress on the analyzed surface was uniaxial tension.

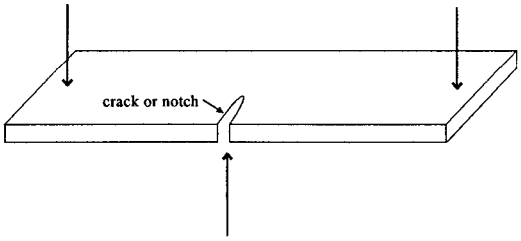

Figure 3.9 - Notched or precracked three-point bend specimen. Nominal uniaxial tension on outer bend surface.

The samples were characterized for grain boundary structure by using both the Coincident Site Lattice (CSL) and angle/axis (θ / l) schemes. Terminology used in the thesis for CSL theory and θ / l pairs is explained in Randle

and Engler (2000). Generally, boundaries that have a good geometric fit, so called special in nature, often have properties that are different than those that are general, or have no especially good fit. Grain boundaries taken as special had sigma (Σ) values less than or equal to 29.

The fracture path data was analyzed in two distinct ways. First, the grain boundary structure distribution of cracked boundaries was compared to the grain boundary structure distribution of uncracked grain boundaries. Second, uncracked grain boundaries adjacent to the crack were included in the analysis. Grain boundaries that abut the fracture path represent a path that was not chosen by the crack when the crack arrived at a triple junction. These grain boundaries therefore give information on the nature of the intergranular crack path-grain boundary structure relationship. Grain boundary statistics were categorized using CSL theory as a length fraction, and also plotted as discrete misorientation distribution plots in stereographic space using θ / l pair representation. The Brandon criterion (Brandon 1966) was used to specify the maximum deviation from an exact CSL orientation that is permissibly accommodated by dislocations, and is given by $15^{o}\ \Sigma^{n}$ where a value of $n = -1/2$ was used. The misorientation distribution function (MDF) gives the probability of finding a grain boundary of misorientation ΔM. The misorientation distribution, when plotted as a continuous function, was constructed from binned measured data.

3.13 Transmission Electron Microscopy

A FEG TEM/STEM (JEOL 2010F) was used with X-ray energy dispersive spectroscopy (XEDS) to examine grain boundary segregation and the associated structure. Detection of relatively low levels of grain boundary segregation of phosphorus in α-Fe is rarely done due to the need for an extremely small probe size, a high current density and a windowless detector. This approach differs from the usual method, Auger electron spectroscopy (AES), and has advantages, as fine grain boundary structure, misorientation and segregation can be determined. Also, grain boundaries that are resistant to fracture can be investigated, unlike AES which requires in-situ grain boundary fracture.

3.13.1 Thin Foil Preparation for Transmission Electron Microscopy

Samples were prepared by grinding the 800 μm thick sheet down to a thickness of 200 μm; an equal amount of material was taken off each side. A electro-discharge cutter or a mechanical punch was used to cut 3 mm diameter discs. These were mechanically polished with 400 grit silicon carbide paper to a thickness of 90 μm, dimple ground a further 20 μm using a 3 μm diamond paste, and then polished with a napped wheel using a 1 μm diamond paste. The discs were thinned to electron transparency using a jetpolisher with a 10% perchloric acid - 90% methanol solution with an applied voltage of 15-20 V maintained at -35 °C.

3.13.2EDS Analysis of Grain Boundary Segregation

A JEOL 2010F FEG scanning transmission electron microscope, coupled with an Oxford ultra-thin window XEDS detector and a Gatan Parallel Electron Energy Loss Spectroscopy (PEELS) detector, were used with LINK's ISIS software to analyze grain boundary segregation. The window of this detector consists of polymer supported by a grid of silicon. The accelerating voltage used was 200 kV with an incident probe size of approximately 1 nm and an effective counting time of 100s or 500s. A beam tracking device was used, which automatically corrects for drift. The drift correction interval was set at 2 seconds as the foil exhibited significant drift. The grain boundaries chosen for analysis were oriented parallel to the electron beam. This condition is essential, especially when using a small incident beam size.

3.13.3Quantifying the Grain Boundary Segregation

To quantify grain boundary composition, the thickness of the area examined, an estimate of the shape of the interaction volume and an approximation of the proportionality factor are required. The Cliff-Lorimer method (Cliff and Lorimer 1975) was used to estimate the grain boundary composition. This method assumes a proportionality factor can be used to relate the ratio of the intensities to the ratio of the concentrations,

$$\frac{C_A}{C_B} = k_{AB}\frac{I_A}{I_B} \tag{3.11}$$

where C_n is the concentration of element n and $C_A + C_B + C_C \ldots C_n = 1$, I_n is the intensity of element n, and k_{AB} is the k-factor. A standardless approach was used to obtain the k-factors. The background intensity was digitally filtered and the intensities of the characteristic peaks were obtained by scaling library standard peaks. The STEM-XEDS measurements underestimate the degree of segregation because the probe size is larger than the grain boundary width and because of beam broadening. To calculate the actual grain boundary composition the probe size and beam broadening must be taken into account. To estimate the beam broadening an analytical expression for the beam broadening of a small probe was used. This derivation assumes each electron suffers a single large angle Rutherford type elastic scattering event in the middle of the foil and emerges over a distance b defined as the beam spreading. The expression for b in cm is:

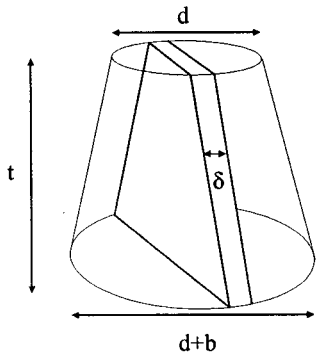

Figure 3.11 - Geometry used to estimate interaction volume to calculate the absolute amount of segregant.

$$b = 625\left(\frac{\rho}{A}\right)^{1/2}\left(\frac{Z}{E_o}\right)t^{3/2} \tag{3.12}$$

Where ρ is the specimen density in g/cm^3, E_o is the operating voltage in kV, A is the atomic weight of the specimen, Z is the atomic number and t is the thickness of the foil in cm. The expression for the beam broadening arbitrarily assumed that 90% of the scattered electron and hence 90% of the X-ray generation is contained within the volume enclosed by the broadening estimate. The incident beam diameter can be added to the equation for beam broadening and for a thin foil it is assumed that the beam spreads into a cone. A mass balance can be performed assuming the segregating element has segregated to a thin layer of thickness, δ, the grain boundary width. The mass balance is based on simple geometric considerations that assume the bulk concentration has been measured and is valid for the concentration of the matrix adjacent to the grain boundary that is encompassed by the interaction volume.

$$C_{measured}V_{cone} = C_{layer}V_{layer} + C_{bulk}(V_{cone} - V_{layer}) \tag{3.13}$$

The geometry used for the mass balance is given in Figure 3. 11, where the volume of the truncated cone is,

$$V_{cone} = \pi\left[\frac{b^2t}{12} + \frac{dbt}{8} + \frac{d^2t}{4}\right] \tag{3.14}$$

and the volume of the segregated layer, V_{layer}, is,

$$V_{layer} = d\delta t + b\delta t \tag{3.15}$$

where d is the incident electron probe diameter.

3.13.4Determination of Foil Thickness From Zero Energy Loss Peak

The thickness of the thin foil near the vicinity of the grain boundaries was analyzed using electron energy loss spectroscopy (EELS). The foil thickness can be accurately measured by comparing the intensities of the zero loss peak and the plasmon peak. The probability $P(m)$ of an electron exciting m plasmons and losing an energy $m \cdot E_{PL}$ is given by the Poisson distribution,

$$P(m) = \frac{1}{m!}\left(\frac{t}{L_{PL}}\right)^m \exp\left(\frac{-t}{L_{PL}}\right) \tag{3.16}$$

where Lp is the mean free path for plasmon excitation. The ratio of the probabilities of exciting zero plasmons compared to the total, P(0) and P(T) gives the foil thickness as,

$$t = L_{PL}\ln\left(\frac{P(1)}{P(T)}\right) \tag{3.17}$$

On the energy loss spectrum this is given by the ratio for the integrated intensities of the first plasmon peak and the total energy loss spectrum. The EELS analysis was carried out using Gatan Parallel EELS (PEELS) system. The program used deconvolutes and integrates the peaks to determine the intensities. The expression for the mean free path for energy losses is given by Malis et al., 1988,

$$L_p = \frac{106FE_o}{\left\{E_m \ln\left(\frac{2\beta E_o}{E_m}\right)\right\}} \tag{3.18}$$

where L_p is in nm, the beam energy E_o in keV, β is the spectromter collection angle in mrad, F is a relativistic correction factor and E_m is the average energy loss in eV. For a material of average atomic number Z is given by $E_m = 7.6Z^{0.36}$. The realtivistic factor, F, is ,

$$F = \frac{\left(1+\frac{E_o}{1022}\right)}{\left\{1+\left(\frac{E_o}{511}\right)^2\right\}} \tag{3.19}$$

3.13.5Errors Associated with Quantification

The main errors are in quantifying grain boundary segregation using XEDS involve determining the thickness of the foil, the k-factors, and assuring the grain boundary is encompasses by the electron beam throughout the foil thickness. As mentioned this is best accomplished by having the grain boundary parallel to the electron beam. As well, the grain boundary width and the distribution of segregant across the boundary have to be assumed for many cases. The choice of these parameters can significantly change the results of the quantification as will be discussed.

4.0 EXPERIMENTAL RESULTS

Determination of the controlling variables in CWE necessitates a wide range of experimental study. The transition from ductile to brittle behaviour will depend on the plastic and brittle mechanical response to these controlling variables. The stress necessary to cause plastic flow can be varied by changes in temperature, strain and strain rate. Forming operations serve to work harden the steel sheet, raising the stress required for plastic flow. In addition, non-uniform strains during the forming operation can lead to large internal stresses. Factors, which influence the intergranular fracture stress, include the amount and potency of grain boundary segregant, the crack-size, and the strain path. Detailed microstructural and mechanical characterization was performed and transition temperatures were used to describe the susceptibility to CWE as a function of flow stress, strain path, level of segregation, and internal stress. Cold work embrittlement also depends on mechanical events at the grain boundary; brittle response depends on local grain boundary structure and the associated chemistry. Therefore, grain boundary structures and local chemical compositions have been studied by EBSD and AEM with XEDS and are presented at the end of the chapter.

4.1 Microstructure of Undeformed As-Received Materials

The grain size and shape of the batch and continuously annealed materials was characterized. The extremely low carbon content of IF steels are below those which form pearlite or spheroidized carbides and therefore the microstructure of IF steels consists of ferrite grains (Figures 4.1 and 4.2). The grain size distribution of both steels is shown in Figures 4.1 and 4.2. The equivalent grain diameter, taking into account sectional effects, is 9.0 μm for the RP CA steel and 10.3 μm for the RP BA steel. The grains are essentially equiaxed, although a slight elongation was found along the rolling direction in the transverse plane (Figures 4.1b and 4.2b). Little variation in grain size or shape occurred in the through-thickness direction of either heat treated materials (Figures 4.3 and 4.4).

4.2 Precipitate Analysis

A fine dispersion of small round, 5 to 20 nm diameter, Nb rich precipitates, presumably carbides, were found dispersed in the matrix and at the grain boundary (Figure 4.5). Larger precipitates, between 100 and 1000 nm in length, were found to be mostly comprised of Mn and S. Most of the Mn sulphides were round in shape, although some were also found to be elongated (Figure 4.6). Titanium and aluminum rich precipitates were also found. These precipitates were usually cubic in shape and between 200 and 600 nm. The precipitates found are consistent with a Nb-stabilized rephosphorized grade; e.g. aluminum is added to stabilize the nitrogen, niobium is added to stabilize the carbon, and manganese is added to stabilize the sulphur, and are different from those found in Ti or Ti-Nb stabilized grades (for instance see Subramanian et al. 1991). Satoh,

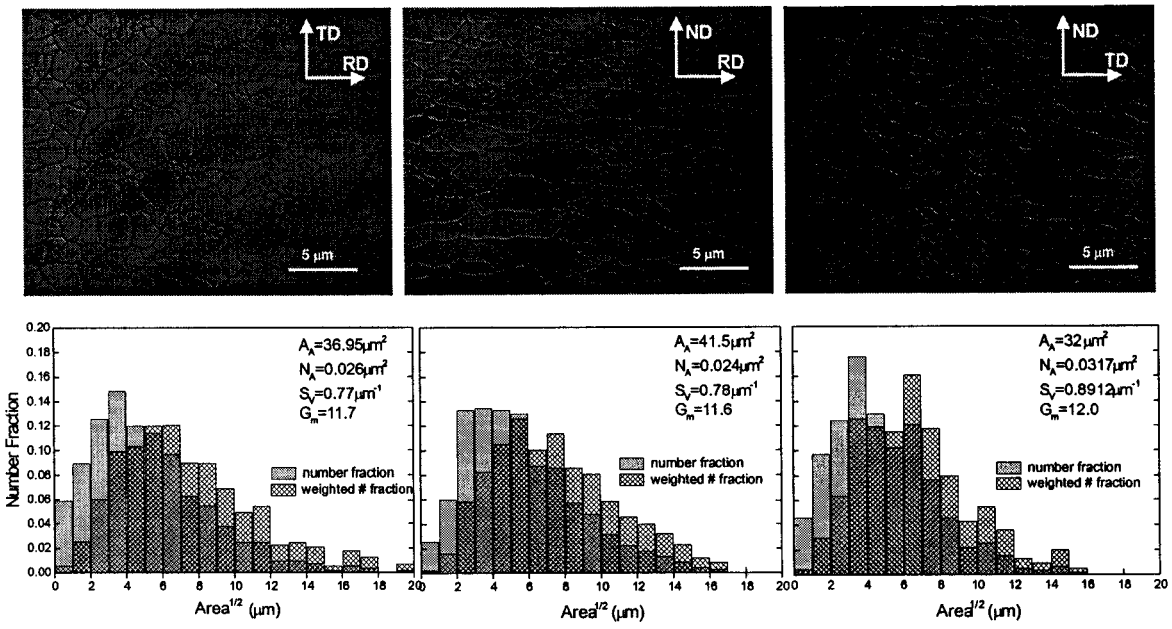

a) normal plane *b) transverse plane* *c) rolling plane*

Figure 4.1 - Optical micrographs and grain area section distributions for RP CA material in the three orthogonal directions of the sheet.

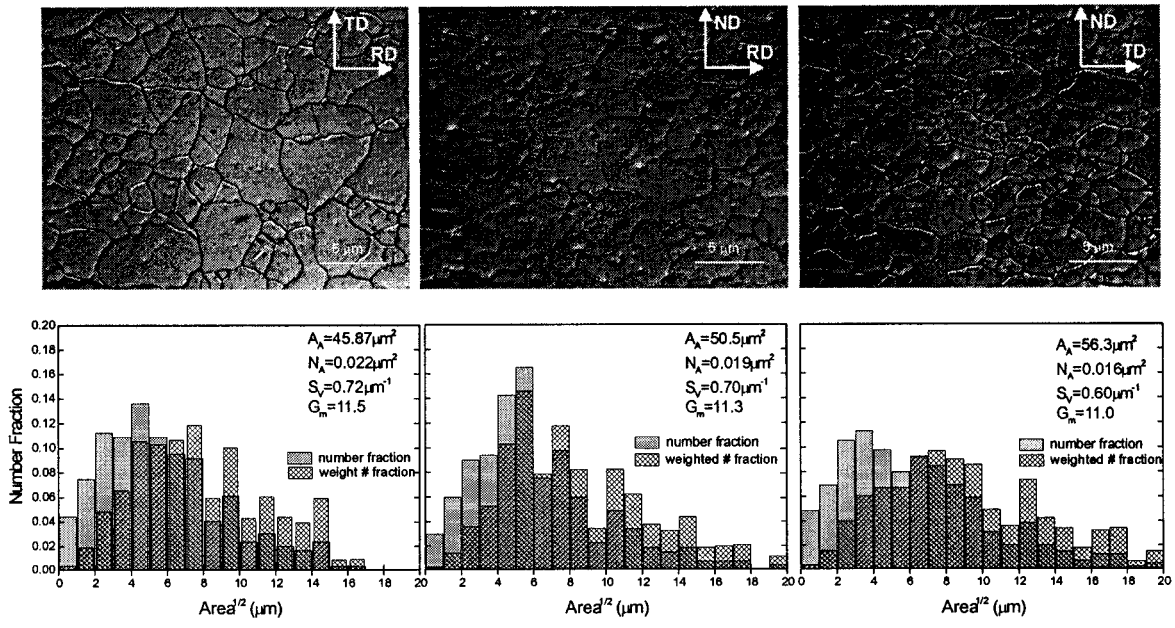

a) normal plane *b) transverse plane* *c) rolling plane*

Figure 4.2 - Optical micrographs and grain area section distributions for RP BA material in the three orthogonal directions of the sheet.

Obara and Tsunoyama (1986) have studied precipitate size and distributions in a Nb-stabilized IF steel with a similar chemistry and found Nb(C, N), AlN, and MnS precipitates. The Nb(C, N) precipitates were densely distributed ($8.8x10^{-14}$ cm^{-3} or $4.6x10^{-14}$ cm^{-3}) with an average precipitate diameter of 11 or 14 nm depending on the hot rolling schedule. In the present work, no differences were found in precipitate morphology or size between the batch or continuously annealed steels. Also, no cracked precipitates were found in either the annealed or deformed materials. The brittle fracture surfaces and planar sections beneath the brittle fracture surface for deformed and undeformed samples were also examined for evidence of fractured precipitates. No evidence of crack initiation at precipitates or inclusions was found, suggesting that fracture initiation is not controlled by precipitate fracture.

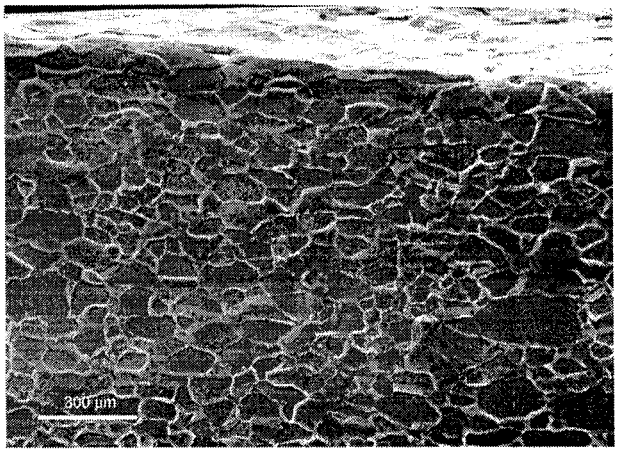

Figure 4.3 - Through-thickness microstructure of RP BA steel etched with 5% Nital.

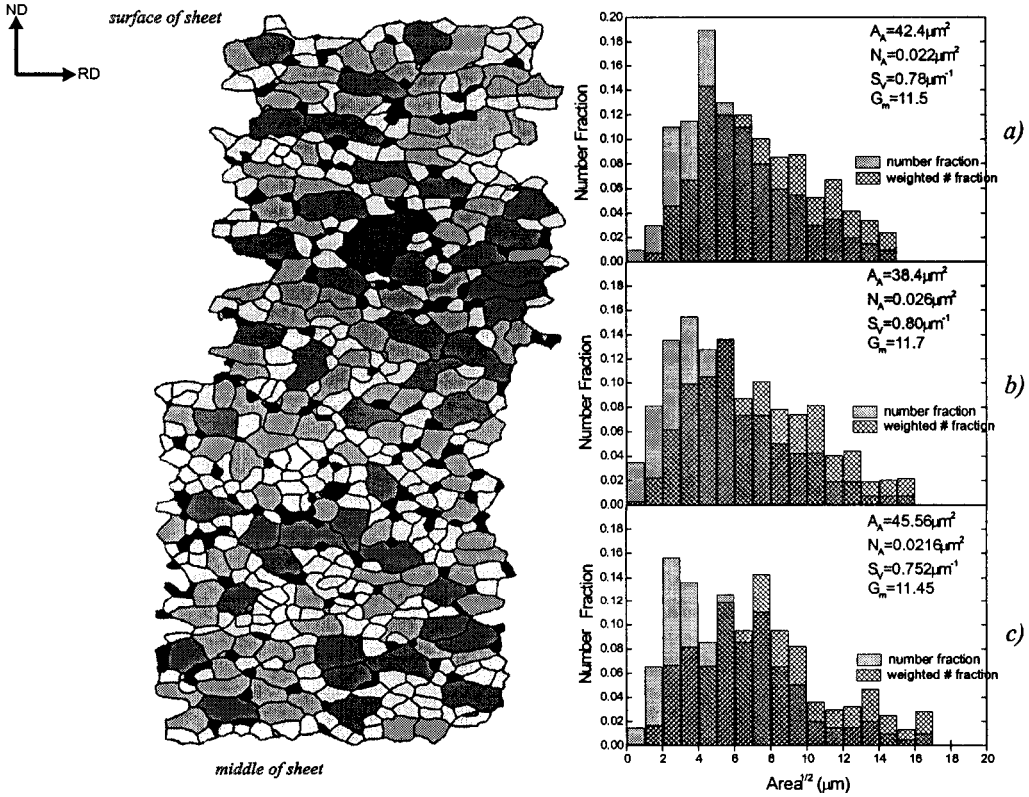

Figure 4.4 - Variation of sectional grain area as a function of through-thickness position in the RP CA material.

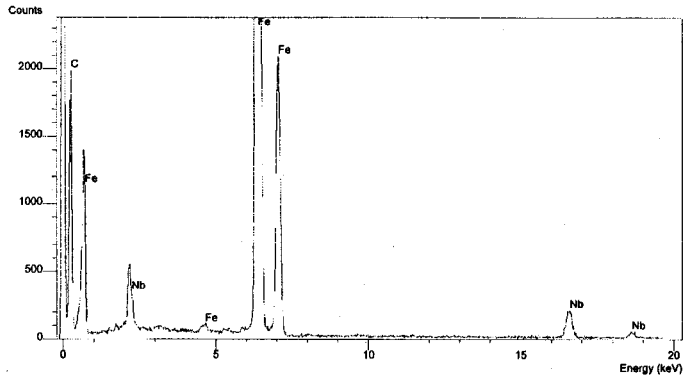

Figure 4.5 - X-ray energy dispersive spectrum from fine niobium carbide precipitates found in rephosphorized IF sheet steel.

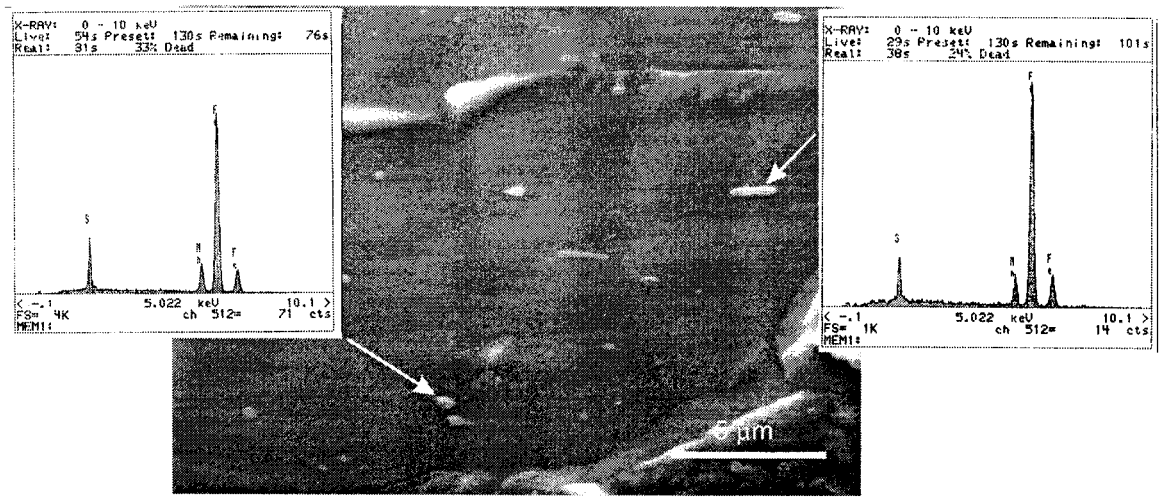

Figure 4.6 - Micrograph and the associated XEDS spectrum of typical manganese sulphide precipitates found in RP CA steel.

4.3 Uniaxial Tensile Testing

4.3.1 Ambient Temperature Properties

Tensile properties of the RP CA light gage sheet were characterized in the longitudinal, transverse and diagonal directions in the plane of the sheet. The steel exhibited little planar anisotropy as characterized by the differences in the yield stress (Table IV-II). The existence of planar anisotropy was more evident from the variation of r-value in the plane of the sheet (Table IV-II). The average r-value is 2.06. The tensile behaviour for the batch annealed and continuously annealed materials is similar (Table IV-I). No yield point elongation is found for any of the materials tested. The average 0.2% offset yield strength for this high-strength grade of IF sheet steel is 218 MPa.

Table IV-I Mechanical properties of as-received RP CA light gage tested in rolling, diagonal and transverse directions

RP CA	0.8 mm					
Orientation	σ_{YS} (0.2%)	σ_{TS}	ε_u	$r_{15\%}$	n	ε_f
RD	215 MPa	463 MPa	0.235	2.10	0.22	2.5
45°	220 MPa	437 MPa	0.18	1.74	0.21	2.43
TD	219 MPa	450 MPa	0.225	2.31	0.21	2.47

Table IV-II Mechanical properties of as-received materials tested in RD

RP tested in RD					
Grade	σ_{YS} (0.2%)	σ_{TS}	ε_u	n	ε_f
CA 0.8mm	215 MPa	463 MPa	0.235	0.22	2.5
BA 0.8mm	217 MPa	461MPa	0.225	0.21	2.46
CA 1.5mm	217 MPa	465MPa	0.20	0.20	2.4

Fracture strains were calculated by measuring the area at fracture from SEM micrographs and by assuming constant volume for plastic behaviour, $A_o l_o = A_i l_i$. The strain at fracture is therefore $\varepsilon_f = \ln(A_o / A_f)$. An estimate can be made of the fracture stress by dividing the last measured fracture load by the area at fracture. Due to the large amount of necking (Figure 4.10) and void coalescence before fracture, a direct match between the measured load and area at fracture is difficult, but nonetheless a good estimate of the work hardening rate after necking can be made. The slope of the flow curve past necking was further verified by measuring the cross-sectional area during tensile testing and matching this to the load at the time of measurement. Data points are therefore added onto the flow curve after the point of necking. Flow behaviour past necking is shown in Figure 4.9. A diffuse neck forms at the true maximum stress, σ_{TS}. Localized necking then occurs at a strain of about $\varepsilon_n^{diffuse} = (1+r)\varepsilon_u \approx 3\varepsilon_u$ (Semiatin and Jonas 1984, 195). Failure occurs soon after the formation of the localized neck. The maximum neck acuity does not occur at the onset of fracture. Tensile tests were stopped just prior to fracture, and a rough measurement of the notch radius was made. These notches were found to be more severe than

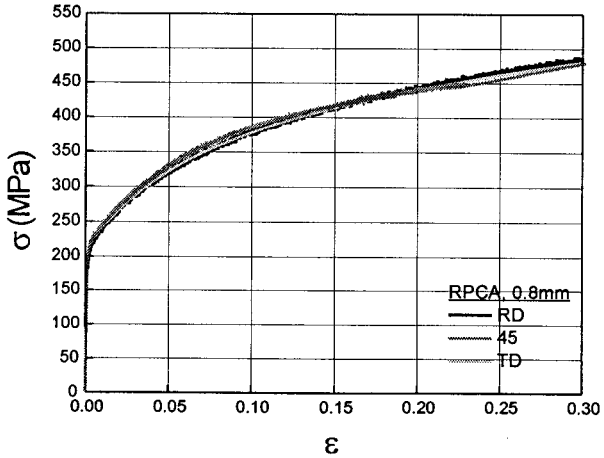

Figure 4.7 - Uniaxial flow properties of RP CA light gage tested in rolling, diagonal, and transverse directions.

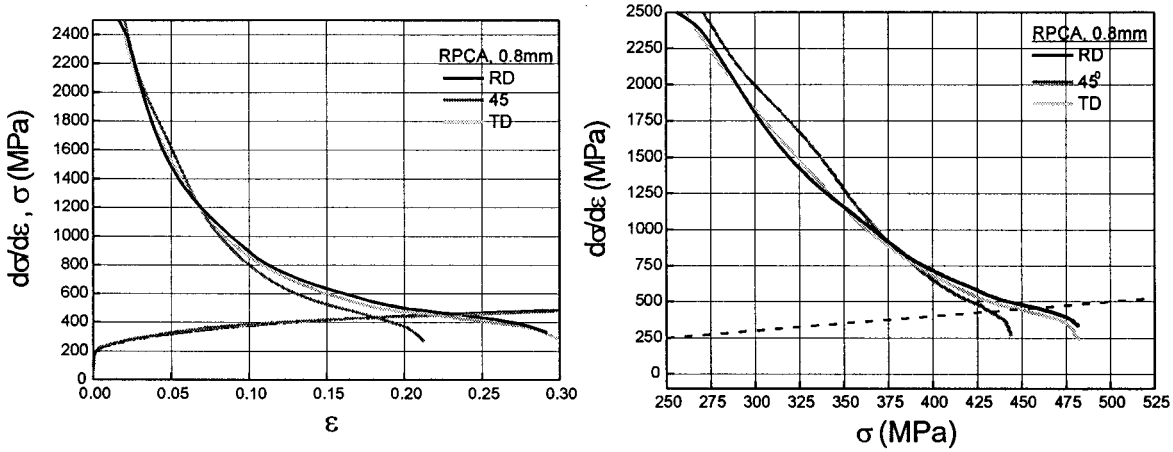

Figure 4.8 - Work hardening properties of the as-received RP CA light gage tested in rolling, diagonal, and transverse directions.

those measured after fracture. The implications of the localized necking induced notch will be more apparent when the results of the low temperature tests are presented.

Work hardening plots indicate that although material tested in the rolling direction has the lowest yield strength, it also has the highest work hardening rate, which leads to the highest true tensile strength (Figure 4.8). As well, Considere's criterion is followed for all samples tested, e.g. necking occurs at $d\sigma / d\varepsilon = \sigma$ (Figure 4.8). Formability for the continuously annealed material will be lowest in the diagonal direction (Table IV-II). Strain rate tests using separate samples for each rate give a strain rate sensitivity index of 0.014 at true strain of 0.15.

Both annealing heat treatments produce material with very similar mechanical properties (Tables IV-I).

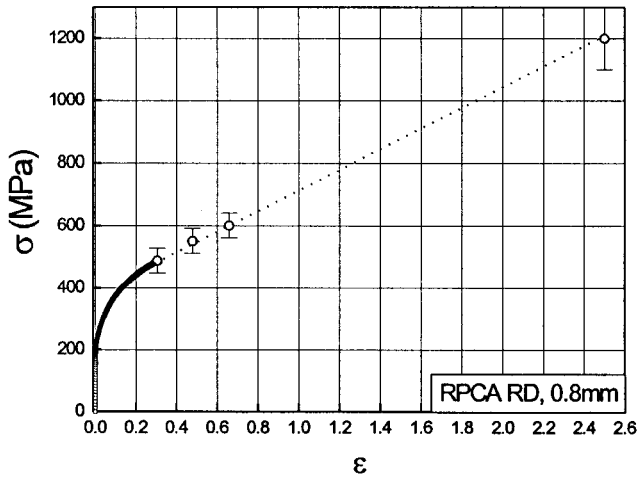

Figure 4.9 - Flow behaviour to fracture for RP CA material in rolling direction. Bridgeman correction not

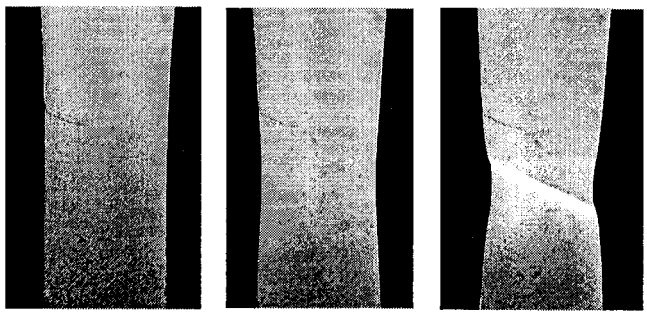

Figure 4.10 - Progression of necking from diffuse to localized for the continuously annealed light gage grade tested in uniaxial tension in the rolling direction.

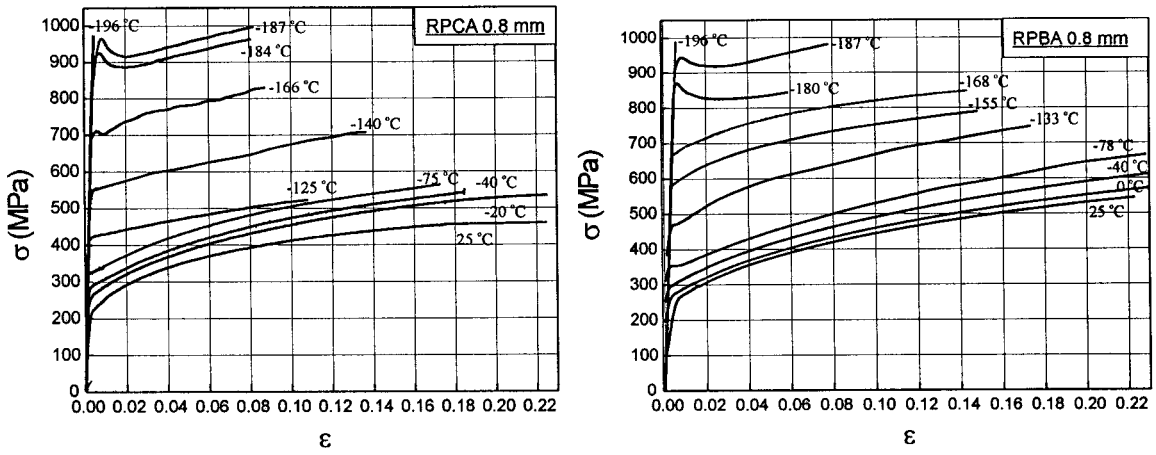

Figure 4.11 - Flow curves for a) RP CA and b) RP BA steels as a function of temperature.

4.3.2 Low Temperature Mechanical Testing

Tensile tests performed over a range of temperatures were used to gain a more quantitative understanding of the ductile-to-brittle transition, as the yield, fracture and maximum tensile stress, uniform strain, and the strain to fracture can be directly measured. The influence of predeformation and deformation path on the DBTT was also investigated. The steel was deformed in plane strain by cold rolling. Cold work embrittlement usually occurs after deep drawing, which is often approximated as a plane strain operation. The cold rolling predeformation strain was converted into an effective strain for comparison with the uniaxial flow behaviour. The fracture surfaces of all samples were investigated in detail using the SEM.

The flow curves of the RP CA and RP BA light gage steels were measured as a function of temperature (Figure 4.11). Both steels exhibit similar flow properties as a function of temperature. The 0.2% offset yield stress and the

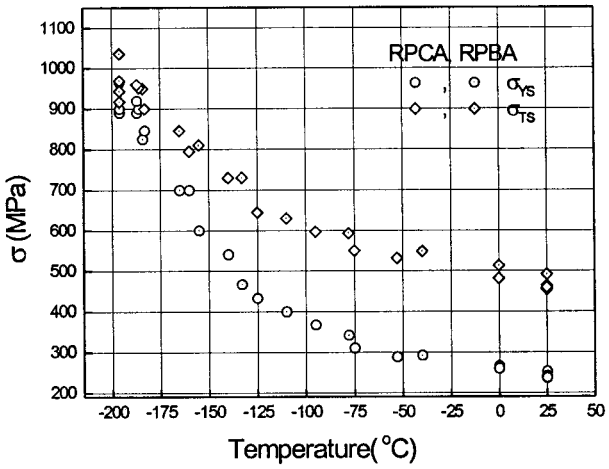

Figure 4.12 - Yield and tensile stress with temperature for the continuously and batch annealed steels.

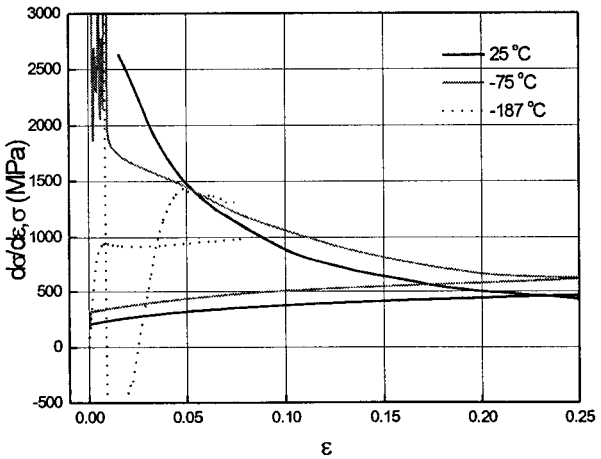

Figure 4.13 - Work hardening plots for RP BA at 25°C, -78° C, and -187°C.

tensile strength are plotted in Figure 4.12. A gradual return of yield point elongation with decreasing temperature is observed for both CA and BA heat treatments (Figure 4.11).

Work hardening behaviour was examined in more detail for three temperatures, 25°C, -75°C, and -187°C. Diffuse necking at -187°C is interrupted by intergranular fracture, although possible localized flow in the form of Ludering negates the physical meaning of the differential of the stress-strain data until the band has been exhausted.

The transition to a brittle behaviour, characterized by fully elastic behaviour, occurred at -196°C for continuously annealed steel, while the batch annealed steel still had minimal plastic deformation in liquid nitrogen, although the fracture surface was brittle intergranular. The transition to fully elastic behaviour is predicted at -200°C. The intergranular fracture stress is therefore obtained from the samples tested at -196°C. No difference in brittle fracture stress could be measured between either CA or BA materials, although significant scatter was observed. The intergranular fracture stress, for both the continuously annealed and batch annealed material tested at -196°C, is 980 ± 60 MPa.

Yield behaviour as a function of cold rolling predeformation is summarized in Figure 4.14. Different flow properties are observed between material tested in the rolling and transverse directions and cross-rolled material. Anisotropic flow behaviour present in the as-received steel is accentuated by the cold rolling. For instance, the ratio of the yield stress in the transverse and rolling directions at room temperature is 1.02 for the as-received material, and approximately 1.10 for the material

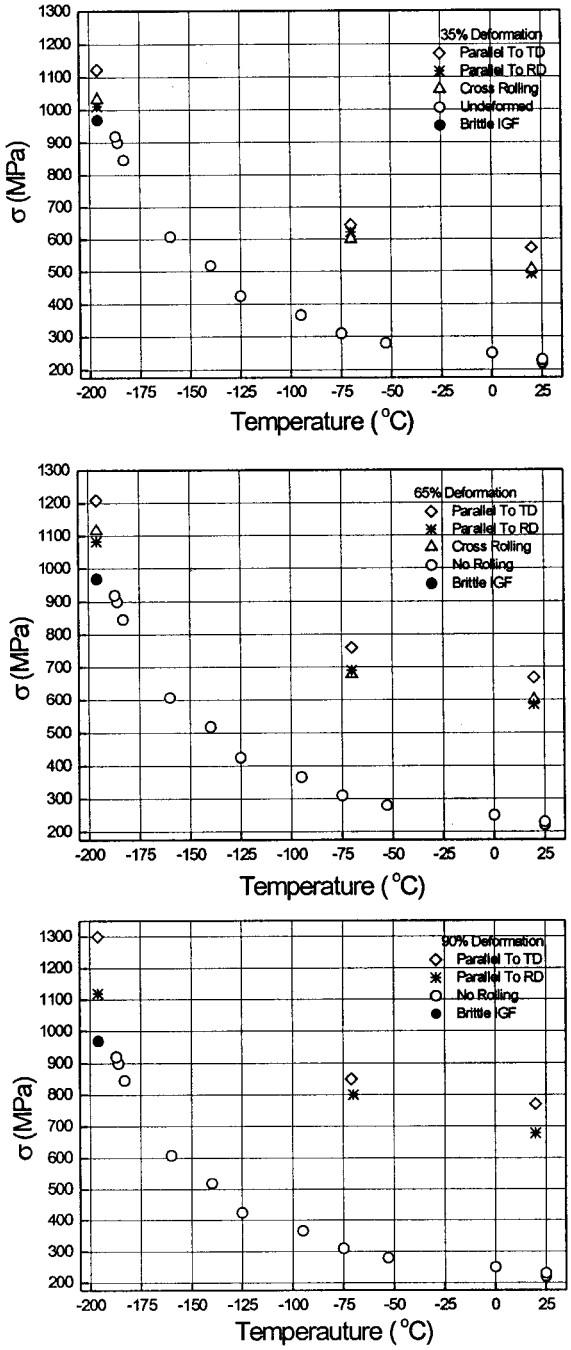

Figure 4.14 -Yield stress as a function of temperature for continuously annealed material predeformed by cold rolling to $\varepsilon_1 \approx 0.35$, 0.65 and 0.90.

predeformed to a true thickness strain of 0.65. The flow behaviour of cold rolled material tested in the transverse direction is higher than material tested in the rolling direction for all predeformations and temperatures, while the flow stress of the cross-rolled steel lies between these limits. Despite the anisotropy, the flow curves of the predeformed material follow those of the undeformed material for a given temperature. Figure 4.15 compares the flow curves of the predeformed and as-received materials, both tested in the rolling direction. Work hardening, at a given temperature, is consistent considering the errors in determining the fracture stress accurately. Material tested in the transverse direction demonstrates the same behaviour.

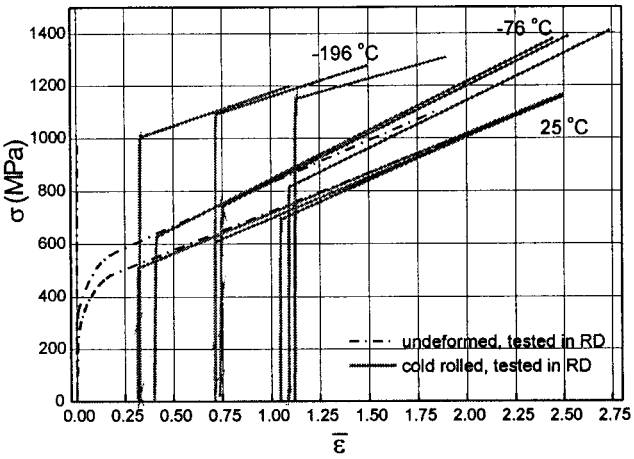

Figure 4.15 - Flow behaviour of predeformed RP CA grade tested parallel to the subsequent cold rolling direction as a function of temperature compared to the flow behaviour for the undeformed material.

A transition to a fully brittle IGF was only observed for material cold rolled 35% and tested in the transverse direction (Figure 4.26) at -196°C. These samples yielded at 1100 MPa and failed at a true strain of 0.10 and a fracture stress of 1180 MPa. Therefore, a direct measurement was made of the brittle fracture stress for a different grain shape. Samples cold rolled by 65% and tested in the transverse direction yielded at 1200 MPa and failed at true strain of 0.2 and a fracture stress of 1300 MPa by a combination of delamination and ductile fracture. Increasing the strain rate for material cold rolled by 65% and tested in the transverse direction at -196°C did not influence the fracture mode, although the yield stress increased from 1200 to 1260 and 1300

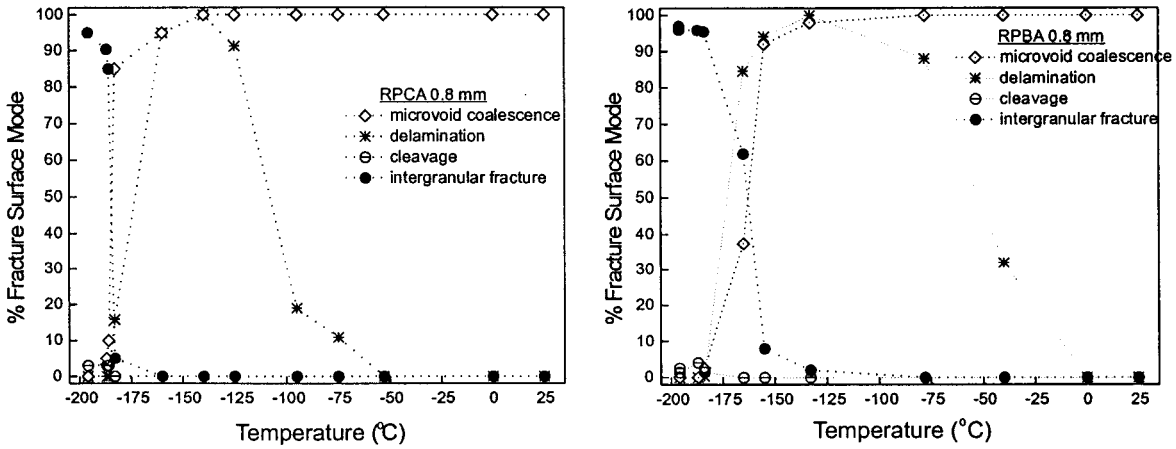

Figure 4.16 - Percent fracture mode for RP CA and RP BA tested in tension as a function of temperature.

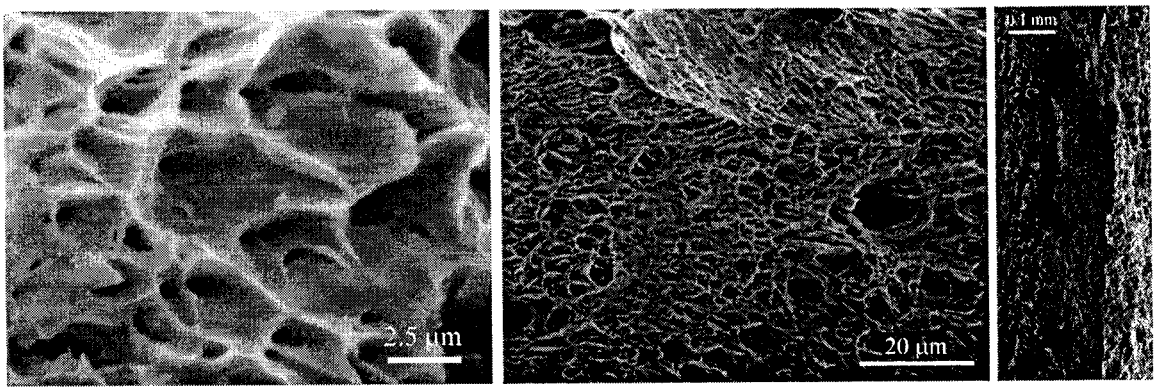

Figure 4.17 - Ductile fracture by microvoid coalescence. Batch annealed material tested at 25°C.

MPa for strain rates of 0.0004, 0.004, 0.02 s^{-1}. Intergranular fracture was not observed for any other predeformed material tested at -196°C. In fact, all other cold rolled material became less brittle even though the yield stress increased above the IGF stress of the undeformed material (Figure 4.15).

4.3.3 Fractography

Fracture surfaces of all samples tested were characterized and reported in terms of the percent of each fracture mode. This is plotted in Figure 4.16 for the continuously annealed and batch annealed materials. General features of the fracture morphology are as follows.

At ambient temperatures, the samples neck and fracture by ductile microvoid coalescence (Figure 4.17). Precipitates nucleate voids under the action of a triaxial stresses in the neck. The voids are elongated and form dimples on the fracture surface (Figure 4.17). As the temperature is lowered the fracture has increasing amounts of delamination fracture (Figures 4.18 -4.20). Delamination is a separation process that occurs in the plane of sheet metals, or in the transverse direction in cylindrical tensile specimens. Delaminations are in part

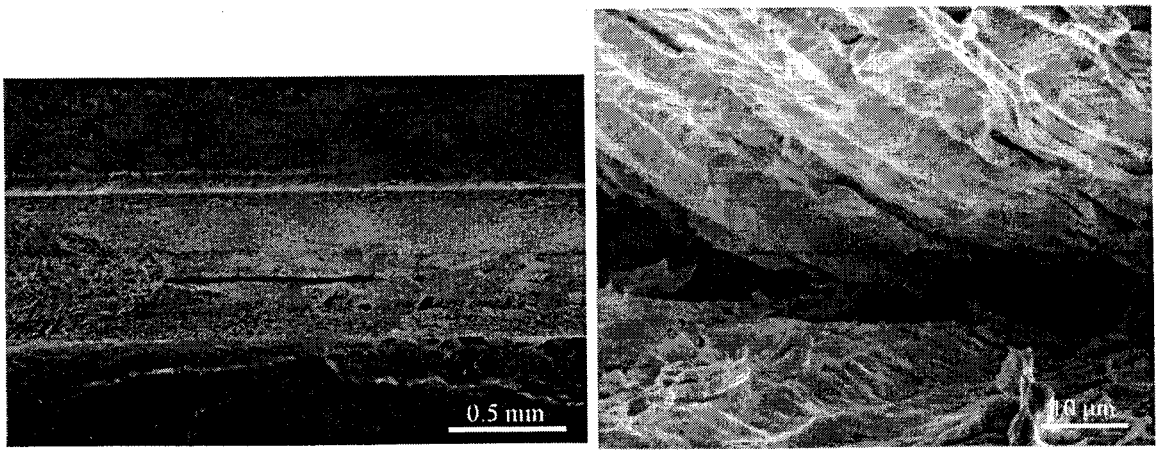

Figure 4.18 - a) Partial delamination crevice for continuously annealed material tested at -75°C b) Inside delamination crevice, batch annealed material tested at -40°C.

due to transverse stresses and a microstructural weakness in this direction, and have been attributed to transgranular cleavage (Hawkins 1976), precipitate or inclusion fracture (Zok and Embury 1989), and intergranular decohesion mechanisms (Kunishige, Fukada and Sugisawa 1979, Bramfitt and Marder 1977).

Delaminations always occur in the center of the sheet, but secondary delaminations do occur in some specimens in the centers of the delaminated halves (Figure 4.26). The percentage of delamination was calculated as the percentage of width which had split open. Certain samples had multiple delaminations running the whole width, in this case the percentage delamination fracture is still taken as one hundred. The delamination is mixed with ductile fracture, except near the transition temperature, where intergranular and delamination fracture co-exist. By probing the delamination crevice, the delamination separations are observed clearly between the elongated grains. Therefore, this type of delamination is due to intergranular

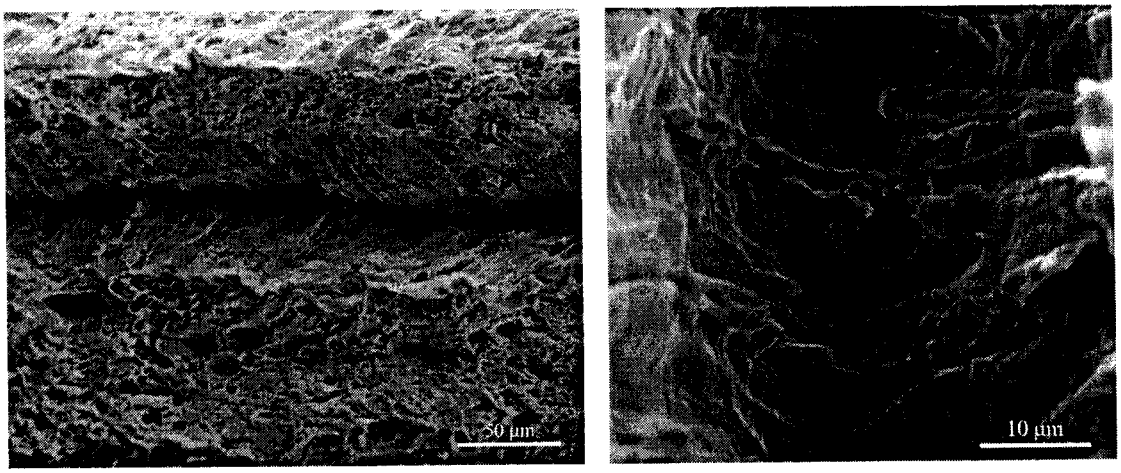

Figure 4.19 - Delamination and intergranular separations for continuously annealed material tested at -140°C.

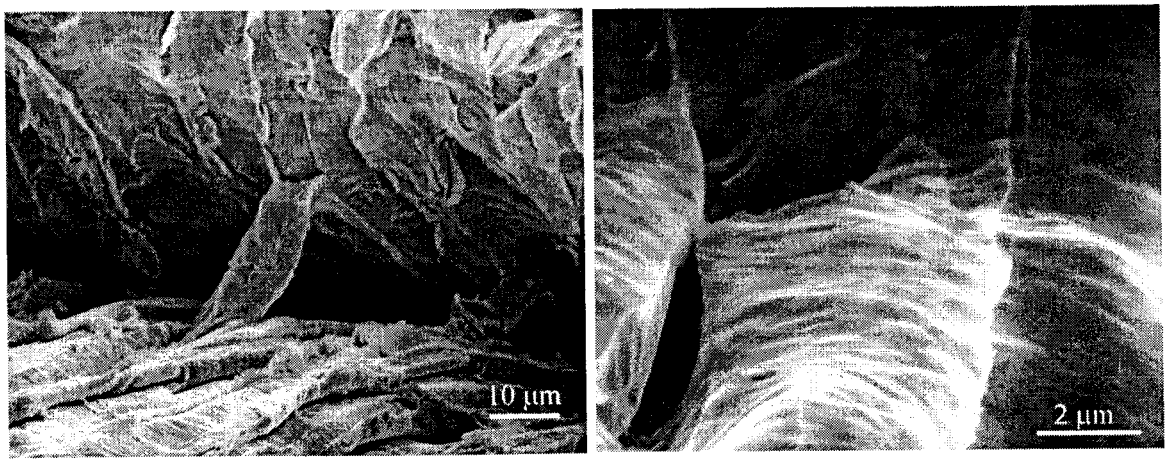

Figure 4.20 - Elongated grain bridging intergranular delamination crevice, batch annealed tested at -75°C. b) Delaminated grains are not as elongated for batch anneal material tested at -165°C.

separation. The grains are highly elongated consistent with the large post-uniform plane strain deformation in the vicinity of the necked specimens. The delamination crevice depth is a maximum at intermediate temperatures (Figure 4.18). Grains bridging the delamination commonly occur inside the crevice (Figure 4.18).

Atypical delaminations occurred in the width direction of the tensile sheet for batch annealed samples tested at -75°C (Figure 4.21). Planar delamination occurred at the middle of the plane of the sheet (the normal plane), while at the edges separations occurred in the transverse plane (Figure 4.21a). These separated fingers are fully intergranular, these grains are slightly elongated but not as flattened as the planar delaminations (Figure 4.21c). As the temperature is lowered near the transition temperature, the fracture mode changes to intergranular. In fact, just above the transition temperature, the fracture is intergranular in nature, but with

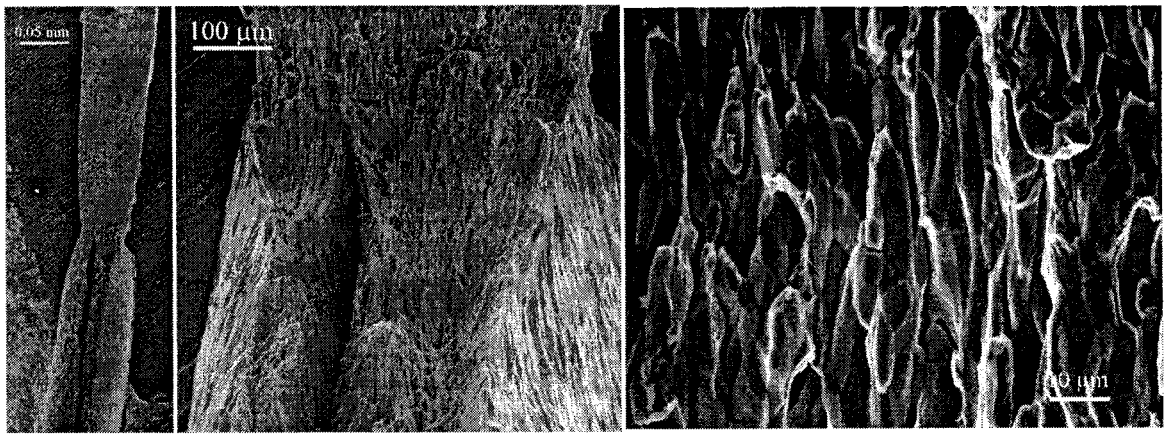

Figure 4.21 - Intergranular delamination in through-thickness direction and width direction in batch annealed material tested at -75°C.

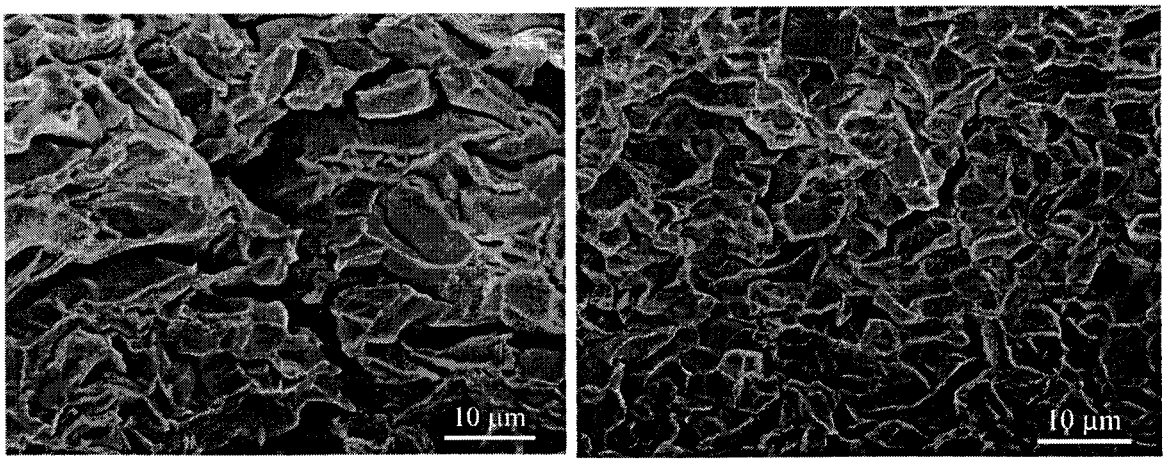

Figure 4.22 - Micrographs of batch annealed sample pulled at -184°C a) Intergranular fracture mixed with microvoid coalescence, fractograph from middle width of sample b) Intergranular fracture showing elongated grains, fractograph from outer width of sample.

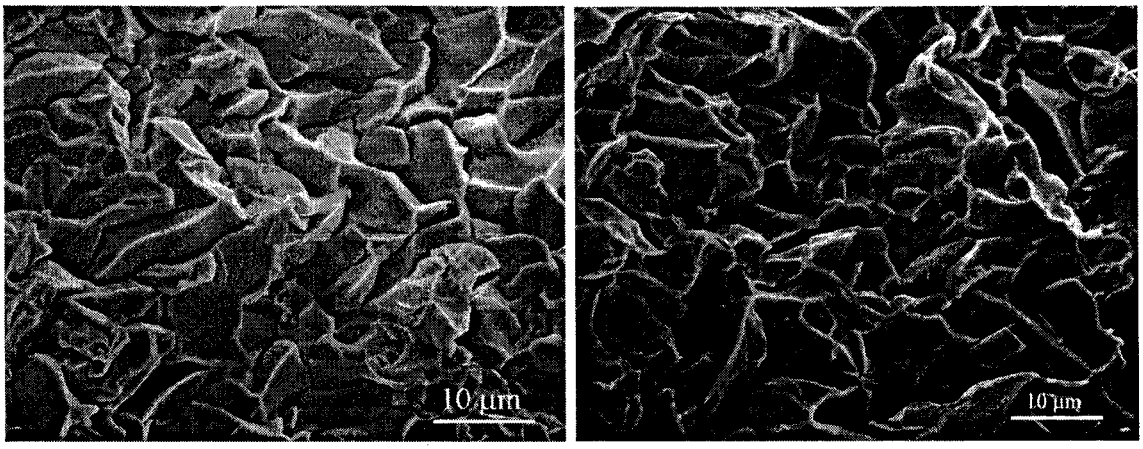

Figure 4.23 - Intergranular fracture observed after uniaxial plastic deformation, continuously annealed material tested at -187°C.

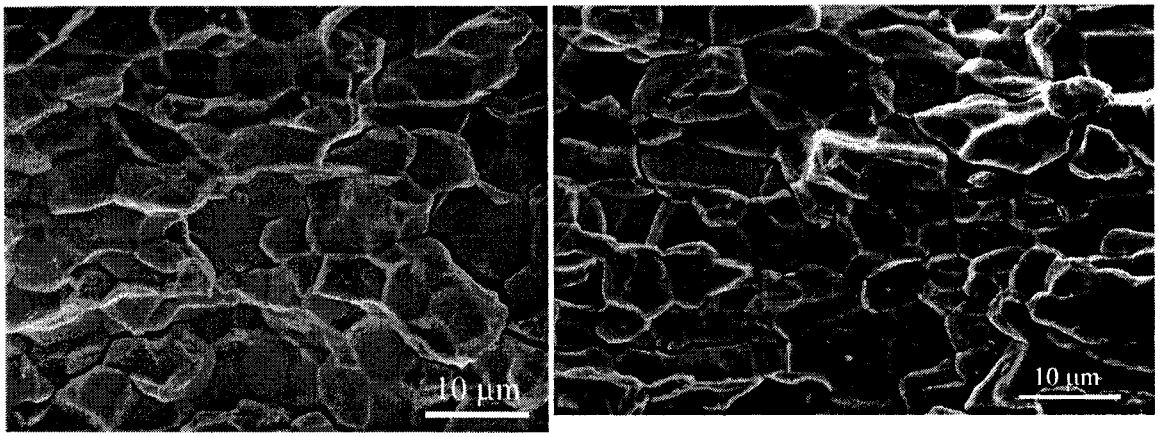

Figure 4.24 - Intergranular fracture in a) continuously annealed material and b) batch annealed material tested at -196°C.

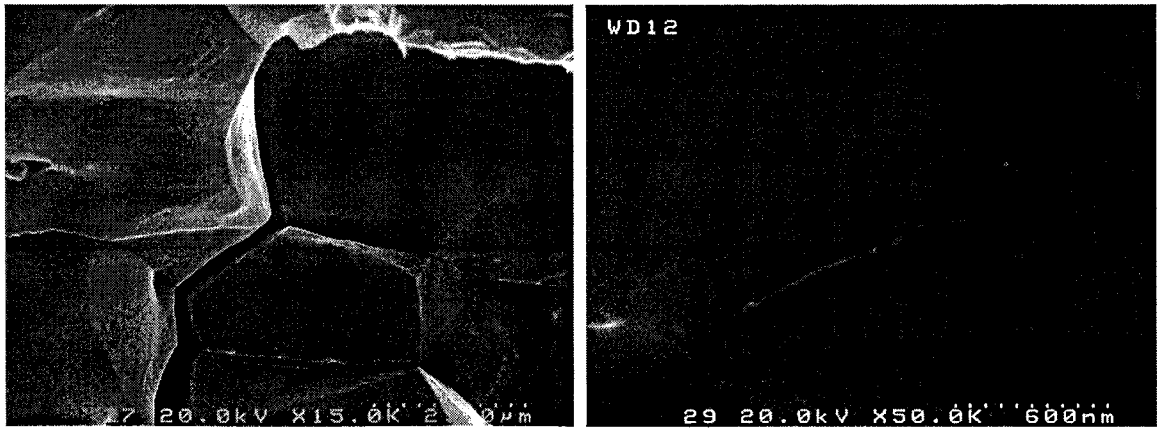

Figure 4.25 - Intergranular fracture of continuously annealed steel tested in tension at -196°C. At high magnifications slip bands are not visible on the intergranular facets due to their absence or due to limiting depth resolution of SEM.

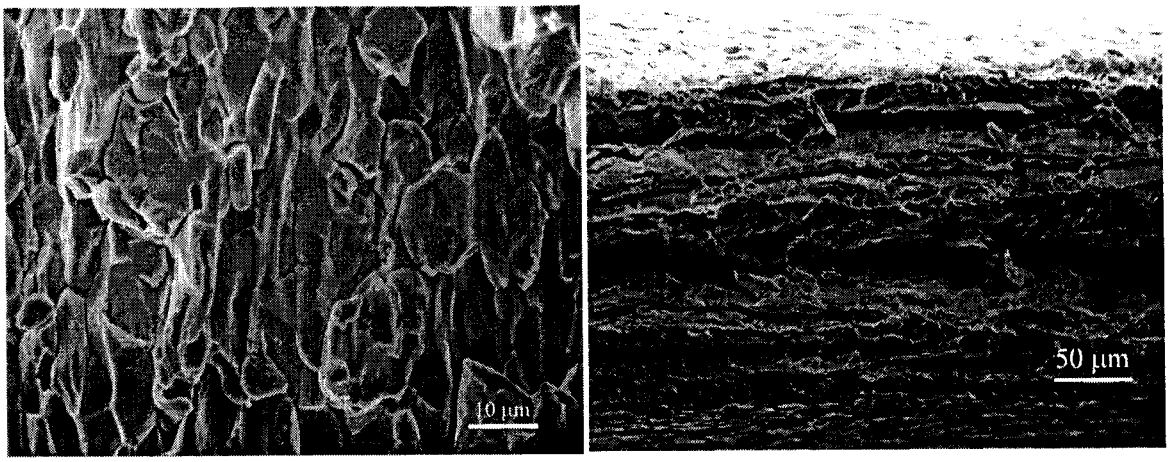

Figure 4.26 - Cold rolled 35%, tested in transverse direction at -196°C, b) cold rolled 90%, tested in transverse direction at -196°C.

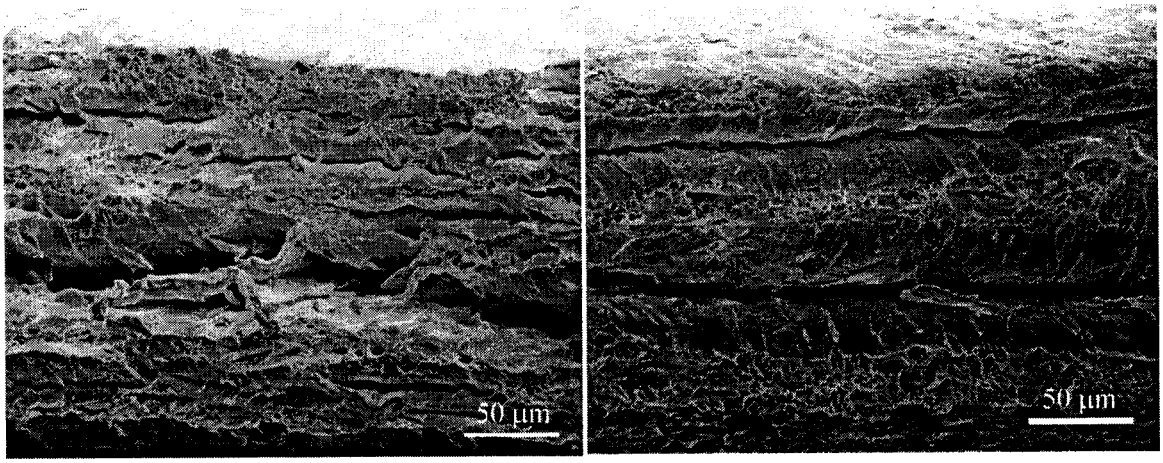

Figure 4.27 - Continuously annealed material cold rolled a) 65% and b) 90% and tested in the rolling direction at -196°C.

significant plastic flow preceding the intergranular fracture. Fracture surfaces consist of some proportion of intergranular fracture of varying grain elongations mixed with transgranular fracture and possibly microvoid coalescence. Fracture occurs on a plane perpendicular to the applied uniaxial stress, and therefore greater thickness strains are observed in the middle width of the sample where the shear bands intersect the fracture surface (Figure 4.22a). The increased strain leads to more ductile fracture in competition with IGF, whereas at the outer width the grains are elongated but no dimples are observed (Figure 4.22b). As the temperature is lowered dimple fracture is no longer observed and the grain elongation depends on the strain to fracture. For instance, at -187°C in the continuously annealed material, IGF occurs at a true strain of 0.2 with the appropriate amount of grain elongation in the tensile direction (Figure 4.23). The amount of transgranular fracture increases in instances when the grains are elongated. At -196°C the fracture changes to fully brittle IGF without any plastic flow prior to fracture. Fracture surfaces are characterized by well-defined exposed

grains that tend to be smooth in appearance (Figure 4.24). No traces or slip bands are visible at high magnification under near optimal microscope operating conditions (Figure 4.25). A small proportion of transgranular (cleavage) fracture, never exceeding 5%, is observed mixed with the intergranular fracture and is usually characterized by river lines on the fracture facets.

Differences in fracture modes between the continuously annealed and batch annealed are summarized in Figure 4.16. Delamination occurs at a higher temperature for the batch annealed material.

Material cold rolled by 35% and tested in the transverse direction, displayed the only predeformed tensile failures by brittle intergranular fracture. All other samples had varying amounts of intergranular delamination and microvoid coalescence (Figure 4.27). Increasing the strain rate for samples cold rolled by 65% and tested in the transverse direction, had no influence on the fracture mode.

4.0

4.4 Cylindrical Flat Bottom Cup Drawing and Characterization

Cold work embrittlement usually occurs after deep drawing, with brittle cracks propagating in the drawing direction. Therefore, accurate characterization of the state of and conditions that affect the deep drawn material is essential for a proper understanding of CWE. Deep drawn cups, which simulate pure drawing, have been characterized in terms of the strain, microhardness, and macroscopic circumferential residual stress as a function of cup wall height for the different drawing ratios and conditions used. Particular attention has been paid to the consequence of the planar and normal anisotropy during cup drawing; a preferential cracking position has been observed during the cup expansion test.

The progression of earing with draw ratio can be seen from Figures 4.28 and 4.30. The cups exhibit six ears; the largest occurring in the RD and two smaller ears occur symmetrically about the TD (Figure 4.29). The formation of six ears in IF sheet steels has been related to the strong intensities of the {111}<112>,

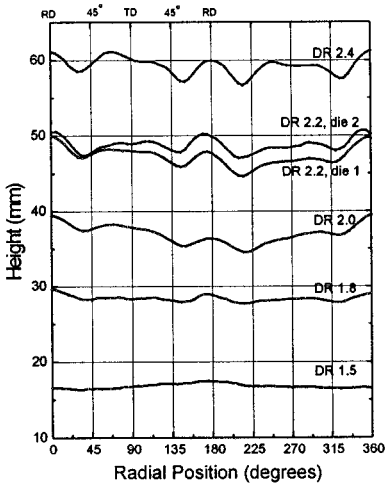

Figure 4.28 - Cup wall height of deep drawn cups as a function of radial position and draw ratio 0.8 mm gage steel.

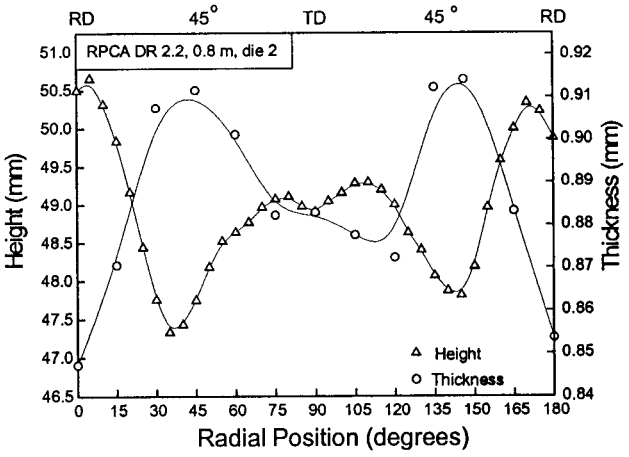

Figure 4.29 - Height and thickness variation as a function of radial position along top of lathed deep drawn cup for a draw ratio of 2.2.

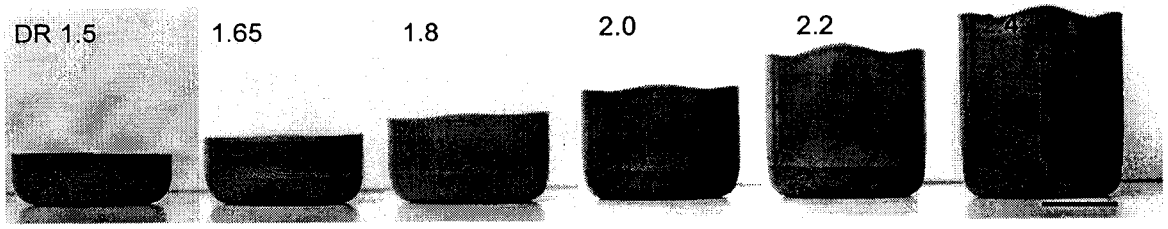

Figure 4.30 - Progression of earing for cylindrical flat-bottomed deep drawn cups, 0.8 mm gage continuously annealed material, as a function of draw ratio.

{554}<225> and {223}<472> texture components as opposed to four ears which are usually found in AKDQ steels (Daniel, Savoie and Jonas 1993). The limiting draw ratio (LDR) for this grade of steel ratio was found to be ~2.40, which is therefore the highest draw ratio tested for CWE. Variation in height with radial position correlates with variation in thickness with radial position as seen in Figure 4.29. Although plane strain deformation is often assumed for deep drawing the average thickness at the top of the cups is 0.889mm, which corresponds to a true thickness strain 0.131. As well, the variation of normal anisotropy in the sheet plane leads to different thickness strains around the circumference of the deep drawn cup. This variation in strain at the top of the cup indicates the possibility of preferential cracking. Evidence for preferential cracking will be presented after the results of the cup expansion tests are presented in section 4.9.

Ironing significantly decreases the macroscopic residual stresses (Ragab and Orban 2000, Danckert 1994). No ironing occurred during the deep drawing, as indicated from the load versus stroke data (Figures 4.31 and 4.32). Ironing was not expected in the light gage material due to the ample die clearances of the different die geometries used. The load increases in a predictable fashion with draw ratio and thickness (Backofen 1972, 235). The force required to deep draw the cups is comprised of 1) bending and unbending around the die radius from the flange to the sidewall, 2) the force required for overcoming the frictional resistance of metal passing between the blank holder and the die, and 3) force required for circumferential compression and radial stretching of metal in flange. Tractrix drawing significantly decreases the maximum load during drawing, for instance, from 105 kN to 65 kN for a draw ratio of 2.2 for the 1.5 mm material (Figure 4.32). This decrease is due to decreased bending-unbending around the die radius and to a lack of blank holder pressure which leads to decreased frictional forces. Decreased drawing loads account for the increased LDR reported for tractrix dies (Oehler 1963).

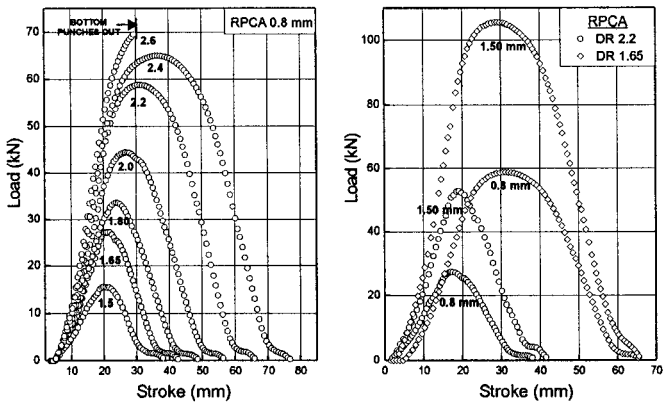

Figure 4.31 - Load versus stroke data during cup drawing as a function of a) draw ratio and b) sheet thickness.

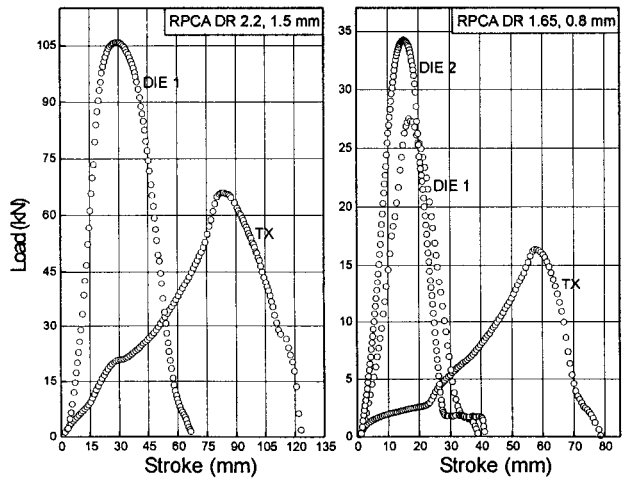

Figure 4.32 - Load versus stroke data during cup drawing comparing different die geometries.

4.4.1 Strain and Microhardness of Deep Drawn Cups

The primary strains were measured in three radial positions (0°, 45°, 90°) in the deep drawn cup and general trends are observed for all draw ratios and die geometries. Both primary strains in the plane of the cup increase with cup wall height and then decrease after reaching a maximum near the top of the cup. Thinning occurs near the cup bottom, while thickening occurs near the cup top. Similar trends are observed for all radial directions (Figure 4.34a). The primary strains in the longitudinal and circumferential directions for draw ratios 1.65 through 2.4 for die 1 are shown in Figure 4.33. The deep drawing is close to a plane strain operation, although there is thinning near the bottom and thickening near the top of the cup (Figure 4.35). The thinning increases with draw ratio due to the higher drawing forces transmitted through the cup wall. Partially drawn blanks, 120 mm in diameter, show that maximum primary strain, which occurs at the flange-wall bend, is 0.34 and is approximately the same as the strain at the top of the lathed cup with draw ratio of 1.8 (Figure 4.35).

The Vickers hardness number (VHN) on undeformed material is 115 ± 6. Hardness has been plotted as a function of cup wall height for the draw ratios used (Figure 4.36). The hardness increases from 140 VHN at the bottom of the cup, to 208 VHN at the top of the cup for a draw ratio of 2.2 (Figure 4.10). Hardness numbers from the base of the cup, well away from the bend radius, indicate biaxial stretching occurred. The increase in hardness is similar for all draw ratios, except near the cup nose radius. All cups show an increase in hardness near the punch nose, but this is accentuated with draw ratio. Increased hardness at near the punch nose radius is due to increased thinning at this position and is most pronounced for a draw ratio of 2.4 as this is at the LDR. Comparing cups with draw ratio of 2.2 show no differences between the continuously or batch annealed material, the 0.8 mm or 1.5 mm gage material, or cups drawn with different die geometries, e.g. tractrix die, die 1 or die 2 (Figure 4.37). Small differences in flow stress cannot be detected with Vickers microhardness. The hardness of the heat treated cups, shown in Figure 4.38, is compared to the non-heat treated cups of the same

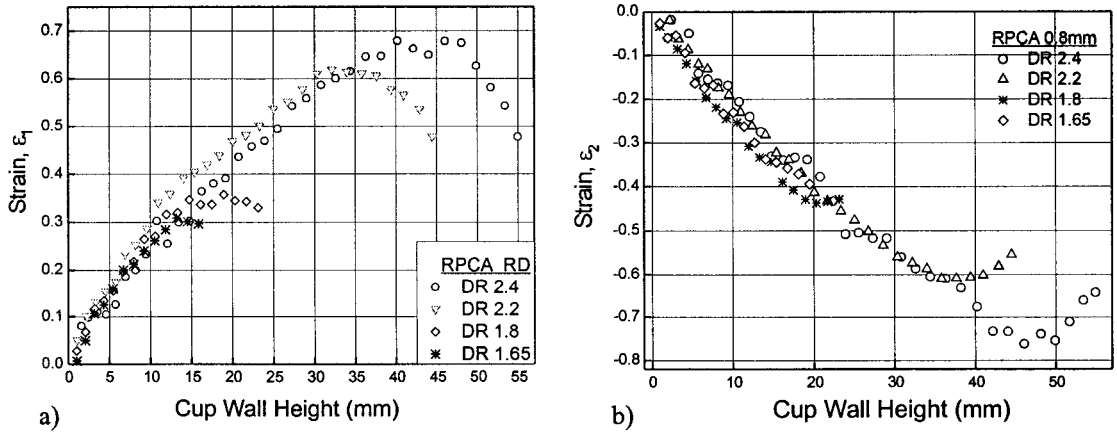

Figure 4.33 - a) Strain in drawing direction, ε_1, and b) circumferential direction, ε_2, along RD as a function of cup wall height for different draw ratios.

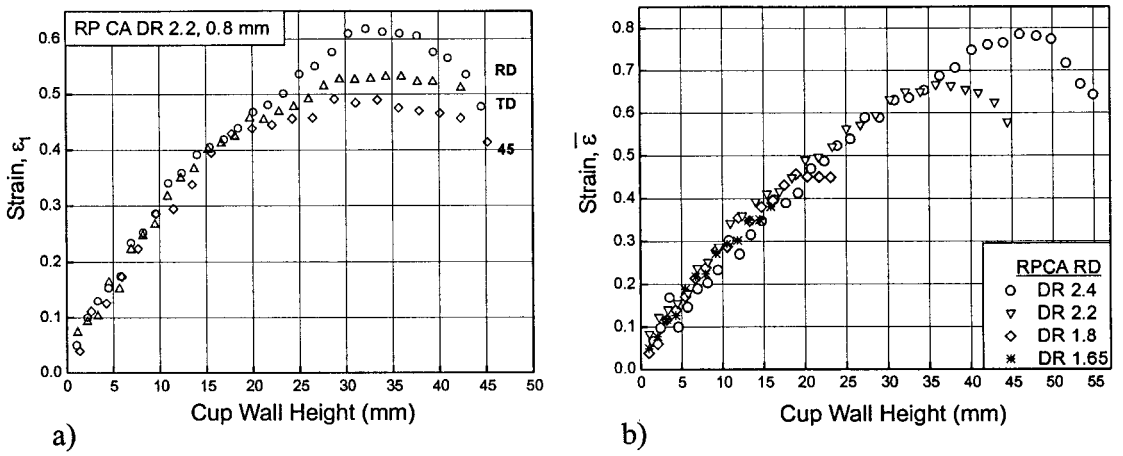

Figure 4.34 - Principal strain in drawing direction in RD, TD and 45° and b) effective strain, $\bar{\varepsilon}$, in RD for a draw ratio of 1.65,1.8,2.2 and 2.4 for the 0.8mm gage material.

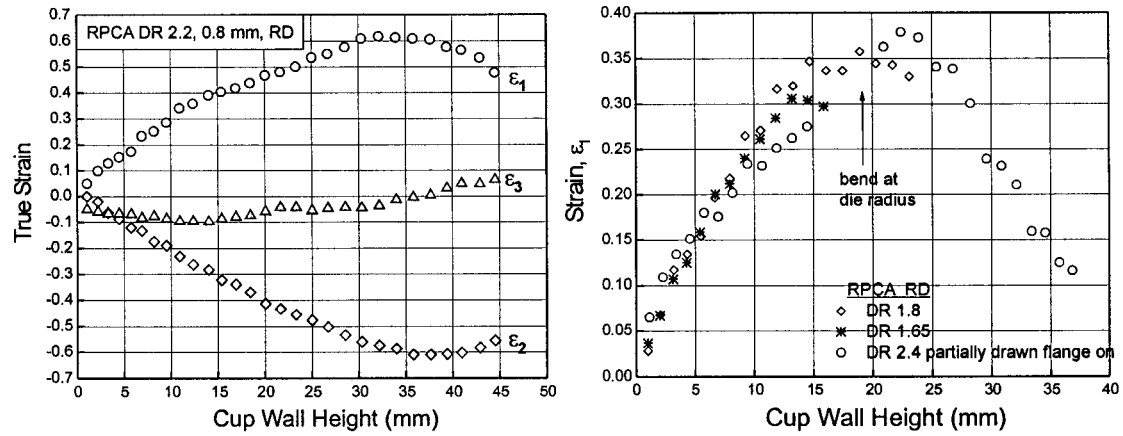

Figure 4.35 - Principal strains ε_1, ε_2 and ε_3 along RD and b) Principal strains in RD for partially drawn cup with flange left on compared to DRs of 1.65 and 1.8.

draw ratio. Cups given a recrystallization heat treatment have recrystallized, as the hardness decreased to that of annealed sheet, except near the bottom of the cup where the hardness increases. Evidently the amount of deformation near the bottom of the cup was not sufficient for recrystallization. Cups heat treated at 550°C for 1 hour did not recrystallize, as evident from the optical micrographs (Figure 4.43), or even soften, as is evident from the hardness tests (Figure 4.38).

Hardness, converted into a flow stress using equation 3.6, and strain measurements were used to determine the hardening behaviour for the deep drawn cups. Hardening behaviour of the deep drawn cups was compared to that measured in uniaxial tension for as-received material and material predeformed by cold rolling (Figure 4.39); the results are consistent. Table IV-III summarizes the hardness and the primary strains at the top of the lathed cup for all draw ratios. This data can be used to analyze the results of the cup expansion test.

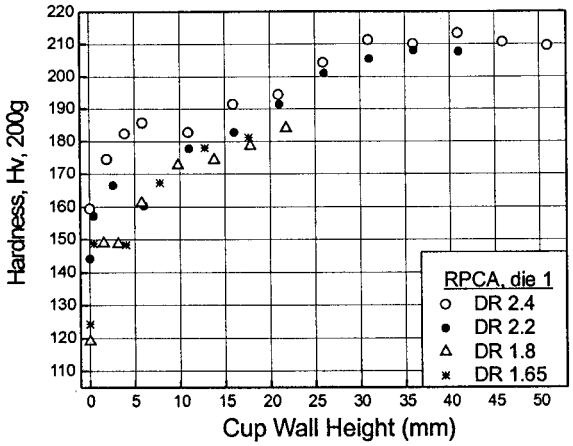

Figure 4.36 - Vickers microhardness as a function of cup wall height for different DRs (in RD).

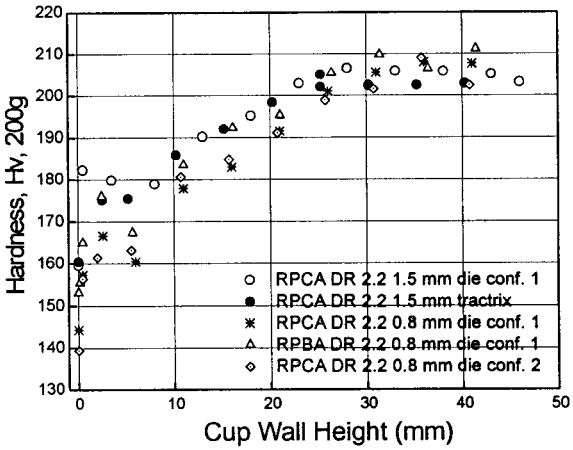

Figure 4.37 - Vickers microhardness as a function of cup wall height for a DR of 2.2 and for different heat treatments, thicknesses and die geometries.

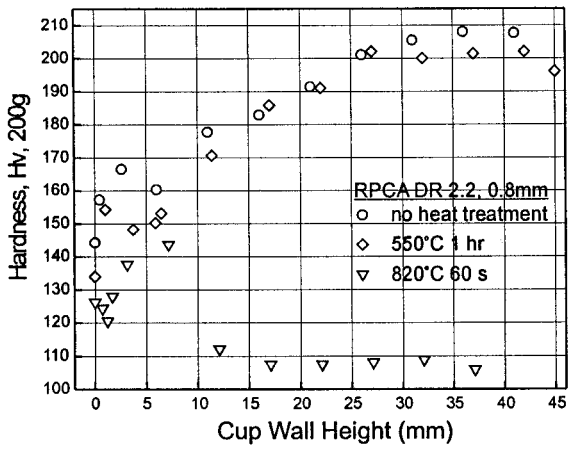

Figure 4.38 - Vickers microhardness as a function of cup wall height for cups heat treated after deep drawing.

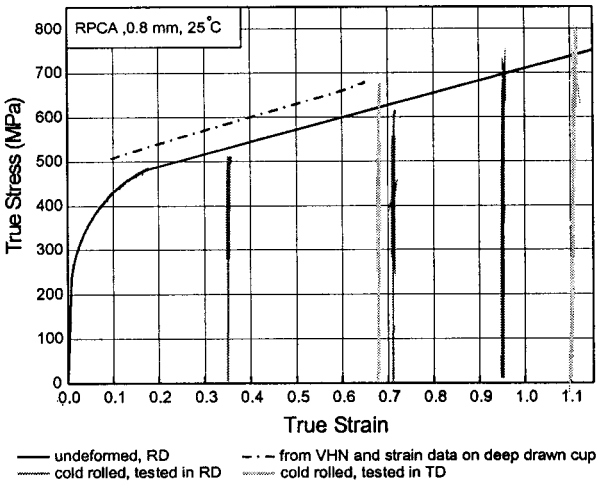

Figure 4.39 - Hardening behaviour. The measured hardness and strain of a deep drawn cup, DR 2.2, is correlated to the stress-strain behaviour of the annealed undeformed material and material predeformed by cold rolling.

4.4.2 Microscopy of Deep Drawn Cups

Grain shape evolution with deformation was documented with optical microscopy. Micrographs taken from the bottom, middle and top of the cups deep drawn to a draw ratio of 2.2 are shown in Figure 4.41. Changes in the average major and minor grain lengths with deformation can be roughly equated to the primary strains, ε_1 and ε_3 in the deep drawn cup. Table IV-III compares the strains calculated from the grain shape and those calculated from the square grid analysis. A good correlation exists which implies the bulk strains can be used to model the change in grain shape. Subgrain formation with deep drawing was investigated with deep drawing deformation. Cells are not fully developed in all grains at the bottom of the cup (Figure 4.42a). With

Table IV-III Primary strains and hardness at lathed edge of deep drawn cup for different draw ratios

DR	h	ε_1	ε_2	$\bar{\varepsilon}$	H_v
1.5	15	.25	0.26	0.30	---
1.65	20	.30	0.32	0.40	177
1.8	26	.35	0.36	0.45	183
2.0	34	.50	0.53	0.58	190
2.2	43	.56	0.58	0.65	203
2.4	54	.60	0.65	0.75	206

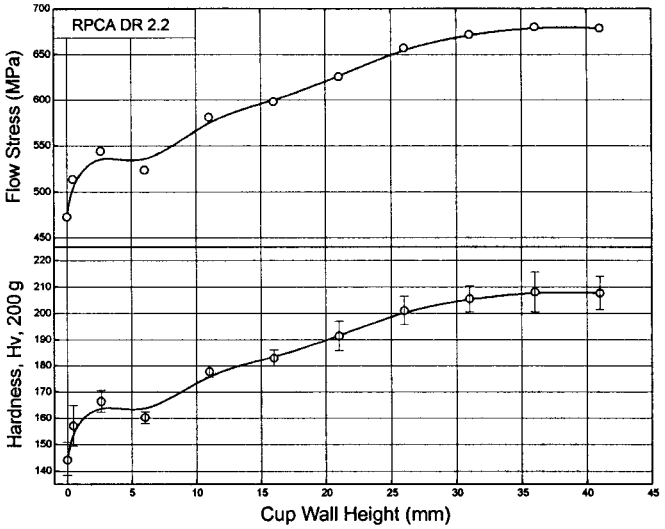

Figure 4.40 - Vickers hardness and the associated flow stress as a function of cup wall height for the RP CA DR 2.2.

increasing deformation more cells are visible (Figure 4.42b). At a bulk effective strain of 0.55 cells are fully developed in every grain (Figure 4.42c).

Cups heated treated at 550°C for one hour have not recrystallized. The grains have the same shape as the as-drawn cups (compare Figures 4.43 and 4.41). Cups heated treated at 820°C have recrystallized most of the way down the length of the cup. Deformation near the bottom of the cup was not sufficient for recrystallization as grains are still elongated (Figure 4.44). Grains at the bottom of the recrystallized cup are nearly equiaxed and have same shape as the as-drawn cups, but it can safely be assumed that these did not recrystallize either.

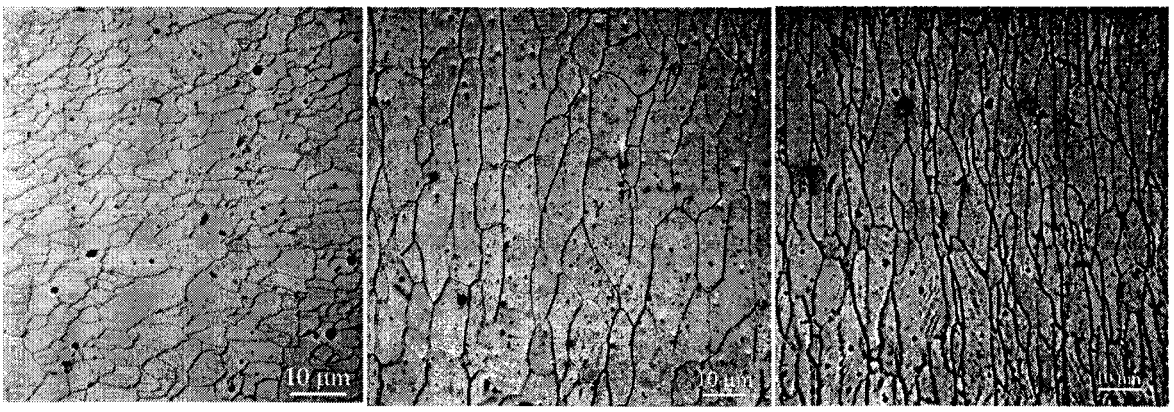

Figure 4.41 - Optical micrographs and from a) bottom b) middle and c) top of a cup deep drawn to a draw ratio of 2.2.

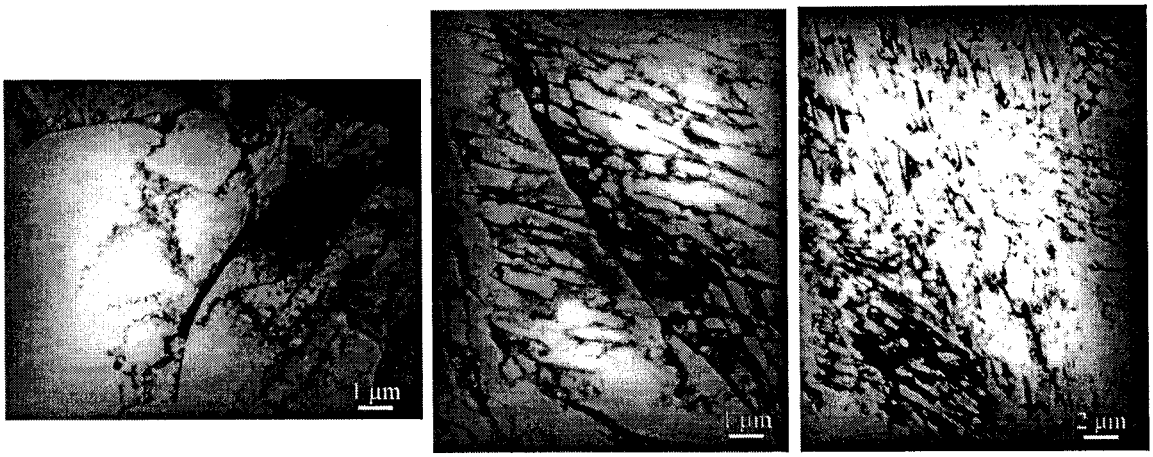

Figure 4.42 - Bright field TEM image from the a) bottom and b) 1.5 mm and c) 16 mm from the bottom of a deep drawn cup.

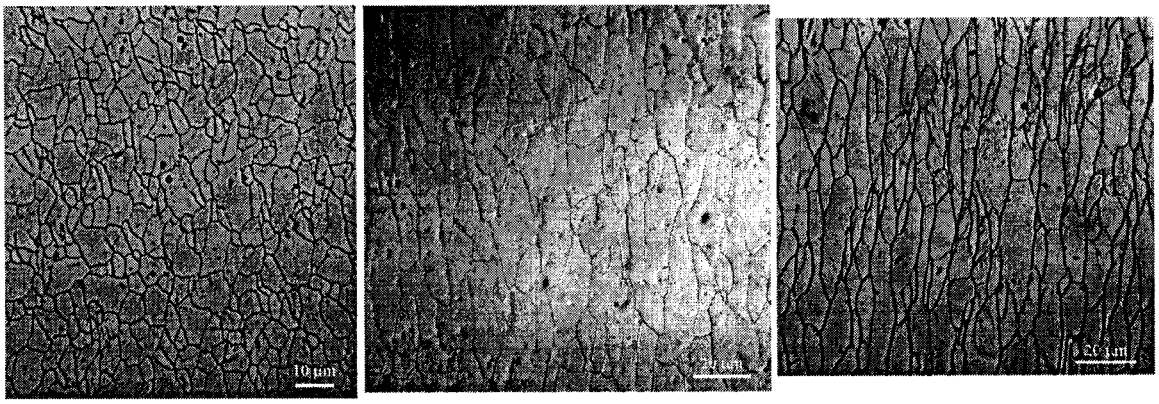

Figure 4.43 - Optical micrographs and from a) bottom, b) middle and c) top of a cup deep drawn to draw ratio of 2.2 and stress relief heat treated at 550 °C for 1 hr.

About 10 mm up the cup wall, the grains are recrystallized and exhibit abnormal grain growth (Figure 4.44b). Abnormal grain growth ends about half way up the cup wall, or at a height of 20 mm. The grains are recrystallized above this point. Grains at the top of the cup have approximately the same equivalent diameter as the undeformed material (12 μm compared to 10 μm).

4.4.3 Residual Stresses Induced by Deep Drawing

The variation in the circumferential residual stresses with cup wall height were determined by using the ring opening method and equation 3.10. The circumferential residual stresses are plotted in Figure 4.47 for draw ratios of 1.65, 2.0, 2.2, and 2.4 for the continuously annealed 0.8mm gage material. Residual stresses increase with cup wall height up to a maximum, which increases with draw ratio, and occurs at approximately half way up the cup wall and then decrease to a much lower value near the top of the cup. For instance, according to

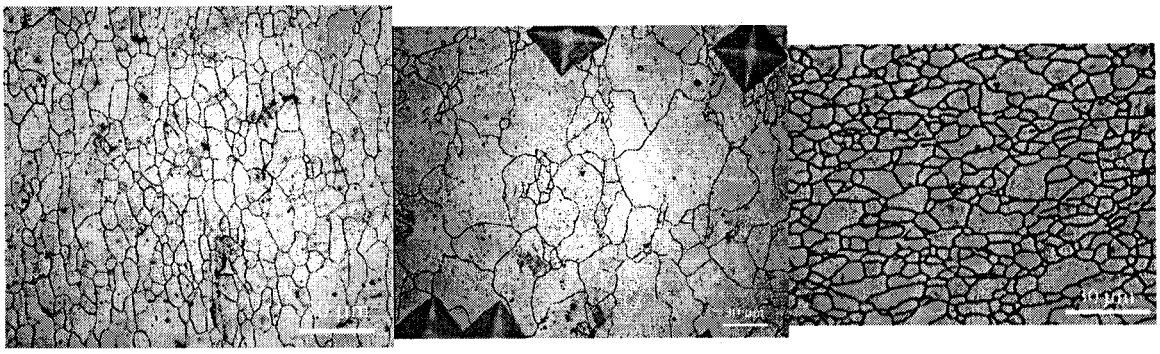

Figure 4.44 - Optical micrographs and from deep drawn cups heat treated at 820°C for 60s, a) bottom of cup, not recrystallized, grains slightly elongated, b) a height of 10 mm, abnormal grain growth, and c) top of cup, recrystallized.

equation 3.6 the maximum circumferential residual stress is 330 MPa for draw ratio 2.4 and is found at a height of 25mm. Additional decreases in residual stresses are noticed near the bottom of certain cups (draw ratio of 2.4 (Figure 4.45), 2.2 batch annealed and 2.2 die 2 (Figure 4.47)). If material yields due to a superimposed tension while it passes over the die profile (Marciniak and Duncan 1992) or is ironed after deep drawing (Ragab and Orban 2000, Danckert 1994), a decrease in residual stress is expected. Evidently, thinning near the cup bottom also reduces the residual stresses. Thinning was most pronounced for a draw ratio of 2.4 as it is nearest to the LDR.

Table IV-IV Strains measured from change in average major and minor axis lengths of deep drawn cup compared to bulk strains measured from square grid analysis

	square grid analysis		grain shape	
cup height (mm)	ε_1	ε_2	ε_1	ε_2
2	0.07	-0.04	0.1	0.02
10	0.27	-0.23	0.29	0.23
20	0.45	-0.4	0.49	-0.18
30	0.6	-0.55	0.63	-0.51
40	0.67	-0.65	0.69	-0.65

Residual stresses for the heat treated cups were compared to non-heat treated cup with the same draw ratio. No residual stresses were found for the fully recrystallized cup (Figure 4.46). Cups heat treated after deep drawing, at 550° C for one hour, show a significant decrease in residual stress. The circumferential residual stresses are decreased to 25 MPa for all heights, although there is a small increase to 75 MPa at a height of 15 mm. Therefore this heat treatment was effective in relieving the residual stresses without changing the grain shape or flow stress (e.g. Figures 4.43 and 4.38). Cups drawn with blanks heat treated at 550°C for one hour before drawing showed no noticeable difference in circumferential residual stresses when compared to non-heat treated cups.

Circumferential residual stresses were investigated for cups drawn with different die configurations. No significant differences in residual stresses were detected for the light gage material with a draw ratio of 1.65 using die 1, 2 or the tractrix die. The residual stresses of the tractrix drawn cups were slightly lowered, but this difference is within the experimental error. To make full use to the tractrix profile, the blank must have the

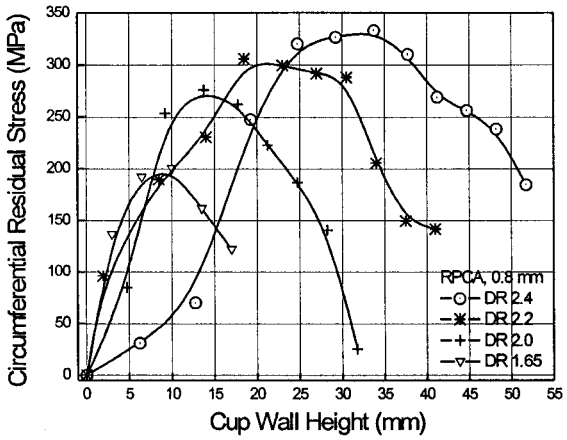

Figure 4.45 - Circumferential residual stresses with cup wall height for different draw ratios for 0.8 mm sheet.

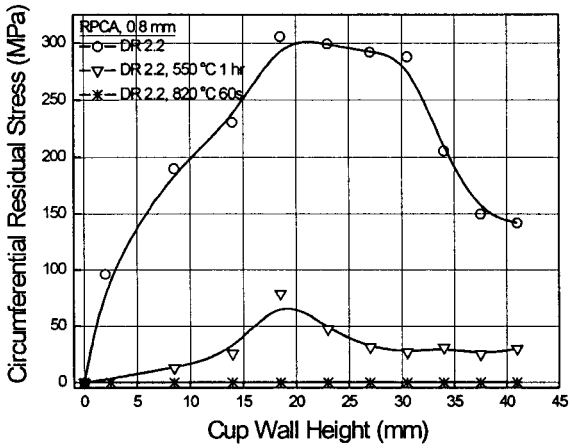

Figure 4.46 - Circumferential residual stress with cup wall height for heat treated cups.

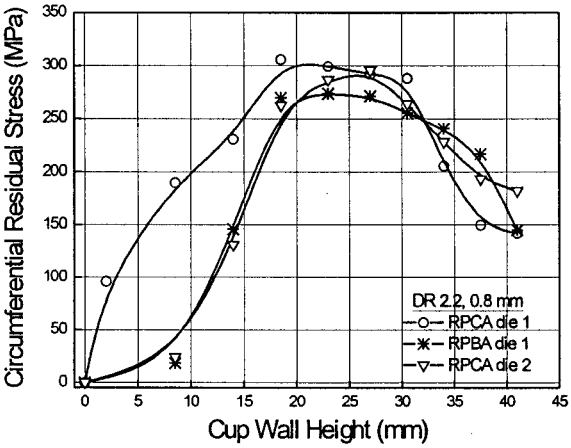

Figure 4.47 - Circumferential residual stresses with cup wall height for a draw ratio of 2.2.

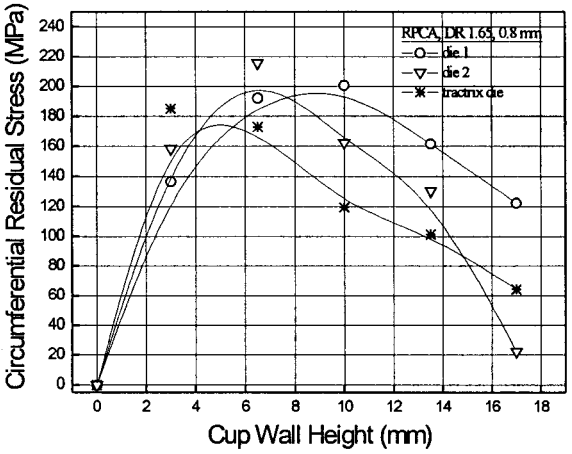

Figure 4.48 - Circumferential residual stresses with cup wall height for draw ratio of 1.65 comparing different die geometries.

same diameter as the width of the die. Therefore a different die must be used for each draw ratio, indeed cost prohibitive. Blanks, 82.5 mm in diameter, did not make full use of the tractrix profile, whereas blanks 110 mm in diameter are nearly the proper diameter. Similar residual stresses were observed for cups drawn to a draw ratio of 2.2 with die 1 and die 2, except as mentioned near the bottom of the cup. Different residual stresses were observed between the tractrix die and die 1 for the 1.5 mm thick material deep drawn to a draw ratio of 2.2. In this case, the circumferential residual stresses were decreased by about 40% along the entire cup wall for the cups drawn with the tractrix die. Longitudinal residual stresses were found to be about 1.5 times higher than the circumferential residual stresses for a draw ratio of 2.2, die 1.

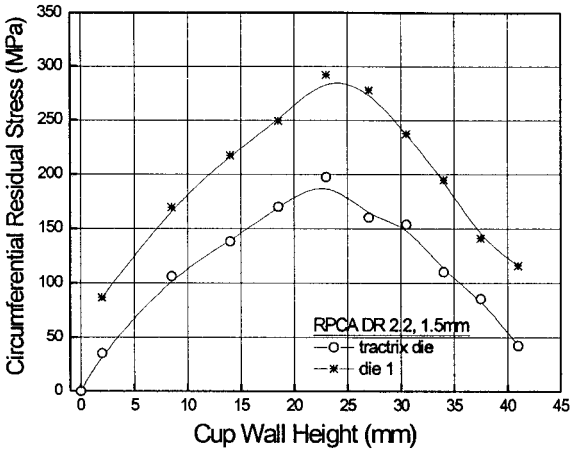

Figure 4.49 - Circumferential residual stress with cup wall height for draw ratio 2.2, 1.5 mm gage, comparing tractrix die and die 1.

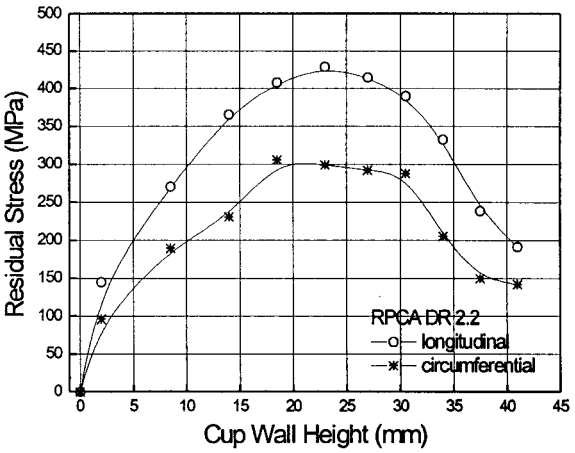

Figure 4.50 - Longitudinal and circumferential residual stresses with cup wall height for draw ratio of 2.2, die 1.

4.5 Cup Expansion Test and Associated Fractography

Cup expansion tests were used to characterize the rephosphorized steel's susceptibility to cold work embrittlement for a variety of test conditions. Experiments were designed to establish a baseline understanding of CWE, fill in gaps in knowledge and to test predictions yielded by the fracture modeling coupled with the Davidenkov approach. Results of the cup expansion tests will therefore be discussed within this constructed framework after the fracture model is developed in the discussion. Results of the CETs are given in terms of the DBTT graphed as bar charts.

Scatter in the measured DBTT depended on the temperature at which the cups were tested: transition temperatures between -30°C and 110°C had a error of ±1°C, transition temperatures between -120°C and -30°C had a error of ±2°C, while transition temperatures between -196°C and -120°C had a error of ±5°C. The larger value reported in the scatter at lower temperatures (between -196°C and -120°C) is partly due to the difficulty in maintaining temperature without the use of a liquid bath. Although load-displacement data was collected during the CET, this was not used to determined changes in fracture stress as the area over which the applied stress acts is not easily determined, partially due to the plastic opening that increases as the brittle to ductile transition is approached (Figure 4.63).

Rephosphorized continuously annealed material, deep drawn into cups with draw ratio 2.2 and tested with a ram speed of 5 mm/s, had a transition temperature of -11°C. This result is taken as a baseline to which the other tests are compared. A 30°C difference in DBTT exists for batch annealed material tested as the same strain rate (Figure 4.51). Testing with a ram speed of 4429 mm/s increases the difference in the DBTT between the continuously annealed and batch annealed materials to 55°C, i.e. 50°C compared to 105°C (Figure 4.51).

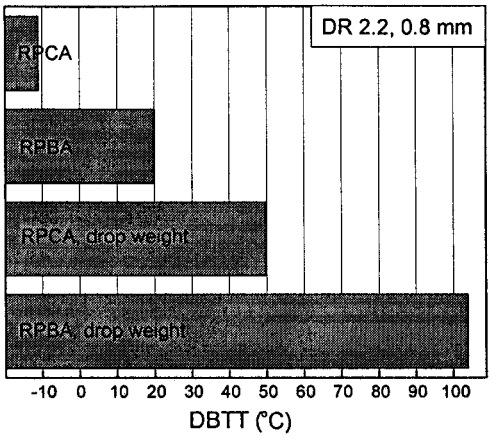

Figure 4.51 - DBTT comparing batch and continuously annealed deep drawn cups tested at low and high strain rates.

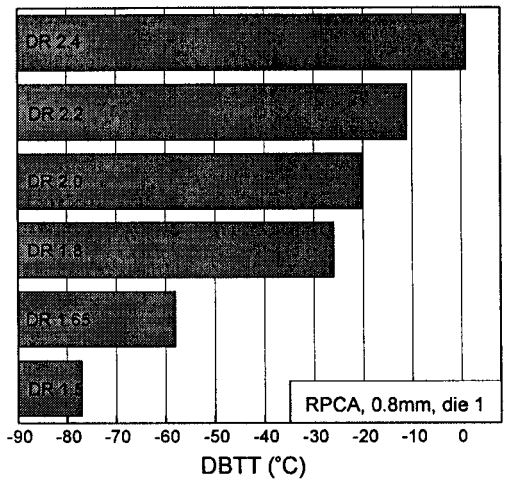

Figure 4.52 - DBTT as a function of draw ratio for RP CA 0.8 mm.

Results of the CET for six different draw ratios for the RPCA 0.8 mm grade are shown in Figure 4.52. Ductile-to-brittle transition temperatures increase from -76°C for a draw ratio of 1.5 to 4°C for draw ratio of 2.4. Cups of draw ratio 2.4 lathed down to the same height as cups of draw ratio 2.2 are brittle at -15°C as compared to -11°C (Figure 4.53). As well, no difference was observed for cups of draw ratio 1.5 with the cup bottom lathed off; the transition temperature was still -76°C.

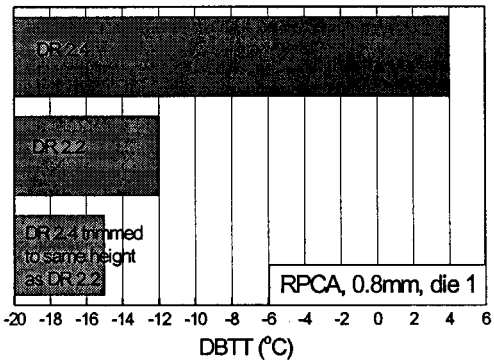

Figure 4.53 - DBTT comparing DR 2.4 lathed to the same height as DR 2.2.

Different die geometries were used for the cup drawing. Transition temperatures increase with a more severe die radius for die 2 compared to die 1 (Figure 4.55). As well, the transition temperature increases slightly, no more than 10°C, with cups drawn using the tractrix die compared to die 1 (Figure 4.55). Differences in transition temperatures were greater with increasing draw ratio and thickness. For instance, the transition temperatures differ by 14°C for a draw ratio 2.2 and by 6°C for a draw ratio 1.65 when comparing cups drawn with die 1 and die 2 (Figure 4.55). Tractrix cups drawn with the 1.5 mm gage material show exception to this pattern, the tractrix die increases the DBTT from -58°C to -49°C for a draw ratio of 1.65, an increase of 11°C, and from 2°C to 9°C for a draw ratio of 2.2, an increase of 7°C (Figure 4.55). The increase is greater for the lower draw ratio.

Cups deep drawn to a draw ratio 2.2 and then recrystallized exhibit a transition temperature of -180°C which is nearly returned to that of the as-received undeformed material (Figure 4.54). Cups stress-relieved at 550°C for one hour show a 20°C increase in the transition temperature (Figure 4.54). The increase for cups heat treated at

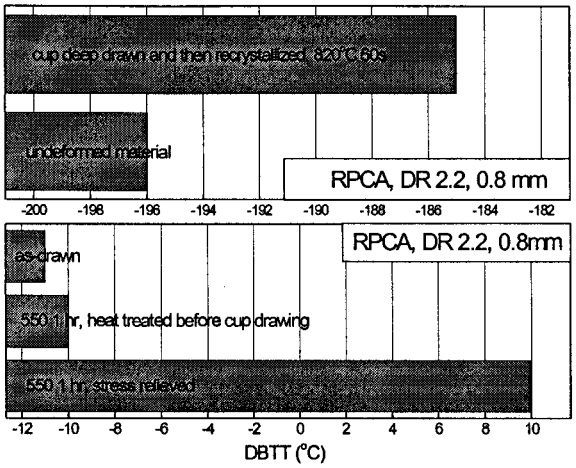

Figure 4.54 - DBTT for recrystallized and stress relieved cups.

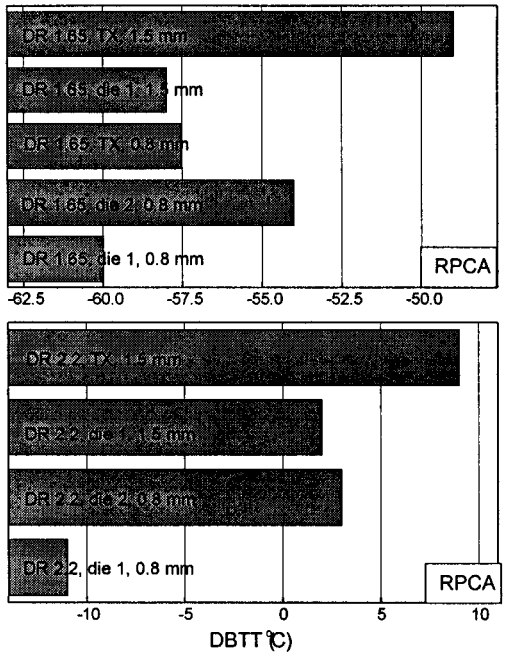

Figure 4.55 - DBTT for different die geometry for the RP CA 0.8 mm and 1.5 mm materials.

550°C was even greater when the oxide coating developed in the salt bath was left on the cups. Blanks heat treated at 550°C for one hour prior to drawing show no difference in transition temperature.

Transition temperatures for cups of continuously annealed material, draw ratio 2.2, tested at three ram speeds are shown in Figure 4.56. The lower ram speed was chosen to give a strain rate equivalent to that used in the uniaxial tensile testing. Transition temperatures -14°C, -11°C and 50°C were recorded for ram speeds of 0.01, 5, and 4429 mm/s respectively.

A comparison of different thickness material, 0.8mm gage compared to 1.5mm gage, reveal essentially the same transition temperatures for draw ratio 1.65 (-60°C compared to -58°C respectively), whereas the difference increases to -13°C (-11°C versus 2°C) for cups of draw ratio 2.2, the thicker material being more brittle (Figure 4.58).

The effect of surface condition on the DBTT was investigated by testing the continuously annealed material in three different conditions: galvanneal coating left on, coating stripped, and coating stripped and

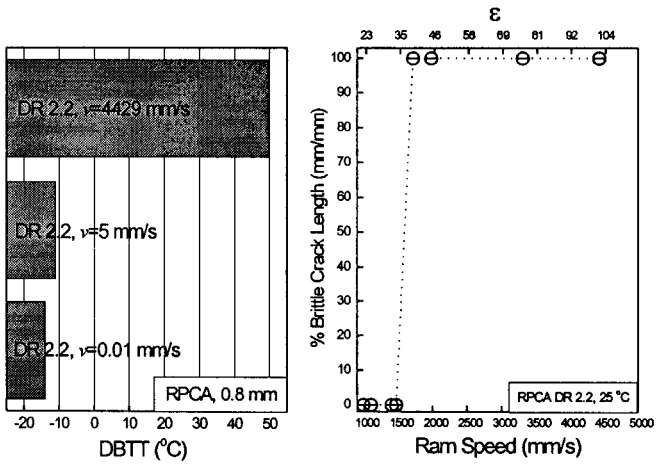

Figure 4.56 - a) DBTT for three different strain rates and b) ductile-to-brittle strain rate for cups tested at room temperature.

surface damage removed. Surface condition had a large influence on the transition temperature and was not dependent on the draw ratio to the same extent as other variables. The galvanneal coating increased the DBTT by 35°C for a draw ratio of 2.2 and 39°C for a draw ratio of 1.65 (Figure 4.57). Removing the surface cracks decreased the transition temperature by 7°C for a draw ratio of 2.2 and by 15°C for a draw ratio of 1.65 (Figure 4.57). A separate series of tests were performed on cups drawn with blanks that were stripped of the galvanneal coating with an iron inhibitor added to the HCl acid solution. The transition temperature of these cups (draw ratio 2.2) was -11°C, not changed from the cups stripped without the iron inhibitor.

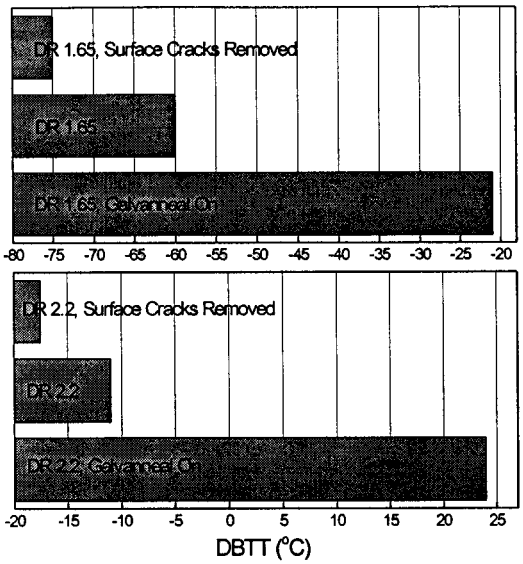

Figure 4.57 - Effect of surface cracks on the DBTT for RP CA DR 2.2, 0.8mm, 5mm/s.

The origin of these cracks was investigated by stripping the light gage material with HCl solution, with and without iron inhibitor added, before and after deep drawing. The iron inhibitor made no difference as to the density or morphology of cracks. Cracks are present before deep drawing, although the density is increased after deep deep drawing. After deep drawing the crack morphology changes, surface grains are rotated and distorted and as a result the cracks appear more open.

Blanks 120 mm in diameter were partially drawn and tested with the flange left on. Usually, partially drawn cups are compared to cups of the same height (Bhat et al. 1994, Lewis 1998). A more accurate comparison can be made by comparing the maximum strain and hardness at the position where the cups are circumferentially expanded (e.g. the edge resting on the cone). Strain levels between the flange and the wall of are less than at the edge of the 1.8 draw ratio cups but more than at the edge of the 1.65 draw ratio cups (Figure 4.35). Figure 4.59

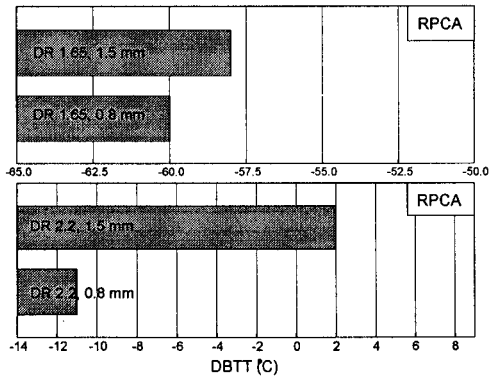

Figure 4.58 - DBTT for different sheet thicknesses for draw ratio of 1.65 and 2.2.

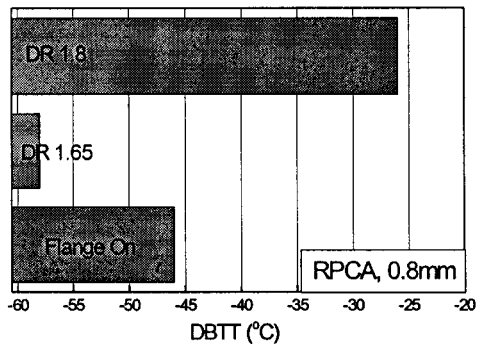

Figure 4.59 - DBTT for partially drawn cup with flange left on and DR 1.8 and 1.65.

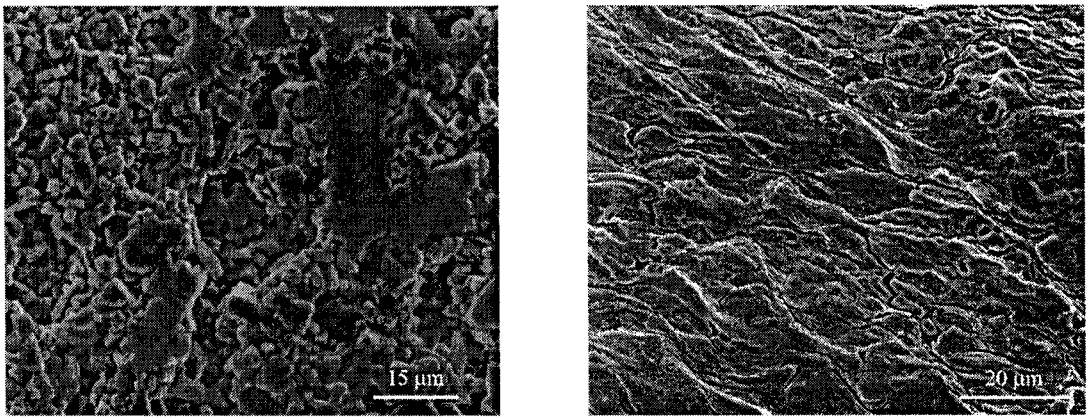

Figure 4.60 - Galvannealed coating on undeformed material and surface cracks for deep drawn continuously annealed material stripped of coating prior to drawing.

compares the transition temperature for partially drawn cups and cups with draw ratios of 1.8 and 1.65. The DBTT of cups with the flange left on is -47°C which is consistent with the strain and hardness levels.

4.5.1 Analysis for cracking position

The cracking position at the top of the cup was recorded and is plotted as a function of draw ratio (Figure 4.61). Cups distinctly crack in the rolling direction for draw ratios 1.5 and 1.65. The radial position of the cracks spread from the rolling direction with increasing draw ratio. At a draw ratio of 2.2, the highest intensity of cracking occurs at about ±20°.

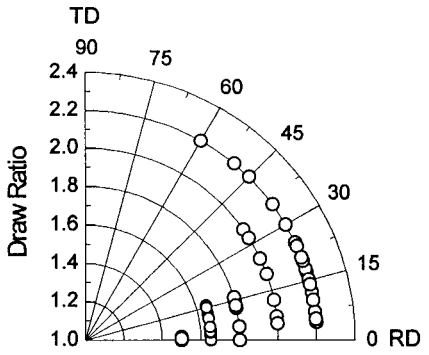

Figure 4.61 - Radial position of brittle cracking for different draw ratios.

4.5.2 Bulk Plastic Deformation for Cups Defined as Brittle

Bulk plastic deformation can occur during the secondary forming operation before brittle fracture, as exemplified by the macro-photographs taken of cups expanded below the transition temperature (Figure 4.62). At the point of brittle fracture audible cracking occurs and the load instantly drops. Attempts to measure the strain prior to fracture by using the square grid analysis system with 0.5 mm grids were unsuccessful and limited by the inherent sensitivity of the technique and the curvature of the workpiece at the cup edge (Figure 4.63a). A typical pattern to the amount of plastic deformation occurred as the test temperature was progressively lowered and is illustrated by the continuously annealed steel with draw ratio 2.2. Just below the transition temperature (i.e. -11°C) at -12°C, the steel exhibits significant plastic opening, the edge of the cup takes on the shape of the conical punch and brittle fracture occurs at what appear roughly to be a limit to the amount of plastic opening. Cups that fractured in a brittle manner did not open any more than this (Figure 4.63a). Further below the transition temperature less plastic deformation occurs (-34°C), the bottom of the cups acts as a

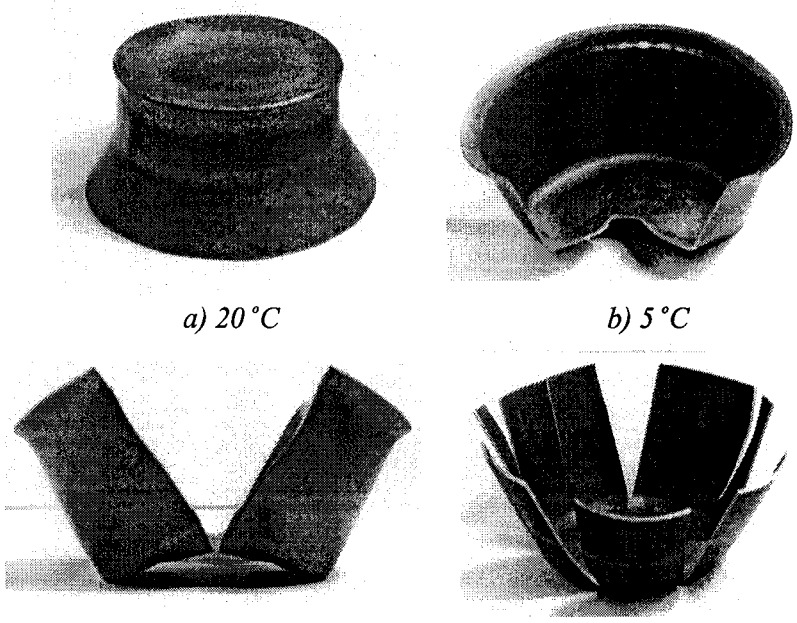

a) 20 °C *b) 5 °C*

c) 0°C *d)-196 °C*

Figure 4.62 - Typical response of cups expanded over a conical punch over a large range of temperatures, a) 20°C b) 5°C c) 0°C d) -196°C. The transition temperature is 10°C.

plastic hinge and the cup plastically opens (Figure 4.63b). Well below the transition temperature (-196°C), no bulk plastic deformation occurs (Figure 4.63c). The curvature in the longitudinal tongue is due to elastic springback. Also, the number of cracks increase as the temperature is lowered (Figure 4.62).

Plastic deformation also occurs during the brittle fracture process but is hard to assess as it depends on the number of cracks and exactly how the cup opens on the punch. For instance, just below the transition temperature the cups often fracture with one crack, which causes the cup to be displaced to one side. This causes a secondary plastic opening (Figure 4.63) and increases the amount of energy absorbed. For this reason the energy absorbed during the cup expansion test does not give a good indication of the transition to brittle behaviour and ductile-to-brittle transition temperatures based on energy absorbed exhibit more scatter (Lau et al. 1998).

4.5.3 Fractography of Expanded Cups

All fractured cups exhibit nearly complete intergranular fracture below the transition temperature; less than five percent area fraction transgranular fracture was found. The transgranular facets showed characteristic river patterns (Figure 4.69b). With increasing deep drawing deformation the intergranular fracture facets lose their smoothness and develop undulations in the surface that appear as striations (Figure 4.69a) and the grains become flattened (Figure 4.64b). Therefore intergranular fracture can become more difficult to distinguish at

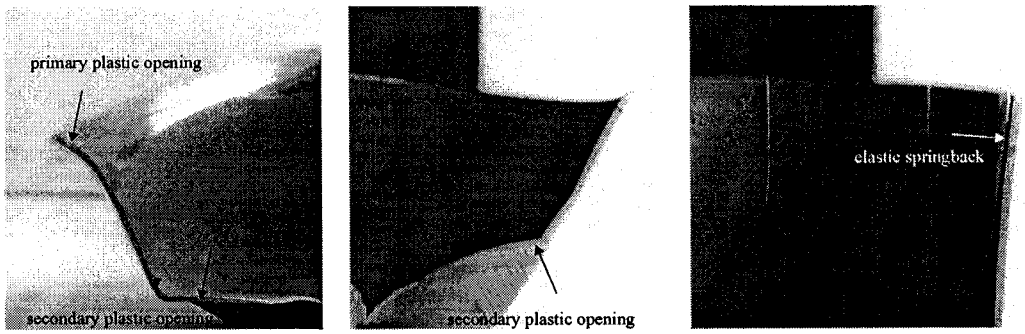

a) -12 °C *b)-34 °C* *b)-196 °C*

Figure 4.63 - Plastic opening for brittle specimens at the top of expanded cups with temperature a) -12°C, notice shiny area due to secondary plastic work, b) -34°C and c) -196°C, total absence of plastic opening. The transition temperature is -11°C.

higher strains. Ductile fracture by microvoid coalescence occurred above the transition temperature (Figure 4.68), although frequently no fracture occurred at all, the cups plastically expanded (Figure 4.62a). No change in fracture mode was observed along the cup wall for cups that fractured in a brittle manner, although a change to ductile fracture can occur near at the base of the cups depending on the temperature as will be discussed below. The evolution of grain shape with deformation is evident, the facets exposed at the cup bottoms more closely resemble those from undeformed material (compare Figures 4.24 and 4.65a). Fracture surfaces from higher draw ratios reveal more highly elongated grains at the top of the cups as would be expected from the bulk strains.

Fracture surfaces from the 1.5mm gage material drawn with die 1 and the tractrix die are compared at both the top and bottom of the cups in Figures 4.65 and 4.66. This comparison is similar to the other fractured cups, no differences are found . For instance, both continuously annealed and and batch annealed are nearly completely intergranular (~97%) down the length of the cup. Cracks can be blunted when tested just below the transition temperature. A particularly good example are the cups of draw ratio 1.65. Cups with this draw ratio

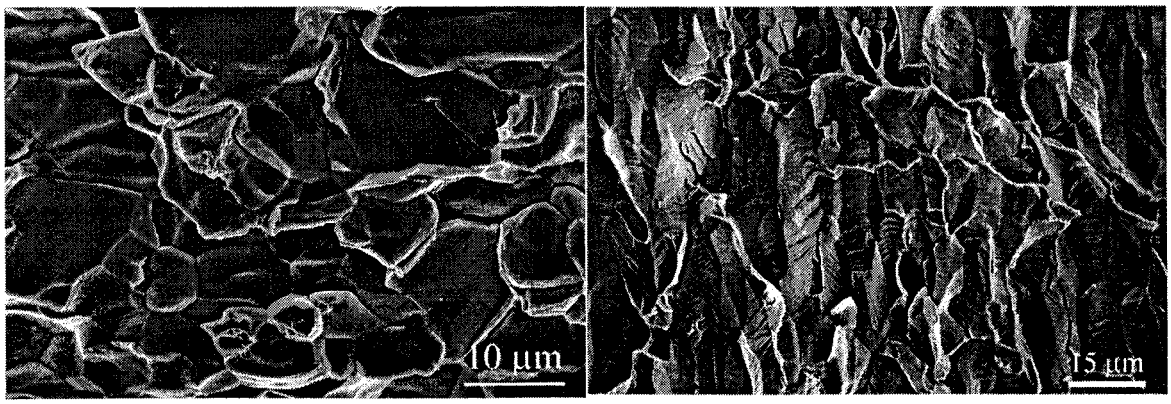

Figure 4.64 - Micrographs of fracture surfaces from the bottom and top of the cup wall for a draw ratio of 2.4.

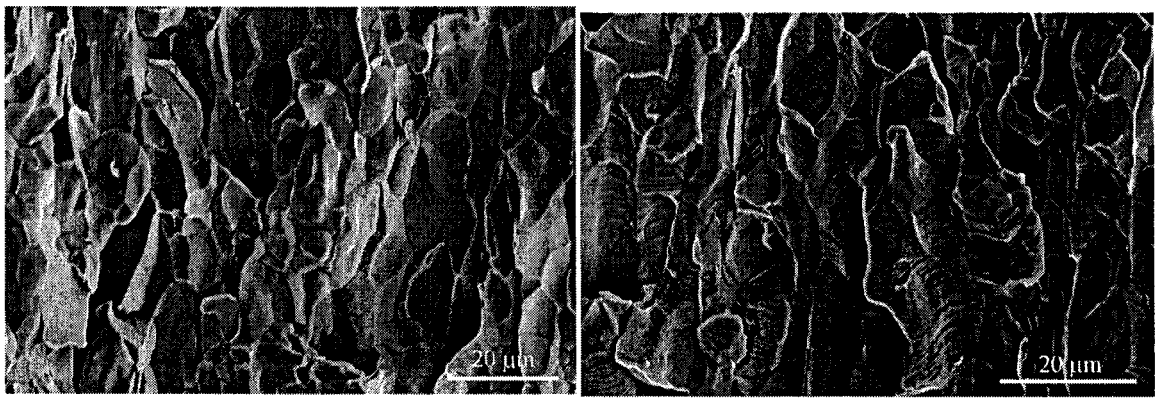

Figure 4.65 - Micrographs of fracture surfaces from the bottom and top of the cup wall for a draw ratio of 2.2, 1.5 mm gage, drdrawn with die 1.

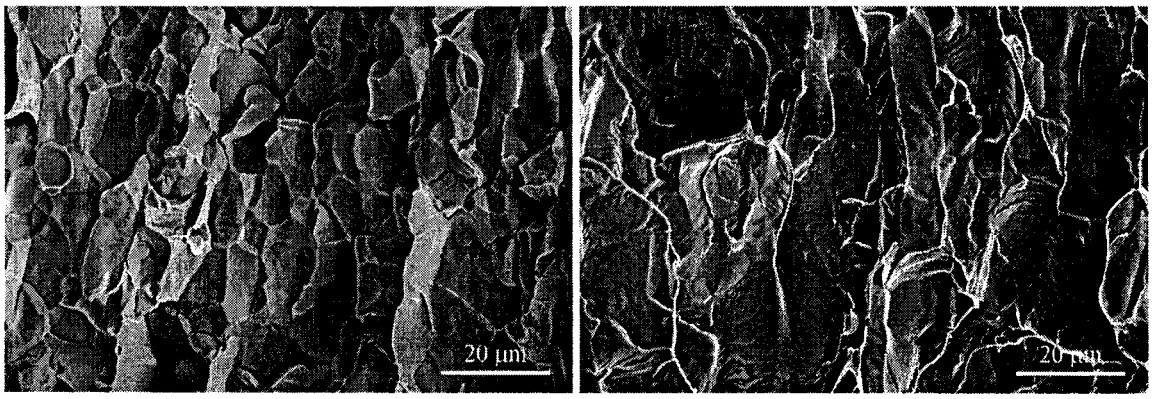

Figure 4.66 - Micrographs of fracture surfaces from the bottom and top of the cup wall for a draw ratio of 2.2, 1.5 mm gage, drawn with the tractrix die.

have a transition temperature of -58°C when drawn with die 1. Just below the transition temperature, at -60°C, the intergranular crack is blunted once as it traverses around the die bend profile (Figure 4.70b). The fracture mode changes from brittle intergranular to ductile microvoid coalescence (Figure 4.67). Further below the transition temperature, crack blunting does not occur, the crack splits the cups in two, and the fracture is entirely brittle intergranular (Figure 4.70a).

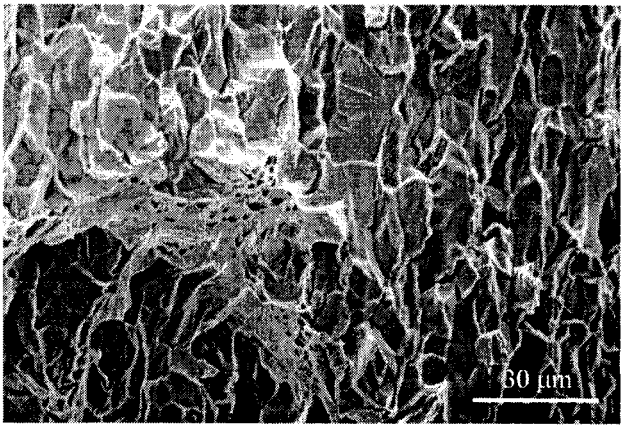

Figure 4.67 - Mixed ductile fracture and intergranular fracture at the cup bottom.

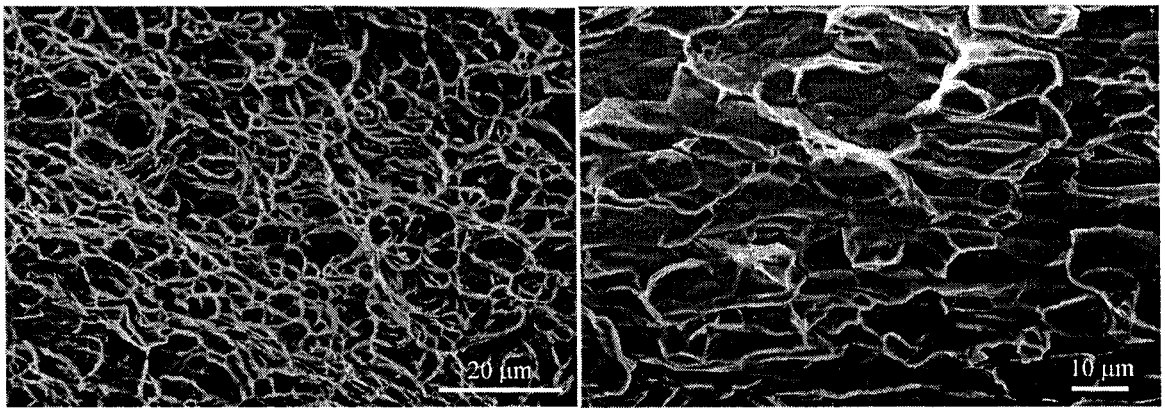

Figure 4.68 - Micrographs of fracture surfaces above the transition temperature and below the transition temperature.

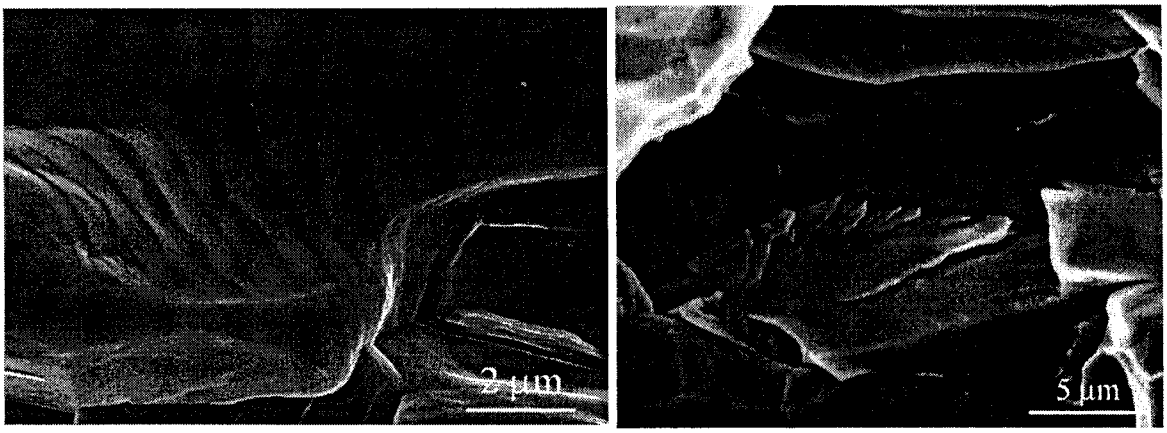

Figure 4.69 - Micrographs of fracture surfaces for the continuously annealed cup (draw ratio 2.2) tested below the transition temperatures, showing an a) intergranular fracture facet and a b) transgranular facet.

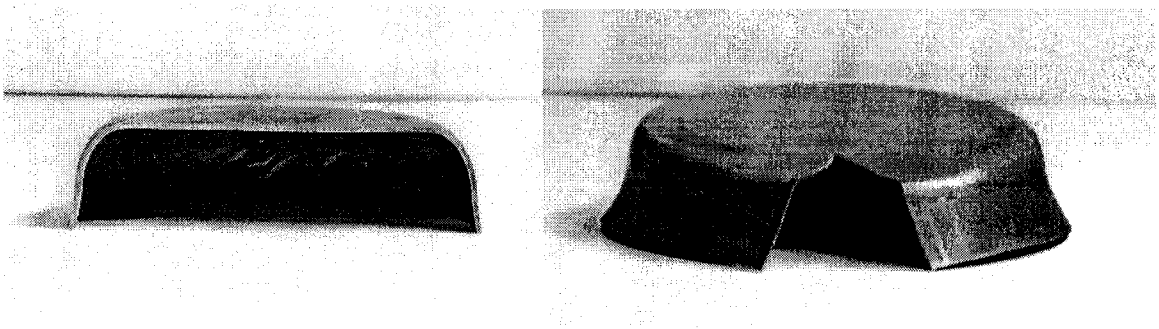

Figure 4.70 - Cups of draw ratio 1.65 tested a) -70°C and at b) -60°C, for draw ratio 1.65. The transition temperature is -58°C.

4.0

4.10 Crack Path Analysis using Electron Back-Scatter Diffraction on Undeformed and Deformed Materials

Fracture path investigations were performed to correlate the propensity for grain boundary fracture to grain boundary structure. The fracture path selection will depend on the grain boundary structure and also on the orientation of the grain boundary with respect to the stress state. Rephosphorized continuously and batch annealed materials were both used for the study in both undeformed and deformed states. No difference in grain boundary structure distributions was detected between either heat treatments (Figure 4.73 and Table IV-V). As well, the angular probability of finding a boundary in the plane of the sheet was the same for both $\Sigma \geq 1$ and $\Sigma = 1 \rightarrow \Sigma = 29$ grain boundaries (Figure 4.72). Therefore the statistics obtained for the cracked and uncracked grain boundaries for the continuously annealed and batch annealed were tabulated together. Table IV-V tabulates the grain boundary structure distribution in terms of the CSL scheme while Figure 4.73 plots the grain boundary structure distribution in terms of the θ / l pair. In both batch and continuously annealed grain boundary structure distributions there are approximately 10% low angle, 20% special and 70% general grain boundaries.

The deep drawn material was found to have a large percentage of $\Sigma = 1$ boundaries, ~85%. Most of these boundaries are subgrain boundaries as they did not correspond to boundaries as delineated by etching and they had spacing equivalent to subgrain boundaries as determined from bright field TEM micrographs (Figure 4.42) taken in the same plane as the EBSD reconstructions. Misorientations less than five degrees were

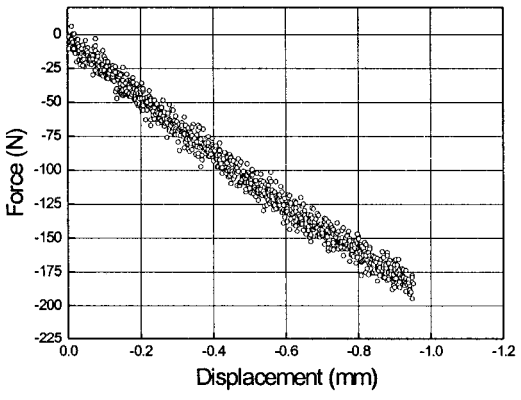

Figure 4.71 - Load-displacement data for notched undeformed specimen bent in liquid nitrogen.

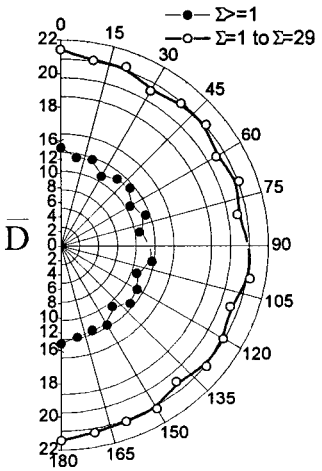

Figure 4.72 - Angular distribution of grain boundary spacing in plane of sheet for $\Sigma \geq 1$ and $\Sigma = 1 \rightarrow \Sigma = 29$ grain boundaries for the batch annealed undeformed material.

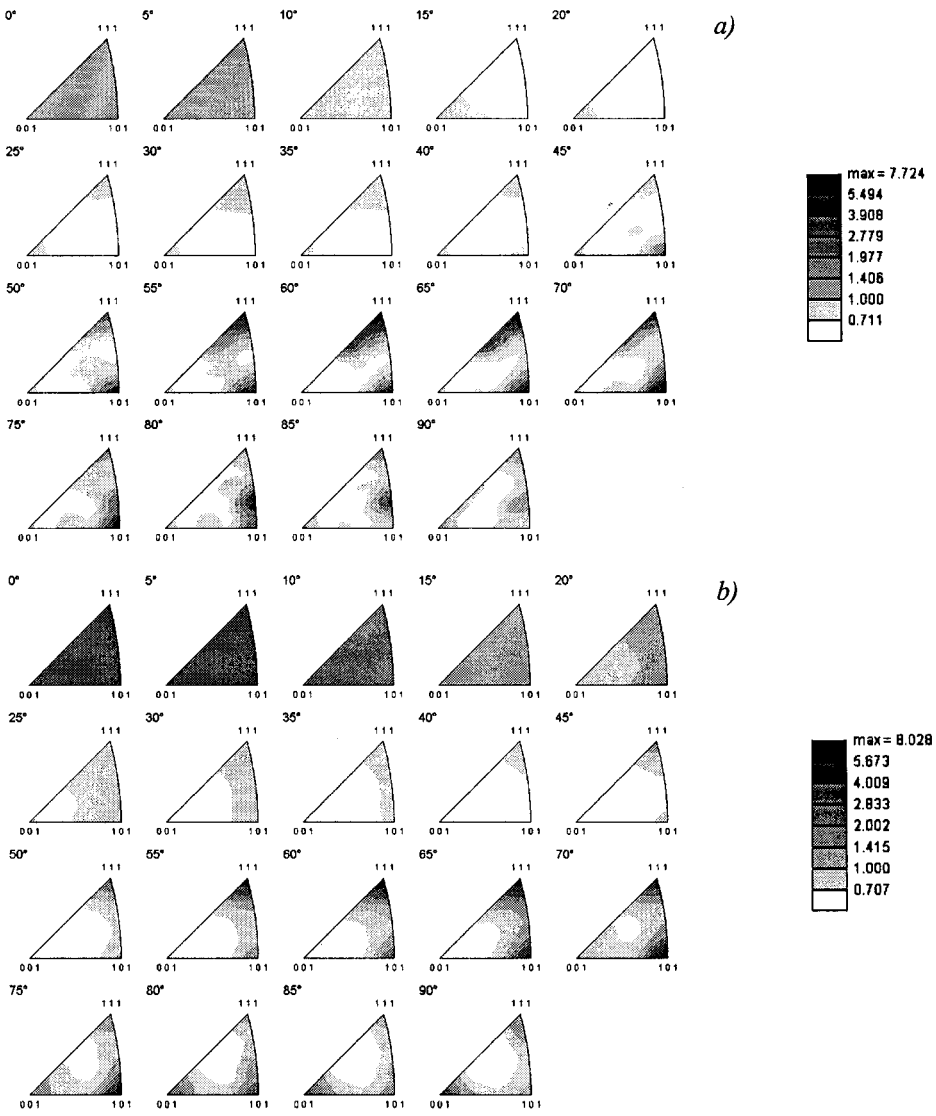

Figure 4.73 - Grain boundary structure distribution for a) continuously and b) batch annealed materials as discrete θ / l stereographic projection.

regarded as subgrain boundaries and therefore a misorientation cutoff of five degrees was chosen to exclude subgrain boundaries from the statistics.

No bulk macroscopic plasticity was observed (Figure 4.71) during the three point bend tests in liquid nitrogen on either undeformed or deformed samples. A micrograph of a precracked deep drawn sample

Table IV-V CSL data for continuously and batch annealed undeformed materials

Grade Structure	CA length fr.	BA length fr.
Σ1	0.092	0.092
Σ3 ≤ Σ29	0.190	0.175
> Σ29	0.718	0.733

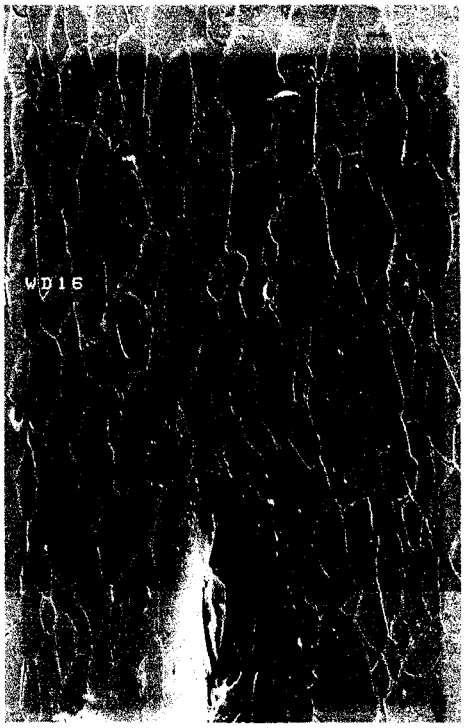

Figure 4.74 - Micrograph of precracked sample taken from deep drawn cup. Carbon contamination delineates scan area.

Figure 4.75 - Micrograph of cracked sample from deep drawn cup.

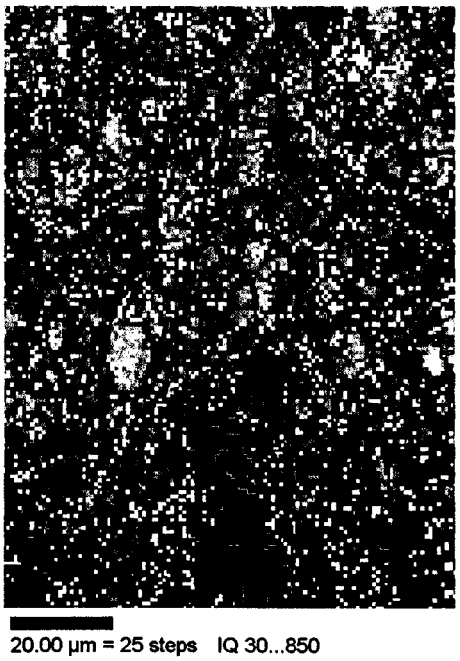

Figure 4.76 - Microstructure reconstructed from EBSD data from same area as Figure 4. 74.

Boundaries: Rotation Angle

	Min	Max	Fraction
—	15	180	0.763
—	5	15	0.237

Boundaries: CSL

	Sigma	Tolerance	Fraction
—	3	8.66	0.03
	5	6.71	0.058
—	7-29	5.29	0.675

taken from the batch annealed material at height of 15 mm ($\varepsilon_1 = 0.55, \varepsilon_2 = 0.52$) is shown in Figure 4.74. A map, reconstructed from the EBSD data, of the spatial distribution of grain boundary structures from the corresponding area analyzed before cracking is shown in Figure 4.76. An optical micrograph of half of the sample

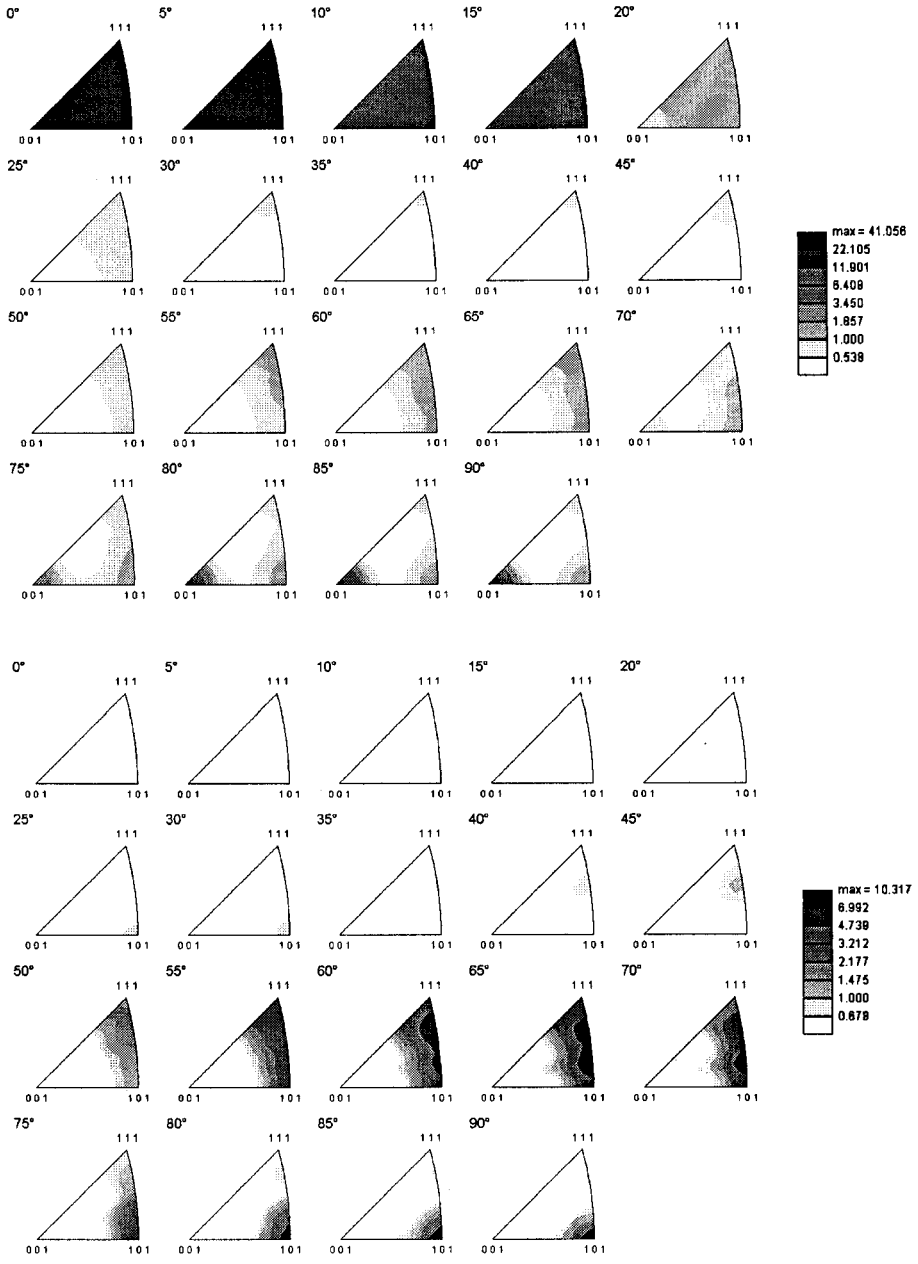

Figure 4.77 - Discrete plot of θ / *l stereographic projection for a) uncracked and b) cracked.grain boundaries from batch annealed deep drawn sample.*

after being fractured is shown in Figure 4.75. The crack path was followed to determine the correlation between grain boundary structure and the probability of fracture.

Table IV-VII Grain boundary structure distributions for cracked and uncracked grain boundaries in undeformed material.

G.B. character	cracked	uncracked	bulk
low	0.02	0.20	0.092
special	0.06	0.17	0.183
random	0.87	0.63	0.723
TGF	0.05	---	---

Table IV-VI Grain boundary structure distributions for cracked and uncracked grain boundaries in deep drawn material.

G.B. character	cracked	uncracked	bulk
low	0.04	0.30	0.20
special	0.03	0.26	0.11
random	0.87	0.41	0.68
TGF	0.06	---	---

A total of three specimens from both the undeformed and deep drawn materials were analyzed in this manner. A decrease in the number fraction of special grain boundaries and an increase in the number fraction of low angle grain boundaries, is observed in the deep drawn material as compared to the undeformed material. Although an anomalously high number fraction of low angle boundaries would contribute to this observation e.g. the inclusion of subgrain boundaries, this was not the case. Therefore, it can be concluded that deep drawing changes the grain boundary structure distribution. The results are tabulated in Tables IV-VI and IV-VII.

A greater correlation exists between the grain boundary structure and the probability to fracture in the heavily deformed material than the undeformed material. Only 4% of cracked boundaries were low angle boundaries in the deep drawn material, whilst they comprised 20% of the grain boundary volume. Similarly, 3% of the cracked boundaries were special boundaries, while special comprised 11% of the bulk. The correlation is even more striking if the uncracked boundaries are analyzed (Table IV-VI). A similar situation is observed when the undeformed boundaries are analyzed. Low angle boundaries and special boundaries crack with a much less frequency than they appear in the bulk, while random grain boundaries have a greater probability of cracking than they appear in the bulk. Averaging both deformed and undeformed materials as the statistics are very close gives the probability of cracking a low angle boundary is 0.11, a special boundary is 0.17 and a general grain boundary is 0.73. The same conclusion can be reached by comparing the grain boundary structure distributions of the cracked grain boundaries to all grain boundaries. Stereographic projections of the grain boundary structure distributions are plotted as θ / l pairs for cracked boundaries and all boundaries (Figure 4.77). An absence of low angle boundaries and a higher density of general boundaries is observed. In conclusion, low angle boundaries are the most resistant to fracture, while special boundaries are less resistant to fracture than low angle boundaries but more resistant to fracture than general grain boundaries.

4.11 Quantitative Transmission Electron Microscopy

The analysis of both the local grain boundary composition was performed in collaboration with Dr. Aleksandra Perovic. A total of ~30 grain boundaries of the continuously annealed material and ~15 grain

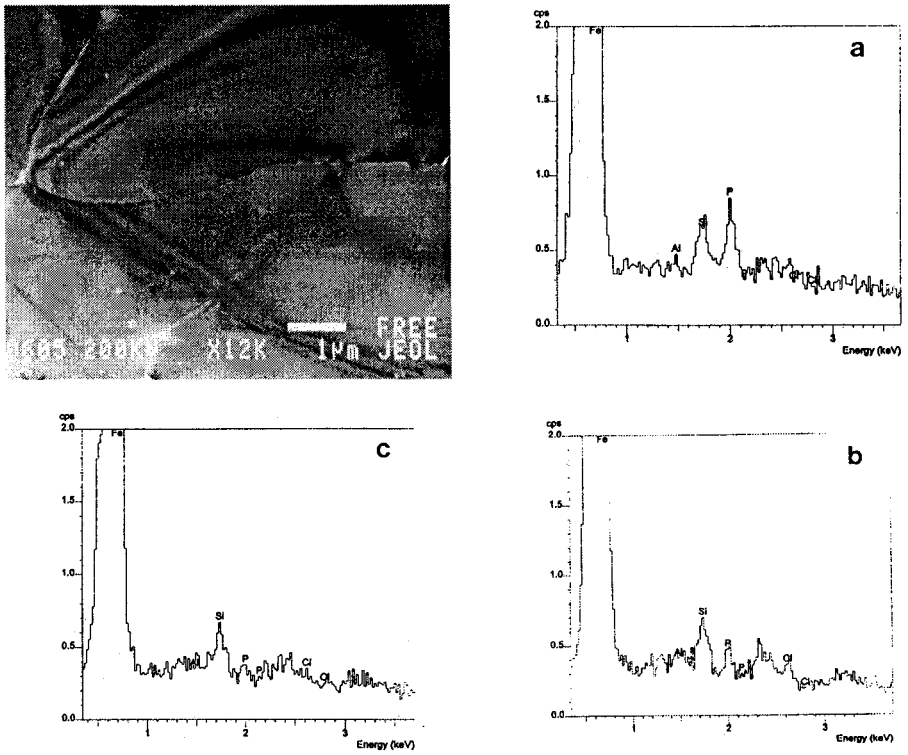

Figure 4.78 - STEM micrographs and the associated XEDS spectra for the continuously annealed grade.

boundaries of the batch annealed material were analyzed for the local grain boundary chemistry with XEDS using JEOL 2010F STEM. Foils of continuously and batch annealed materials in the fully annealed condition were compared to batch annealed foils taken from a deep drawn cup. A point-to-point method was used to determine the phosphorus content along the grain boundary, as the detection of phosphorus was highly variable along the length of any given boundary. Line scans and area scan were performed but these did not give accurate results. The variability along the length of the boundary can be attributed to grain boundary curvature, although the boundaries were chosen to be "edge on" this condition was not always met along the whole length. The structure of the grain boundary varies along the length, independent of the curvature, as well, curvature in the grain boundary introduces a structural change. The detection of phosphorus was highly dependent on the degree of tilt, as boundaries that appeared to be 'edge on' and contain no phosphorus, P segregation could then sometimes be detected with a slight tilt. Therefore, phosphorus detection was contingent on the exact orientation of the grain boundary with respect to the electron beam and to the exact position along the grain boundary length.

Peaks identified in the typical boundaries were, from left to right, the zero peak, a carbon peak, an Fe L peak, an Al Kα peak, a Si Kα (which was not present for all samples analyzed), a P Kα, an Fe escape peak and an Fe Kα and Kβ peak (Figure 4.81). These peaks, except for the phosphorus peak, were clearly present in the

matrix. Carbon contamination, drawn to the beam accumulates due to the long counting time, accounts for the carbon peak. The iron escape peak was found at -1.74 eV from the Fe peak and is added to the integrated intensity of the Fe Kα peak. A hole count was performed to determine the origin of the Si and Al peaks. The Si peak intensity did not change appreciably between the matrix or grain boundary spectrums and did not materialize during the hole count. The silicon peak was attributed to fluorescence of the Si grid supporting the polymer window of the detector and therefore was not used for quantifying grain boundary chemistry. Aluminum was not found to segregate as no significant differences were found between the grain boundaries or matrix. The aluminum peak could not be accounted for by external sources and was therefore used in the quantification.

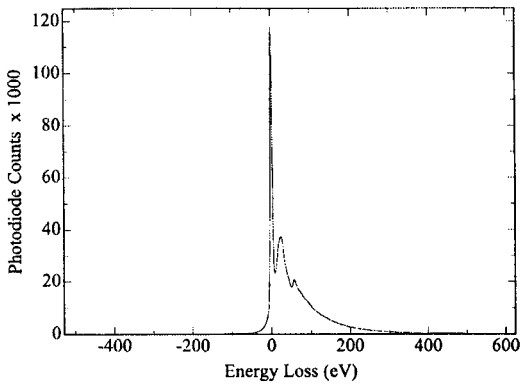

Figure 4.79 - Example of EELS spectrum used to determine the foil thickness.

Experimentally determined k-factors (Sheridan 1989), obtained at 200 kV with silicon as the reference state were used with the Cliff-Lorimer equation to quantify the phosphorus segregation. The values, $k_{PFe} = 0.77$ and $k_{FeFe} = 1.00$, compare favourable to calculated values, e.g. $k_{PFe} = 0.83$ and $k_{FeFe} = 1.00$. Foil thickness at the area analyzed must be known to accurately quantify the amount of grain boundary segregation. An EELS analysis was used to obtain the thickness so the XEDS data could be quantified. Electron-energy loss spectra were obtained near the analyzed grain boundaries to calculate the foil thickness. Not all grain boundaries were analyzed for foil thickness. An example of an energy loss spectrum is presented in Figure 4.79. The calculated mean free path for energy loss in α-iron for an accelerating voltage of 200 KeV is 150 nm (equation 3.18) which gives a foil thickness, $t = 125$ nm. An estimate of the grain boundary width is needed to convert the measured grain boundary concentration to a corrected concentration that accounts for beam spreading. Seto et al. (1999), using a 3-dimensional atom probe combined with field ion microscopy, have ascertained the distribution of boron, carbon and phosphorus across a grain boundary of low phosphorus IF sheet steel. The distribution of boron and carbon extends approximately 1 nm on either side of the boundary, while the phosphorus is not highly segregated (Figure 4.80). Inert ion sputtering alternating with AES analysis on grain boundary fracture surfaces has been the traditional method to determine the depth profile of segregation perpendicular to the grain boundary. Menyhard et al. (1991), using Ar^+ sputtering and AES, showed that excess phosphorus resides 7Å on either side of a $\Sigma = 5$ grain boundary. Balluffi (1979) concludes, from data compiled for the normalized depth distribution profiles of segregated solutes in a number of different steels, that all the solute atoms were located within ~±5Å of the center plane when artificial spreading of solute atoms in the beam direction due to the ion sputtering technique was accounted for. In all of these experimental

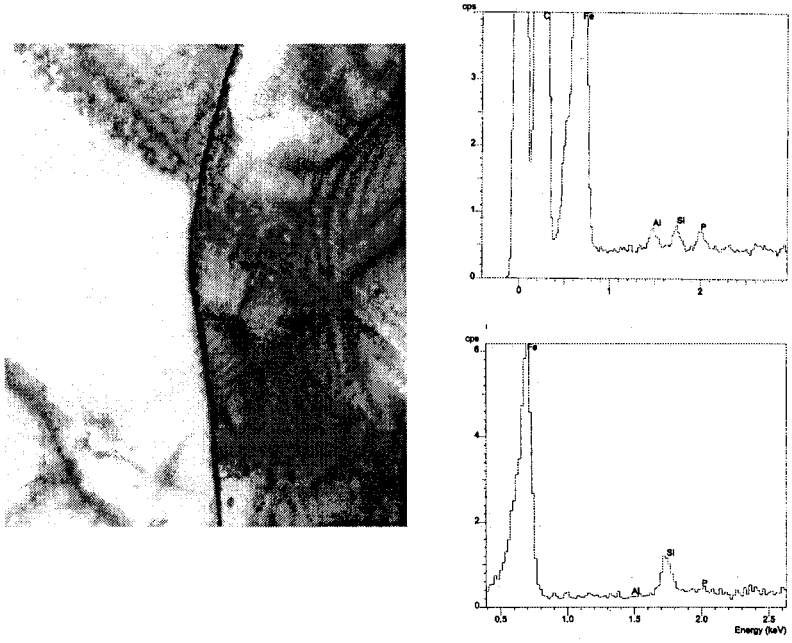

Figure 4.81 - STEM micrographs and the associated XEDS spectra for the batch annealed grade.

results, the influence of the grain boundary extends past a monolayer and the segregant profile is not homogeneous as assumed in many thermodynamical calculations.

Therefore, although the segregation distribution profile will depend on the grain boundary structure, the nature of the segregant and its interaction with the grain boundary, and the extent to which equilibrium has been attained, the grain boundary width for phosphorus segregation in α-iron is taken to be constant for the grain boundaries analyzed. To a first approximation, the grain boundary width is taken to be three times the lattice parameter and the profile of segregant is assumed to be constant. The implication of assuming a more realistic distribution profile, such as a triangular profile, for quantifying the extent of grain boundary segregation, will be more fully explored in the discussion.

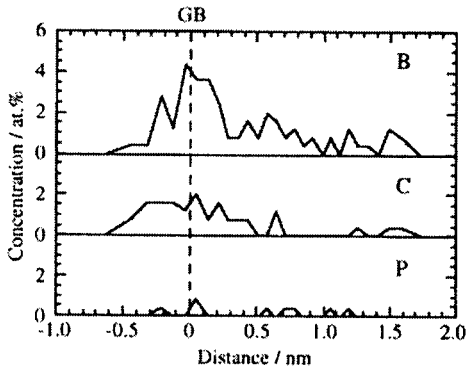

Figure 4.80 - Grain boundary composition for carbon, boron, phosphorus as a function of position across a grain boundary in a low P IF sheet steel determined using a 3-dimensional atom probe combined with field ion microscopy (Seto et al., 1999).

The results of the quantitative transmission electron microscopy for the continuously and batch annealed steel are shown in Tables IV-III and IV-IV. The average values, corrected for beam spreading are 0.129 and 0.428 mol. fraction P. The measured value of segregant for the continuously and batch annealed represent a phosphorus enrichment factor of approximately 120 and 400 compared

Table IV-VIII Measured and Corrected Grain Boundary Segregation Levels for Continuously Annealed IF Sheet Steel

	measured X_P^{ϕ} mol fr.	corrected X_P^{ϕ} mol fr.	$\frac{X_P^{\phi}}{X_P^{B}}$
	$\delta = 3a_o$		
	0.00504	0.127	117
	0.00540	0.138	128
	0.00414	0.098	91
	0.00540	0.1381	128
	0.00486	0.1210	112
	0.00396	0.0925	86
	0.00737	0.2007	186
	0.00701	0.1893	175
	0.00612	0.1609	149
	0.00180	0.0240	22
	0.00414	0.0982	91
	0.00772	0.2120	196
	0.00378	0.0868	80
	0.00504	0.1267	117
	0.00468	0.1153	107
AVE	0.00510	0.1290	119

Table IV-IX Measured and Corrected Grain Boundary Segregation Levels for Batch Annealed IF Sheet Steel

	measured X_P^{ϕ} mol fr.	corrected X_P^{ϕ} mol fr.	$\frac{X_P^{\phi}}{X_P^{B}}$
	$\delta = 3a_o$		
	0.00594	0.155	143
	0.01380	0.405	374
	0.01611	0.478	442
	0.01540	0.455	421
	0.01344	0.393	364
	0.01005	0.286	264
	0.01913	0.574	531
	0.02249	0.680	629
AVE	0.01455	0.428	396

to the bulk value of 0.00108 mol. fraction P. A rough estimate of the enrichment factor for a wide range of chemistries can be made based on the solid solubility segregant in the host solute (Hondros and Seah 1983). An enrichment factor of approximately 100 to 1000 is expected for P in α-iron based on solubility considerations (Figure 4.82). Many of the grain boundaries analyzed were characterized for the grain boundary structure in an associated study (Boyle et al. 1997, Perovic et al. 2001). The general conclusions were that low angle boundaries contained no detectable segregation, while general grain boundaries contained varying amounts of segregant. Not enough low CSL type grain boundaries (e.g. special grain boundaries) were analyzed to obtain any statistically meaningful conclusions with regard to special grain boundaries. Therefore, the grain boundaries measured in the current work are assumed to be general grain boundaries.

Error in quantifying the measured segregant is primarily due to errors in determining the k-factors. As seen, the range for k_{PFe} is approximately ±0.1, which leads to an error of ±0.001 mol. in the measured level of

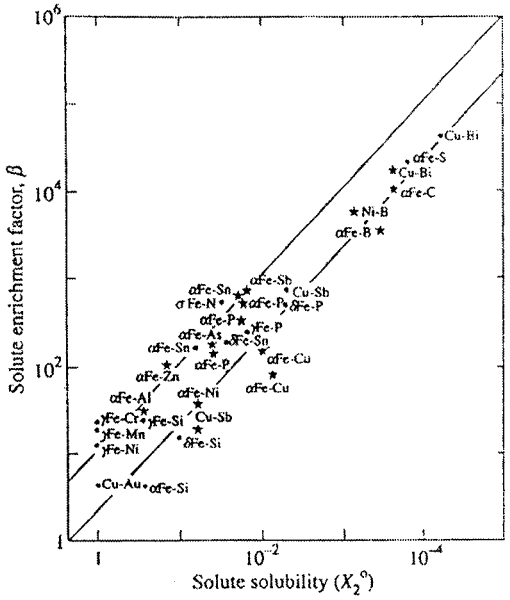

Figure 4.82 - Solute enrichment factor versus solute solubility (Hondros and Seah 1983).

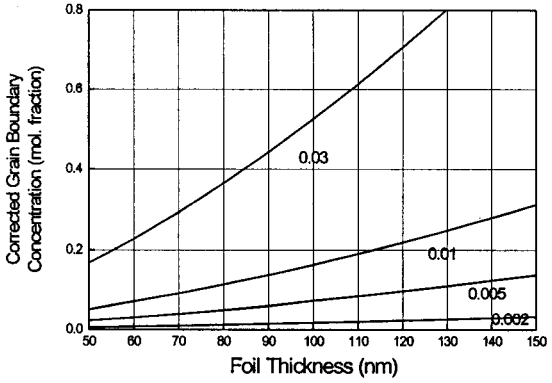

Figure 4.83 - Error in the corrected grain boundary concentration as a function of foil thickness for phosphorus in α-iron, an accelerating voltage of 200 kV, and a grain boundary width of $3a_o$.

phosphorus. Further errors, added when correcting for beam spreading, come from difficulties in determining the foil thickness. In this work, the foil thickness was not measured at every grain boundary analyzed, and therefore the thickness used is only approximately correct for all of the grain boundaries. Thickness inaccuracies lead to errors that are a function of the measured level of phosphorus; as seen in Figure 4.83 a deviation in thickness of ±25 nm for a foil thickness of 125 nm leads to error in the corrected grain boundary concentration of ±0.075 mol. fraction for a measured level of 0.01 mol. fraction and ±0.001 for a measured level of 0.001 mol. fraction. Therefore, foil thickness is a critical parameter for quantifying grain boundary segregation in thin foils. Beam broadening can be assumed negligible for foils that are sufficiently thin. In this case the quantification of grain boundary segregant becomes independent of the foil thickness. This approach has been used by Garratt-Reed and co-workers (Small, Smith and Garratt-Reed 1994, Ikeda et. al. 1995) and Williams and co-workers (Keast et al. 1998).

4.12 Bulk X-ray Texture Measurements

The orientation distributions are plotted using Kocks convention (Wenk and Kocks, 1987) for the Euler angles and equal-area projections in crystal (analogous to pole figures) and sample (analogous to inverse pole figures) space.

Undeformed cold rolled and annealed material was compared to deep drawn material for both the batch and continuous heat treatments. The <111> poles are aligned normal to the plane of the sheet, while the <112> and <110> poles are aligned with the rolling direction. The <110> poles also aligned with the transverse direction.

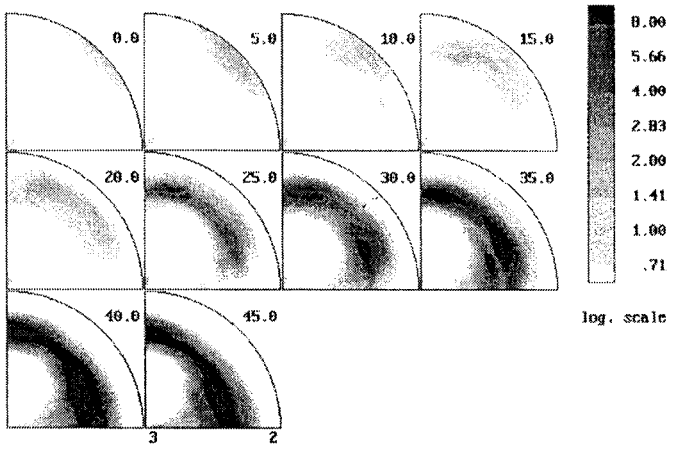

a)batch annealed

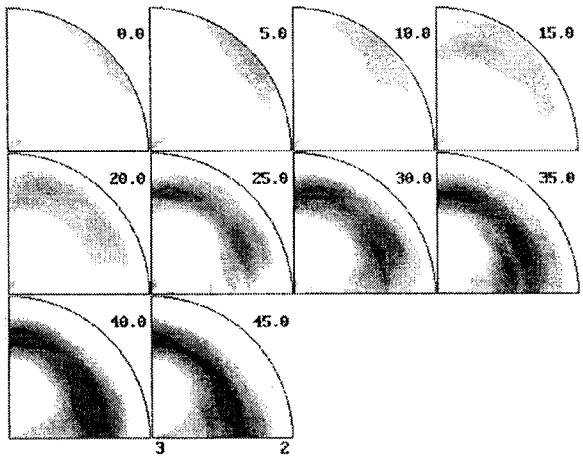

b)continuously annealed

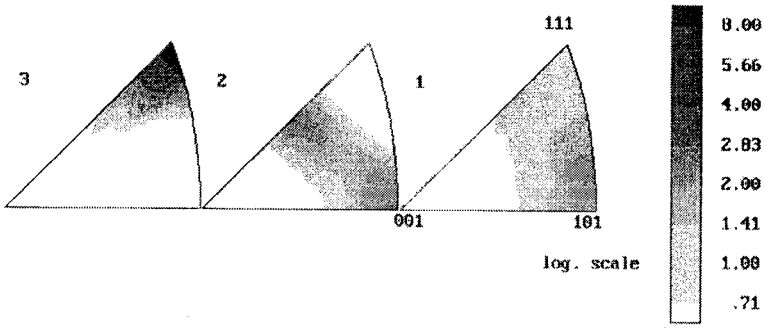

c)batch annealed

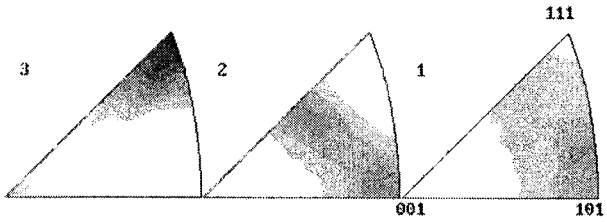

d)continuously annealed

Figure 4.84 -Crystal and sample orientation distributions for batch and continuously annealed as-received material.

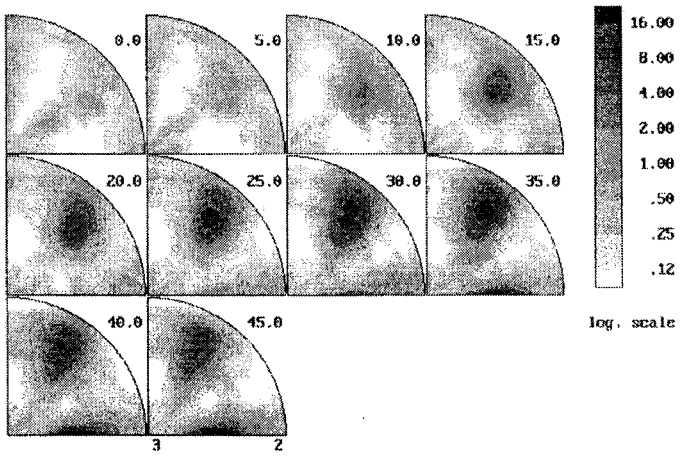

a)batch annealed

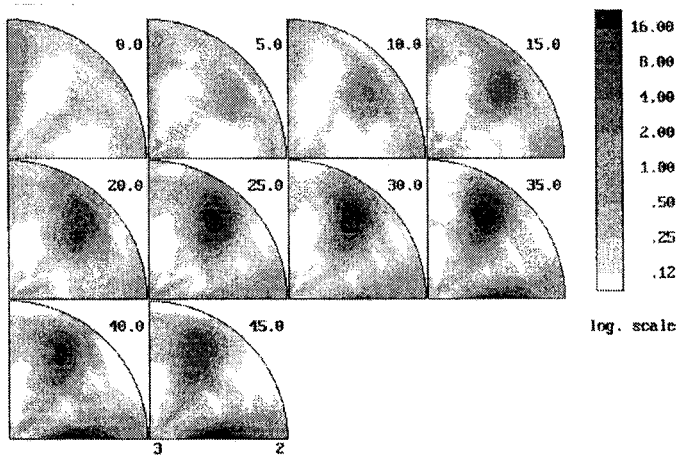

b)continuously annealed

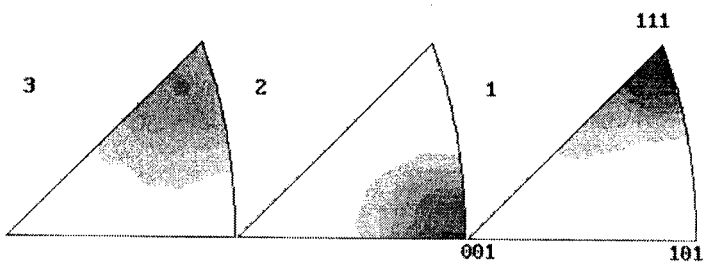

c)batch annealed

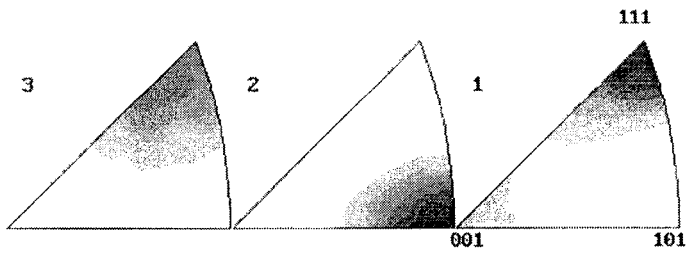

d)continuously annealed

Figure 4.85 - Crystal and sample orientation distributions for batch and continuously annealed deep drawn material.

These relations and the spacial distribution of the relevant texture components are clearly seen by plotting the EBSD data as texture maps (Figure 4.86). The {111}<112> component is stronger than the {110}<110> component. Both annealed sheet have nearly identical recrystallization annealing textures.

Deep drawing rotates the grains such that the <110> poles align with the drawing direction (longitudinal direction), while the <111> and <100> poles align with the circumferential direction (Figure 4.85). These orientations are a combination of the fiber textures expected for axisymmetric deformation in bcc crystals (Mecking 1985); the <110> poles align with tensile axis, while a double fiber texture is expected in compression, the <111>and <100> poles align with the compression axis. Such a compressive fiber texture has been predicted to consist of 70% <111> and 30% <100> (Chin, Mammel and Dolan 1967). A stronger intensity is observed for the <111> fiber (Figure 4.85), qualitatively in agreement with the theoretical predictions. The deep drawing textures are qualitatively the same, very little differences are observed (Figures 4.85c and d).

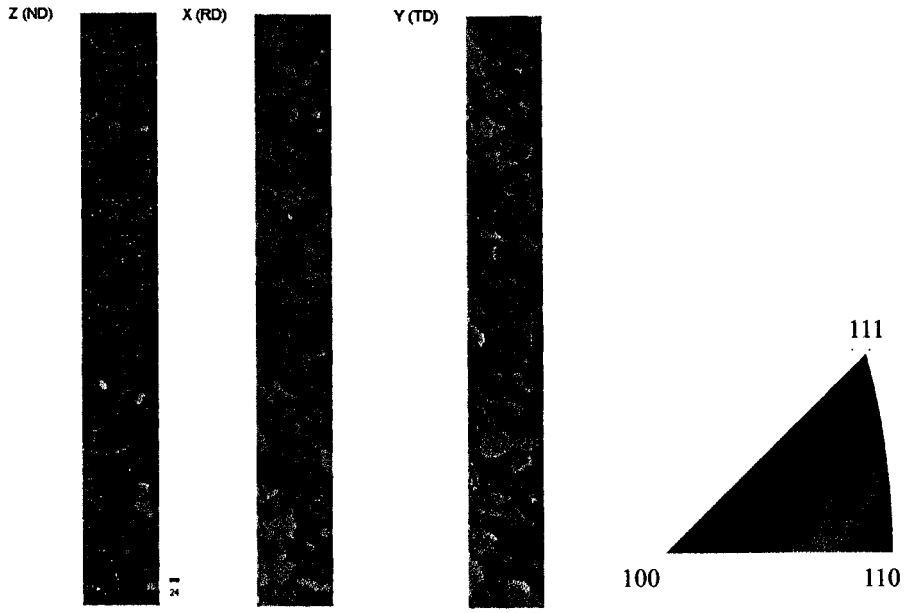

Figure 4.86 - Inverse texture plot from EBSD data for batch annealed material.

4.0

4.13 Synopsis of the Key Results

The salient features of the results section are summarized:

1) No differences were observed in the grain size, morphology or orientation distributions or the mechanical properties (including work hardening behaviour, strain evolution with deep drawing, or circumferential residual stresses of the deep drawn cups) between the continuously annealed and batch annealed rephosphorized grades. The DBTT for undeformed material tested in uniaxial tension was the same for both annealing treatments (~-196 °C), whereas transition temperatures for deep drawn cups (draw ratio 2.2) were vastly different (-11 °C versus 21 °C) for the annealing treatments. However, the level of segregant at the grain boundary measured with analytical electron microscopy was different; grain boundaries of the batch annealed steel were enriched with phosphorus by a factor of 1.5 as compared to the continuously annealed steel. Differences in fracture behaviour can therefore be attributed to the different segregation levels, but the effect is much less on undeformed material.

2) Draw ratio has a large effect on transition temperature (Figure 4.52); the transition temperature increased from -196 °C for undeformed material to 4°C for cups drawn to a draw ratio of 2.4. It has not been clarified to date whether or not the increase in transition temperature with draw ratio is due solely to work hardening as has been assumed in all qualitative graphical attempts (e.g. using the Davidenkov approach) to rationalize the results of the cup expansion test. Two other mechanisms have been proposed to account for the increased embrittlement with draw ratio; they are grain shape and deep drawing induced macroscopic residual stresses. No quantitative experimental work had previously been done to explore these proposals. Therefore, a series of experiments were designed to clarify whether grain shape or residual stresses control the susceptibility to intergranular fracture. All experimental results point to influence of residual stresses being insignificant for CWE.

3) Material predeformed by cold rolling, up to the same effective strain as the deep drawn cups with a draw ratio of 2.2, was tested in uniaxial tension to obtain the DBTT. The cold rolled material became less brittle with deformation in both the rolling and transverse directions. These results indicate that the fracture stress is more sensitive to predeformation than the flow stress. The decreased susceptibility to embrittlement was not due to decreased thickness, as samples chemically thinned prior to testing did not show any significant change in fracture behaviour. Therefore, it can be concluded that the strain path has a dominant effect on CWE. Cold rolling does not induce macroscopic residual stresses, therefore the residual stresses do not factor into the analysis. Although flow stress anisotropy is present in the plane of the sheet, the anisotropy factor stays constant with deformation as measured for plane strain rolling, which implies that there is not any significant kinematic hardening.

4) Local misorientation between the grains determines the grain boundary structure which in turn controls the local chemistry and fracture strength. Fracture path analyses using EBSD clearly show that low angle boundaries are resistant to intergranular fracture. Special grain boundaries are less resistant to IGF than low angle boundaries but more resistant to IGF than general grain boundaries. Therefore, the distribution of grain boundary structures and their influence on embrittlement and fracture processes must be considered.

These results form a basic understanding of CWE that allow for the construction of an intergranular fracture model and a kinetics of segregation model. The models are designed to account for the key microstructural features that control the fracture process and to give predictive capabilities that allow the results obtained in this thesis and those in the literature to be understood. The fracture model primarily deals with intergranular fracture as this was the predominant mode of brittle fracture for the grade of steel studied. The key microstructural mechanisms responsible for CWE that can be extracted from the summary of the prime results are i) the local grain boundary cohesive strength which is controlled by the local chemistry and structure, and ii) the grain shape with respect to the applied stress. When the grains become flattened, the intergranular fracture path becomes much less tortuous, which in turn leads to an increased probability for IGF along the flattened grains. As well, the large residual stresses present in the deep drawn material have no apparent influence on CWE, which is at first not intuitive, but will be justified in the discussion. Based on these observations a model is developed to predict the occurrence of intergranular fracture as a function of grain shape for strain paths commonly used in sheet metal forming. Pure deep drawing is focused on as this deformation path is most susceptible to IGF. The evolution of the yield surface for the various strain paths modeled is also required as brittle fracture is competing with plastic flow. When the yield and fracture surfaces intersect for a given predeformation, temperature or strain rate brittle intergranular fracture is predicted.

5.0 DISCUSSION

Grain shape, crack size, and the local grain boundary chemistry are key variables controlling CWE. Accordingly, this chapter unfolds in two sections; the first develops a fracture model that allows the IGF stress to be predicted as a function of the strain path and hence grain shape, while the second develops a kinetic model to predict the levels of segregation for isothermal and non-isothermal heat treatments. The results are discussed within the frameworks constructed by the fracture and segregation modeling. In order to be utilized, the modeling is related to both current results and data in the literature, some of which were reviewed in Chapter 2. This thesis has attempted to clarify the important variables affecting the structural aspects of CWE, so a quantitative approach can be used to predict the occurrence of CWE for industrial forming and annealing practices.

5.1 Introduction

Significantly different results were obtained when material predeformed by cold rolling and then tested in uniaxial tension was compared to circumferentially expanded deep drawn cups. Material predeformed by cold rolling and tested in the plane of the sheet became less susceptible to IGF, while material predeformed by deep drawing became significantly more susceptible to IGF. Both deformation paths had the same level of effective strain, $\bar{\varepsilon} \approx 0.65$, and flow stress, ~640 MPa at, room temperature. Therefore, it is evident that the resulting work hardening alone does not control the phenomenon of CWE. As well, cups with a draw ratio of 2.2 (e.g. $\bar{\varepsilon} \approx 0.65$) were tested with a ram speed of 0.01 mm/s, resulting in the same strain rate as the tensile tests. Therefore, the difference in transition temperatures is not simply due to strain rate hardening. Transition temperatures of the cold rolled material is shifted to below -196°C, while that of the deep drawn cups with a draw ratio of 2.2 ($\dot{\varepsilon} = 0.00025\,s^{-1}$) was -14°C. As well, samples chemically thinned to the same thicknesses as the cold rolled samples and tested at -196°C did not shown any significant decrease in transition temperature. These results suggest that there is a significant microstructural variable that controls a steel's susceptibility to CWE which is appreciably different for the strain paths tested.

Therefore, in order to understand CWE consideration must be made of how the competition between plastic flow and brittle fracture is affected by different modes of predeformation. The most likely possibilities to consider are the effect of grain shape on intergranular fracture, possible anisotropic or kinematic plastic work hardening, or bulk macroscopic residual stresses which could affect both the brittle fracture and plastic flow behaviour. The work hardening of the cold rolled material is roughly isotropic as the ratio of the flow stresses in the rolling and transverse directions is not appreciably changed with deformation and as the flow curves follow the flow behaviour as measured in uniaxial tension (Figure 4.15). As well, no bulk macroscopic

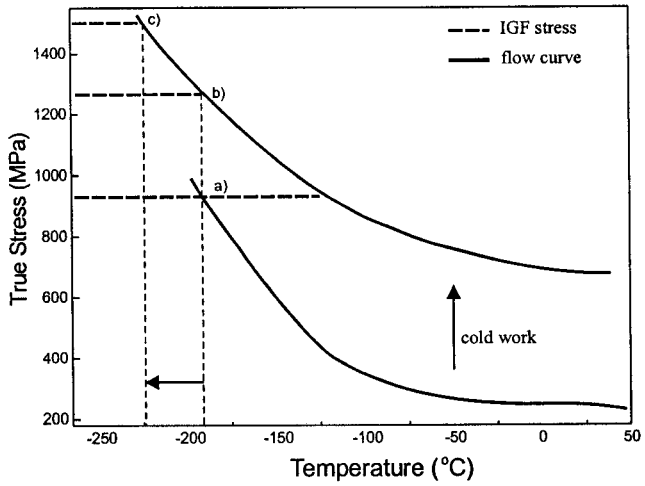

Figure 5.1 - Davidenkov diagram depicting the DBTT for undeformed material a). For the DBTT to remain constant with cold work the IGF stress must increase the same amount as the flow stress b). For a downward shift in the DBTT the IGF stress must increase more than the flow stress c).

residual stresses are developed for cold rolling. Therefore, based on the results from the cold rolled steels alone we can conclude that the grain shape has a dominant effect on CWE. To succinctly convey the main findings throughout the discussion, a graphical representation of the competition between plastic flow and brittle fracture is plotted in two dimensions, stress versus temperature space, by using the concept proposed by Davidenkov (1936). These so called Davidenkov plots depict the flow and fracture stress as a function of temperature. The IGF stress is independent of temperature and is therefore plotted as a straight line, while the flow stress, for a given level of deformation, is plotted as a curve, and will be referred to as the flow curve throughout the discussion. The intersection of the fracture stress and flow curve gives the ductile-to-brittle transition temperature.

The Davidenkov plot can now be used to explain the key results obtained from the tensile tests on the undeformed and predeformed material. The effect of grain shape is considered to be dominating because the intergranular fracture stress is shifted by the predeformation more than the flow stress. As seen from the Davidenkov plot (Figure 5.1), the fracture stress has to increase more than the flow stress for a decrease in transition temperature with increased flow stress (case c in Figure 5.1). Considerable effort is therefore made towards modeling the effect of grain shape on intergranular fracture.

5.2 Fracture Modeling - The Role of Grain Shape on Intergranular Fracture

The occurrence of IGF during sheet metal forming of interstitial-free steels is an example of the competition between plastic flow and a brittle fracture process. To predict this type of failure, it is necessary to consider the key microstructural mechanisms controlling the brittle fracture and plastic flow for the operative stress state and strain history. Deformation processing introduces anisotropy in the microstructure, which is then reflected in both the fracture and flow properties. The flow behaviour depends on the strain path and the subsequent crystallographic texture and subgrain structure, the grain size (and to a lesser extent the grain shape), and the residual stresses that develop during deformation. From a structural viewpoint, IGF behaviour depends on the grain size (Almond, Timbres and Embury 1971, Nakamura and Sakaki 1970) and shape, the grain boundary structure (Lim and Watanabe 1990), the associated local chemistry, and the local stress state in the vicinity of the grain boundary. During forming of IF sheet steels, large changes in the grain shape can precede IGF.

Although some fracture models exist which incorporate grain shape (Lim and Watanabe 1990, Zok 1988), no general models have yet been developed which take grain shape into account for the wide range of conditions encountered in sheet metal forming. Bramfitt and Marder (1977) have shown that the intergranular delaminations that occur in the plane of rolled plate in a low carbon steel (high purity Fe-1.0 wt.%. Mn alloy) are a function of the aspect ratio of the elongated grains. For IF sheet steels, it has been shown that increasing the severity of deep drawing increases the ductile-to-brittle transition temperature (section 2.1.5). It has been noted that the grain shape must play a role in the propensity for IGF, but contributions from the flow stress and the grain shape have not yet been differentiated in current descriptions.

In this work, a simplified static fracture mechanics approach was used to obtain an intergranular fracture stress that depends on the strain path. The evolution of the fracture and yield surfaces in the plane of the sheet for a given strain path were then mapped in stress space. The resulting forming maps, depicting the competition between fracture and flow, linked experimental conditions that promote CWE to the controlling microstructural feature (the grain shape). The results demonstrated that in order to predict the ductile-to-brittle transition temperature, the effect of grain shape on the IGF stress must be considered.

5.2.1 Basis of Model

The IGF stress was modeled as a function of the geometry of the grain shape - the geometrical parameters modeled as the grains changed shape with plastic deformation were the length of the crack facet, the inclination of the crack facet and the angle of crack deflection. The mode of fracture was assumed to be entirely intergranular brittle. It was also assumed that the plastic energy dissipated during the fracture process was unaffected by the amount of prior cold work. For simplicity, isotropic linear elasticity was used and therefore the elastic compatibility stresses near the grain boundary were ignored.

Two-dimensional hexagonal grains of the equivalent size and shape were used to model the microstructure. Two initial grain configurations were modeled, one with the apex of the hexagon pointing in the direction of the major applied stress (grain orientation 1) and the other with a grain boundary facet perpendicular to the major applied stress (grain orientation 2) (see Figure 5.2). The idealized grains were then used to model the change in grain shape caused by proportional deformation paths common in forming operations, e.g. pure drawing ($\varepsilon_2 = -\varepsilon_1$), uniaxial tension ($\varepsilon_2 = -0.5\varepsilon_1$), plane strain deformation ($\varepsilon_2 = 0$), and balanced biaxial stretching ($\varepsilon_2 = \varepsilon_1$). The grains of a deep drawn cup are compared to the simplified two-dimensional microstructure as shown in Figure 5.3.

Experimental work indicates that the IGF stress in pure iron is grain size dependent but not dependent on temperature or strain rate, as long as the initiation is not controlled by twinning (section 2.2.6). These results suggest that the IGF stress for relatively pure iron can be modeled with a propagation controlled criterion. Therefore, a crack one facet in length was assumed to be initiated at the grain boundary by a stress

concentration. The stress concentration is associated with a concentrated shear band or dislocation pile-up (Zener 1949, Stroh 1954) caused by micro-yielding within individual grains (see section 2.2.4). The initiated crack must deflect at a triple junction in order for the crack path to follow the grain boundary. For continued propagation, a criterion for fracture must be locally attained on one of the adjacent grain boundary planes. An energy criterion is the obvious choice. A critical strain energy release rate or a critical mode I stress intensity factor could be chosen. A critical value of the mode I stress intensity was chosen as the condition necessary for fracture, although the choice of a critical strain energy release rate gives essentially the same results.

The initiated crack is under mixed-mode loading, as the grain boundary facet is not necessarily perpendicular to the applied stress. A state of plane stress was assumed as the through-thickness stress in most sheet forming operations is a few percent of the flow stress (Duncan 1985). For mixed-mode loading, the resolved nominal mode I (K_I) and mode II (K_{II}) stress intensity factors for the initiated crack are given by,

$$K_I = (\cos^2\theta + \beta\sin^2\theta)K_{Io} = f_1(\theta,\beta)K_{Io} \tag{5.1}$$

$$K_{II} = (\cos\theta\sin\theta)(1-\beta)K_{Io} = f_2(\theta,\beta)K_{Io} \tag{5.2}$$

$K_{Io} = \sigma\sqrt{\pi a}$ is the nominal mode I stress intensity when $\theta = 0$ for a through-thickness crack in an infinite plate, σ is the major applied stress, a is the half crack length, θ is the angle formed between the crack and the normal of the larger applied stress (Figure 5.2), and β is a biaxiality ratio equal to σ_2/σ_1.

To determine the local stress intensities for the deflected crack, solutions to the kinked crack problem (Bilby, Cardew and Howard 1977, Lo 1978, Cotterell and Rice 1980) can be used. An approximate solution for cracks kinking out of their own plane can be obtained by using the stress field associated with the incipient crack (Cotterell and Rice 1980, Lawn 1993). This approximation is valid when the kinked portion of the crack is much smaller than the incipient crack, yet deviates from the solutions presented in the literature at large deflection angles and high transverse stresses (Cotterell and Rice 1980). As the kinked crack grows, the stress field based on the initial crack is less accurate, but this is not of any consequence as the first deflection is taken as the critical event. When the main crack has far field loading resolvable as K_I and K_{II}, the local mode I stress intensity, k_I, at the crack tip is given by,

$$k_I = a_{11}K_I + a_{12}K_{II} = (a_{11}(\phi)f_1(\theta,\beta) + a_{12}(\phi)f_2(\theta,\beta))K_{Io} = Q_I K_{Io} \tag{5.3}$$

The coefficients (Cotterell and Rice 1980) are given as,

$$a_{11} = \frac{3}{4}\cos\frac{\phi}{2} + \frac{1}{4}\cos\frac{3\phi}{2} \tag{5.4}$$

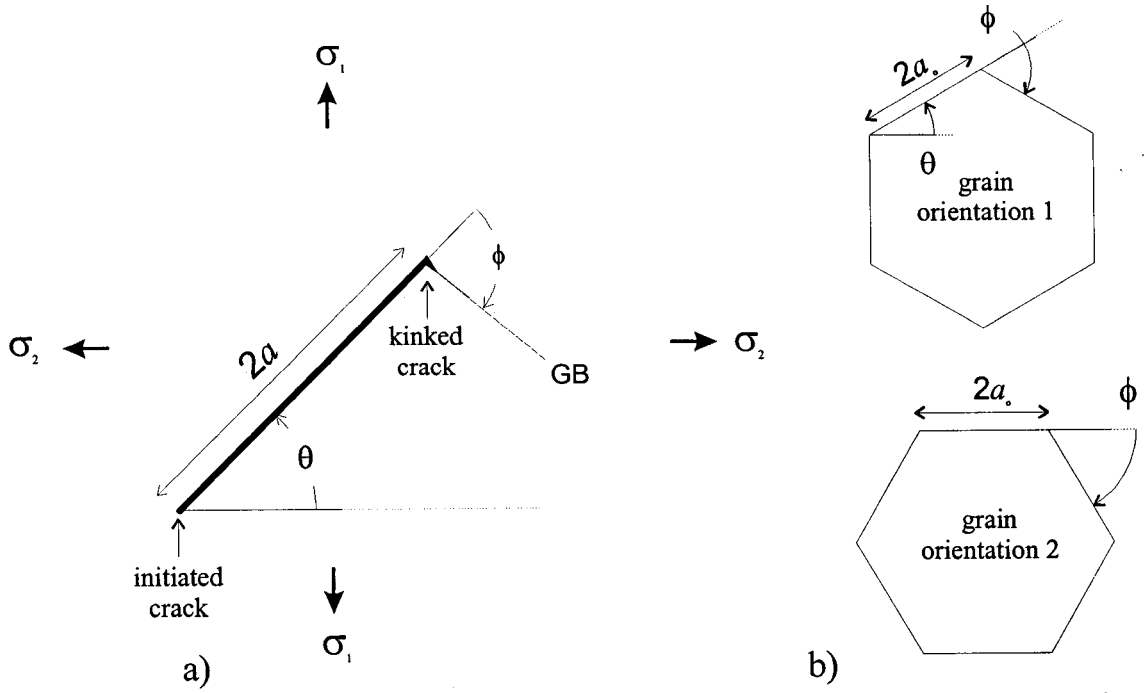

Figure 5.2 - a) An initiated crack in an infinite isotropic elastic medium b) Two orientations were used to model the initial geometry of the hexagonal grains.

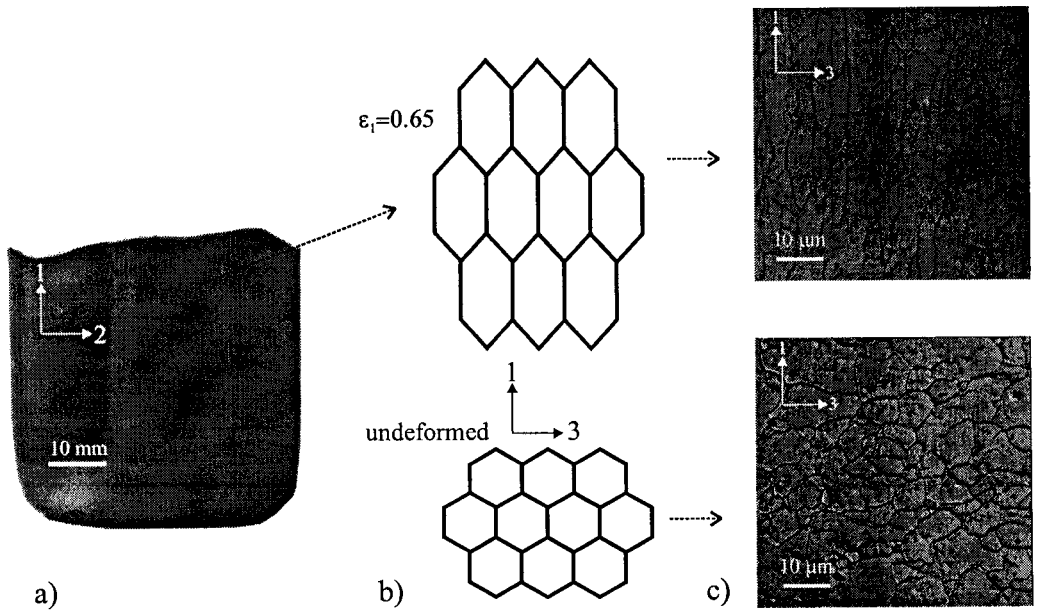

Figure 5. 3 - a) Deep drawn cup of rephosphorized IF steel sheet b) Idealized microstructure for two different levels of strain and c) the associated optical micrographs of the microstructure (1 and 2 are the directions of major and minor strains respectively in the plane of the sheet, and 3 is the through-thickness direction).

$$a_{12} = -\frac{3}{4}\left[\sin\frac{\phi}{2} + \sin\frac{3\phi}{2}\right] \tag{5.5}$$

where ϕ is the angle of deflection for the initiated crack (Figure 5.2). For crack propagation, the driving force acting on the kinked crack must reach the critical value. The critical stress intensity, k_{CR}, for the k_I criterion is given by,

$$k_{CR} = k_I = a_{11}K_I + a_{12}K_{II} \tag{5.6}$$

Equations 5.3-5.6 were used to predict the IGF stress as a function of strain according to,

$$\sigma_F = \frac{k_{CR}}{Q_1\sqrt{\pi a}} \tag{5.7}$$

The half crack length, a, and Q_1 are functions of the applied strain. The exact relation depends on the strain path being modeled. For each deformation path under consideration, the grain shape is followed as a function of strain (for example, see Figure 4.3). For any level of strain for a given deformation path, the IGF stress, equation 5.7, can be solved for any applied biaxiality in both primary directions in the plane of the sheet.

5.2.2 Flow Behaviour

To predict the occurrence of IGF during forming operations, the flow behaviour of the steel must be included in the analysis, as flow and fracture are in competition. To demonstrate the applicability of this approach, the plastic flow behaviour was modeled with Hill's 1950 (Hill 1950) planar isotropic yield criterion as discussed in section 3.6. The work hardening was assumed to be isotropic. Isotropic hardening implies that the yield surface expands symmetrically about the initial yield surface for all deformation paths. Therefore kinematic and anisotropic hardening were not considered. Non-isotropic hardening is possible for IF sheet steels, but the results from cold rolled steel tested in the relevant quadrant of the yield surface (e.g. the tensile quadrant) suggested that the hardening was nearly isotropic. Further experimental work would be necessary to determine the evolution of the flow surface for different strain paths.

The influence of strain, temperature, and strain rate on the flow behaviour can be conveniently represented by a constitutive equation. An example of a constitutive relation used to model cold forming simulations for IF sheet steel is given by Lin and Wagoner (1986),

$$\bar{\sigma} = K_S(\bar{\varepsilon} + \varepsilon_o)^n\left(\frac{\dot{\varepsilon}}{\dot{\varepsilon}_o}\right)^m\left(1 - \kappa(T - T_o)\right) \tag{5.8}$$

where K_S is the strength coefficient, ε_o is the strain associated with predeformation, n is the strain hardening exponent, $\dot{\varepsilon}$ is the strain rate, $\dot{\varepsilon}_o$ is the base strain rate, m is the strain rate sensitivity index, T is the temperature, T_o is a reference temperature, and κ is a temperature coefficient. This type of constitutive relation is not applicable for the large range of temperatures used for the CET as n and m are not independent of the temperature. The flow behaviour for the RP IF steel at ambient temperatures and a strain rate of 0.00025 s^{-1} was found to follow a power law strain hardening relation with $K_S = 716\,\text{MPa}$, $\varepsilon_o = 0.00$ and $n = 0.225$.

5.2.3 Results of Modeling

To calibrate the model, the intergranular fracture stress for an undeformed continuously annealed rephosphorized IF sheet steel was measured in tension at -196°C and found to be between 940-1020 MPa. A scanning electron micrograph of a predominantly intergranular fracture surface from a specimen fractured at 980 MPa without any associated plasticity is shown in Figure 5.4. The measured intergranular fracture stress compares favorably with the results presented by Yu-Qing and McMahon (1987) and Nakamura and Sakaki (1970). Yu-Qing and McMahon (1987) report an IGF stress, for a Fe-P alloy with comparable amounts of phosphorus, between 750-1000 MPa depending on the length of decarburization, and a transgranular cleavage fracture stress of 1350 MPa. Transgranular fracture can be expected to compete with IGF when the IGF stress is increased by changes in grain morphology, decreased amounts of segregation, or less potent embrittling elements. A fracture stress of 950 MPa is obtained if the data presented by Nakamura and Sakaki (1970) is extrapolated to account for the grain size of the steel used in this work.

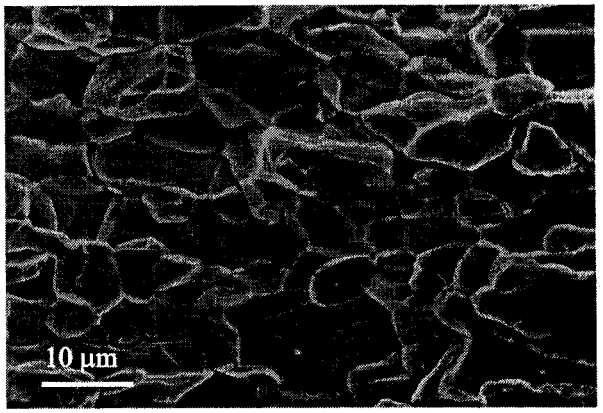

Figure 5.4 - Predominantly intergranular fracture in a continuously annealed rephosphorized IF sheet steel tested in uniaxial tension in liquid nitrogen (-196°C).

The proposed fracture criterion depends on a local critical stress being reached at some distance ahead of the kinked crack on the grain boundary plane. Unlike the constant maximum principal stress criterion usually assumed for IGF (Kantidis Marini and Pineau 1994, Murr 1975, Nakamura and Sakaki 1970), the chosen criterion depends on strain, as the resolved stresses and the local stress intensities depend on the geometry of the grains.

5.2.3.1 Shape of the Intergranular Fracture Map

Differences in the magnitude of the IGF stress are predicted between the two initial grain orientations. For grain orientation 2 (refer to Figure 5.2), the fracture stress was not a function of the applied biaxiality as an initiated crack parallel to the applied stress does not cause a stress concentration. In this case, the fracture

envelope was represented by a horizontal and a vertical line (Figure 5.5). For grain orientation 1, the fracture stress was a function of the biaxiality. Therefore, the orientation of the initiated crack, with respect to the applied stress, is predicted to have an effect on the stress necessary for fracture during sheet metal forming. The most likely configuration for the initiated crack will depend on the grain shape with respect to the operative stress state. Assuming cracks are initiated in both grain orientations, an envelope consisting of the lowest fracture stress is applicable; alternatively, the average can be chosen as the fracture stress (Figure 5.5).

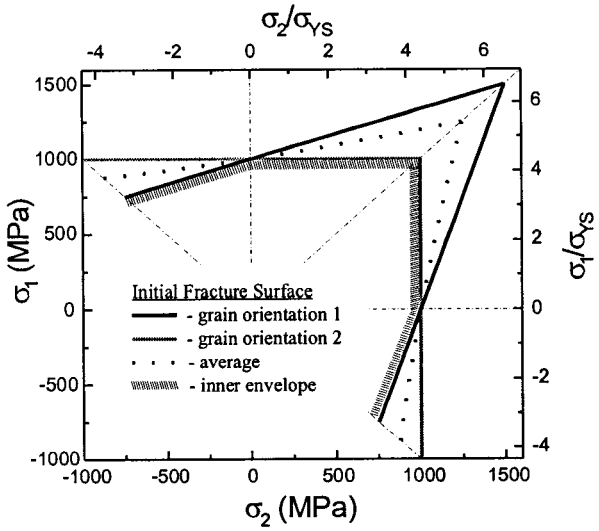

Figure 5.5 - Fracture maps for the undeformed microstructure for grain orientation 1, grain orientation 2, the minimum and average fracture

Very few studies have investigated the effect of stress state on IGF. Kantidis et. al. (1994) concluded that effect of biaxiality on the measured IGF stress was due to increased plastic constraint. They state that as the yield stress must be reached for IGF, a biaxial state of stress will increase the stress required for IGF as the yield surface follows the von Mises criterion. As explained in section 2.2, the yield stress does not have to be reached for IGF. This leads to the possibility that the IGF stress is dependent on the state of stress, as the grain facets, on average, are not perpendicular to the applied stress. In fact, the only other study, to the author's knowledge, to examine the effect of stress state on IGF, besides those from Pineau's group at École de Mine (Kantidis, Marini and Pineau, 1994, Kantidis et al. 1994, Yahya et al 1998) is that of Zok (1988) (see Figure 2.28). If Zok's data is examined carefully, we see that there is an apparent contradiction. For the bismuth embrittled copper tested under hydrostatic pressure, a constant maximum stress criterion is found. If the tests are stopped before localization, and tested at room temperature, the IGF stress is found to have increased as predicted by the grain shape change. To reiterate, the tests conducted under hydrostatic pressure tell us that the IGF stress is constant and does not change with deformation, while the uniaxial tests tell us there is a significant change in fracture stress with changes in grain shape. This apparent contradiction can be rationalized by recognizing that the intergranular fracture surface is not constant and is a function of stress state. As the hydrostatic pressure, p_{HYD}, is increased, the absolute magnitude of positive stress required for yield in uniaxial tension remains constant. For a constant maximum fracture stress criterion, the applied uniaxial stress must reach $\sigma_{IGF} - p_{HYD}$ for IGF (Figure 5.6a).

Next, consider fracture criteria that depend on grain shape. For a fracture criterion that is not a function of stress state, the IGF stress must increase as the grains change shape in uniaxial tension (Figure 5.6a). If the fracture criterion depends on the stress state as predicted by the modeling, a situation is possible where the IGF

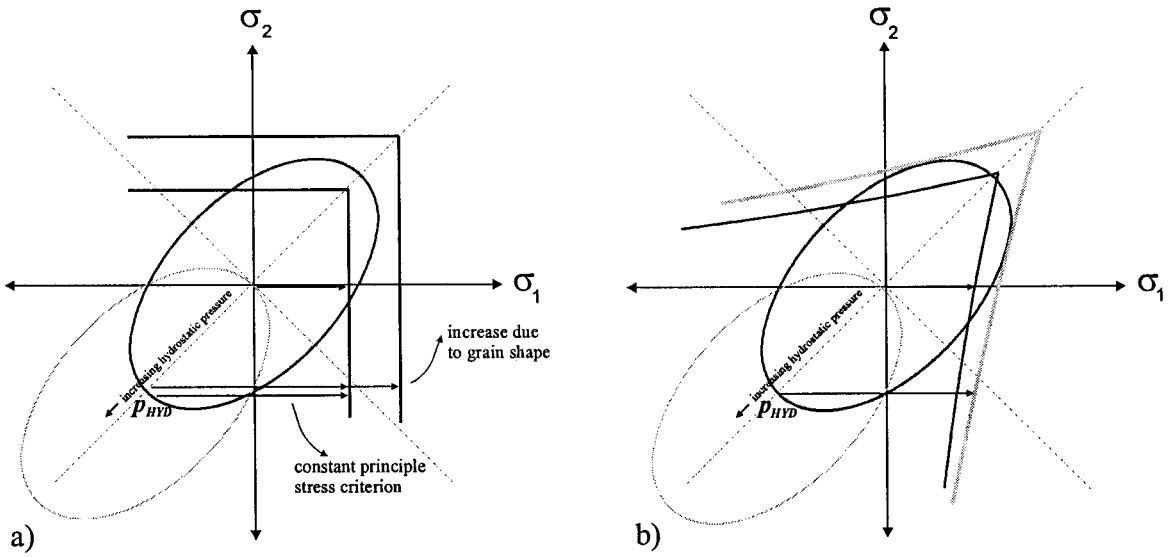

Figure 5.6 - Intergranular fracture criteria and the effect of hydrostatic pressure on the IGF stress.

stress remains constant when tested in uniaxial tension under a superimposed hydrostatic pressure and increases when tested in uniaxial tension with no superimposed pressure (Figure 5.6b). Figure 5.6 is a two-dimensional projection of the three dimensional situation just described (i.e. the yield surface is not kinematically hardening). Therefore, the apparent contradiction of Zok's experiments give evidence supporting an IGF surface that evolves with deformation and is a function of the stress state. It is evident that more research must be done in this area to clarify these points.

5.2.3.2 Applications in Metal Forming - Evolution of Fracture Maps with Strain

Failure maps illustrate the competition between fracture and flow, and can be depicted in a variety of stress or strain spaces (Glover, Duncan and Embury 1977). For sheet metal forming, it is convenient to use principal strain space, traditionally used for forming limit diagrams, or principal stress space, the conventional way of representing plane stress loading. These two spaces were chosen to display the evolution of the intergranular fracture and yield surfaces, allowing changes in temperature, strain rate or strain path (stress state) to be accounted for in the competition between fracture and flow for various idealized forming operations.

5.2.3.3 Proportional Strain Path, Primary Forming Operations

The evolution of the intergranular fracture stress (or equivalent strain) for proportional strain paths common in sheet metal forming was compared to the limit strain as adapted from Raghavan (1991) for an IF sheet steel (Figure 5.7). The limit strain gives an indication of the level of useful strain prior to localized necking in the sheet. The results indicate that the IGF stress (represented as an equivalent strain) increases at a greater rate than the applied strain in the direction of the primary strain (Figure 5.7), and necking and ductile fracture are predicted to occur well before IGF. Intergranular fracture is therefore not expected for proportional straining

under typical forming conditions. This suggests that a change in strain path or stress state, or a secondary forming operation is required for IGF. For example, during deep drawing, buckling of material in the flange, caused by insufficient hold down pressure, led to IGF down the length of the drawn cup (Figure 5.8).

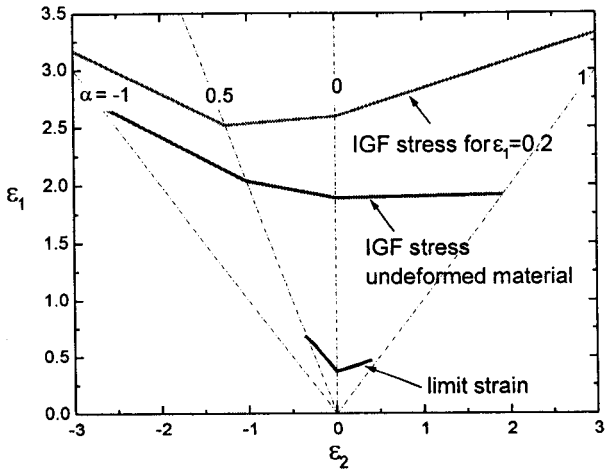

Figure 5.7 - Forming limit diagram for a RP IF steel. The IGF stress, expressed as an equivalent strain, increases in the direction of the major applied strain

The results for the uniaxial strain path ($\alpha = -0.5$) can be examined in more detail. If general yield precedes the stress required for intergranular fracture, the rate of work hardening must be sufficient such that the flow stress reaches the increasing IGF stress; otherwise another fracture mechanism intervenes. This predicted increase in the intergranular fracture stress with uniaxial strain was found for a temper embrittled low alloy steel (Kantidis et. al. 1994), and a Cu-Bi alloy predeformed in tension under hydrostatic pressure and then tested in tension under atmospheric conditions (Zok 1988). The results of a uniaxial tensile test at -187°C on the continuously annealed IF steel sheet further illustrate this concept; the steel yielded and work hardened until IGF occurred at a true strain of 0.15 (Figure 5.9a). The intergranular fracture surface appears different compared to that where no plastic deformation occurred (Figure 5.4); the grains are elongated as one would expect after this amount of strain (Figure 5.9b). Therefore, there is a physical basis for the increase in the intergranular fracture stress with uniaxial strain which must be considered when studying IGF.

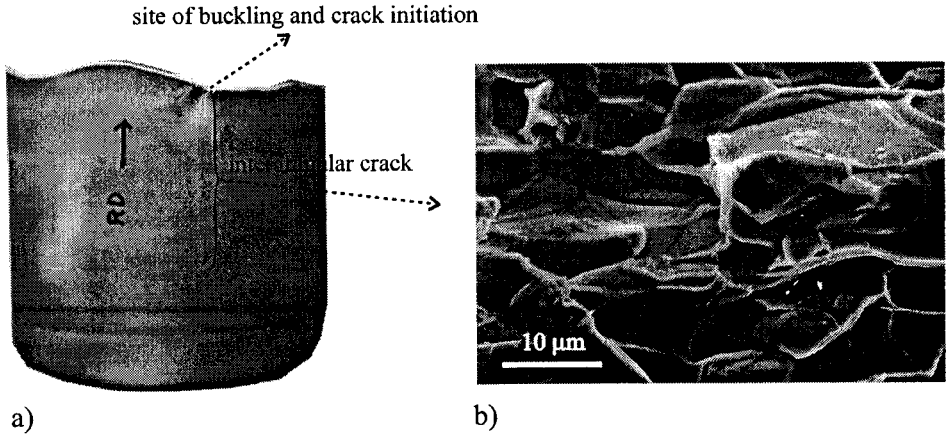

Figure 5.8 - Buckling of batch annealed rephosphorized IF sheet steel during deep drawing (drawing ratio=2.2) leading to an intergranular crack down the cup wall and b) the associated micrograph of the fracture surface.

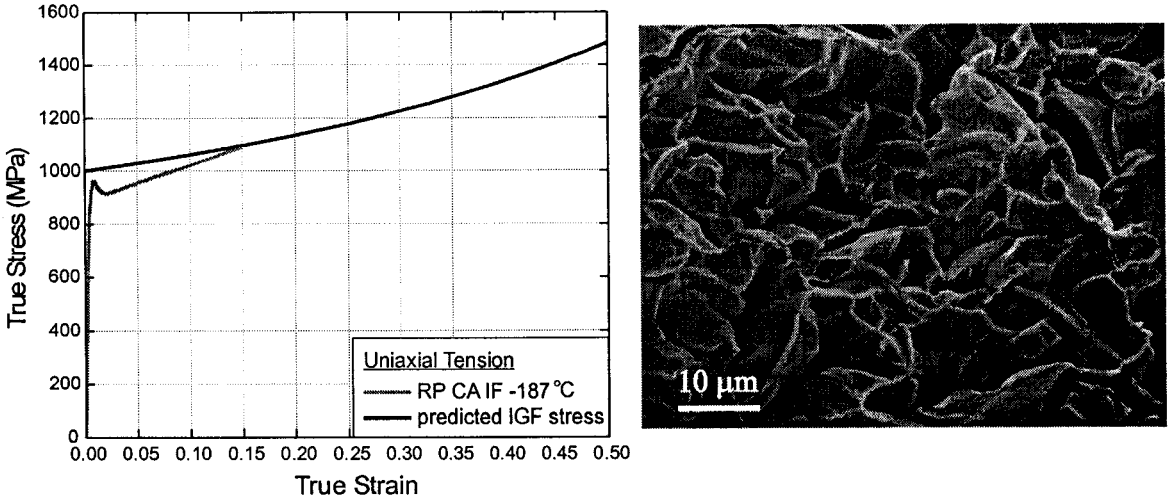

Figure 5.9 - Uniaxial tensile test data for continuously annealed IF sheet steel tested at -187°C and the predicted evolution of the IGF stress, and the associated scanning electron micrograph of the fracture surface.

5.2.3.4 Changes in Strain Path, Secondary Forming Operations

To develop a better understanding of the conditions necessary for intergranular fracture, maps in stress space were constructed, taking into account the possibility of a change in strain path or a secondary forming operation (Figures 5.10a-d). Proportional loading was assumed for the primary forming operation and the yield surface expanded according to Hill's 1950 yield criterion and isotropic hardening. The intergranular fracture surface also evolved according to the grain shape change associated with the primary forming operation. The secondary forming operation assumes the possibility of any combination of in-plane stresses. Therefore, IGF is predicted if the yield surface intersects or is sufficiently close to the fracture surface. Failure maps are plotted in Figure 5.10 for pure drawing, cold rolling, uniaxial tension, and biaxial stretching as the primary forming operations.

The results for pure drawing indicate the intergranular fracture stress increases in the longitudinal direction and decreases in the circumferential direction with deep drawing deformation. At a primary strain of 0.6, intergranular fracture is predicted to occur in the circumferential direction at ambient temperatures over a range of biaxialities, from $\beta = 0$ to $\beta = 1$ with the primary tensile stress in the circumferential direction. For cups drawn to a draw ratio of 2.2 with die 1, the true primary strain at the top of the cup is 0.56, while the DBTT is -11°C. Although the yield surface does not intersect the fracture surface for all biaxiality ratios less than one, brittle intergranular fracture is still possible; as mentioned the yield surface must be sufficiently close to to the fracture surface. The same competition between plastic flow and intergranular fracture occurs during the secondary forming operation. This competition is observed experimentally for cups fracturing just below the transition temperature. These cups fracture in a completely brittle manner after some amount of plastic deformation (Figure 4.63), which depends on the ability of the flow stress to surpass the intergranular fracture

stress as it evolves with the secondary deformation (Figures 5.9 and 5.11). The secondary competition is depicted for uniaxial tension in the circumferential direction after cup drawing to a true primary strain of 0.68 (Figure 5.11).

Richards, Reid and Smallman (1968) performed low temperature uniaxial tension tests at -196°C on hot-rod rolled high purity iron, heat treated for one hour at 720°C and quenched in brine at 0°C. Specimens did not recrystallize and as a result the grains are elongated along the rod axis. The grain shape for hot-rod rolled material is the same as material deformed in uniaxial tension. Samples were cut at 0, 45, and 90 degrees to the

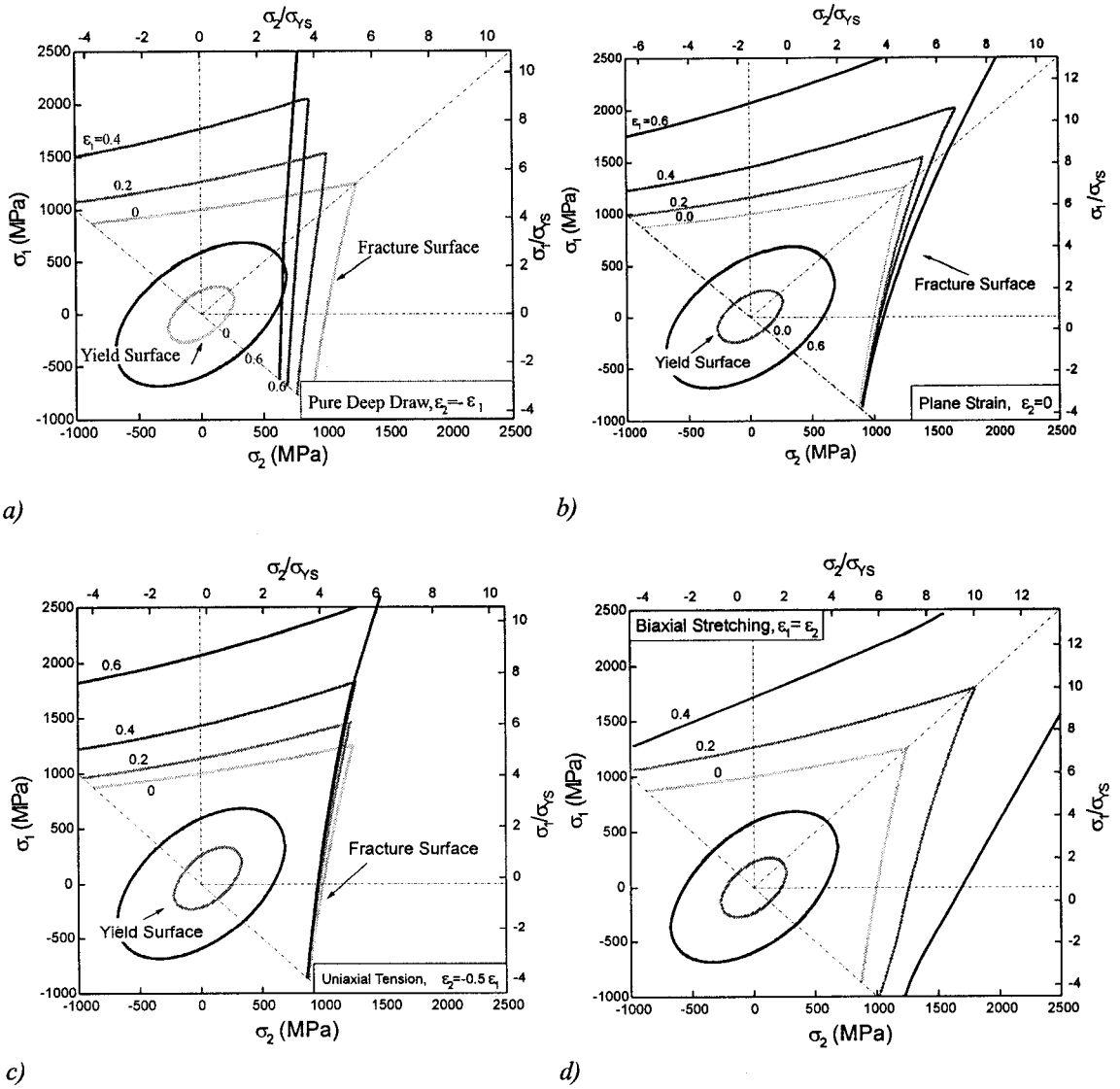

Figure 5.10 - Evolution of the intergranular fracture and yield surface in the plane of the sheet for a) pure drawing and b) plane strain rolling deformation c) uniaxial tension and d) pure biaxial stretching.

working direction. Table V-I summarized their results in terms of the intergranular fracture stress, percent intergranular fracture and strain to fracture. The intergranular fracture stress has decreased in the radial direction and has increased in the tensile direction as cleavage fracture is observed at much higher fracture stresses. A large number of non-propagating cracks were revealed with metallographic examination in samples tested at 90 degrees to the working direction, confirming a propagation controlled intergranular fracture mechanism. The measurements of Richards, Reid and Smallman (1968) agree with the modeling predictions shown in Figure 5.10c, the intergranular fracture stress increases in the principle tensile direction and decreases in the compressive direction of the sheet.

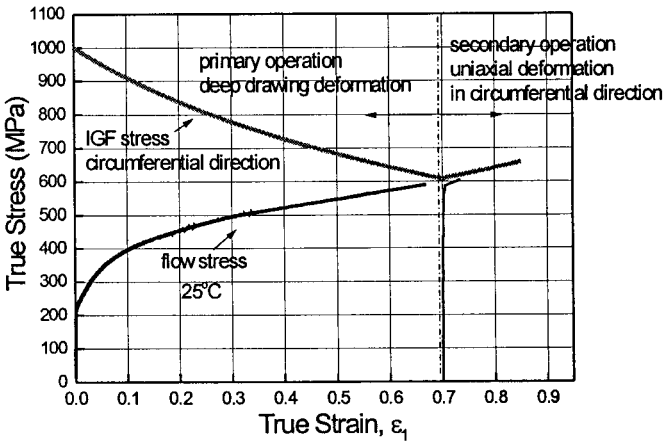

Figure 5.11 - Evolution of IGF stress and flow stress with primary and secondary forming operations.

The IGF surface evolves with cold rolling by expanding for all biaxialities, although the increase is far greater in the rolling direction than the transverse direction (Figure 5.10b). Anisotropy in the IGF surface with cold rolling has been measured in the present work. The stress required for IGF in the transverse direction, after a cold rolling strain of 0.35, increased from 980 MPa to 1180 MPa, and increased further with a cold rolling strain of 0.65 to above 1300 MPa, although the IGF stress was not measured directly, as delamination and ductile fracture intervene. Intergranular fracture was not observed after a cold rolling strain 0.35 in the rolling direction, although the flow response is softer in this direction. Maîtrejean (2000) has reported a similar anisotropy in intergranular fracture behaviour after cold rolling a Ti-stabilized IF steel. Transition temperatures, for notched specimens cut in the rolling and transverse directions after cold rolling to a true thickness strain of 0.75, were <-175°C and -145°C respectively. The transition temperature of the undeformed material was -150°C indicating that the IGF stress increased in both rolling and transverse directions with cold rolling deformation, although the increase in much greater in the rolling direction. Maîtrejean's

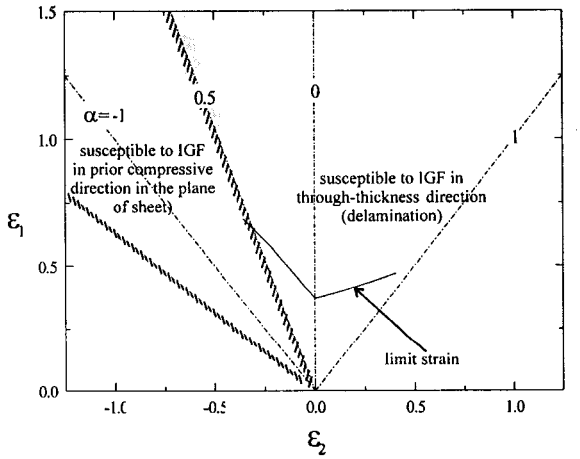

Figure 5.12 - The FLD is roughly divided into two areas: 1) the material is susceptible to IGF in the prior compressive direction, 2) the material is susceptible to IGF in the plane of the sheet.

Table V-I Fracture stress, percent IGF and strain to fracture for high purity iron with elongated grains (Richards, Reid and Smallman 1968)

Orientation	σ_f (MPa)	%IGF	ε_f
0	640	5	11
45	297	80	0
90	324	75	0

results support the current modeling (Figure 5.10b) and experimental measurements obtained in this thesis. Evidently, grain morphology leads to anisotropy in the predicted and observed fracture behaviour.

The results, for these and other strain paths relevant to forming operations, indicated that IGF occurs for forming operations when the primary operations are close to pure drawing and the secondary operations have a major tensile component in the direction of prior compressive strain. These are precisely the conditions that have been found to promote CWE. Instead of calculating the IGF stress in the plane of the sheet, the frame of reference can be changed such that the IGF stress is calculated in the through-thickness direction. The results indicated that the IGF stress decreased as the grains became flattened in this direction. Therefore, forming space was roughly divided into two areas: one in which the IGF stress decreased in the prior compressive direction in the plane of the sheet and one in which the IGF stress decreased in the through-thickness direction (Figure 5.12).

5.2.3.5 Intergranular Fracture Occurring After Deep Drawing (CWE)

The change in the IGF stress for pure deep drawing as the primary forming operation and uniaxial tension in the prior compressive direction as the secondary forming operation is given in Figure 5.13. The fracture stress decreases significantly with strain, from 1000 MPa for the undeformed equiaxed material to 517 MPa for material deep drawn to a true primary strain of one. Since the amount and embrittling power of the segregant and the grain size affect the intergranular fracture stress (Kameda and McMahon 1981) other initial intergranular fracture stresses are assumed (Figure 5.13). The IGF stress scales in a similar manner for equivalent amounts of strain: the fracture stress decreases by about 50 percent with a primary true strain of one.

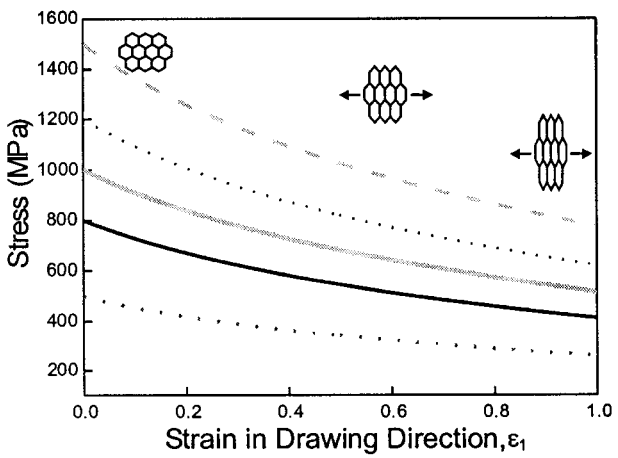

Figure 5.13 - Change in IGF stress with strain for a pure drawing operation and an applied tensile stress in direction 2 as the secondary operation for different assumed initial fracture stresses (average k_f criteria).

The results are directly applicable to the sequence of forming operations simulated by the CET, as the material is deep drawn then tested in tension in the prior compressive direction. Therefore, the Griffith plot (Figure 2.27) can be updated to include the results of the modeling. Figure 5.14 shows the grain size (i.e. crack size) dependence of the IGF stress for equiaxed grains and deep drawn grains tested in the prior compression direction. A

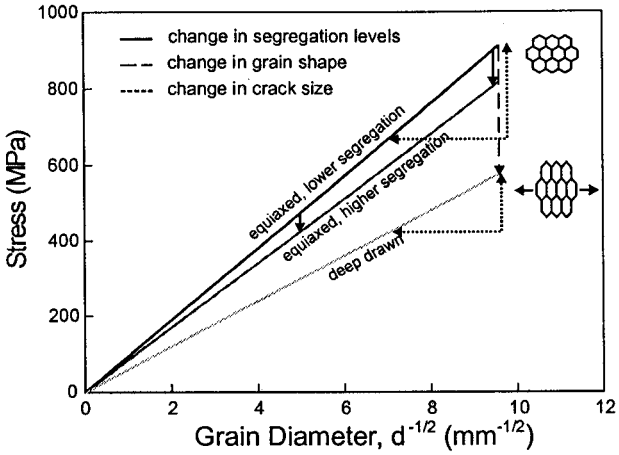

Figure 5.14 - a) Grain size dependence of the IGF stress based on the Griffith fracture stress (equations and), and the consequence of changes in segregation levels, grain shape and crack size.

change in crack size will have a larger absolute effect on IGF stress for equiaxed material as compared to deep drawn material. Increased segregation will decrease the IGF stress of fine grain material more than coarse grained material. Lastly, the change in the IGF stress with grain shape will be greatest for fine grained material. These simple observations indicate that the crack size dependence of the intergranular fracture stress and its dependence on the grain shape must be taken into account when studying CWE.

These results presented in Figure 5.13 and 5.14 will be used to explain many of the trends in the present work and reanalyzed data in the literature. This approach provides a promising basis for predicting the occurrence of CWE. However, the accuracy will depend on refining the prediction of the flow behaviour to include features such as deformation texture, possible kinematic and anisotropic hardening, and the Bauschinger effect, and by verifying the fracture maps by direct measurement of the intergranular fracture stress on deformed material. No direct experimental verification was made of these key predictions as it is very difficult to measure the IGF stress in the prior compressive direction in highly deep drawn material. In fact, this has never been done on sheet materials, although it has been attempted on hot rolled materials using a plane strain compression apparatus and tensile specimens cut from the flange of partially deep drawn cups (Charpentier and Piehler 1980). Essentially, one has to deep draw material and keep the material flat so tensile specimens can be cut for uniaxial tensile testing. It is possible to cut tensile specimens out of the flange on material that is partially deep drawn, although the deformation is not uniform and there is a limit to the amount of deep drawing that can be attained. Piehler and Jarvis (2000) have recently developed a sheet-metal deformation apparatus that simulates deep drawing and keeps the material flat. The controlled strain rate servo-hydraulic biaxial sheet metal simulator allows controlled tension-compression deformation in the plane of the sheet by using four independently controlled hydraulic cylinders. This unique apparatus would be ideal to simulate deep drawing to measure the post-formed fracture and yield properties.

5.2.4 Extension of Model to Include Transgranular Fracture

The fracture modeling has only considered IGF but in many grades of IF sheet steels TGF competes with IGF. The result of this competition is often mixed intergranular and transgranular fracture on the surface of deep drawn cups tested below the transition temperature. The model developed in the previous sections is extended to consider the competition between IGF and TGF by using a statistical approach. Normal distributions are

given to each fracture process (Figure 5.15). The TGF stress is assumed to remain constant with deformation. The formation of texture during deformation can influence the TGF process (Knorr 1988, Inagaki, Kurihara and Kozasu 1977) but it is not considered a significant factor for deep drawn IF sheet steels as the degree of texture is essentially unchanged with deep drawing compared to the undeformed material. The IGF stress decreases with deep drawing deformation as predicted by Figure 5.13. When the fracture stress distributions overlap, mixed mode fracture results. The fracture process ends after the cumulative summation of the IGF stress and TGF stress equals one. Therefore, the percentage of each type of fracture will depend on the ratio of the IGF and TGF stresses in the undeformed condition and will change with deep drawing strain as predicted in Figure 5.16. The mean fracture stress for mixed-mode fracture is given by the mean of the cumulative distribution. For instance, the results predict a change in fracture mode from predominantly intergranular to predominantly transgranular from the top to bottom of the deep drawn cup for a draw ratio of 2.2 and $\approx 1.1 > \sigma_{IGFo}/\sigma_{TGF} > 1.25$. This prediction is backed by the observation that in many grades of IF steels there is a transition from IGF to TGF from the top to bottom of the fractured cup (Lewis 1998, Maehara, Mizui and Arai 1991). The results are significant; they indicate that the response of the ductile-to-brittle transition temperature to the studied variable will depend on draw ratio in a complex manner. In fact, the trends found in the literature for different grades of steel have not been fully understood due to this complexity. Data taken from the literature and re-analyzed, will be used to highlight these findings.

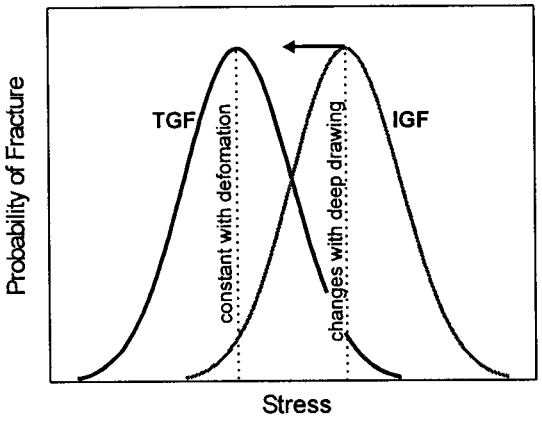

Figure 5.15 - Modeling competition between TGF and IGF by using a statistical approach.

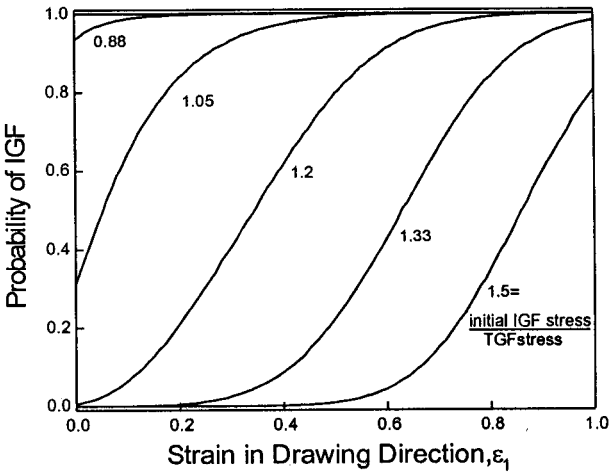

Figure 5.16 - Probability of IGF in the prior compressive direction with deep drawing strain for fully brittle material with different initial values of the IGF stress normalized by the TGF stress.

5.3 Intergranular Delamination

Intergranular fracture in the plane of the sheet is not common, as through-thickness tensile stresses are usually not significant for press forming operations. Nonetheless, IGF did occur during uniaxial tensile tests when the

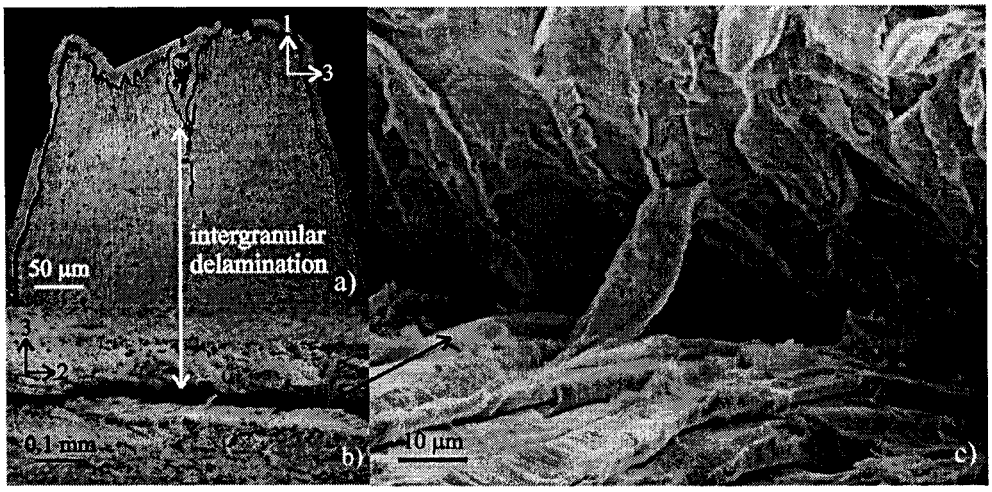

Figure 5.17- Intergranular delamination during uniaxial tension at –78 °C for a) an optical micrograph of the 1-3 plane, b) a scanning electron micrograph of the fracture surface (2-3 plane), and c) the highly flattened and elongated grains (near plane strain deformation) inside the intergranular delamination crevice.

localized neck was of sufficient acuity at a given flow stress to generate tensile through-thickness stresses high enough to coincide with the decreasing fracture stress. Intergranular fracture in the through-thickness direction (intergranular delamination) is shown in Figure 5.17. The bend-unbend test, used to test for susceptibility to CWE (see section 2.1.3.2), does test for IGF in the through-thickness direction. Strains developed in the inner bend radius for a 0t bend are similar to those in cups deep drawn to a draw ratio of 2.4, but the frame of reference is rotated by ninety degrees. On the inner bend radius, the grains are flattened in the plane of the sheet, while the unbending allows a tensile stress to act against the flattened grains. Forming operations with significant bending-unbending could therefore lead to CWE.

Intergranular delamination during uniaxial tension is analyzed in more detail by considering the transverse stresses that arise due to the localized necking. The localized neck creates a plane strain notch, no strain occurs in the width direction of the sheet. Bridgeman (1952) has derived the stress states for flat notched specimens in plane strain plastic deformation. The stress state for a notch with a radius of curvature, R, and a minimum thickness, t_m, is,

$$\sigma_3 = \bar{\sigma} \ln\left[1+\frac{1}{2}\frac{t_m}{R}+\left(1-\frac{x^2}{t_m^{\,2}}\right)\right] \tag{5.9a}$$

$$\sigma_2 = \bar{\sigma}\left\{\frac{1}{2}+\ln\left[1+\frac{1}{2}\frac{t_m}{R}+\left(1-\frac{x^2}{t_m^{\,2}}\right)\right]\right\} \tag{5.9b}$$

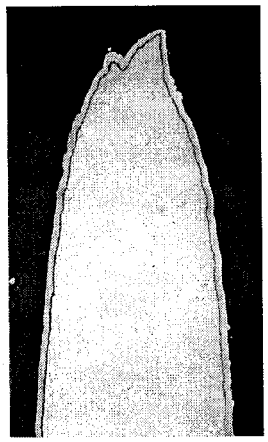

Figure 5.19 - Example of notch profile sectioned from the middle of the width for batch annealed uniaxial tensile specimen tested at -40°C.

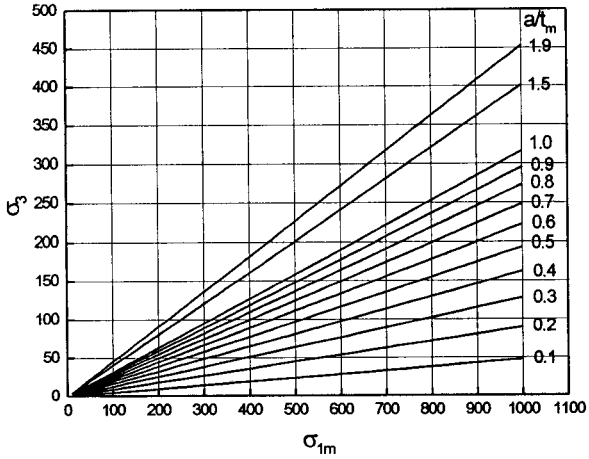

Figure 5.18 - Maximum through-thickness stress as a function of the uncorrected flow stress for different measured flow stresses and notch acuities.

$$\sigma_1 = \bar{\sigma}\left\{1+\ln\left[1+\frac{1}{2}\frac{t_m}{R}+\left(1-\frac{x^2}{t_m^{\,2}}\right)\right]\right\} \tag{5.9c}$$

The measured flow stress, $\sigma_{1\,m}$, is multiplied by a correction factor to obtain the corrected flow stress, $\bar{\sigma}$,

$$\bar{\sigma} = \frac{\sigma_{1m}}{\left(1+2\frac{R}{t_m}\right)^{1/2}\ln\left[1+\frac{t_m}{R}+\left(\frac{2t_m}{R}\right)^2\left(1+\frac{1}{2}\frac{t_m}{R}\right)^{1/2}\right]} \tag{5.10}$$

Using equations 5.9b and 5.10, the maximum through-thickness stress, σ_3, which occurs in the middle of the sheet, is plotted as a function of the measured flow stress for different notch acuities (Figure 5.18). An estimate of σ_3 was made by measuring t_m/R after fracture. The maximum value for t_m/R is assumed to occur near failure and the measured flow stress at this strain is used to obtain the through-thickness stress. Grain shapes can be estimated from the amount of uniform strain and plane strain deformation in the localized neck, which is $\sim \varepsilon_f - 3\varepsilon_u$. Intergranular fracture stresses are obtained from the grain shape change.

Table V-II Through-thickness stresses based on Bridgeman analysis for flat sheet and IGF stress based on grain shape for batch annealed material.

T (°C)	t_m/R	n	σ_3	σ_{IGF}
25	0.65	0.225	290	320
0	0.67	0.24	300	325
-40	0.84	0.235	360	340
-75	0.84	0.24	365	355
-140	0.91	0.18	350	500
-160	0.63	0.1	280	550
-185	0.5	0.05	200	980
-196	0	0	0	1000

The predicted through-thickness stresses based on the notch acuity measurements are considerably lower than 1000 MPa, the IGF stress of the undeformed material, for all temperatures tested (Table V-II). Therefore, this analysis indirectly confirms that the IGF stress has been lowered as the grains become flattened in the through-thickness direction. Delamination is predicted if the through-thickness stress generated by the formation of the localized neck is larger than the predicted IGF stress in this direction. The predictions given by Table V-II can be compared to the quantitative fractography (Figure 4.16).

5.4 Influence of Draw Ratio on Cold Work Embrittlement

A fundamental characteristic of CWE is the increased brittleness with deep drawing (Lewis et al. 1998, Yan and Gupta 1996, Bleck and Heßling 2000). Deep drawing increases the susceptibility to CWE more than other modes of deformation. Although deep drawing work hardens the materials, raising the flow stress, it also severely elongates the grains parallel to the draw axis. These elongated grains, tested in tension when the cup is crushed or expanded, have been suspected to be the cause of the increased susceptibility to IGF (Konishi, Osawa and Yoshida 1974, Gupta and Scime 1979, Bhat et al. 1995). The ductile-to-brittle transition has often been determined by a critical draw ratio. Although very fundamental to the nature of the embrittlement, the influence of deep drawing has been ignored in comparison to the influence of material chemistry and thermo-mechanical processing. There are two studies that have investigated the effect of draw ratio on CWE over a large range of draw ratios (more than two). One, an industrial round robin (cited in Yan and Gupta 1998) used no standard test method, and the other is a citation by Oka and Takechi (1987) to unpublished research. It was therefore deemed necessary to investigate the influence of draw ratio on CWE.

The validity of the IGF model can be tested by using the Davidenkov approach to predict the transition temperature as a function of draw ratio. Strain measurements from the lathed edge of the cup (Table IV-III) were used to replot the transition temperatures with draw ratio as a function of the effective strain (Figure 5.20). Figure 5.13, the IGF stress in the circumferential direction after deep drawing, is overlaid (after being converted into stress versus effective strain) onto the flow curves as a function of temperature (Figure 4.11). The intersection of the flow and fracture stress gives the transition temperature as a function of the effective strain (Figure 5.20). The IGF stress of the undeformed material is taken to be between 950-1000 MPa, and therefore gives the limit

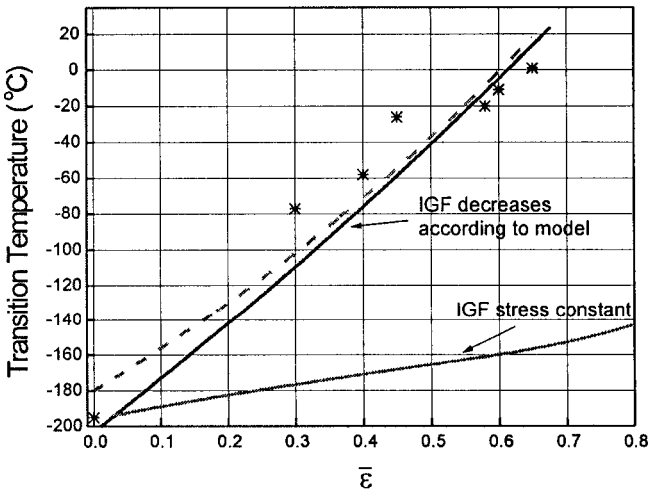

Figure 5.20 - Measured and predicted transition temperatures as a function of true effective strain.

between the grey hatched and black line. The same procedure can be used with the assumption of a constant IGF stress (Figure 5.20, grey line). The measured transition temperatures have an almost linear relationship with the effective strain (up to a draw ratio of 2.4). Predictions based on a decreasing fracture stress fit the measured transition temperatures. Predictions based on a constant IGF stress are found to deviate significantly from the measured values. For instance, for a draw ratio of 2.2 (e.g. a true effective strain of 0.6) the transition temperature is predicted to be ~-160°C, whereas the measured value is -14°C. Therefore, a decreasing IGF stress based on the morphological change in the grain is required to rationalize the transition temperatures measured as a function of draw ratio and provides a convincing explanation of the observed trends.

Although the Davidenkov plots are a very useful representation of the competition between plastic flow and brittle fracture, a more general method of representing this competition was presented in the form of maps in stress space (Figure 5.10). The plastic flow surface and the intergranular fracture surface both evolve with deformation, and can be inspected at any point along the strain history. These maps allow any form of hardening, i.e. work, strain or temperature, and any biaxiality to be represented. If the evolution of the IGF stress is not accounted for, IGF in the prior compressive direction is not predicted at ambient temperatures. When the decreased fracture stress is accounted for, IGF is predicted over a range of biaxialities (~ $\beta = 1$ to $\beta = 0$). This representation is therefore more suitable to forming operations as the secondary operation is not necessarily uniaxial tension.

Variations in transition temperature with draw ratio for different steel chemistries of formable sheet steel are shown in Figure 5.22 (Oka and Takechi 1987). The increase in transition temperature with draw ratio depends on the steel chemistry. The modeling in the previous section can be used to examine the influence of draw ratio and material chemistry on the DBTT. Three steel chemistries are selected as examples. One grade is chosen such that the IGF stress remains greater than the TGF stress in the circumferential direction during deep drawing. This steel would not be susceptible to CWE, as is the case for most AK deep drawing quality (DDQ) steels. The second grade is chosen such that the IGF stress starts below the TGF stress for the undeformed material, as is the case for many rephosphorized IF steels. The third grade is chosen to lie between the two previous cases; which would be the case for a stabilized IF grade or a RP IF grade with free carbon or boron additions. These three cases are summarized in the form of a Davidenkov diagram (Figure 5.21).

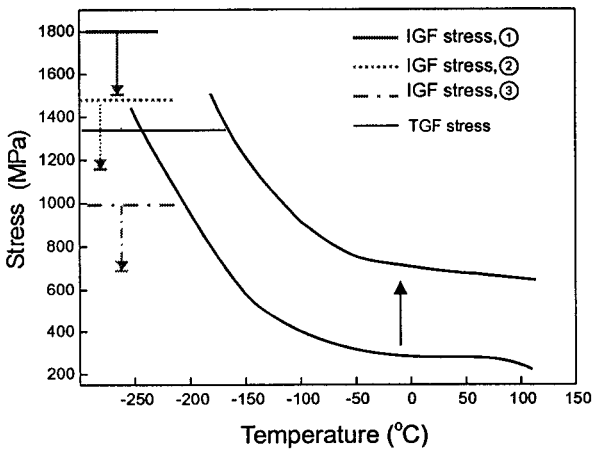

Figure 5.21 - Davidenkov diagram illustrating the evolution of the transition temperature with deep drawing for three different steel chemistries.

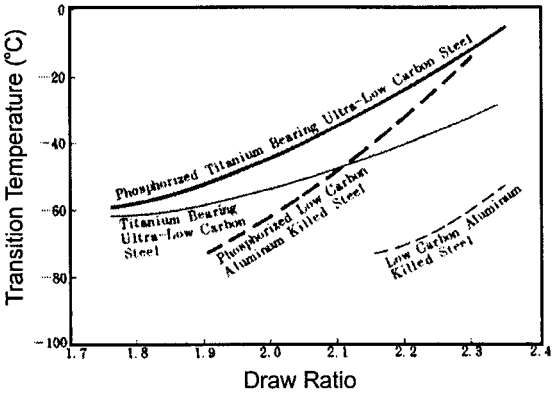

Figure 5.22 - Cold work embrittlement transition temperature versus draw ratio for different grades of low carbon and interstitial-free steels (Oka and Takechi 1987).

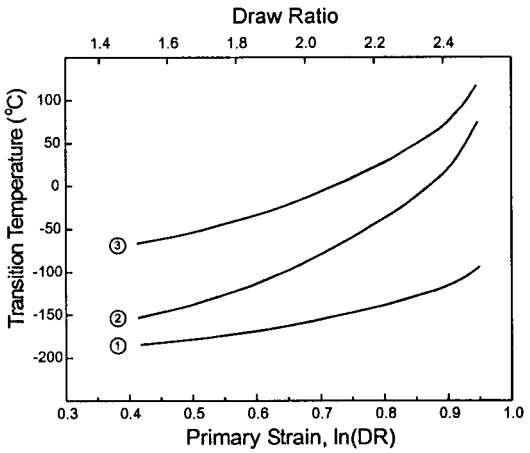

Figure 5.23 - Predicted evolution of the transition temperature with deep drawing deformation for three different grades of sheet steel.

The transition temperature, for these three grades, can be predicted by following the evolution of the fracture stress and flow curve with deformation. The same work hardening behaviour was assumed for all grades. The transition temperature is predicted to evolve differently with draw ratio for each grade (Figure 5.23). The fracture mode of the AK DDQ steel remains transgranular in nature. The increase in transition temperature is solely due to work hardening, and is therefore more gradual. The partially stabilized RP IF grade changes from fully TGF to mixed transgranular and intergranular fracture, until finally at high draw ratios the fracture is mostly IG in nature with the transition temperature increased accordingly. The transition temperature of the RP IF steel is highest as the fracture is entirely IG. The gradient of the transition temperature with draw ratio is greatest for the partially stabilized RP grade due to the transition in fracture mode. These predictions are in direct agreement with the sole experimental work in this area (Figure 5.22). Correlation between model predictions and experimental data gives credence to the influence of grain shape on the susceptibility to IGF and hence CWE, and is a convincing explanation of the role of both chemistry and severity of deep drawing on the transition temperature.

5.5 Recrystallization Annealing, Grain Boundary Segregation Level

The Davidenkov-Orowan plot of Figure 5.24 compares the results of the continuously annealed and batch annealed materials in the undeformed and deep drawn states. Although different amounts of segregation were measured for these two heat treatments (the batch annealed steel has greater than twice the amount of phosphorus at the grain boundary), the transition temperatures measured from tensile tests on the annealed undeformed materials are nominally the same (Figure 5.24). There is also little difference in temperature dependence of the flow behaviour measured in uniaxial tension, grain size and shape distributions or residual stress distributions between the BA or the CA steels. The measured transition temperature on the undeformed

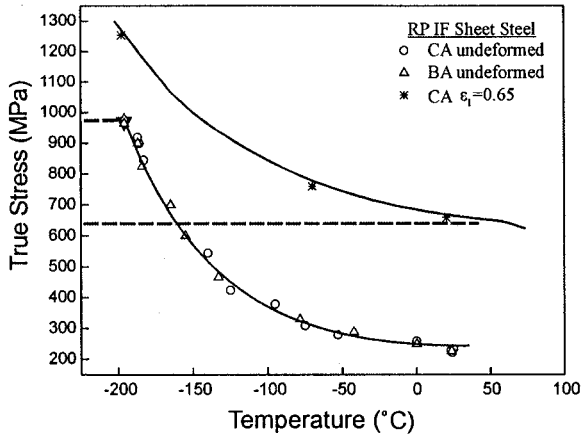

Figure 5.24 - Davidenkov plot for undeformed and deep drawn (tested in prior compression direction) batch and continuously annealed steels.

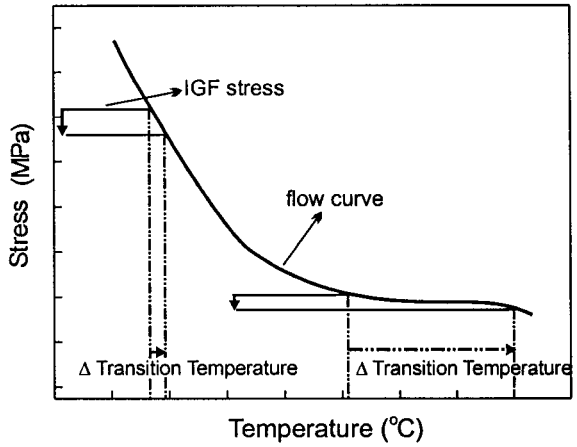

Figure 5.25 - Davidenkov diagram illustrating how the response of the transition temperature for a change in intergranular cohesive strength depends on the shape of the flow curve.

material, based on the intersection of the yield curve and the fracture curve, was -196°C for the CA steel and -200°C for the BA steel (Figure 2.13). Transition temperatures as measured by the cup expansion test differ by 30°C when tested at 5 mm/s and 55°C when tested at 4429 mm/s.

Again, the results can be understood by considering the evolution of the fracture and flow behaviour (refer to Figure 5.25). At low temperatures, when the yield stresses increase exponentially with temperature, small differences in the IGF stress will not lead to large differences in transition temperature. When the steel has been embrittled and deformed to such an extent that the fracture and yield surfaces coincide in the temperature range where the flow curve is nearly constant, small differences in the fracture stress can lead to large changes in transition temperature. This explains the apparent discrepancy between the transition temperatures of the batch and continuously annealed steels as measured in uniaxial tension and by the cup expansion test. Therefore, the ductile-to-brittle transition temperature not only depends on the response of the fracture stress and flow curve to various conditions, but also depends on where the two curves intersect.

5.6 Macroscopic Residual Stresses

Significant macroscopic residual stresses develop during cup drawing. Of particular interest when studying CWE are the circumferential residual stresses, as cracks propagate in the longitudinal direction. To understand the effect of residual stresses on CWE we must first review the residual stress state induced by cup drawing and then previous investigations on the influence of macroscopic residual stresses on intergranular fracture will be discussed.

Residual stresses develop during cup drawing due to bending-unbending that occurs over the die profile radius. As the bending is in plane strain, the residual stresses in the circumferential direction are about half of the residual stresses in the longitudinal direction. More severe die radii introduce greater residual stresses (Danckert 1995, Lange and Bruckner 1990). This conclusion can be deduced from a simple analysis of the bending process (Marciniak and Duncan 1992). The distribution of residual stresses after deep drawing, before being released by the cracking or ring opening have been measured in the through-thickness direction using pickling methods (Sachs and Espey 1942), x-ray and neutron diffraction (Lange and Bruckner 1990), and Sachs boring method using strain gages (Saito and Shimahashi 1978). Saito and Shimahashi (1978) have successfully modeled the though-thickness circumferential residual stress distribution during deep drawing. Danckert (1995) has investigated the origin of the deep drawing induced residual stresses with finite element modeling. Both the circumferential and longitudinal stresses follow a pattern similar to the linear distribution assumed when deriving the maximum residual stress using the ring opening method. The maximum circumferential and longitudinal stresses roughly coincide in the through-thickness direction, both are tensile on the outside surface and compressive on the inside surface. A schematic of the residual stresses in the through-thickness direction is shown in Figure 5.26.

Residual stresses in deep drawn cups and sunk tubes have been studied with relation to stress corrosion cracking, particularly in brass products (which has often been called season cracking) (Lange and Bruckner 1990). Deformation induced residual stresses increase the sensitivity to stress corrosion cracking. Residual stresses accelerate intergranular corrosion by augmenting the microscopic intergranular stresses. This phenomenon is different than CWE as the cracking does not involve competition between plastic flow and brittle fracture.

The only work to investigate the effect of residual stresses on CWE was that of Matsudo et al. (1977). Charpy specimens, cut from the top of as-drawn cups and heat treated cups (450 °C for 1 hour), were used to find the DBTT. Reduction of the circumferential residual stresses, to one-tenth the value found in the as-deep drawn cups, occurred upon heat treating as measured using the ring opening technique. The flow stress of the cups was not changed with the heat treatments. No trend was observed for the change in the DBTT with heat treating and transgranular fracture was the predominant fracture mode. These tests did not probe the unbending residual stress, e.g. the residual stresses before opening release, but the final residual stress state, as the unbending circumferential stresses were

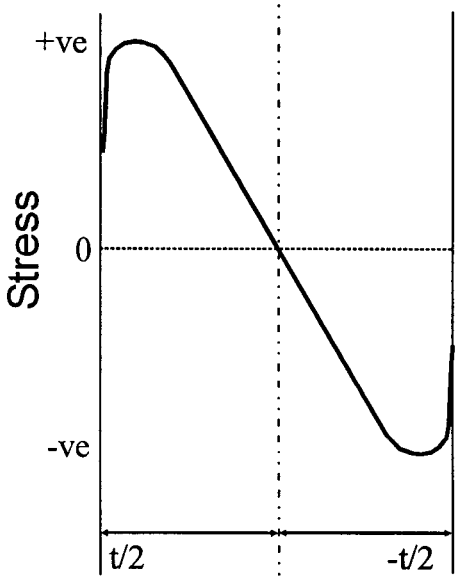

Figure 5.26 - Schematic circumferential residual stress distribution in through-thickness direction in deep drawn cups.

released once the Charpy specimens were cut from the cup. Yasuhara et al. (1994) mention that the transition temperature would be strongly influenced by the drawing ratio as severe deep drawing induces both work hardening and circumferential tensile residual stresses. Spalek et al. (2000) attribute the increased brittleness with deep drawing to the multi-axial residual stress state leading to increased plastic constraint, thereby increasing the transition temperature. Clearly, the question as to whether deep drawing induced macroscopic residual stresses affect CWE has not been answered.

Experiments were designed to clarify whether the residual stresses affect IGF and therefore CWE in deep drawn cups. Three approaches were used to investigate the influence of the macroscopic residual stresses on CWE; these include using stress relieving heat treatments, different die geometries to produce different residual stress distributions and the variation in CRSs with cup height and draw ratio to advantage (e.g. see Figure 4.45).

Heat treatments at 550°C for one hour on deep drawn cups with a draw ratio of 2.2 successfully relieved the circumferential residual stresses without changing the flow stress of the material (Figures 4.38 and 4.46). The same heat treatment was used on blanks prior to deep drawing to determine if segregation occurred during the 1 hour hold at 550°C. Cups drawn with heat treated blanks had the same flow and residual stress distribution with cup height as the non-heat treated cups, as expected. Transition temperatures of the as-drawn cups, stress-relieved cups and cups drawn with heat treated blanks were -11°C, 10°C and - 8°C respectively. Heat treating at 550°C prior to deep drawing does not change the transition temperature significantly and therefore it can be concluded that little phosphorus segregated during the stress-relief heat treatment. Stress-relieved cups had the same grain shape and flow stress as the as-drawn cups, and therefore a significant decrease in residual stresses should translate into a decrease in transition temperature as the fracture stress intersects the flow curve in the nearly constant region. The transition temperature of the stress-relieved cup has increased even though the residual stresses have been relieved. It therefore appears that the residual stresses are not aiding the brittle fracture process. The increased transition temperature could be due to a redistribution of segregant on the grain boundary, although no experiments to investigate this possibility were attempted.

Different die geometries were used to investigate the effect of residual stresses on CWE. Three different die configurations were used (Figure 3.4). No measurable differences in the circumferential residual stresses were found in cups drawn to the same draw ratio with different die geometries. An exception were the cups drawn to a draw ratio of 2.2 with the thick gage material using die 1 and the tractrix die. Residual stresses for the tractrix drawn cups were lowered by 40% and the transition temperature has not decreased with the decrease in residual stress, but has increased slightly from 5°C to 12°C. Although a difference is observed in the circumferential residual stress distribution, the absolute value of the difference is not great at the lathed edge (Figure 4.49).

Finally, differences in circumferential residual stresses with cup height for different draw ratios (Figures 4.45 - 4.50) were used to investigate the effect of residual stresses on CWE. Cups with a draw ratio of 2.4 were lathed to an equivalent height (43 mm) as cups with a draw ratio of 2.2. The flow stress and effective strains are approximately equal at this height, whereas the CRSs differ by 100 MPa. If residual stresses were controlling or contributing to CWE, a significant difference in transition temperature would be observed, again as the fracture and flow curves intersect in the nearly constant region for material with this level of deep drawing deformation. Nearly identical transition temperatures are observed; -11°C for draw ratio 2.2 and -15°C for the lathed cups (Figure 4.53). The small difference in transition temperature can be attributed to small differences in strains; the strain are marginally greater for cups with a draw ratio of 2.2 at a height of 43 mm (Figure 4.33). It should be kept in mind that the difference in transition temperature would have been greater had the steel exhibited mixed transgranular and intergranular fracture due to the steeper gradient in the change of the DBTT with deep drawing strain (e.g. Figure 5.23). Once again, the results indicate the macroscopic residual stresses are not contributing to CWE.

All of the experiments investigating the effect of residual stresses on CWE yield the same result; the residual stresses do not have a major influence on CWE. This conclusion, which at first seems counter intuitive, will be explained using the framework developed in this thesis.

The residual stresses, which are given by the primary circumferential and longitudinal stresses, have well defined distributions in the through-thickness direction. Such a macroscopic residual stress distribution will round the yield portion of the flow curve as discussed by Sowerby, Uko and Tomita (1979). The stresses can be considered on a local scale, for instance by imagining the material to be constructed of geometrically identical slabs each with a constant residual stress state. A biaxial stress state does admit the possibility that residual stresses can affect the transition temperature due to differences in the shape of the yield and brittle fracture surfaces (Figure 5.27). In most cases, biaxiality acts to constrain both plastic flow and brittle fracture equally. Again, the exact outcome will depend on the relative shapes of the yield and fracture surface and the magnitude of the biaxial stress state with respect to the above mentioned surfaces. For highly deep drawn material tested in the circumferential direction, the effect of the biaxial stress state on the transition temperature is negligible (Figure 5.27).

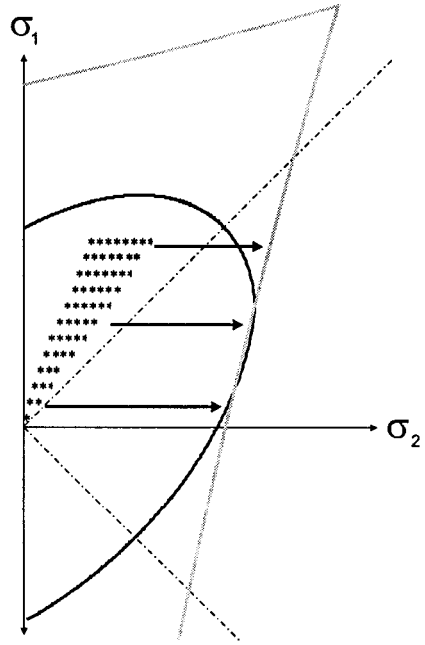

*Figure 5.27 - Effect of biaxial residual stresses on local plastic and brittle constraint, * indicates possible residual stress state.*

Locally, residual stresses aid yield and brittle fracture processes equally and both the brittle fracture stress and flow curve are shifted by the same amount. As a result the transition temperature is not changed. This conclusion is clarified by the use of a Davidenkov diagram in Figure 5.28. Therefore residual stresses do not make a significant difference in the competition between plastic flow and propagation controlled brittle fracture.

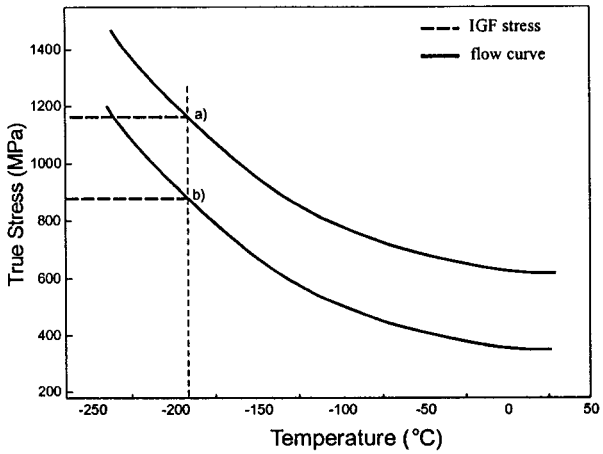

Figure 5.28 - Davidenkov plot illustrating effect of residual stresses aiding the local flow and fracture stress. a) Transition temperature without aid of residual stresses. b) Lowered fracture stress and flow curve due to local tensile residual stresses.

A final point is made by returning to the data presented by Oka and Tacheki (1987) (Figure 5.22). For the different grades of sheet steel tested no significant differences in residual stress distribution are expected (especially if the flow behaviour is similar) and therefore differences in the transition temperatures are due to the change in grain shape and the resulting competition between intergranular and transgranular fracture and not due to the residual stresses.

5.7 The Influence of Strain Rate

The IGF stress is independent of the strain rate. Therefore, the effect of the strain rate on CWE is due solely to the response of the flow stress to strain rate changes. This response is characterized by the strain rate sensitivity, which is usually specified by a strain rate sensitivity index, m, which is usually assumed to be independent of strain rate, but not independent of temperature or strain. The flow stress, as a function of strain rate, for a constant strain and temperature, can be approximated by ,

$$\sigma = K\dot{\varepsilon}^m \tag{5.11}$$

The flow stress, for a change in the strain rate at constant strain and temperature is therefore given by,

$$\frac{\sigma_2}{\sigma_1} = \left(\frac{\dot{\varepsilon}_2}{\dot{\varepsilon}_1}\right)^m \tag{5.12}$$

Uniaxial tensile tests, on undeformed material at room temperature, gave an m value of 0.014. This value compares favorably with the value, $m = 0.015 - 0.014$, obtained at a true uniaxial strain of 0.25 on a Ti-stabilized IF sheet steel (Shi and Meuleman 1995). The strain rate sensitivity index for cups of continuously annealed material drawn to draw ratio 2.2 and expanded at three different rates can be taken as approximately constant as the transition temperatures were between -14°C and 50°C. The effective strain at

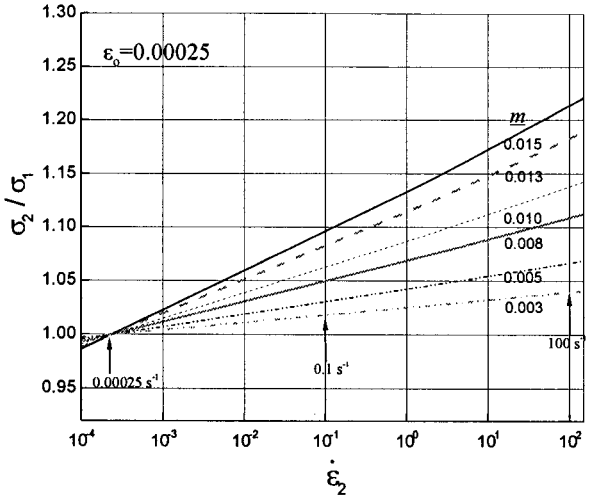

Figure 5.29 - Strain rate hardening for strain rate sensitivity index, m, of 0.015 to 0.003.

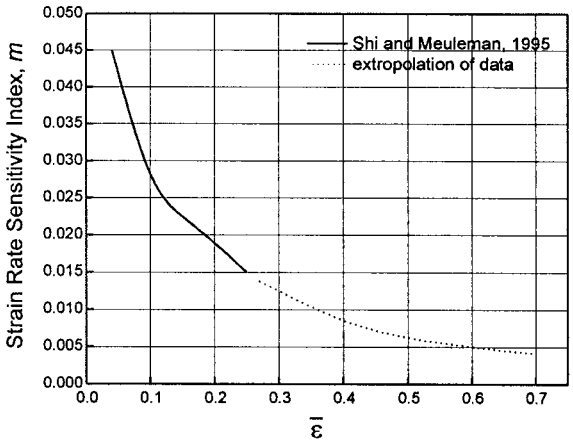

Figure 5.30 - Strain rate sensitivity index, m, for IF sheet steel as a function of strain (Shi and Meuleman 1995).

the top of the deep drawn cup of draw ratio 2.2 is approximately 0.65. Extrapolating strain rate sensitivity index obtained by Shi and Meuleman (1995) from uniaxial tension tests on IF sheet steel gives an m value of nearly 0.005 at an effective strain of 0.65.

To investigate the effect of strain rate on the results of the CWE, the ram speed, v, had to be translated into a circumferential strain rate. The circumferential strain rate was derived in terms of the ram speed in Appendix B as,

$$\dot{\varepsilon}_{CET} = \frac{1}{r}\frac{v}{\tan\theta_p} \tag{5.13}$$

Circumferential strain rates for the three different ram speeds used, 0.01 mm/s, 5 mm/s, and 4429 mm/s, are 0.00023 s^{-1}, 0.115s^{-1}, and 102 s^{-1}. The hardening expected for these strain rates is shown in Figure 5.29. A ram velocity of 0.01 mm/s was chosen to give a strain rate approximately equal to that used in the uniaxial tension tests. For $m = 0.005$, the flow curve is increased by 1.03 times at 0.115 s^{-1} and 1.06 times at 102 s^{-1}.

The Davidenkov diagram can be used to predict the change in transition temperature with increasing strain rate. The IGF model predicts an IGF stress of 642 MPa for the cups with a draw ratio of 2.2. Shifting the flow curve by the appropriate strain rate hardening index gives predicted transition temperatures of -14°C, 20°C and 45°C (Figure 5.31). These predictions compare to the measured transition temperatures of -14°C, -11°C and 50°C (Figure 4.56). The general trend predicted by this approach is consistent with the measured values, although the predicted values are found on the most sensitive part of the flow curve, which lead to greater uncertainly and explains the differences. The increase in transition temperature is quite significant, as the IGF stress has decreased to such an extent that it intersects the flow curve in the nearly linear region.

The flow stress responds less to changes in strain rate, than to changes in temperature or strain. Therefore, the results of the CET can be used as an indirect measure of the IGF stress, if the work hardening is effectively characterized for a given strain state. Predictions of the change in IGF stress yielded by the modeling (Figure 5.13) can be verified by the measured transition temperatures. Characterization of the work hardening behaviour at room temperature, for a strain rate of 0.00025 s^{-1}, is shown in Figure 4.9. The flow curve shifts upward by a factor of 2.81 for an effective strain of 0.65. Therefore, using the measured transition temperature of -14°C for a draw ratio of 2.2 and strain rate of 0.00025 s^{-1}, gives an intergranular fracture stress of 640 MPa. The analysis indirectly confirms the decrease in IGF stress from 980 MPa, as measured on the undeformed material, and agrees with the IGF stress of 642 MPa predicted by the modeling. In contrast, if the IGF stress was assumed to remain constant, a transition temperature of -160°C is expected.

The transition temperature was measured using the CET as a function of strain rate at a constant draw ratio and temperature. This approach has not previously been attempted in the literature. The ductile-to-brittle stain rate, at room temperature, was 36.8 s^{-1}. Measuring the transition temperature as a function of strain rate is not a practical test for most grades of IF sheet steels, but the data can be used to verify the magnitude of the strain rate sensitivity index. The flow stress, at room temperature, is 620 MPa for the cups with a draw ratio of 2.2, and according to the IGF model, the flow stress must increase to 642 MPa for IGF. This amount of strain rate hardening at 36.8 s^{-1} corresponds to a strain rate sensitivity index of 0.003. This confirms the extrapolated value of m; the strain rate sensitivity index does decrease significantly from the value obtained from the uniaxial tensile tests.

Strain rate can have a large effect on the mechanical response of a steel, especially for highly embrittled steel, e.g. grain boundaries compromised by deleterious segregation and material highly deep drawn. The DBTT for the batch annealed steel was increased from 30°C to 110°C for a change in strain rate from 0.115s^{-1} to 102 s^{-1} (Figure 4.51). In this case, the IGF stress intersects the flow curve in the nearly constant region, which explains the large increase in transition temperature. Characterization of the strain rate sensitivity, as a function of deformation and temperature, is needed for proper predictive capabilities, especially when comparing fracture during slow deformation with that of high strain rate (impact) loading.

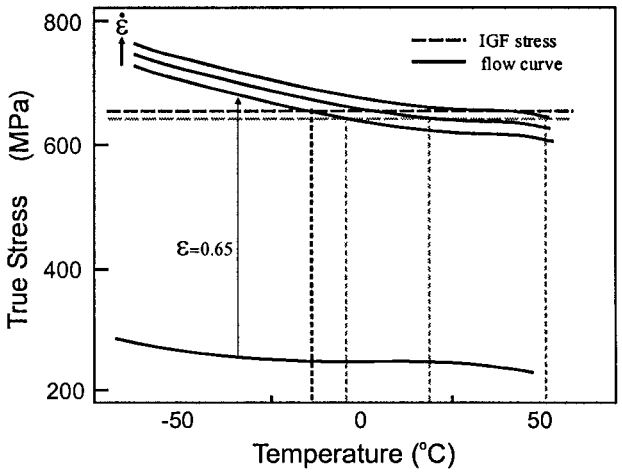

Figure 5.31 - Davidenkov diagram predicting the change in transition temperature with increased strain rate for deep drawn cups with a DR of 2.2.

5.8 Galvannealed Coating

For added corrosion resistance, especially for exposed parts, interstitial-free sheet steels are hot-dip galvanized or galvannealed, or electro-galvanized The influence of coating on the sensitivity to CWE was studied by determining the DBTT for the rephosphorized IF sheet steel with the surface of the steel in three different conditions; the galvannealed coating was left on, the coating was removed, and the coating and all surface damage was removed. The galvannealed coating was found to have a significant effect on the transition temperature; for instance, the transition temperature decreased from 24°C to -11°C when the galvannealed coating was stripped with hydrochloric acid prior to drawing to a draw ratio of 2.2.

When the coating was stripped from the as-received material, surface cracks were observed. These fissures, present in the coating and substrate before deep drawing deformation, are due to either outbursts (accelerated iron-zinc intermetallic formation along the grain boundaries) or to the coating cracking during temper rolling and coiling. The coating was found to further crack with deep drawing deformation, resulting in increased density of cracks in the ferrite substrate. No surface cracks were observed on the ferrite substrate when the material was thinned prior to deep drawing, confirming that the increased surface cracks are clearly due to the presence of the coating. Galvannealed coating cracking with deep drawing deformation has also been observed by Lau, DeCooman and M. Vermeulen (1998), Deits and Matlock (1990)and Martin et al. (2000). Each of these studies reported observation of cracks penetrating into the ferrite substrate with deep drawing deformation. The cracks originated from the galvanneal coating or from the coating/substrate interface.

Therefore the conclusion gained from the present study and from the literature is that the galvanneal coating introduces surface damage in the form of cracks. These cracks increase the effective crack size and thereby lower the stress necessary for fracture. As explained in section 5.2.3.5, an increase in crack size will decrease the intergranular fracture stress of an equiaxed grained material more than an elongated grain material. This observation helps explain why the transition temperature increased more, comparing stripped to coated, for material with lower deep drawing deformation, i.e. draw ratio 1.65 compared to draw ratio 2.2. Another possibility is that increased drawing serves to blunt initiated surface cracks, although this effect was not measured.

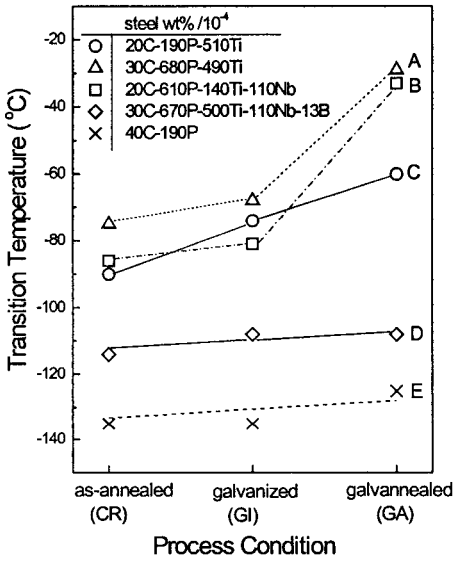

Figure 5.32 - Effect of coating on the transition temperature for trimmed cups with a draw ratio 2.3,and initial sheet thickness of 0.8mm (Kase et al. 1993).

Comprehensive work by Kase et al. (1993) examining the effect of coating on CWE for four grades of IF steel and

one unstabilized grade can now be rationalized through the fracture modeling and by considering the modified Griffith plot (Figure 5.14). Each grade, whose chemistry is given in Figure 5.32, was evaluated with the CET in the uncoated (CR), galvanized (GI), and galvannealed (GA) state. The boron added and unstabilized grades, which are relatively resistant to CWE, show little variation in transition temperature with coating. The transition temperature of the other three grades of IF steel increased slightly with galvanizing, and increased significantly with galvannealing (see Figure 5.32). The coating increases the initial crack size from ~ half a grain to a few grain diameters (see Figure 5.32). The increase in crack size will depend on the nature of the coating, but is more severe for galvannealed coatings. The two grades that are resistant to IGF and fail by TGF (grades D and E in Figure 5.32) will be the least susceptible to changes in crack size as i) the Griffith slope is greater for TGF and ii) the fracture stress intersects the flow curve in the exponentially increasing region. Therefore, as seen from Figure 5.32, the coating has relatively little effect on the transition temperatures of grades D and E. The opposite holds for the rephosphorized grades as the increased crack size leads to a greater absolute decrease in the IGF stress, and the fracture stress and flow curve intersect in the nearly constant region. The crack size is estimated to change from 5 μm for uncoated material to 10 μm for galvannealed material, which roughly gives a 100 MPa change in the IGF stress for a highly embrittled deep drawn steel (Figure 5.32). This decrease in the IGF stress will lead to a large increase in the transition temperature as seen in Figure 5.32. Therefore, an increased crack size will lead to the most severe increase in transition temperature for the high strength (rephosphorized) embrittled steels as confirmed by the experimental results presented in this thesis and those presented by Kase et al. (1993).

5.9 Grain Boundary Structure and Intergranular Fracture

Low angle grain boundaries are found to be resistant to intergranular fracture. Low angle grain boundaries have low free volume (Mehta and Smith 1993), and as a result are expected to have low levels of phosphorus segregation. It is not clear whether low angle boundaries are strengthened via carbon segregation or are intrinsically strong, but is clear that they are resistant to fracture. Special grain boundaries are not as resistant to fracture as low angle boundaries, but are more resistant to fracture than random high angle boundaries.

The question to ask then is to what effect does the grain boundary structure distribution have on a steels susceptibility to CWE? In this work, both industrial annealing recrystallization heat treatments produced steels with roughly the same crystallographic texture and grain boundaries structure distributions (section 4.12 and 4.10). Therefore, no experimental observations were made on the influence of different misorientation distribution arresting intergranular fracture. A coarse assessment of the resistance to intergranular fracture can be obtained by turning to intergranular fracture models that have included grain boundary structure distributions (Palumbo et al. 1991, Gertsman and Tangri 1997, Lim and Watanabe 1990). Palumbo et al. (1991) use a geometrical-probabilistic model and consider the distance required to blunt 99% of the intergranular cracks. The crack arrest distance decreases with increased percentage of resistant grain boundaries. Very high fractions of resistant grain boundaries are required to decrease the crack arrest distance

to within a few multiples of the grain boundary length, and to arrest nearly all of the cracks within a reasonable crack arrest distance. In this regard, propagation of only one crack may be needed to cause failure in IF sheet steels. As well, many of these models consider the grain interior to be resistant to fracture. Transgranular fracture is a distinct possibility when large stresses are needed to cause IGF. For example, the crack path has often been observed to change to transgranular fracture as the crack traverses down the length of the cup wall, e.g. fracture is not necessarily arrested. Most of these models have been developed to address intergranular degradation phenomena such as stress-corrosion cracking. It is unlikely that these models can be applied with great confidence to brittle intergranular fracture as they do not capture the physics of brittle fracture. A model based on fracture mechanics which includes grain size, deflection angle and grain boundary character distributions would be preferred.

Watanabe (1984) was the first to propose the general concept of grain boundary engineering, which includes control of the distribution of grain boundary structures to improve the properties of polycrystalline materials. Producing steel with an increased density of low angle and special grain boundaries would require great control over the thermo-mechanical processing and the technological and economical feasibility on the industrial scale has not been addressed. Most of the work on increasing the proportion of special grain boundaries has focused on increasing the proportion of $\Sigma = 3$ boundaries in the form of annealing twins (Randle 1999). The processing used to introduce a high level of annealing twins fall into multi or single-step recrystallization annealing or multi or single-step strain annealing. No papers have yet been published on how to increase the number of special grain boundaries in bcc iron, although, it has been inferred that increasing the crystallographic texture should increase the proportion of low angle boundaries. For instance, one can calculate the grain boundary structure distribution by assuming a grain shape and an orientation distribution. The prospect of increasing the texture to such an extent as to toughen an IF steel while simultaneously keeping the properties necessary for good formability is questionable.

The grain boundary plane has been shown to be important for a variety of physical properties. Coincidence at the grain boundary can deviate significantly from the highest density of coincident sites. Grain boundary planes can be determined using EBSD, but this requires serial sectioning a known amount of material and thereby determining the orientation of the plane (Randle 1992). The grain boundary plane was not obtained in the present analysis. In the present case, the grain boundary plane could be more easily determined as the fracture path was analyzed before fracture and the intergranular crack is completely opened exposing the grain facets. Therefore, a stereological method could be used to obtain the orientation of the grain boundary plane. Special boundaries that fractured could then be reanalyzed to determine the planar coincidence site density.

5.0

5.10 Kinetics of Grain Boundary Segregation During Recrystallization Annealing of Cold Worked Interstitial-Free Sheet Steel

The amount of grain boundary segregation and the embrittling power of the segregant determines the degree of grain boundary embrittlement in low alloy steels. Therefore, an understanding of the kinetics of grain boundary segregation occurring during the thermo-mechanical processing is important, as equilibrium segregation conditions are not necessarily encountered. To date, the kinetics of grain boundary segregation has been modeled by assuming a static grain boundary (McLean 1956, Tyson 1978) and a local equilibrium at the grain boundary-bulk interface. The final processing stage for IF sheet steel involves annealing the highly cold worked steel; during annealing the process of grain boundary segregation occurs concurrently with the recovery, recrystallization and grain growth. The grain boundaries are not static during the annealing cycle, and it therefore must be determined whether the process of grain boundary migration affects the kinetics of segregation.

Direct evidence of phosphorus segregation to the grain boundaries was obtained with analytical transmission electron microscopy. Different levels of segregant were found for the batch and continuous recrystallization annealing heat treatments. The amount of segregant at the boundary was shown to directly influence the susceptibility to CWE; the batch annealed steel had higher levels of phosphorus residing at the grain boundary and had a higher transition temperature as compared to the continuously annealed steel. Grain boundary structure was found to exert influence upon the local segregation levels (Boyle et al. 1998) and the probability of intergranular fracture on a local scale (section 4.11).

To explore these issues, a model was developed to predict the kinetics of grain boundary segregation of phosphorus in IF steel taking into account the dynamic process of grain boundary migration during the recrystallization annealing process. Cahn's model of solute drag (Cahn 1962) was used to determine the grain boundary velocity and concentration associated with the dynamic equilibrium for the moving grain boundary. The boundary was assumed to migrate during recrystallization and to be static during grain growth. The kinetics of segregation determined by this approach was then compared to the kinetics of segregation when the grain boundary is assumed to remain static through the entire process. Isothermal annealing profiles and time-temperature profiles associated with batch and continuous annealing were simulated. The analysis is extended to include the local grain boundary structure.

5.10.1Solute Drag

When a steady state velocity is reached during grain boundary migration, (i.e. $dv/dt = 0$ where v is the grain boundary velocity), the driving force can be equated to the sum of the resistive forces (equation 5.14). Various

resistive forces to grain boundary migration can be encountered. These include forces exerted by crystalline imperfection such as vacancies, dislocations, or external crystal surfaces, or by precipitates or solute atoms (Bauer 1974). The interaction of solute with a moving boundary has been termed solute drag. A force balance, considering only the intrinsic grain boundary drag and the solute drag as resistive forces, may then be written as,

$$F_{driving} = F_{instrinsic} + F_{solutedrag} \tag{5.14}$$

F can be thought of as a pressure or force per unit area (N/m^2), or an energy per unit volume (J/m^3). For recrystallization, the driving force is usually found to be proportional to the steady state grain boundary velocity. The constant of proportionality, M in m^4/Js, is a mobility term which can be separated into an intrinsic grain boundary mobility, M_i, and a mobility due to solute being dragged with the boundary, M_s,

$$F_{driving} = v\left[\frac{1}{M_i} + \frac{1}{M_s}\right] \tag{5.15}$$

The theoretical foundations for solute drag are given by Cahn (1962), Lücke and Stüwe (1971), and Hillert and Sundman (1976). The approach developed by Cahn for solute drag in a binary system is followed with the basic principles outlined below. The chemical potential of the impurity species is assumed to be given by, $\mu_2 = kT \ln C_2(x) + \Delta g_s(x) + const.$ The free energy of segregation, $\Delta g_s(x)$, is a function of position across the boundary and for the dilute solution approximation the constant is chosen such that $\Delta g_s(\infty) = 0$. The flux of atoms, J, is written in terms of a mobility, a concentration, C, and a driving force, $\partial\mu/\partial x$. For an ideal solution,

$$J = -MC\frac{\partial \mu}{\partial x} = -\frac{DC}{kT}\frac{\partial \mu}{\partial x} = D\frac{\partial C}{\partial x} + \frac{DC}{kT}\frac{\partial \Delta g_s}{\partial x} \tag{5.16}$$

where k is Boltzmann's constant, and D is taken equal to the volume diffusion coefficient of the impurity. By applying Fick's second law and changing the coordinate system to be fixed to the grain boundary, i.e. $\frac{\partial c}{\partial t} = 0$, the diffusion equation for a grain boundary moving with a velocity, v, is,

$$0 = \frac{\partial}{\partial x}\left[D\frac{\partial C}{\partial x} + \frac{DC}{kT}\frac{\partial \Delta g_s}{\partial x} + vC\right] \tag{5.17}$$

The equilibrium concentration, C^{ϕ}_{2dyn}, for the moving boundary is given by the solution to equation 5.17 as,

$$C^{\phi}_{2dyn} = C_2^B v \exp\left\{\frac{-\Delta g_s(x)}{kT} - \frac{v}{D_2}\int_{x_o}^{x} d\eta\right\}\frac{1}{D_2}\int_{-\infty}^{x}\exp\left\{\frac{-\Delta g_s(\xi)}{kT} - \frac{v}{D_2}\int_{x_o}^{\xi} d\eta\right\} d\xi \tag{5.18}$$

The equilibrium concentration for a stationary boundary, $v = 0$, the limit to which equation 5.18 approaches, is given by,

$$C_2^{\phi} = C_2^B \exp(\Delta g_s / kT) \tag{5.19}$$

Cahn (1962) assumed a triangular potential well for the grain boundary binding energy. The concentration profiles across the grain boundary for this assumed energy profile are shown in Figure 5.33. The concentration profile becomes asymmetric as the velocity increases. This leads to a retarding or drag pressure exerted by the solute atoms on the grain boundary given by (Cahn 1962),

$$F_{solutedrag} = -N_v \int_{-\infty}^{\infty} (C_2^{\phi} - C_2^B) \frac{d\Delta g_s}{dx} dx \tag{5.20}$$

where N_v is the number of atoms per unit volume.

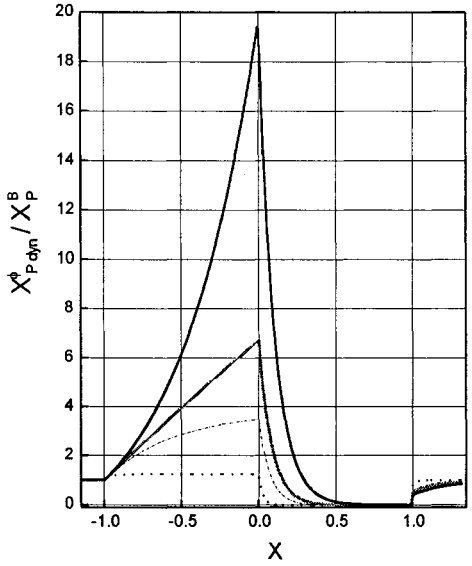

Figure 5.33 - Composition profiles across a moving grain boundary according to Cahn's solution to solute drag for different boundary velocities of P in α-iron using parameters discussed in text.

5.10.2Procedure and Assumptions

The kinetics of grain boundary segregation was modeled by considering the grain boundary moving with a velocity, v, during recrystallization and being static during grain growth. The results of the analysis are referred to as the dynamic results. The dynamic analysis was then compared to the kinetics of segregation where the grain boundary is assumed to remain static throughout the process. During the annealing process strain free grains nucleate and grow, and it is assumed that they instantaneously reach a steady state velocity. Grain boundary migration occurs with this constant velocity until the grains impinge upon other strain free grains at which point grain growth starts. The driving force for recrystallization is assumed to remain constant. During grain growth, the grain boundaries are modeled as static. The grain boundary velocity was solved by using Cahn's approximate solution for the solute drag force and equation 5.12, the force balance, and is given by,

$$F_{driving} = \frac{v}{M_i} + \frac{\alpha X_2^B v}{1 + \beta^2 v^2} \tag{5.21}$$

where,

$$\alpha = \frac{\delta / 2 N_v (kT)^2}{\Delta g_s D_P} \left(\sinh \frac{\Delta g_s}{kT} - \frac{\Delta g_s}{kT} \right) \tag{5.22}$$

$$\beta^2 = \frac{\alpha k T \delta/2}{2N_v \Delta g_s^2 D_P} \tag{5.23}$$

where δ is the grain boundary width. The migration velocity, v, was then substituted into an analytical solution (Bréchet and Purdy 1992) to equation 5.18 for the dynamic equilibrium concentration as a function of grain boundary position,

$$C_{2dyn}^{\phi} = C_2^B \qquad -\delta/2 > x \quad (5.24a)$$

$$C_{2dyn}^{\phi} = C_2^B \frac{\left(1 + a\exp(-V(1+a)(X+1)\right)}{(1+a)} \qquad \delta/2 < x < 0 \quad (5.24b)$$

$$C_{2dyn}^{\phi} = C_2^B \frac{1+\exp(-V(1-a)X)\left(\frac{a(1-a)\exp(-V(1+a))}{(1+a)} - 2\frac{a}{(1-a)}\right)}{(1-a)} \qquad 0 < x < \delta/2 \quad (5.24c)$$

$$C_{2dyn}^{\phi} = C_2^B\left(1+\exp(-VX)\left(\frac{a\exp(-V)}{(1+a)} - 2\frac{a\exp(Va)}{(1-a^2)} + \frac{a\exp(V)}{(1-a)}\right)\right) \qquad x > \delta/2 \quad (5.24d)$$

where

$$a = \left(\frac{D\Delta g_s}{kTv\,\delta/2}\right), \qquad V = \frac{v\delta/2}{D}, \qquad X = \frac{x}{\delta/2} \tag{5.24e}$$

The dynamic equilibrium concentration was solved for at $x = 0$, which gives the maximum concentration for the moving grain boundary. By assuming a distance traveled, 5 μm for a 10 μm grain diameter, until grain impingement and grain growth starts, the velocity also gives the time of flight during which the boundary has the dynamic equilibrium concentration. Once the grain boundary has stopped, the dynamic grain boundary concentration is then taken as the starting concentration for a kinetic analysis based on McLean's analytical solution for grain boundary segregation (equation 2.43).

5.10.2.1 Material Parameters

The rephosphorized IF sheet steel was modeled as a binary alloy with a bulk phosphorus composition of 0.06 wt% (0.0011 mol. fraction). The assumption of a binary alloy is reasonable, as there is typically less than 3 ppm carbon or nitrogen left in solid solution after hot rolling. Grain boundary pinning due to precipitates was ignored in the present analysis. There is little experimental research considering the segregation process during the entire thermo-mechanical history. The amount of phosphorus segregation during the coiling stage of hot rolling determines the segregation level at the grain boundaries prior to recrystallization annealing.

Although a question still remains as to whether phosphorus stays at the grain boundary during the large cold reduction during cold rolling. Therefore, the concentration of phosphorus at the grain boundary prior to annealing must be assumed for the static approach, while it is not required for the dynamic approach. A starting concentration of 0.06 wt.% P was chosen and compared to a starting concentration of 6.0 wt.% P (Figure 5.44).

5.10.2.2 Driving Force for Recrystallization, Driving Pressure Due to Stored Dislocations

During recrystallization, essentially dislocation free grains grow into the highly dislocated surroundings. The decrease in free energy per unit volume (the driving pressure) arises from the elimination of these dislocations during recrystallization. The stored energy per unit volume due to a dislocation density, ρ, can be estimated from,

$$F^{\rho}_{driving} = 0.5\rho G b^2 \qquad (5.25)$$

where G is the shear modulus, and b is Burgers vector of the dislocations. The shear modulus of α-iron is 80 GPa, the magnitude of a Burger's vector, $b = a_o/2\langle 11 1\rangle$, is 2.47-2.76x10^{-10} m, and heavy deformation typical in cold rolled sheet steel the dislocation density is estimated to vary from 10^{15} to 10^{16} m^{-2}. The driving pressure is therefore estimated to be between 2 and 20 MPa. During recovery, dislocations are expected to arrange into a more stable configuration, and as a consequence the driving pressure is estimated to be less than given by equation 5.23, perhaps between 1 and 10 MPa. For instance, Samajdar et. al. (1997) explain sluggish recrystallization kinetics in IF steels on certain grain orientations completely recovering. Enhanced recoverability was in part attributed the the near absence of interstitial elements and second phase particles.

5.10.2.3 Free Energy of Segregation, Binding Energy

A triangular potential well was used for the binding energy of the grain boundary. The depth of the potential well is taken to be $\Delta g_s = \Delta G_s / N_a$ where N_a is the Avogadro constant, 6.023x10^{23} mol^{-1}. The thickness of the grain boundary in Fe, δ, was taken to be three times the lattice parameter, or $\delta = 3 \times 2.86$Å. This corresponds closely to the grain boundary width of 10 Å, as determined experimentally in an IF steel using a three-dimensional atom probe combined with field ion microscopy and a focused ion beam method (Seto et al. 1999).

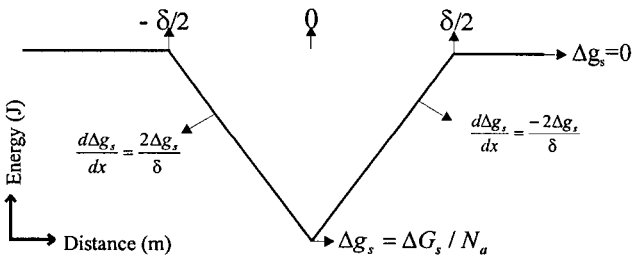

Figure 5.34 - Potential well for free energy of segregation of phosphorus in α-iron.

The molar binding energy of the segregant (free energy of segregation) for phosphorus in α-iron

was taken to be $\Delta G_s = -35000 - 215T$J/mol (Erhart and Grabke 1981). These values were obtained by measuring the mean value of segregation enthalpy and entropy in a binary system from the temperature dependence of averaged concentration of many grain boundary facets using Auger electron spectroscopy (AES) on *in situ* fractured surfaces. Similar values ($\Delta G_s = -33000 - 22T$ J/mol) have been reported for the free energy of segregation of phosphorus in α-iron using AES by averaging well characterized general grain boundaries (Lejcek 1994).

5.10.2.4 Diffusion Coefficient of Phosphorus in α-Iron

There is a large range of values reported for the diffusion coefficient of phosphorus in α-iron, D_P. This is to some extent due to the different experimental methods used, e.g. radioactive tracer method, grain boundary segregation with AES, surface segregation with AES, and microprobe analysis. Different values for D_P are reported in Figure 5.35 below. The value chosen for the analysis, D_P=0.000158exp(-219kJ/RT) m^2/s, was obtained by the radioactive tracer method between the temperature range 973-1173 K (Gruzin and Mural 1964).

5.10.2.5 Intrinsic Grain Boundary Mobility of α-Iron

The value for the intrinsic grain boundary mobility, M_i, in α-iron is not well established. Hillert (1975) has estimated, from grain growth data, the mobility of grain boundaries in pure iron as, M_i= 0.0035exp(-147 160/RT) $m^4/(Js)$. This estimation was based on an estimation of the driving force during grain growth and the assumption of a parabolic law between the average grain diameter and the intrinsic grain boundary mobility. Tsurekawa et al. (1996) have measured the intrinsic mobility in a Fe-3wt.%Si bicrystal as a function of driving pressure. The intrinsic mobility of random grain boundaries was taken from the data to be M_i=0.002exp(-165 000/RT) $m^4/(Js)$. A value between the two reported values, M_i= 0.003exp(-165 000/RT) $m^4/(Js)$, was chosen for the analysis.

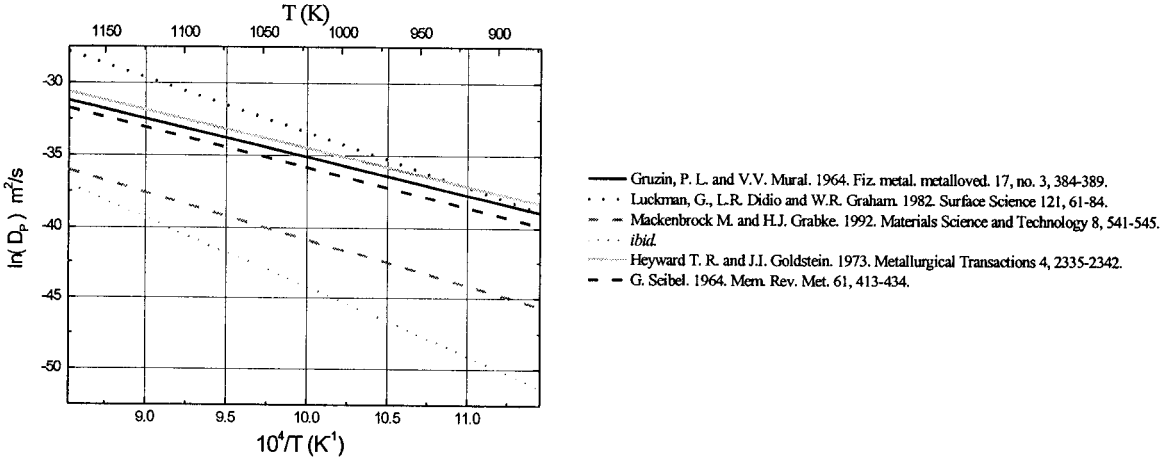

Figure 5.35 - Diffusion coefficient for phosphorus in α-iron, D_P.

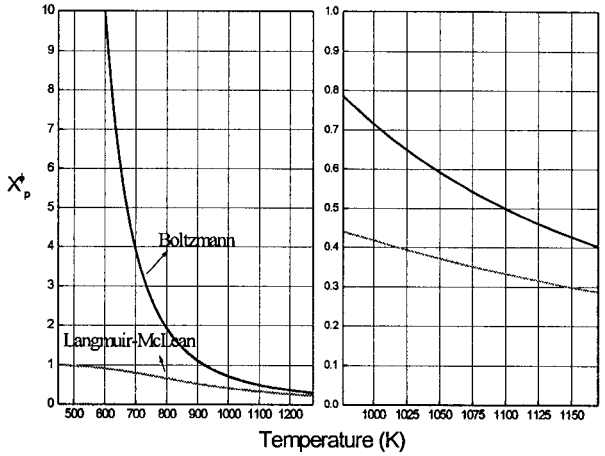

Figure 5.37 - Equilibrium concentration as function of temperature comparing the Boltzmann and Langmuir-McLean isotherms.

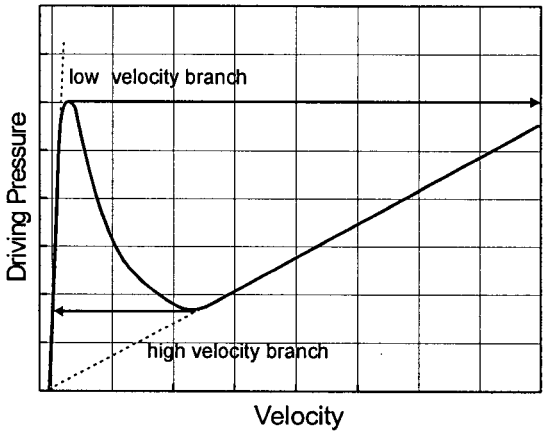

Figure 5.36 - Grain boundary velocity as a function of driving pressure according to Cahn's solution for solute drag showing transition from low to high velocity branch and vice versa.

5.10.2.6 Equilibrium Segregation

The equilibrium grain boundary concentration is plotted as a function of temperature in Figure 5.37 for the isotherms applicable to a binary system using the parameters described above and equations 2.34, 2.35 and 2.37. The Boltzmann isotherm, which assumes a dilute solution and low segregation levels (equation 2.37), deviates considerably from equations 2.34 and 2.35, especially at low temperatures (Figure 5.37). This isotherm assumes no limit to the amount of grain boundary segregation; at 0 K all of the solute would be at the grain boundary at equilibrium. Cahn's solution for the grain boundary concentration approaches the Boltzmann isotherm as the boundary approaches stasis. To overcome this difficulty a modification was made to the grain boundary binding energy for the moving grain boundary; it was forced to follow the Langmuir-McLean isotherm. The binding energy for the moving grain boundary is therefore,

$$\Delta g_{s\,FORCED} = \Delta g_s + kT \ln(1 + C_2^B \exp\frac{-\Delta g_s}{kT}) \qquad (5.26)$$

Therefore, a more realistic impurity concentration is expected for the moving boundary which can now be compared to kinetics of segregation based on Langmuir-McLean isotherm and a static grain boundary.

5.10.3Kinetics of Grain Boundary Segregation During Recrystallization

The grain boundary velocity is plotted as a function of driving pressure in Figure 5.38 for a bulk phosphorus content of 0.01, 0.06 and 0.08 wt% at 973 K and for temperatures of 923 K, 973 K, 1023 K at 0.06wt.% P. Low and high velocity branches are predicted for the temperatures and concentrations of interest. The transition is expected to occur at the local maximum when climbing the low velocity branch, and at the local minimum while coming down the high velocity branch (Figure 5.36). The nature of this transition has implications when

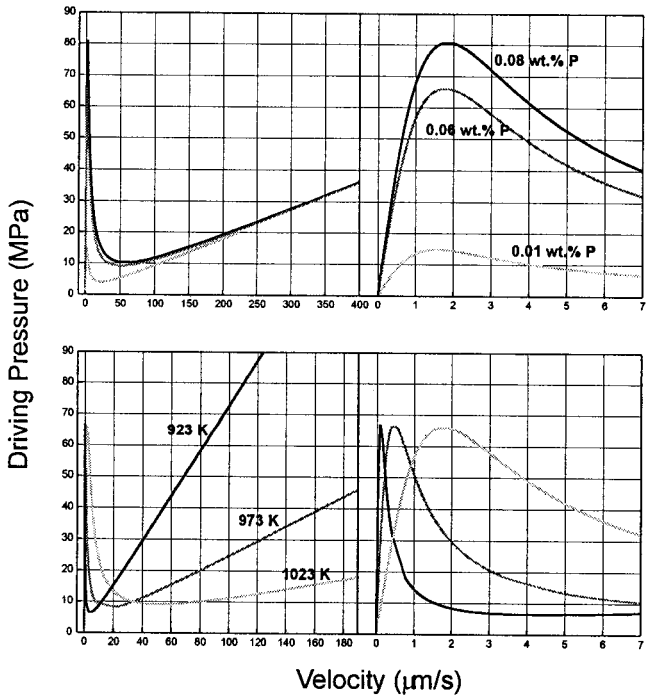

a) 973 K

b) 0.06 wt.%

Figure 5.38 - Relation between grain boundary velocity and driving pressure according to Cahn's solution for solute drag.

considering the transitory period before a dynamic equilibrium is attained. There are two scenarios envisioned for a grain boundary starting from zero velocity. If the initial grain boundary concentration is greater than that given by the dynamic equilibrium, the grain boundary can tear away from the extra solute carrying its dynamic equilibrium concentration. If the grain boundary concentration is less than that given by the dynamic equilibrium, the grain boundary will have a higher velocity, possibly given by the high velocity branch. In this case, the grain boundary will decelerate as it sweeps through and picks up solute, until the dynamic equilibrium concentration and velocity are reached. In either of these cases, a steady state velocity is arrived at quickly, and we can therefore assume that this transitory period is negligible. Experimentally, grain boundary velocities are found to be proportional to the driving pressure, confirming the steady state assumption. As the grain boundaries are starting from a velocity of zero, the local maximum must be reached for a transition to the high velocity branch. For high phosphorus steels, such as those studied in this thesis, the transition driving pressure is above the driving pressures encountered in the recrystallization process. For low phosphorus levels, as found in non-alloyed IF steels, a transition to the high velocity branch is predicted. The implication of this transition will be discussed in the next section.

5.10.3.1 Isothermal Kinetics of Segregation

The kinetic segregation isotherms for the moving grain boundary are compared to those of the static grain boundary for driving pressures of 0, 1, 5 and 20 MPa (Figure 5.39) and a bulk phosphorus concentration of

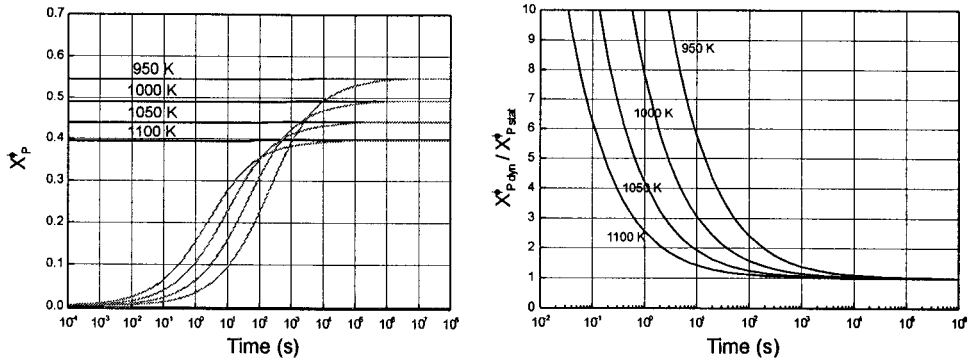

a) F= 1 MPa

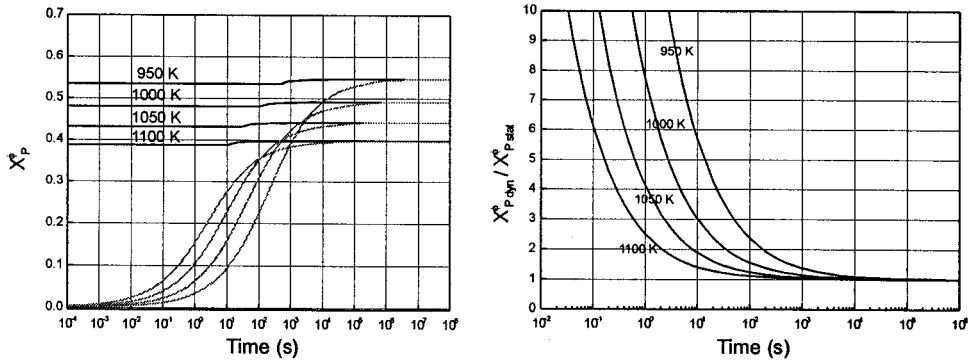

b) F= 5 MPa

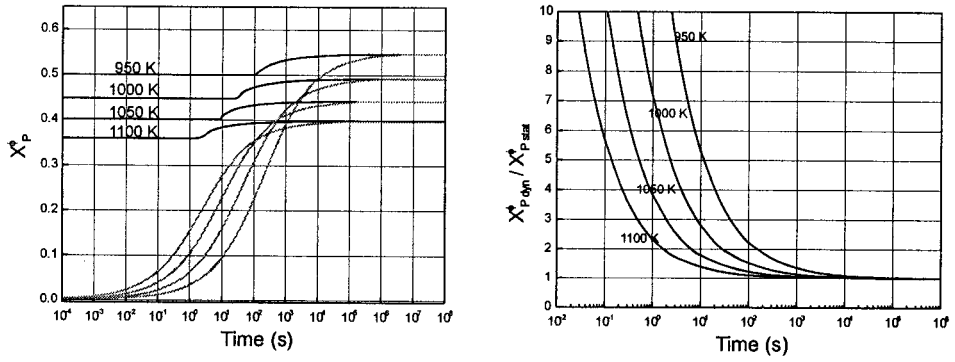

c) F=20 MPa

Figure 5.39 - Segregation isotherms and the ratio of the grain boundary concentrations for dynamic and static approach to the kinetics of grain boundary segregation. The results of the dynamic analysis are black, where the results of the static analysis are grey for X_P^{ϕ} versus time.

0.06 wt.%. The dynamic analysis predicts a significantly higher grain boundary concentration than the kinetic analysis at short times. As time proceeds, the segregation levels predicted by the dynamic analysis approach those predicted by static analysis, as the grain boundary is modeled as being static during grain growth. The ratio of grain boundary concentrations predicted for both approaches ranges from approximately 2.5 to 15

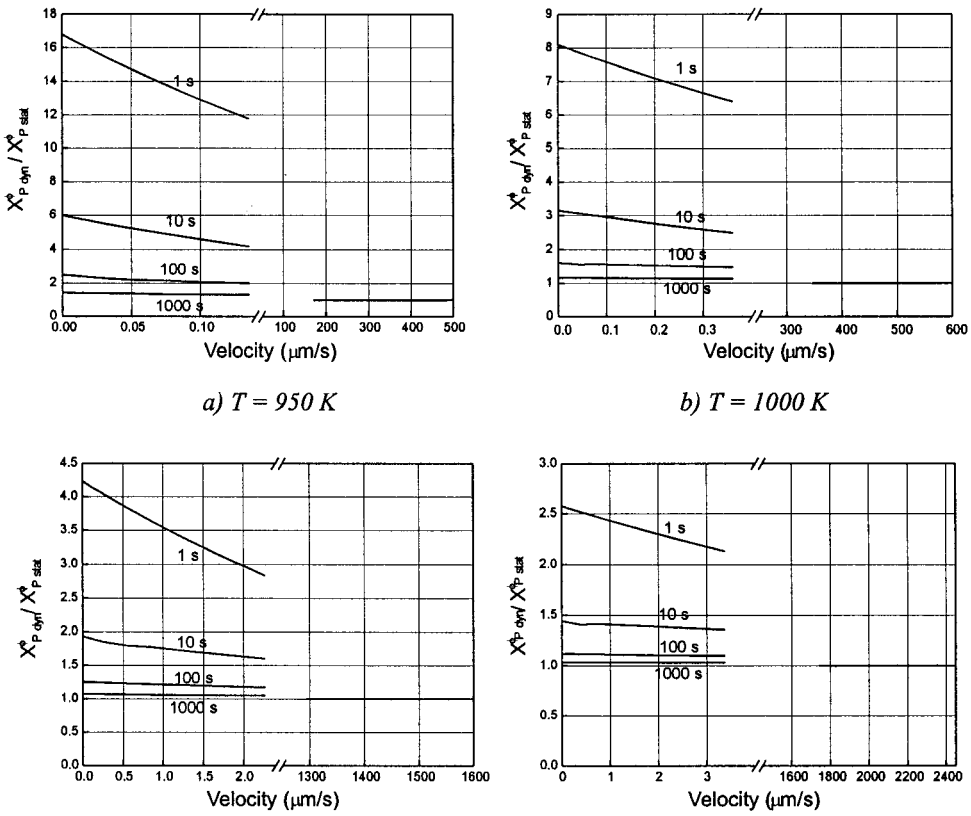

a) T = 950 K *b) T = 1000 K*

c) T =1050 K *d) T = 1100 K*

Figure 5.40 - The concentration ratio, $X^{\phi}_{Pdyn}/X^{\phi}_{Pstat}$, as a function of grain boundary velocity. The grain boundary velocity is fixed by the driving pressure at the temperature of interest for the bulk concentration of 0.06 wt.% P.

times at 1s and converges at 10^4s for typical recrystallization annealing temperatures (Figure 5.39).The difference between the two approaches is greatest for low driving pressures and low temperatures, as the grain boundary is able to retain more solute, and as a consequence is considerably slowed down. As the driving pressure or temperature is increased, the amount of solute the grain boundary can retain is lowered and the velocity of the grain boundary increases. With increased grain boundary velocity the recrystallization stage ends more quickly and the concentration increases according to the analysis based on the static grain boundary. Another way of depicting the difference in segregation kinetics is to plot the ratio of the dynamic and static grain boundary concentrations as a function of the grain boundary velocity for different temperatures (Figure 5.40). The same trends are observed, with increased time the dynamic and static approaches converge to the equilibrium concentration. The transition to the high velocity branch occurs at ~70 MPa for the temperatures considered and is shown on the graphs as a discontinuity in the grain boundary velocity. The transition to the high velocity branch signifies a transition to the static analysis as the grain boundary velocity is high enough that the recrystallization stage ends almost instantaneously. The transition

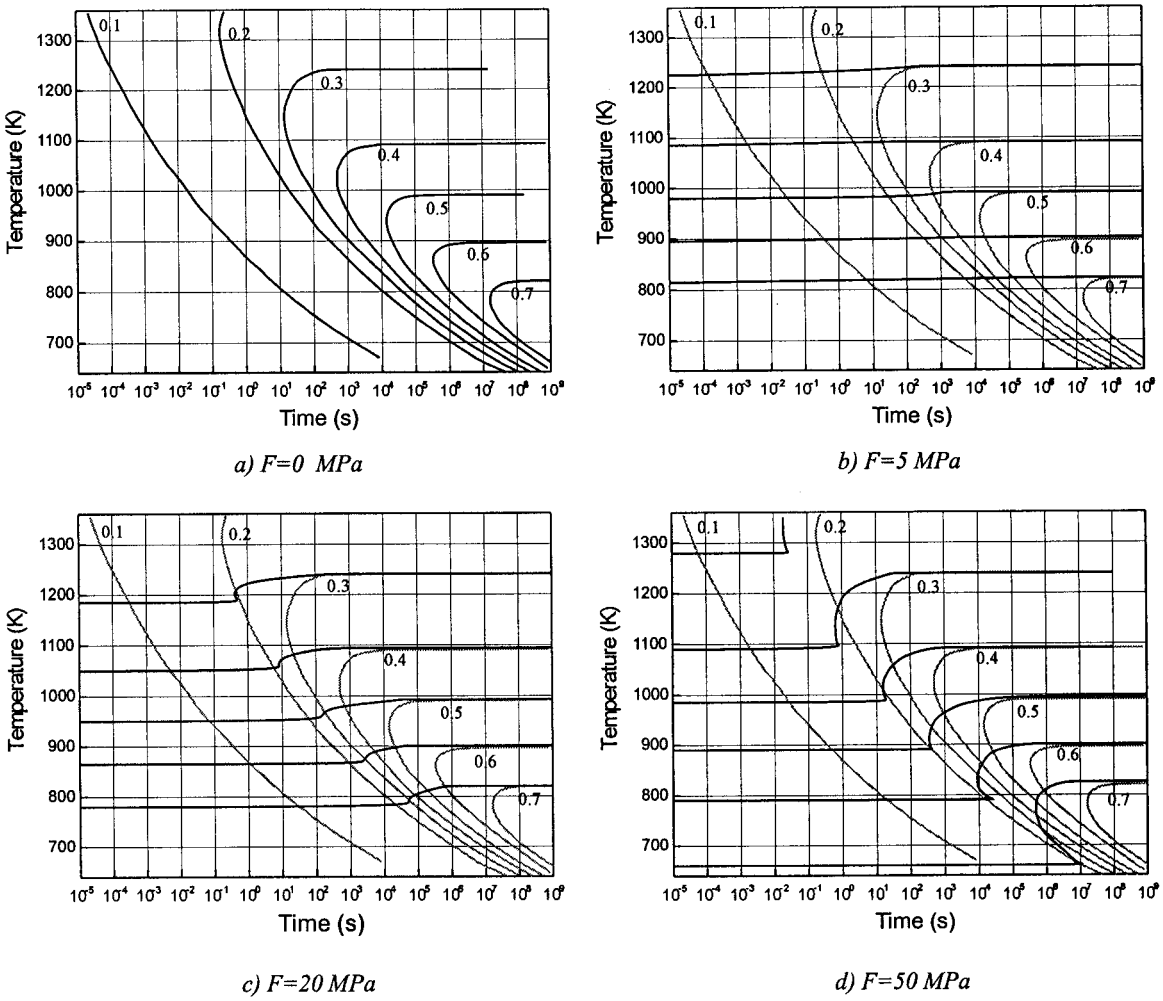

a) F=0 MPa *b) F=5 MPa*

c) F=20 MPa *d) F=50 MPa*

Figure 5.41 - Isoconcentration lines comparing the kinetics of grain boundary segregation for a static grain boundary to a moving grain boundary, for P in -iron, for different driving pressures for

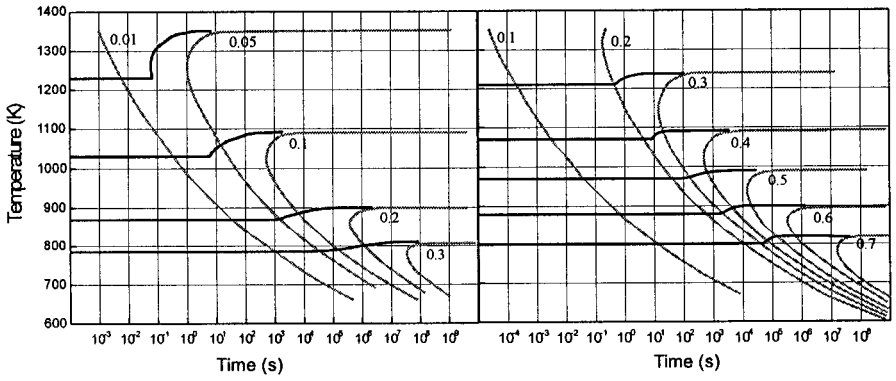

a) 0.01 wt.% P *b) 0.06 wt.% P*

Figure 5.42 - Isoconcentration contours for static and moving grain boundary for concentrations of a) 0.01 and b) 0.06 wt% P and a 10 MPa driving pressure.

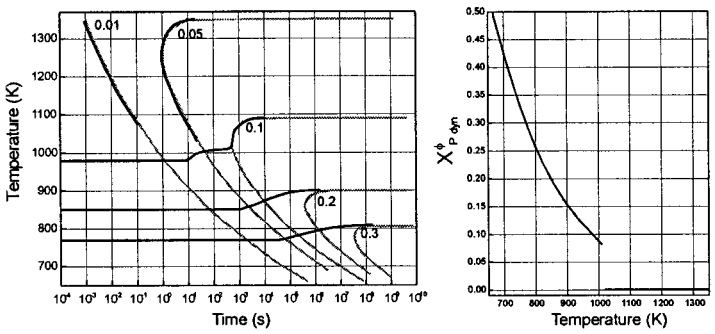

Figure 5.43 - a) Isoconcentration contours for a bulk concentration of 0.01wt% P and a driving pressure of 15 MPa and b) the dynamic equilibrium concentration as a function of temperature for the same conditions.

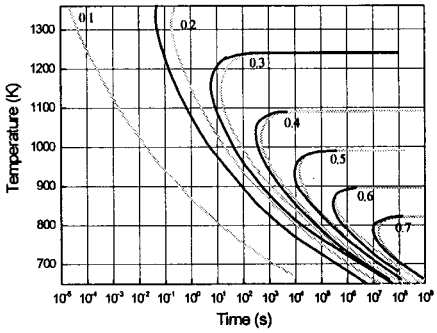

Figure 5.44 - Isoconcentration contours for static grain boundary for an assumed initial grain boundary concentration of 0.06 wt.% and 6.0 wt.%.

from the low velocity branch to the high velocity branch for a bulk concentration of 0.06 wt% P is academic, as 70 MPa is an unrealistically high driving pressure.

The interplay between the driving force for segregation and the diffusion kinetics is best observed when the isotherms are plotted as isoconcentration lines over a large range of temperatures (Figure 5.41). Figure 5.41a) shows the classic c-curve kinetics for a static grain boundary. The isoconcentration contours are modified for the dynamic analysis. When the driving pressure is low, the grain boundary is able to retain a solute concentration near the equilibrium concentration (Figure 5.41b). Therefore, the isoconcentration lines lose the c-curve appearance and become straight lines. At higher driving pressures, the grain boundary is able to retain less solute, the grain boundary has a higher velocity and grain growth starts sooner. Therefore, a transition from constant line contours to c-curve behaviour is observed (Figure 5.41c).

The dynamic analysis is only valid when recrystallization is possible and therefore has a limit which is a function of the driving pressure (e.g. the amount of stored energy due to deformation) and temperature. The dynamic approach to grain boundary segregation is independent of the initial amount of segregant at the grain boundary, unlike solutions based on the Langmuir-McLean kinetics. When the grain boundary starts to move the past segregation history is annihilated and the dynamic grain boundary concentration, given by Cahn's solution, is taken as the initial grain boundary concentration for any further analysis. This is in contrast to the kinetic analysis based on the static grain boundary; the initial concentration at the grain boundary must be assumed. The kinetics can significantly change when a high initial concentration is assumed (Figure 5.44).

Solute drag is highly dependent on the bulk impurity levels as seen in Figure 5.38. In lieu of this, the segregation kinetics are compared for bulk phosphorus levels of 0.01 and 0.06 wt.% and for a driving pressure of 10 MPa (Figure 5.42). These phosphorus levels corresponds to typical levels found in IF sheet steels (0.01 wt.%) and high strength RP IF sheet steels (0.6-0.8 wt.%). The difference in the kinetics is more pronounced

with higher bulk phosphorus levels, and has the same effect as lowering the pressure, the contours lose their c-curve shape. As well, the isoconcentration contours for both the dynamic and static analysis are shifted to higher temperatures and lower times with increasing bulk phosphorus levels.

The transition from a low to high grain boundary velocity is most likely for low phosphorus alloys (e g. Figure 5.38). An isoconcentration map for an alloy with 0.1 wt.% P and driving force of 15 MPa is shown in Figure 5.43. At this driving pressure, a transition to the high velocity branch occurs at 1020 K (Figure 5.43b). This transition can be seen on the 0.1 mol. fraction isoconcentration contour. Above 1020 K, the kinetics follow those given by static analysis. At lower temperatures, the driving pressure is below the maxima required for the transition to the high velocity branch, and the kinetics show the modified c-curve behaviour.

5.10.3.2 Simulation of Kinetics of Segregation for Industrial Recrystallization Annealing

Two annealing treatments are typically used for recrystallization annealing IF sheet steels, batch and continuous annealing. The kinetics of grain boundary segregation were simulated for both annealing treatments by stepping the dynamic and static kinetic analyses through the relevant industrial time-temperature profiles given section 3.2. The effect of heating and cooling rate on the kinetics of grain boundary segregation was also investigated.

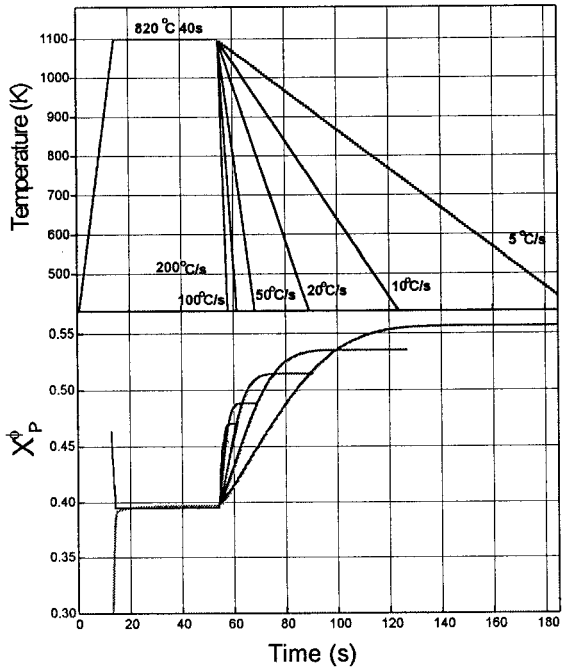

Figure 5.45 - Simulation of segregation kinetics for continuous annealing recrystallization heat treatment, 820°C for 40s, heating rate of 50°C/s and a driving pressure of 2 MPa.

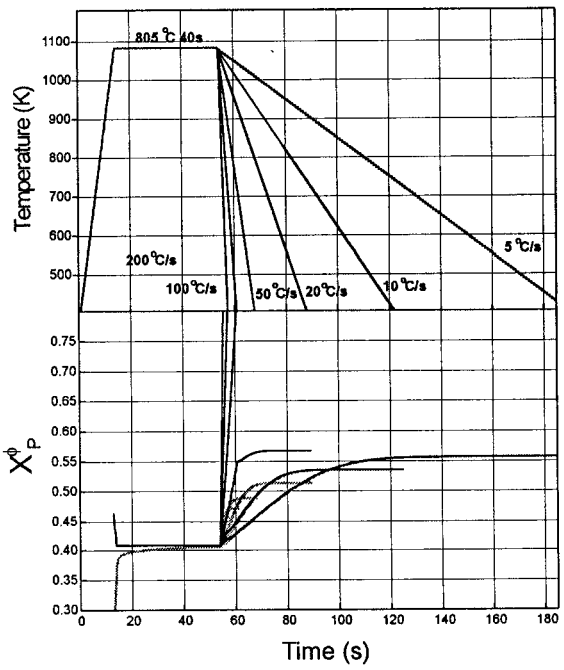

Figure 5.46 - Simulation of segregation kinetics for continuous annealing recrystallization heat treatment, 805°C for 40s, heating rate of 50°C/s and a driving pressure of 2 MPa.

5.10.3.3 Continuous Annealing

Simulations of the kinetics of segregation for continuously annealed steel are compared for hold temperatures of 820, 805 and 790°C, for a heating rate of 50°C/s and cooling rates of 5, 10, 20, 50, 100 and 200°C/s. These are typical annealing temperature used for IF sheet steels and are higher than conventional quality sheet steels due to the sluggish recrystallization behaviour associated with IF steels and to the greater drawing quality required. All of the cooling rates chosen are achieved in practice (ASM Handbook on Heat Treating). At 820°C, the grain boundary concentration for the static boundary essentially approach the static equilibrium concentration by the time the hold temperature has been reached on heating. As the moving grain boundary has a low velocity the grain boundary concentration is close to the static equilibrium value. Therefore, little difference in segregation kinetics is noticed between either approach (Figure 5.45). At 790°C a different situation is observed as recrystallization does not completely finish at any cooling rate. As the temperature is lowered, the grain boundary slows down instantaneously reaching the new dynamic equilibrium concentration. Equilibrium segregant levels are not reached at any temperature during cooling for the static grain boundary. Therefore, a large difference is predicted for the kinetics of segregation at 790°C between both approaches (Figure 5.47). At a hold temperature of 805°C, recrystallization has not been completed at the onset of cooling. For cooling rates of 5°C/s and 10°C/s the grain boundary stops soon after the isothermal hold. A 20°C/s cooling rate is sufficiently fast that the grain boundary stops migrating during cooling. In this case, the grain boundary concentration increases rapidly following the dynamic equilibrium, and when the boundary stops migrating a transition to the more usual kinetics is seen as the concentration levels off to 0.57 mol. fraction. This value compares to a concentration of 0.51 mol. fraction for the fully static case. The grain boundaries do not cease migrating for cooling rates of 50, 100 or 200°C/s, and therefore X_P^{ϕ} approaches saturation as the temperature is lowered. These results suggest that the kinetics of segregation will be very different if the grain boundary is still moving during cooling. The implications apply to situations where the cooling schedule is modified to alleviate grain boundary segregation.

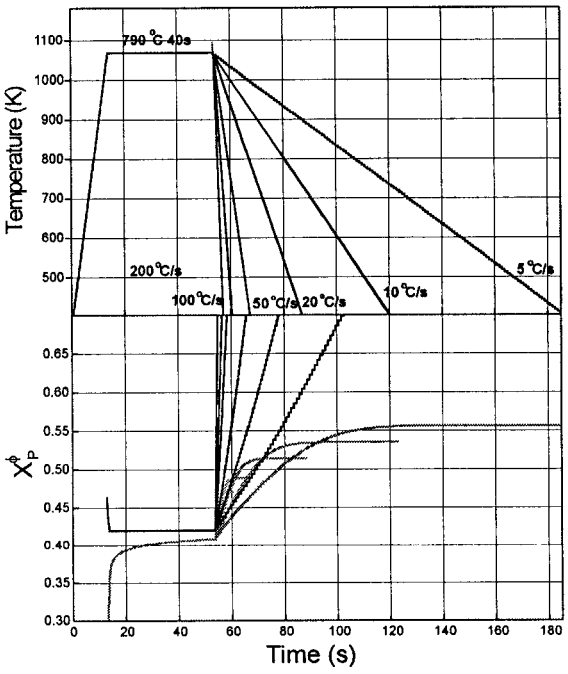

Figure 5.47 - Simulation of segregation kinetics for continuous annealing recrystallization heat treatment, 790°C for 40s, heating rate of 50°C/s and a driving pressure of 2 MPa.

The assumption of instantaneously reaching dynamic equilibrium is suspect, especially for fast cooling rates at low temperatures. For these cases the grain

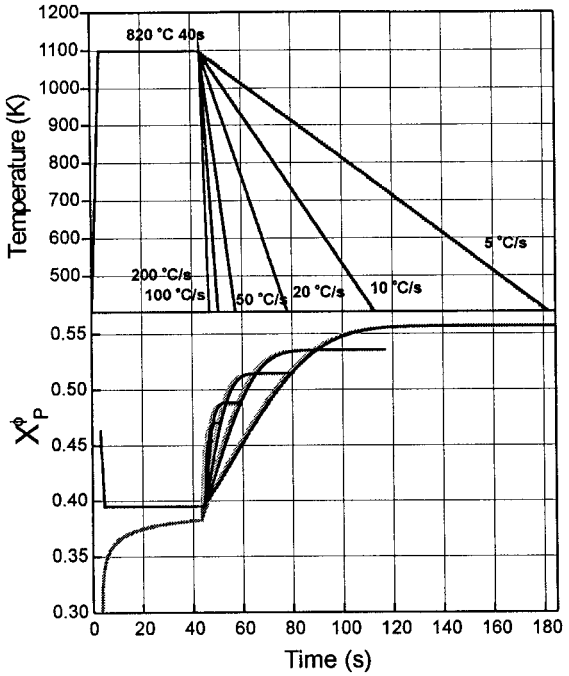

Figure 5.48 - Simulation of segregation kinetics for continuous annealing recrystallization heat treatment, 820°C for 40s, heating rate 200°C/s and a driving pressure of 2 MPa.

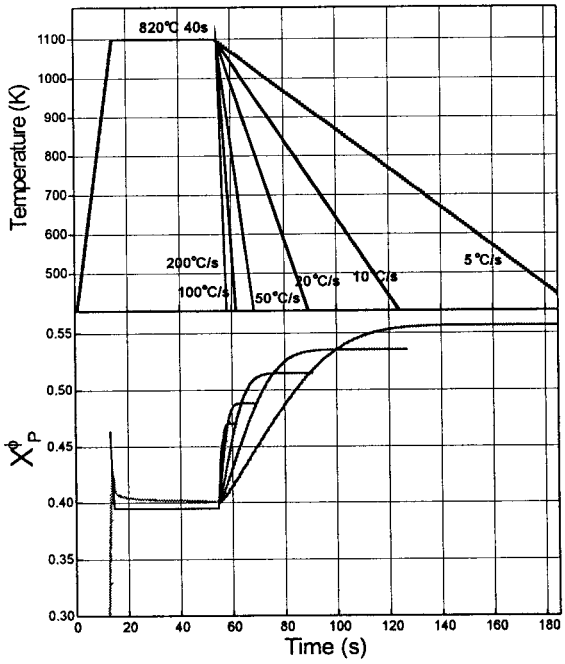

Figure 5.49 - Simulation of segregation kinetics for continuous annealing recrystallization heat treatment, 820°C for 40s, heating rate 15°C/s and a driving pressure of 2 MPa.

boundary could be in a transition to dynamic equilibrium. In any case, the moving boundary sweeping segregant will ensure that the kinetics of segregation are faster than those given by the static grain boundary.

Faster heating rates, for a given hold temperature, will lead to greater differences between the grain boundary concentrations at short times. Figures 5.48, 5.45 and 5.49 compare heating rates of 200°C/s, 50°C/s and 15°C/s for a hold temperature of 820°C. If the heating rate during continuous annealing does not affect the recrystallization start temperature, the segregation kinetics based on a moving grain boundary would not be affected. The heating rate does effect the segregation kinetics for a static boundary; at 200°C/s (Figure 5.48) the boundary has yet to reach the equilibrium concentration by the end of the isothermal hold, while at 15°C/s the grain boundary has yet to desegregate to the equilibrium concentration by the end of the isothermal hold (Figure 5.49).

5.10.3.4 Batch Annealing

The kinetics of segregation for batch annealing with a hold temperature of 690°C are compared for different heating and cooling rates and hold times (Figure 5.50). Recrystallization is assumed to commence at the start of the isothermal hold. The dynamic analysis predicts a grain boundary concentration below that predicted by the static analysis at the start of migration, but after some time the solutions converge and there is no difference

for any cooling rate chosen. Therefore the unexpected increase in grain boundary concentration upon cooling is not anticipated for batch annealing as the time of flight at this temperature and concentration is an order of magnitude less than the hold time.

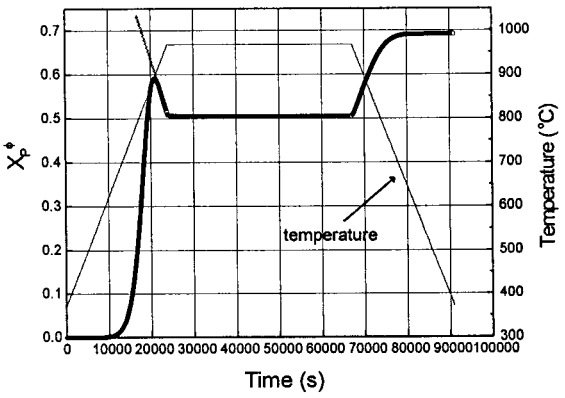

Figure 5.50 - Simulation of segregation kinetics for comparing industrial batch annealing with industrial continuous annealing heat treatment for both dynamic and static analysis.

5.10.4Implications of Modeling Kinetics of Segregation for Moving Grain Boundary

No experimental evidence was obtained to prove or refute the general trends predicted by the model. A direct method for investigating the predictions of the model would be to compare measured segregation levels for migrated and static grain boundaries at short isothermal annealing times using an analytical method such as FEGSTEM coupled with XEDS or AES. This could be accomplished in the Fe-P system by solution treating samples at high temperatures to evaporate the phosphorus residing at the grain boundary which would have accumulated during previous thermo-mechanical treatments. Of course this approach is complicated by the ferrite-to-austenite phase transformation at ~910°C, which effectively limits the lower bound on the initial grain boundary concentration. Samples would be deformed and heat treated. The heat treatments, stopped before the completion of recrystallization, would be repeated on the undeformed material. A low isothermal annealing temperature, sufficient to recrystallize the highly deformed material, would be chosen to maximum the difference in the initial and dynamic equilibrium concentrations. Significant differences in the level of grain boundary segregation between the undeformed and recrystallized samples would then confirm the predictions of the model .

Although there has been little experimental work on segregation during recrystallization annealing, Chéron et al. (1994) have studied the surface segregation of phosphorus during rapid recrystallization annealing of a low carbon steel by AES. It was concluded that rapid recrystallization annealing induces very rapid phosphorus segregation to the surface. It was proposed that the high levels of phosphorus very rapidly accumulate at the moving grain boundaries and dislocations, which then also act as a path for pipe diffusion to the free surface. Similar work was also performed on nickel with impurity levels of sulphur (Saindrenan et al. 1989). Segregation of sulphur to the free surface of nickel during recrystallization and grain growth at 600°C was divided into three stages, an initial very rapid stage, a subsequent rapid stage, and a final leveling off. The stages roughly correspond to primary recrystallization, grain growth, and grain boundary stasis. The work described above essentially supports the main findings of the modeling: the kinetics are significantly changed by the process of recrystallization, and therefore to model the segregation behaviour properly one must take into account the dynamics of the moving grain boundary.

An important implication that arises from these simulations is the influence of segregation on the recrystallization kinetics. Although not the focus of the present investigation, phosphorus is predicted to considerably slow the recrystallization kinetics. Consequently, experiments to this effect would give evidence supporting grain boundary migration with a velocity given by the low velocity branch. A grain boundary moving with an intrinsic velocity would not be influenced by the solute concentration (Figure 5.38). Inagaki (1988) has studied recrystallization kinetics in high purity Fe-P alloys (to 0.22 wt.%P) cold rolled 70%. Phosphorus was found to have a strong retarding effect on the recrystallization kinetics for all concentration ranges studied. The recrystallization behaviour at 550 °C is plotted in Figure 5.51. The general conclusions are quite repeatable, for instance Leslie, Michalak and Aul (1963) also found that recrystallization kinetics of high purity iron were considerably retarded by the addition of 0.028 wt.% P.

The segregation levels predicted from the modeling are based on binding energies calculated from segregation levels measured using AES. Apart from difficulties quantifying the segregation levels using this method, there are other inherent assumptions used to calculate the free energy of segregation that need addressed. These issues are discussed below and arise in part from the AES segregation measurements being performed on samples fractured *in situ*.

Binding energies are calculated from measured equilibrium isothermal segregation levels by choosing a segregation isotherm, such as the Langmuir-McLean isotherm, and by assuming that the segregant is evenly distributed on both halves of the fractured grain boundary facet. The measured segregation levels in polycrystalline materials usually exhibit large scatter from facet to facet. This scatter is partly due to the spectrum of grain boundary structures that are exposed during fracture and as shown in the experimental results, the fracture path is not random, general grain boundaries are more frequently cracked.

Therefore, various schemes have been proposed to determine the free energy of segregation. The concentration of many grain boundary facets can be averaged to obtain an average free energy of segregation, $\Delta\overline{G}_s$. Alternatively, the maximum concentration can be chosen as was done by Tatsumi et al. (1986). The maximum can be ascribed to general grain boundaries, which are assumed to behave similar to one another and therefore have similar free energies of segregation. The spectrum of measured concentrations can

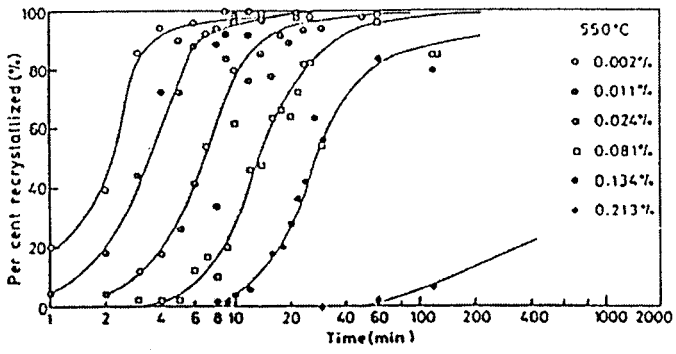

Figure 5.51 - Recrystallization behaviour as a function of phosphorus content in cold rolled high purity iron at 550°C (Inagaki 1988).

be converted into a spectrum of binding energies, but the spectrum of grain boundary structures for the fractured grains cannot be determined with AES. A more physically sound method to determine the thermodynamic properties of the grain boundary is to measure the free energy of segregation on well-characterized bicrystals. This approach has been used by Lejcek and Hofmann (1991) for Fe-3.55at.%Si-0.0089at.%P-0.014at.%C tilt bicrystals characterized for the grain boundary structure. The segregation enthalpies and entropies for phosphorus for [100] symmetrical tilt boundaries are listed in Table IV-I. The free energy of segregation increases with decreasing coincidence and according to their results, grain boundaries $\geq \Sigma = 17$ are not special.

The variation in the segregant concentration on individual facets is often found to be quite uniform, for instance within 5-10%. Although, a uniform facet concentration is not always the case as was shown for $\Sigma = 5(013)$ bicrystals of Fe-3wt.%Si doped with 270 ppm P (Menyhard et al. 1991). Significant variation in phosphorus concentration was found on the fracture surface. When matching spots on opposite sides of the fracture surface were compared, a phosphorus ratio of 2 to 1 was observed. The non-uniform phosphorus distribution was associated with deformation markings, many of which appeared to be mechanical twins. The crack propagated off center switching from one side of the boundary to the other. Mechanical twinning is not associated with all intergranular fractures, therefore non-uniformities in concentration must not be a general phenomenon. In most studies, only one side of the fractured facet is measured and is assumed to hold half of the grain boundary segregant. This assumption could therefore lead to errors in determining the grain boundary chemistry and associated binding energies. The proper ratio of segregant on the matching facets must also depend on the grain boundary structure.

Depth resolution for AES must be considered when measuring grain boundary segregation. The depth of resolution will depend on the energy of the Auger electrons being emitted, and is expected to be less than 0.5 nm for phosphorus. Therefore, the concentration is averaged over a finite depth near the maximum position of the potential well, but it is not necessarily at the maximum. The segregation modeling implicitly assumed that the concentration measured with AES was the maximum concentration in the solute distribution and was therefore the maximum binding energy. Details of the distribution profile of segregant across the grain boundary is important when comparing the kinetics of segregation modeling with the quantitative AEM.

Table IV-III Segregation enthalpies and entropies for [100] symmetrical tilt grain boundaries

Boundary	Σ	ΔH_P^o	ΔS_P^o
{012}	5	-10.3	43.0
{013}	5	-12.5	45.9
{015}	13	-15	39.0
{014}	17	-33	20.0
{059}	53	-32	21.0
{058}	89	-35	18.0
{0 7 15}	137	-29	26.0
{0 5 12}	189	-34	20.0

Analytical transmission electron microscopy can be used to overcome many of the difficulties related to AES. Segregation levels can be measured and quantified, and the associated grain

boundary structure can be determined in great detail. Grain boundaries that do not fracture open, e.g. non-embrittled grain boundaries, can also be analyzed. Therefore, analytical TEM is a powerful tool for studying grain boundaries and grain boundary segregation. As well, errors in quantifying the grain boundary segregant due to errors in measuring the foil thickness can be reduced by using foils thin enough to neglect beam broadening as referenced in section 3.12.

The usual method (Doig and Flewitt 1978, Baumann and Williams 1981, Skogsmo and Atrens 1994) of correcting for beam broadening in spot mode was followed. The segregant is assumed to be contained within a layer of width, δ, and the level of segregant within this level is assumed to be constant. The assumption of a square potential well is applicable to AES as discussed, but for AEM the whole grain boundary width is sampled (for most cases) and therefore the actual distribution profile across the boundary must be considered. As discussed, the concentration profile across the grain boundary is not constant as is usually assumed, and can be approximated by a triangular distribution. Therefore, the segregation levels are re-quantified by assuming a triangular potential well of varying widths. The maximum level of segregant for a triangular distribution profile is twice that for a square distribution profile for the same width of grain boundary. If we assume that the width of a monolayer type segregation of constant concentration is about one lattice spacing, a_o, then the maximum concentration at the grain boundary for a triangular potential well is,

$$X^{\phi}_{2^{MAX}} = \frac{2}{\Lambda} X^{\phi}_{2^{Square}} \qquad (5.27)$$

where $\delta = \Lambda a_o$ gives the width of the boundary. The segregation levels for an incident electron beam of 2 nm penetrating a foil a thickness 125 nm, are calculated for different grain boundary widths for square and triangular potential wells (Table V-II). The geometry for the potential wells is given in Figure 5.52. Therefore, assuming monolayer type segregation will only give the correct maximum concentration for a triangular potential well of width $2a_o$. As the grain boundary width increases, the inaccuracy of assuming monolayer type segregation increases. The average segregation levels at the maximum in the triangular potential well for widths between 3 to 5×2.86 Å are 0.258-0.156 and 0.858-0.516 mol. fraction P for the continuously and batch annealed materials respectively. These maximum values are the correct values to compare to the kinetics of segregation simulations. The corrected segregation levels measured using quantitative AEM show that the batch annealed material has segregation levels ~3.3 times higher than those of the continuously annealed material, while the

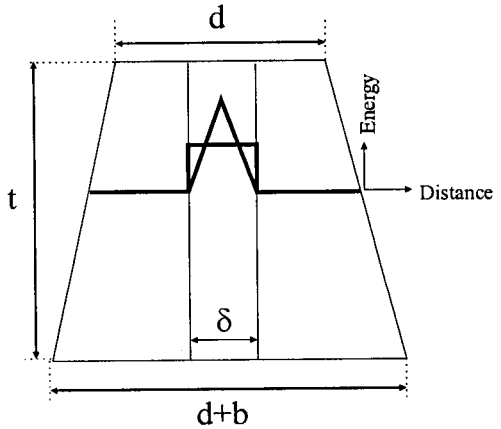

Figure 5.52 - Geometry for an incident electron beam penetrating a grain boundary with a triangular or square concentration profile of width δ

kinetics of segregation simulations predict segregation levels for the batch annealed material ~2.5 times higher than those for the continuously annealed material. The absolute values compare most favourable for a grain boundary width of ~3.5× 2.86 Å .

Table V-IV Corrected segregation levels for different grain boundary widths for triangular and square potential wells

	CA	mol.	BA	mol.
δ (Å)	■	▲	■	▲
a_o	0.384	0.768	1.284	2.568
$2a_o$	0.192	0.384	0.643	1.286
$3a_o$	0.129	0.258	0.429	0.858
$4a_o$	0.097	0.194	0.322	0.644
$5a_o$	0.078	0.156	0.258	0.516

The fracture path analysis (section 4.10) demonstrates a correlation between the probability of fracture and the grain boundary structure. Low angle boundaries were found to be resistant to fracture and have no measurable phosphorus segregation. Special grain boundaries were found to be less resistant to fracture than the low angle boundaries but more resistant to fracture than general grain boundaries. Therefore, the segregation analysis can be extended to consider the specific grain boundary structure. Here we assume that the grain boundary width is constant, although in reality it is a function of the grain boundary structure. A continuous potential well is used; the sites potentials are averaged over some length of grain boundary. The actual potential well profiles for different grain boundary structures would have to be determined from atomistic studies, but for simplicity a triangular potential well is used. Therefore, potential wells can be constructed for these three classes of grain boundaries to extend the analysis to include grain boundary structure as shown in Figure 5.53.

Values for the entropy of segregation reported in Table IV-I, lead to higher binding energies for the special boundaries as compared to the general boundaries at temperatures greater than ~1000K. Lecjek and Hofmann (1991) attribute the unrealistically high values to systematic error arising from uncertainties in the measurement of bulk phosphorus concentrations and they concluded that the segregation enthalpies have greater validity. The segregation levels for a boundary with low free volume must be lower than those for a boundary with higher free volume. A better value for entropy can be obtained by assuming that the binding energies for different grain boundary structures converge as the melting temperature is approached, although there is no physical basis for the entropies to converge as the melting temperature (or equivalently a phase boundary) is approached. Grain boundaries do not melt much below the melting temperature of the bulk solid, for example melting occurs heterogeneously at grain boundaries at ~0.98T_M (Howe 1997). Therefore, using Lindemann's model (Tabor 1991, 269-270) to approximate the melting temperature for α-iron and taking the segregation enthalpies to be correct, gives a better estimate of the segregation entropies. The new values of the segregation entropies are listed in Table IV-II. The binding energies and segregant concentration for the different boundary structures now converge at 1800 K.

No values for the free energy of segregation for low angle boundaries have been reported in the literature, as low angle boundaries are resistant to fracture. An estimate can be made for the low angle grain boundary

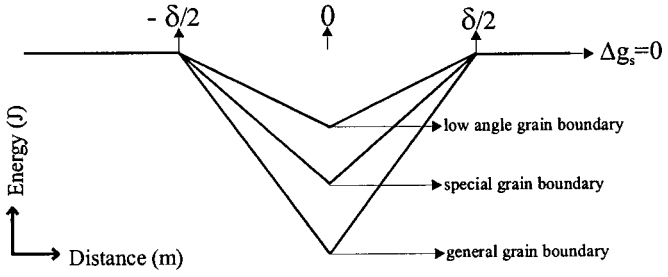

Figure 5.53- Modified potential well for different grain boundary structures.

Table IV-V Segregation enthalpies and entropies for P in α-iron according to grain boundary structure

Boundary	Σ	ΔH_P^o	ΔS_P^o
low	1	-5000	38.2
special	5	-10000	35.4
special	13	-15000	32.6
general	≥Σ17	-35000	21.5

binding energy from the quantitative AEM analysis. As no phosphorus was detected at low angle grain boundaries (Boyle et al. 1997, Perovic et al. 2001) the amount of grain boundary segregation must be less than the detectability capabilities of the JEOL 2010 FEGSTEM. Correcting for beam spreading using a triangular potential well of width $3a_o$ allows for a maximum concentration of 0.2 mol. fraction P at low angle boundaries in either the batch or continuously annealed steels. Therefore, the low angle grain boundary binding energy must be below the value reported for the symmetrical tilt boundaries (Lejcek and Hofmann 1991) and must produce a final segregation concentration at or below the detectability limit for continuous and batch annealing simulations. The free energy of segregation of phosphorus in iron for low angle grain boundaries is therefore taken to be $\Delta G_s^P = -5000 - 38.2T$J/mol. Classification of the binding energies according to grain boundary structure can be used together with the MDF to calculate a true average segregation level for any given distribution of grain boundary structures.

5.0

5.11 Suggestions for Reducing Impact of Cold Work Embrittlement

Although the focus of this thesis was to gain a more fundamental understanding of CWE, suggestions for preventing CWE in the engineering context are discussed. Grain shape, grain boundary chemistry and the level of work hardening are controlling microstructural features for CWE. Improvements in CWE resistance therefore focus on changing these microstructural features.

Present methods for improving susceptibility to CWE focus on controlling steel chemistry and have focused on leaving small amount of carbon in solution or adding small quantities of boron. Carbon in solid solution degrades the formation of favourable recrystallization texture for good formability (Ray, Jonas and Hook 1994). Boron additions can have adverse effects including increased hardenability, which delays the recrystallization of austenite and leads to increased hot rolling loads. Boron also raises the ferrite recrystallization temperature and reduces the r-value, again through degrading the recrystallization texture. Therefore, the extent to which carbon and boron can be added is limited: boron additions higher than ~12 ppm are tied up as precipitates, and small quantities of carbon left in solution form bake hardenable grades but formability degrades with increasing carbon levels (Ray, Jonas and Hook 1994).

The effectiveness of carbon and boron at preventing CWE will depend on the amount of embrittling elements present. For instance, boron additions effectively decreased the transition temperature but did not prevent increased transition temperatures with increased phosphorus (Figure 2.6). The same trend is observed for carbon, higher levels of free carbon are needed to counteract higher levels of phosphorus (Figure 2.7). Therefore, high levels of boron and carbon are needed to remedy CWE for high strength IF steel, but as mentioned a loss in formability and ease of processing are encountered. Moreover, the effectiveness of boron and carbon additions decrease with large deep drawing strains (Figure 5.23). The competition between IGF and TGF does not just depend on the cohesive strength of the grain boundary but also on the ability of an initiated crack to propagate. Therefore, alternative methods for lessening CWE are worth exploring, and can be used in tandem with chemistry modifications to effectively nullify CWE.

A novel method of introducing carbon into IF sheet steel is by controlling the atmosphere during continuous annealing (Kitamura, Tsukatani and Inoue 1994). Carburizing after recrystallization, at 850°C for 60s in a 10 vol.% H_2-N_2 and 3 vol.% CO gaseous atmosphere, did not degrade the r-value and increased the resistance to CWE. Therefore, carburizing after recrystallization is a viable method for obtaining a premium deep drawing quality steel, while controlling the bake hardening and decreasing the susceptibility to CWE.

As the elongated morphology of the grains develop with deformation, the IGF fracture stress develops in an anisotropic manner. The most susceptible deformation path is deep drawing, with a secondary operation

having a tensile component in the prior compressive direction. Susceptibility to CWE can be reduced by careful control of the secondary working process. The general idea is to avoid subjecting highly flattened grains to a tensile component. Otherwise, secondary operations on highly deep drawn material should be conducted under large hydrostatic pressures if the secondary operation has a tensile component acting against the flattened grains. Hydrostatic pressure shifts the yield surface without affecting the IGF surface (Figure 5.6), allowing plastic flow prior to brittle fracture.

Recrystallization annealing controls the local chemistry of the cold rolled and annealed sheet. In the rephosphorized IF steel studied, batch annealing resulted in phosphorus levels at general grain boundaries ~2.5 times higher compared to continuous annealing. This increased phosphorus segregation results in a 50 MPa decrease in the IGF stress. The influence of segregation on the fracture stress will depend on the grain size (Figure 5.14). The influence of holding time is not as significant for a moving boundary as the boundary attains the dynamic equilibrium concentration instantly and for the low driving pressures predicted for IF steels (1-3 MPa) the dynamic equilibrium is close to the static equilibrium. Hold temperature and cooling rate are the controlling variables, although cooling rate dominates. Therefore continuous annealing is advised, as the hold temperature is higher and fast cooling is not viable for batch annealing. Simulations of the kinetics of segregation (section 5.10) for continuous annealing indicate that the cooling rate control the final segregation level (e.g. differences in dynamic equilibrium concentrations are not significant for between 790°C and 850°C). Cooling must be started after the material is fully recrystallized (i.e. when the boundaries have stopped moving) as the kinetics of segregation for a moving boundary is accelerated as the boundary moves towards to the solute. If cooling commences with the grain boundary moving, large levels of segregation are predicted (Figures 5.46 and 5.47). Manipulating the thermal cycle to control the grain boundary phosphorus levels therefore involves annealing at a high temperature (e.g. 840°C) of sufficient hold time to ensure the completion of recrystallization and cooling at a fast rate (e.g. 100°C/s) to prevent phosphorus accumulation.

Recrystallization annealing successfully returns the transition temperature to that of the undeformed material. The dramatic decrease in transition temperature is due to the decreased flow stress and the return of equiaxed grains. In many situations, the loss in strength that accompanies recrystallization annealing is not acceptable. Therefore, local recrystallization annealing of highly deep drawn areas before secondary working or on the finished part would reduce CWE and leave the part with sufficient strength. This could be accomplished with laser heat treatments of confined areas.

Grain refinement leads to increased strength and increased toughness as the brittle fracture stress increases more than the yield strength, i.e. $k_f > k_y$. The potential for significant strengthening has led to the current interest in achieving ultra-fine grain sizes (<1 μm) in many structural materials. A novel thermo-mechanical processing has recently been applied to achieve ultra-fine grain sizes in IF sheet steel (Saito et al. 1999). There have been questions as to the stability of ultra-fine grain sizes. Decreasing the grain size from 10 μm to 5 μm is

more technologically feasible and will not lead to gross plastic instabilities. For the rephosphorized IF sheet steel used in this thesis, a reduction in grain diameter to 5 μm will increase the IGF stress to 1345 MPa (e.g. see Figure 2.25) and the yield stress at ambient temperatures to roughly 240 MPa. The same approach used to derive the transition temperature as a function of the applied effective strain (Figure 5.20) is used for a grain size of 5 μm. The results, shown in Figure 5.54, predict significant improvements in transition temperatures, for instance, the transition temperature decreases from -5°C to -80°C for an effective deep drawing strain of 0.6. Grain size refinement serves to strengthen and significantly decreases the susceptibility to CWE for highly embrittled steels and is therefore highly desirable.

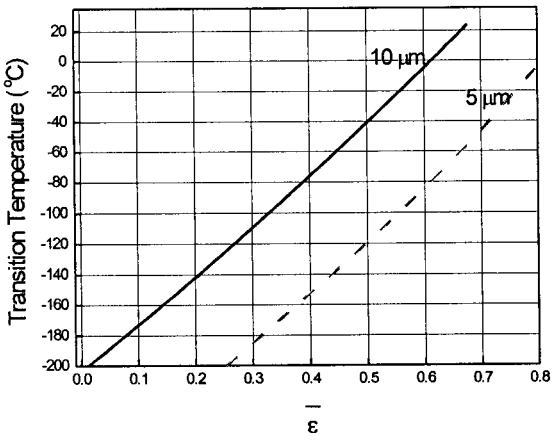

Figure 5.54 - Transition temperature as a function of draw ratio for a change in grain size for rephosphorized unprotected grade of IF sheet steel.

Low angle grain boundaries are resistance to IGF. Therefore increasing the density of low angle and special boundaries in IF sheet steel would increase the toughness, although as discussed a critical level of low angle and special boundaries would be required. At present no method for increasing the density of special grain boundaries in alpha-iron has been published.

A little used method to engineer grain boundaries for resistant to IGF involves controlling the smoothness of the grain facets. Irregular, undulating and jagged grain boundaries have increased resistance to IGF as the altered grain boundary configuration prevents crack propagation along the grain boundaries. Sadosvsky, Bogacheva and Umova (1972) used special heat treatments to change the configuration of austenitic grain boundaries in a grade of steel susceptible to temper embrittlement. The fracture mode changed from intergranular to transgranular when the grain boundaries were changed from smooth to jagged and irregular. An example of smooth and irregular boundaries is shown in Figures 5.55a and b. Increased irregularity in the grain boundary shape has been observed in the hot rolled steel compared to the cold rolled and annealed steel in the present work (Figure 4.1). The undulations on the grain facets caused by large deformations are not sufficient to prevent IGF (Figure 4.69). Therefore a critical level of tortuosity in the grain boundary morphology is required to impede IGF. The required tortuosity could be achieved through the promotion of massive ferrite (also called quasi-polygonal ferrite) or bainitic ferrite. Massive ferrite is achievable in IF sheet steels within reasonable cooling rates with the addition of small amounts of boron, which serves to delay the austenite to ferrite transformation kinetics (Krielaart et al. 1998). Reduced grain size accompanies massive ferrite formation, and therefore the grain raggedness, size and shape, and proportion of polygonal to massive ferrite could be controlled for optimal formability and CWE resistance. Changing the grain boundary

morphology through special heat treatments would be highly effective in increasing the resistance to IGF and CWE.

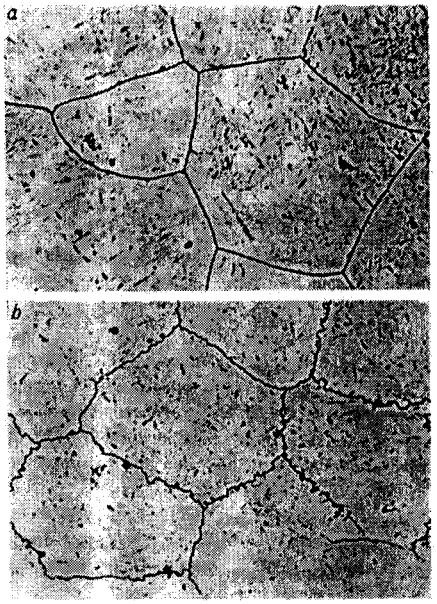

Figure 5.55 - Smooth and jagged grains (Sadosvsky, Bogacheva and Umova 1972).

Galvannealed coating is known to increase CWE; this increase is especially pronounced for high phosphorus grades of IF sheet steel. Increasing the resistance to CWE by other means, such as by increasing the cohesive strength of the grain boundary, reduces the influence of the galvannealed coating on CWE. Moreover, the coating can be tailored to increase the resistance to CWE by considering the coating as a functionally graded layer. During galvannealing the Fe-Zn compounds form in order of increasing iron content, the highest iron intermetallic is the gamma layer which is also the most brittle. A fully alloyed coating appears at longer times and higher temperatures and is characterized by a thicker gamma layer and possible cracks in the delta layer (Marder 1990, 1991). As the iron content of the coating increases, i.e. the gamma and delta layers thicken, the amount of powdering increases. Transition temperatures have been measured as a function of iron content in the galvannealed coating on a low phosphorus Ti-stabilized IF sheet steel (Figure 5.56) (Lau, De Cooman and Vermeulen 1998). Decreased transition temperatures with higher iron content were attributed to cracks in the delta layer deflecting into the gamma layer and delaminating the coating from the substrate, as opposed to penetrating into the ferrite substrate (Tokunaga 1986). Powdering is undesirable for good formability. At low iron contents (less than 4%) the galvannealed coating is not fully alloyed and has good resistance to CWE (Figure 5.56). Reducing the thickness of the delta layer increases the resistance to powdering. Evidently, increasing the thickness of the delta layer leads to larger cracks and more crack propagation, although this can be offset by crack deflection into the gamma layer with increasing gamma layer thickness, at the expense of powdering. Therefore, unalloyed layers with thin delta and gamma layers would reduce the size of the surface defects, and increase the adherence of the coating compared to a fully alloyed coating.

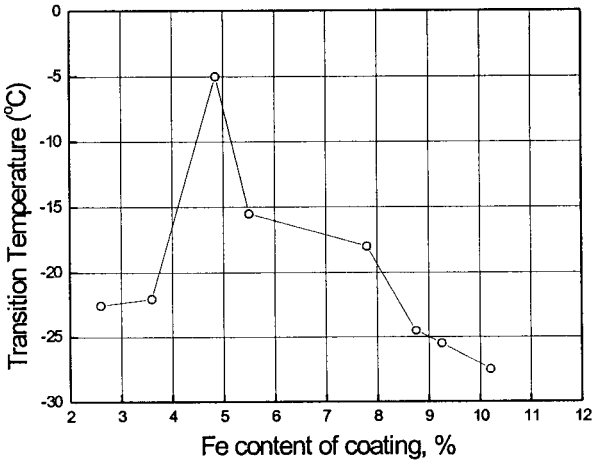

Figure 5.56 - Variation of transition temperature as a function of Fe content in the galvannealed coating of Ti-Nb stabilized low phosphorus IF sheet steel (Lau, De Cooman and Vermeulen 1998)

6.0 CONCLUSIONS

The primary focus of this study was to gain a more fundamental understanding of CWE in interstitial-free sheet steel. The origin of amplified intergranular fragility with deep drawing deformation had not previously been determined, although the possible roles of grain shape and residual stresses have been referred to in the literature. A rephosphorized grade of IF sheet steel was chosen as a model material to study CWE, as it exhibited nearly complete intergranular fracture below the transition temperature even in the undeformed state. The main conclusion deduced from the experimental results coupled with fracture modeling, was that grain shape controls intergranular fracture (for a given grain boundary cohesive strength) during sheet metal forming operations. This resulted in a deformation path dependent criterion for intergranular fracture.

A fundamental understanding of the mechanisms and micro-mechanics of intergranular fracture are necessary to fully understand CWE. Cold work embrittlement is associated with intergranular fracture, which can compete with other modes of fracture such as transgranular fracture and ductile fracture. In general, brittle fracture mechanisms compete with plastic flow and strain localization during deformation, and therefore CWE was studied within this framework. Brittle intergranular fracture in IF sheet steels was determined to be propagation controlled, with the grain size dependence of the fracture stress arising due to the size of the initiated crack scaling with the grain facet size. A combination of different variables controls the susceptibility to CWE. These include deformation path (only deep drawn material is susceptible to CWE in the plane of the sheet), steel chemistry (only steel susceptible to intergranular fracture will be compromised) and the amount of deep drawing deformation (increased deep drawing deformation increase the CWE response to other variables). The experimental results indicated that the key microstructural feature controlling CWE was the grain shape, and that the grain shape must be taken into account in order to rationalize the transition temperature observed in deformed material.

Incorporating grain shape allowed the intergranular fracture stress to be predicted for any deformation path. In essence, a grain shape, and hence strain path, dependent critical local mode I stress intensity (or local strain energy release rate) was used as the criterion for brittle intergranular propagation. The modeling results indicated that intergranular fracture is not expected for primary forming operations, a change of strain path (or stress state) is needed and deep drawing is the deformation path most susceptible to CWE, in agreement with known experimental results. Deep drawing is the most severe forming operation with regards to CWE as strain localization is delayed for deep drawing and therefore ample work hardening and large changes in grain shape are permitted, and the change in grain shape is such that the flattened grains are susceptible to in-planar tensile stresses. Grains flattened in the plane of the sheet, such as during cold rolling, are not commonly cracked since

through-thickness tensile stresses are not prevalent during forming operations. Fracture maps, depicting the evolution of the fracture and yield surfaces with deformation, were constructed and allowed predictions of the transition temperature for different deformation paths and changes in deformation path for any planar stress state. The evolution of the intergranular fracture stress in the prior compressive direction after deep drawing was studied in detail. Modeling results indicated that the IGF stress can decrease in the prior compressive direction from, for instance, 1000 MPa for the undeformed material to 640 MPa for material deep drawn to a true effective strain of 0.65.

The competition between intergranular and transgranular fracture was included in the model to extend the understanding gained from the modeling and experimental work to other grades of IF sheet steel. Transition temperatures were predicted to increase gradually for material resistant to intergranular fracture; the increase is solely due to work hardening. Samples that fail by intergranular fracture have higher transition temperatures and increase more rapidly than transgranular fracture. Results indicated that the change in transition temperature with deformation was most severe for material undergoing a transition form transgranular to intergranular fracture. Steels that are resistant to CWE and fail by transgranular fracture at low deformations can become highly susceptible to CWE at high deep drawing deformations as the fracture mode changes to intergranular fracture.

The transition temperature has been defined as the temperature where the yield stress equals the fracture stress. Therefore the response of the transition temperature to changes in external variables depends on the gradient of the flow curve at the point of intersection. If the fracture stress intersects the flow curve where it rapidly changes with temperature, small shifts in either the fracture stress or flow curve will not lead to large changes in transition temperature. Conversely, if the fracture stress intersects the flow curve where it slowly changes with temperature, small shifts in either the fracture stress or flow curve will lead to large changes in transition temperature. Rephosphorized steels, without free carbon or added boron, can become highly sensitized to CWE with large deep drawing deformations, in part due to the higher yield stress and the lowered intergranular fracture stress with the added phosphorus. Fracture that remains transgranular, even at very high level of deformation, will not become highly sensitized, as the fracture stress does not decrease appreciably with deep drawing deformation.

Macroscopic residual stresses induced during deep drawing were found not to influence the transition temperature. This result, which at first seems counter intuitive as the residual stresses can be quite large, can be rationalized by realizing that the residual stress state aids both fracture and flow equally. Any constraint induced by the biaxiality will depend on the relative shapes of the flow and fracture surface with respect to the state of stress, but for most cases the effect will be negligible.

Low angle boundaries were found to be resistant to intergranular fracture. Increasing the density of resistant grain boundaries in grades susceptible to intergranular fracture could potentially increase the resistance to CWE. It has not been determined if this approach is feasible.

Local grain boundary chemistry controls the cohesive strength of the grain boundary and the propensity for intergranular fracture. For cold rolled steels, solute segregates during the final thermal processing heat treatment, a recrystallization annealing heat treatment. A new approach was used to model the segregation kinetics, which accounted for the process of grain boundary migration. Cahn's theory of solute drag (1962) was used to determine the velocity and concentration associated with the dynamic equilibrium for the moving grain boundary. Much higher segregation levels were predicted at short times, compared to models that assume the grain boundary remains static. The results suggested that one cannot separate the migration from segregation as is commonly done. Quantitative analytical electron microscopy detected higher levels of phosphorus segregation for batch annealed steel as opposed to continuously annealed steel. The higher level of segregation resulted in a greater susceptibility to CWE, especially for severe deep drawing.

Through experiments and modeling, quantitative capabilities for predicting failure by CWE were developed and can be applied to any strain path for any chemistry of IF steel sheet. For proper predictive capability the flow properties must be accurately characterized as a function of deformation, temperature and strain rate, i.e. good constitutive laws are required. The criterion for intergranular fracture developed in this thesis can be programmed into finite element modeling for sheet metal forming simulations. Inputs needed are the IGF stress for undeformed material and the transgranular fracture stress for a given grain size. Only one data point is needed for each as fracture stress varies linearly with the inverse square root of grain size. A good estimate of the intergranular fracture stress can be made by measuring the proportion of intergranular and transgranular fracture on a cup tested below the transition temperature. As the transgranular fracture stress is essentially only a function of grain size, an estimate of the IGF stress can be made by referring to Figure 5.23.

6.1 Future Work

Very few studies have measured changes in brittle intergranular fracture stress with grain morphology; notable exceptions include the work or Zok (1988) and Richards, Reid and Smallman (1969). Measurement of the IGF stress in the prior compressive direction after deep drawing deformation has not yet been accomplished. A systematic study to measure the effect of grain shape on the intergranular fracture stress is proposed. A change from thin sheet to a bulk material is suggested. The iron-phosphorus system has an advantage over the copper-bismuth system for instance, as iron can be worked above a certain temperature, while bismuth embrittled copper must be worked under hydrostatic pressure to prevent intergranular damage and failure. Phosphorus embrittled iron rod, of sufficient diameter to cut tensile sub-size tensile specimens in the radial direction, would be hot rolled (e.g. with 90 degree rotations after each pass) or swaged to produce highly flattened grain in the radial direction. These highly flattened grains could then be tested in tension by cutting

sub-size tensile specimens in the radial direction as a function of swaging deformation. As mentioned, the shape of the intergranular fracture surface can indicate the most appropriate criterion for IGF and could be probed by testing notched specimens of different notch acuity.

Extending the fracture modeling to predict the scatter in the measured fracture stress could be accomplished by developing a physically based statistical model. Grain size (e.g. crack size), the resulting deflection angle and grain boundary structure distributions, as well as the competition between intergranular and transgranular fracture, could be used to predict the fracture stress as a function of grain shape.

In many grades of IF sheet steel, carbon and/or boron segregate to the grain boundary and may compete with phosphorus for grain boundary sites. Therefore, extending the kinetics of segregation modeling to a multi-component system may be most appropriate. For segregation in a ternary system without chemical interactions between species, an interactive approach may be used to obtain the solute profile and the resulting drag force. For elements that chemically interact, two aspects of the solute drag need considered; the ability of the solute to keep up with the boundary (i.e. the diffusivity) and the ability of the grain boundary to drag the solute (i.e. the binding energy). At the boundary the cross-interaction terms (equation 2.40) become significant with increased solute enrichment and therefore the diffusivities and binding energies will both be modified. The difficulty lies in determining appropriate interaction coefficients, as the nature of the solvent-solute and solute-solute interactions may be changed at the grain boundary as compared to the bulk. For instance, interactions due to elastic strain energies could change at the grain boundary.

APPENDIX

A.0 Physical Metallurgy of Interstitial-Free Steels

The basic metallurgy of IF sheet steels will be reviewed very briefly with the intent to familiarize the reader with the terminology used throughout this text and with the class of steels used in this thesis and most susceptible to CWE.

A.1 *Historical Development*

Vacuum degassing was applied in the 1950s and 1960s to make cleaner steels with more precise and uniform chemistry. Most of the products made by the vacuum degassing process were forging ingots, wrought bars, tube products and large castings. It was realized in the early fifties that titanium could be added in quantities of about 4 to 5 times the carbon content to improve the mechanical properties of low-carbon steel by forming compounds with C, N, and S. The earliest titanium treated IF steels were developed and produced in the late 1960s and early 1970s. The first type of Ti stabilized ordinary IF steel was developed at the Yawata Iron and Steel Co. Ltd. (now Nippon Steel Corp.). Armco Steel Corp. (now AK Steel Corp.) was the first US steelmaker to make IF steel starting in 1970. The term 'I-F Steel' was a registered trade mark of Armco Steel Corp. Most major steel companies were producing IF grades by the early to late 1980s. This early titanium treated IF steel had better deep drawing quality compared to low carbon Al killed deep drawing quality steel but required further degassing and Ti alloying. Typically the amount of Ti and/or Nb added was considerably more than needed to combine with the free C and N. This made the steel very expensive to produce and consequently this grade of steel was used only in small quantities for applications such as oil pans which required excellent deep drawability.

The development of ultra low carbon (ULC) IF steel came about as a result of the introduction to steelmaking technology of the bottom blown converter and a reformed RH vacuum degasser, which enabled significantly lower C and N levels to be attained consistently and economically. The use of IF steel started to increase substantially in the late 1980s and early 1990s with the realization of better production facilities in the continuous annealing and hot dip coating lines, the increasingly stringent requirements with respect to the material properties for sheet steels, and a greater demand for such steels by the automotive industry. The improvement in the vacuum degassing allows the carbon content of the sheet steels to be precisely controlled with carbon levels < 50 ppm or even < 30 ppm. Steels with this low carbon content are called ultra low carbon (ULC) steels or extra low carbon steels (ELC). With sophisticated steelmaking and casting technology the nitrogen can be limited to < 30 ppm. This class of IF steels has improved properties compared to other deep

drawing quality steels (DDQ) steels. These include improved formability through improved recrystallization textures, no aging or pronounced yield point elongation and a lower yield stress.

A.2 *Grades of Interstitial-Free Sheet Steel*

To improve the formability and strain aging properties it is necessary to remove the the interstitial carbon and nitrogen from solid solution. Titanium and/or niobium are added to effectively tie up the carbon and nitrogen in the form of carbides and nitrides. Interstitial-free steels are often classified according to the elements used for stabilization (Table A1-I).

Table A.1-I IF steel classified according to stabilizing

grade
Ti
Ti-Nb
Nb

Table A1-II The effect of substitutional alloying elements on TS

element	amount	Increase in TS
Mn	0.01 wt.%	0.4 MPa
Si	0.01 wt.%	1.0 MPa
P	0.01 wt.%	10 MPa

Interstitial-free steels are also classified according to their mechanical properties. Typical IF steels have a yield strength between 115 and 180 MPa whereas high strength IF steels typically have a yield strength between 220-320 MPa. Substitutional alloying elements such as Mn, Si and P are used to strengthen IF steels. Phosphorus is the most widely used because is has little adverse effect on the formability compared to the other elements. Phosphorus increases the strength most effectively (Table A1-II) and therefore less P has to be added compared to the other elements. Phosphorus also increases the phosphatability of the steel. The disadvantage is the increased susceptibility to cold work embrittlement. Silicon is rarely used to strengthen IF sheet steels as it degrades the phosphatability (Tokunaga and Kato 1990) and the hot dip galvanizability and increases cold work embrittlement. The addition of Mn is costly as it often has to be added in the form of carbon free metallic manganese and in greater quantities than P or Si to achieve the same amount of strengthening.

IF steels can be produced as deep-drawing quality (DDQ) steel, super extra DDQ or as a high-strength IF steel with excellent formability. The r-value and the total elongation for different drawing quality classifications are shown in Figure A.1.

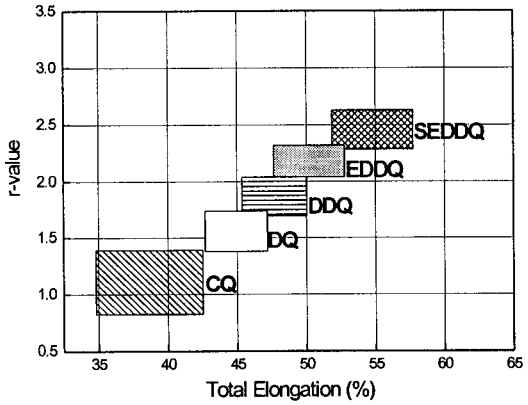

Figure A.1- Classification of drawing quality according to r-value and total elongation.

B.0 Circumferential Strain Rate During Cup Expansion Test

A simple model was used to derive the circumferential strain rate during the cup expansion test. The velocity of the ram, when dropped from a height, Δh, is $v = \sqrt{2g\Delta h}$. The circumferential strain of the deep drawn cup is, $d\varepsilon = \frac{dl}{l}$, where $l = 2\pi r$ is the circumferential perimeter of the cup. The strain rate is therefore $\frac{d\varepsilon}{dt} = \frac{dl}{dt}\frac{1}{l}$. Replacing the rate of circumferential lengthening by a radial expansion gives, $\frac{d\varepsilon}{dt} = \frac{2\pi dr}{dt}\frac{1}{2\pi r}$. The velocity of the ram must then be converted into a circumferential rate of expansion. From Figure C.2 we can see that the circumferential rate of expansion, $\frac{dr}{dt}$, given in terms of the ram velocity, v, is, $\frac{dr}{dt} = \frac{dh}{dt}\frac{1}{\tan\theta_p} = \frac{v}{\tan\theta_p}$. Therefore,

$$\dot{\varepsilon}_{CET} = \frac{1}{r}\frac{v}{\tan\theta_p} \qquad \text{(B.1)}$$

This equation predicts that as θ_p approaches zero, the strain rate approaches an infinite value. This limit is conceptually valid but in practice the cup would buckle as θ_p approaches zero. As well, frictional effects have been ignored. Friction between the cup and workpiece would increase with decreasing die angle as the resolved forces normal to the punch are increased.

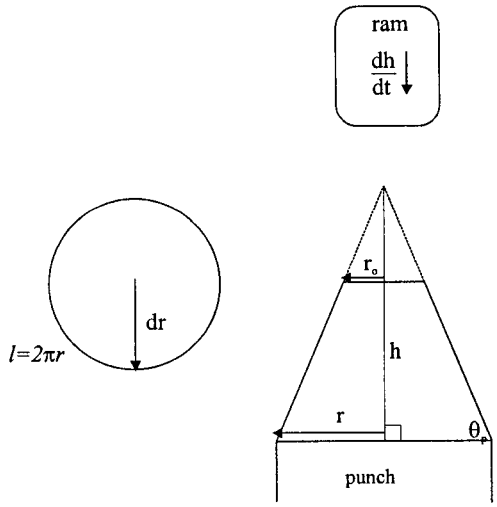

Figure B.2- Schematic of geometry used to derive the circumferential strain rate for a given ram velocity in the cup expansion test.

C.0 Bending During Cup Drawing

A general analysis of pure bending is used to calculate the residual stress distribution acting to open the circumferentially cut ring or longitudinally cut tongue. The coordinate system used in the bend analysis is shown in Figure C.1. The pure bending moment, M, per unit width, w, released is,

$$\frac{M}{w} = \int_{-t/2}^{t/2} \sigma_1 z dz \tag{C.1}$$

$$\frac{M}{w} = 2\int_{0}^{t/2} \sigma_1 z dz \tag{C.2}$$

In thin sheets, normal section planes are assumed to remain plane on bending and the neutral surface remains undeformed and therefore the bending strain is $\varepsilon_1 = \ln(1+z/r)$. The bending moment released remains elastic, therefore the strains are small enough that $\varepsilon_1 \approx z/r$. The appropriate constitutive equation for an elastic material is, $\sigma = A'\varepsilon$. The width of the rings are thin enough such that they are not constrained, therefore, $A' = E$. Therefore,

$$\frac{M}{w} = 2K_s' \int_0^{t/2} \left(\frac{z}{r}\right) z dz \tag{C.3}$$

and integrating gives a general equation for an elastic bending moment released during the springback,

$$\frac{M}{w} = \frac{E}{r}\frac{t^3}{12} \tag{C.4}$$

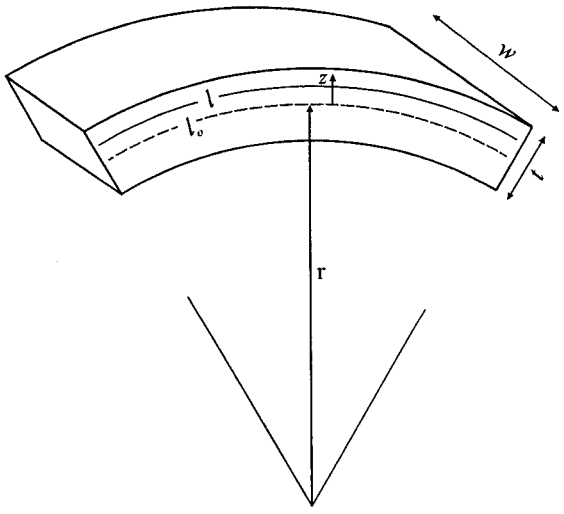

Figure C.1- Coordinate system and notation for analysis of bending.

or

$$\frac{M}{\frac{t^3}{12}} = \frac{E}{r} = \frac{\sigma_1}{z} \tag{C.5}$$

The maximum opening stress occurs at $z = t/2$. Therefore, for the maximum change in residual stress when the ring elastically springs open by $\frac{1}{\Delta r}$ is,

$$\Delta\sigma_1 = \frac{t \cdot E}{2}\frac{1}{\Delta r} \tag{C.6}$$

or

$$\sigma_2 = \frac{t \cdot E}{2}\left(\frac{r_1 - r_o}{r_o r_1}\right) \tag{C.7}$$

This equation applies to the ring opening or to the tongue opening. The curvature of the longitudinal tongues varies with position, therefore we use the relation,

$$\frac{1}{r} = \frac{d^2 y}{dx^2} \tag{C.8}$$

The profile of the tongue is measure before and after slitting to determine the change in curvature. A fifth order polynomial, $y = f(x)$, can be fit to the profile. The unbending residual longitudinal stress is therefore,

$$\sigma_1 = \frac{t \cdot E}{2}\left(y_1'' - y_o''\right) \tag{C.9}$$

REFERENCES

Almond, E. A., D. H. Timbres, and J.D. Embury. 1969. Proceedings of the 2nd International Conference on Fracture. ed. P. L. Pratt. Chapman and Hall, London. 253.

Almond, E. A., D. H. Timbres, and J. D. Embury. 1970. Acta Metallurgica. 971-976.

Almond, E. A. , D. H. Timbres and J. D. Embury. 1971. The Philosophical Magazine 23, no. 184, 971-976.

Armstrong, R.W. 1964. Deformation Twinning. Metallurgical Society of AIME. Gordon and Breach Science Publishers, New York. 356-377.

Armstrong, R.W. 1974. Canadian Metallurgical Quarterly 13, no. 1, 187-202.

ASM Handbook on Heat Treating, 9th Edition, Volume 4. 1991. Continuous Annealing. ASM International, Metals Park. 56-66.

ASM Handbook on Forming and Forging, 9th Edition, Volume 14 .1988. ed. S. L. Semiatin. Deep Drawing. ASM International, Metals Park. 575-590.

Aust, K. T. 1993. Grain Boundary Engineering. CIM, Montreal, 197-228.

Aust, K. T, S. J. Armijo, E.F. Kock and J. A. Westbrook. 1967. Transactions ASM 60, 360.

Backofen, W. A. 1972. Deformation Processing. Addison-Wesley, Don Mills, ON. 227-241.

Balluffi, R. W. 1979. Interfacial Segregation. eds. W. C. Johnson and J. M . Blakely. ASM, Metals Park, Ohio. 193-236.

Bauer, C. L. 1974. Canadian Metallurgical Quarterly 13, no. 1, 303-308.

Baumann, S. F. and D. B. Williams. 1981. Journal of Microscopy 123, pt. 3, 299-305.

Beltz, G. E. and J. R. Rice. 1991. Modeling the Deformation of Crystalline Solids. ed. T.C. Lowe et al. TMS, Warrendale, PA. 457-480.

Bhat, S. P., B. Yan, J. S. Chintamani and T. A. Bloom. 1994. High -Strength Steels for Automotive Symposium Proceedings. ISS, Warrendale, PA. 209-222.

Bilby, B. A., G. E. Cardew and I. C. Howard. 1977. Fracture 77 3, ed. D. M. R. Taplin. University of Waterloo Press, Waterloo, Canada. 197-200.

Bleck, W. and G. Heßling. 2000. IF Steels 2000 Proceedings. ISS, Warrendale, PA. 279-288.

Boyle, K. P., A. Perovic, J. D. Embury, J. G. Thomson, J. E. Hood and D. D. Perovic. 1998. 39th MWSP Conference Proceedings. ISS, Warrendale. 159-165.

Bramfitt, B. L. and A. R. Marder. 1977. Metallurgical Transactions A 8A, 1263-1273.

Brandon, D. G. 1966. Acta Metallurgica 14, 1479.

Bréchet, Y. J. M. and G. R. Purdy. 1992. Scripta Metallurgica et Materialia 27, no. 12, 1753-1757.

Bridgeman, P.W. 1952. Studies in Large Plastic Flow and Fracture. McGraw-Hill, New York. 9-37.

Cahn, J. W. 1962. Acta Metallurgica 10A. 789-798.

Cahn, J. W. 1979. Interfacial Segregation. ed. W.C. Johnson and J.M. Blakely. ASM, Warrendale. 3-23.

Charpentier, P. L. and H. R. Piehler. 1980. Memoires Scientifique de la Revue de Metallurgie 77, no. 3, 281-292.

Charpentier, P. L. 1981. The Influence of Deformation Mode During Cold Forming on the Post-Formed Flow and Fracture Behaviour of Low Carbon and High Strength Low Alloy Steel Sheets. Ph.D. Thesis. Carnegie-Mellon University, Pittsburgh, Pennsylvania.

Chéron, R., X. Quillard, J. M. Roland and D. Roptin. 1994. Scripta Metallurgica et Materialia 31, no. 4, 423-426.

Chin, G.Y., W. L. Mammel and M. T. Dolan. 1967. Transactions AIME 239, 1854.

Cliff, G. and G. W. Lorimer. 1975. Journal of Microscopy 103, 203.

Conrad, H. and G. Schoek. 1960. Acta Metallurgical 8, 791.

Cotterell B. and J. R. Rice. 1980. International Journal of Fracture 36, no. 2, 155-169.

Cottrell, A. H. 1963. The Relation between the Structure and Mechanical Properties of Metals, Symposium No. 15 National Physical Laboratory, HMSO, London, 456-473.

Cottrell, A. H. 1983. Yield, Flow and Fracture of Polycrystals. ed. T. N. Baker, Applied Science Publishers, London, 123-129.

Cottrell, A. H. 1989. Materials Science and Technology 5, 1165.

C.R.M. Annual R.&D. Report. 1995. 25.

Danckert, J. 1994. Annals of the CIRP 43, no. 1, 249-252.

Danckert, J. 1995. Annals of the CIRP 44, no. 1, 259-262.

Daniel, D., J. Savoie and J. J. Jonas. 1993. Acta Metallurgica and Materialia 41, no. 6, 1907-1920.

Davidenkov, N. N. 1932. Zeitschrift fur Metallkunde 24, no. 2, 25-29.

Davidenkov, N. N. 1936. Dinamicheskaya Ispytania Metallov, Moscow.

deCelis, B., A. S. Argon and S. Yip. 1983. Journal of Applied Physics. 54, no. 9, 4864-4879.

Defay, R. and I. Prigogine. 1951.Tension Superficielle et Adsorption, Dunod, Paris.

Deits, S. H. and D. K. Matlock. 1990. Zinc-Based Steel Coating Systems: Metallurgy and Performance. ed. G. Krauss and D. K. Matlock. TMS, Warrendale, PA. 297-317.

Duncan, J. L. 1985. An Introduction to the Mechanics of Sheet Metal Forming: A Short Course on Formability. McMaster University, Hamilton.

Du Plessis, J. and G. N. van Wyk. 1988. Journal of Physics and Chemistry of Solids 49, no. 12, 1441-1450.

Erhart, H. and H. J. Grabke. 1981. Metal Science 15, 401-408.

Ference, T. G. and R. W. Balluffi. 1988. Scripta Metallurgica 22, 1929.

Floreen, S. and J. H. Westbrook. 1969. Acta Metallurgica 17, 1175-1181.

Fowler, R. and E. A. Guggenheim. 1965. Statistical Thermodynamics, Cambridge University Press, Cambrige, 429.

Freund, L. B. and J. W. Hutchinson. 1985. Journal of Mechanics Physics of Solids 33, no. 2, 169-191.

Gertsman, V. Y. and K. Tangri. 1997. Acta Materialia 45, no. 10, 4107-4116.

Gibbs, J.W., 1948. Collected Works - Vol. 1, Yale University Press. 218.

Gilman, J. J. 1958. Transactions of the AIME 212, 783

Glover, G., J. L. Duncan and J. D. Embury. 1977. Metals Technology. 153-159.

Gruzin, P. L. and V. V. Mural. 1964. Physics of Metals and Metallography 17, no. 3, 384-389.

Guggenheim, E. A 1933. Modern Thermodynamics By The Methods of Willard Gibbs. Methuen and Co., London, 160-181.

Gupta, I. and R. Scime. 1979. 21st MWSP Conference Proceedings Vol. 17. ISS-AIME, 260-276.

Guttmann, M. 1975. Surface Science 53, 213-227.

Guttmann, M. 1977. Metallurgical Transactions A 8A, 1383-1401.

Guttmann, M. 1995. Journal de Physique IV 5, C7-85-C7-96.

Guttmann, M. and D. McLean. 1979. Interfacial Segregation, ed. W.C. Johnson and J.M. Blakely. ASM. 261-348.

Hahn, G. T. 1984. Metallurgical Transactions 15A, 947-959.

Hatfield and Thirkell. 1919. The Journal of the Institute of Metals 22, no. 2, 69-91.

Hawkins, D. N. 1976. Metals Technology. 417-421.

Henning, L. A. 1992. 33rd MWSP Conference Proceedings, ISS-AIME. 9-13..

Heslop, J. and N. J. Petch. 1956. Philosophical Magazine 1, 1866-.

Higashino, T., Y. Ogawa, M. Inoue and K. Sakata. 1987.Transactions ISIJ 27, no.1, S1381.

Hill, R. 1950. Mathematical Theory of Plasticity. Oxford University Press, Oxford.

Hillert, M. 1975. Metallurgical Transactions 6A, 5-19.

Hillert, M. 1998. Phase Equilibria, Phase Diagrams and Phase Transformations:Their Thermodynamic Basis. Cambridge University Press.

Hillert, M. and B. Sundman. 1976. Acta Metallurgica 24, 731-743.

Hirth, J. P. 1965. Energetics in Metallurgical Phenomena. ed. by W.M. Mueller. Gordon and Breach.

Hirth, J. P. and J. Lothe. 1982. Theory of Dislocations. Wiley, New York.

Hoagland, R. G. 1997. Philosophical Magazine A 76, no. 3, 543-563.

Hondos, E.D. and D. McLean. 1976. Grain Boundary Structure and Properties. ed. G. A. Chadwick and D. A. Smith. Academic Press, London. 353-383.

Hondros, E. D. and M. P. Seah. 1983. Physical Metallurgy. ed. R.W. Cahn and P. Haasen. North-Holland, Amsterdam. 855-931.

Hood, J. E. 1999. Private Communication. Stelco Report.

Hosford, W. F. and R. M. Caddell. 1993. Metal Forming - Mechanics and Metallurgy, 2nd Edition. Prentice-Hall, Englewood Cliffs, NJ.

Howe, J. M. 1997. Interfaces in Materials. John Wiley & Sons, New York.

Hull, D. 1963. Fracture of Solids. ed. D. C. Drucker and J. J. Gilman. Gordon and Breach, New York. 417-460.

Ikeda, J. A. S., Y.-M. Chiang, A. J. Garratt-Reed and J. B. Vander Sande. 1995. Journal of the American Ceramic Society 76, no. 10. 2447-59.

Inagaki, H. 1988. Zeitschrift für Metallkunde 79, no.2, 109-118.

Inagaki, H., K. Kurihara and I Kozasu. 1977.Transactions ISIJ 17, 75-81.

Inman, M. and H. Tippler. 1963. Metallurgical Revue 8, 105.

International Iron and Steel Institute. 2000. IISI Steel Statistical Yearbook.

Irie, T., S. Satoh, A. Yasuda and O. Hashimoto. 1982. Metallurgy of Continuous-Annealed Sheet Steel. ed. B. L. Bramfitt and P. L. Mangonon, Jr. The Metallurgical Society of the AIME, Warrendale, PA. 155-171.

Inagaki, H. 1988. Z. Metallkde 79, no.2, 109-118.

Irwin, G. R. 1958. Fracture. Handbuch der Physik Vol. 6. Springer-Verlag, Berlin, 551.

Isabell, T. C. and V. P. Dravid. 1997. Ultramicroscopy 67, 59-68.

Jokl, M. L., V. Vitek and C. J. McMahon Jr. 1980. Acta Metallurgica 28, 1479-1488.

Jokl, M. L., V. Vitek, C. J. McMahon Jr. and P. Burger. 1989. Acta Metallurgica 37, no. 1, 87-97.

Joshi, A. and D. F. Stein. 1970. Metallurgical Transactions 1, no. 9, 2543-2546.

Joshi, A. and D. F. Stein. 1971. Journal of the Institute of Metals 99, 2543-2546.

Kallend, J.S., U. F. Kocks, A. D. Rollet and H.-R. Wenk. 1991. Materials Science and Engineering A A132. 1-11.

Kameda, Jun and C. J. McMahon, Jr. 1980. Metallurgical Transactions A 11A, 91.

Kameda, Jun and C. J. McMahon, Jr. 1981. Metallurgical Transactions A 12A, 31-37.

Kantidis, E., B. Marini and A. Pineau. 1994. Fatigue and Fracture of Engineering Materials and Structures 17, no. 6, 619-633.

Kantidis, E., B. Marini, L. Allais and A. Pineau. 1994. International Journal of Fracture 66, no. 3, 273-294.

Kase, T., T. Iwai, Y. Okano, M. Urai and H. Shirasawa. 1993. CAMP-ISIJ 6, 1719.

Keast, V. J., J. Bruley, P. Rez, J. M. Maclaren and D. B. Williams. 1998. Acta Materialia 46, no. 2, 481-490.

Keeler, S. 1969. Machinery. December, 141-142.

Kelly, A., W. R. Tyson and A. H. Cottrell. 1967. Philosophical Magazine 15, 567-.

Kitamura, M., I. Tsukatani and T. Inoue. 1994. ISIJ International 34, no. 1, 115-122.

Knorr, D. B. 1988. Metallurgical Transactions A 19A. 1009-1019.

Knott, J. F. 1971. Material Science and Engineering 7, 1.

Knott, J.F. 1973. Fundamentals of Fracture Mechanics. Halsted Press, New York.

Knott, J.F. 1977. Fracture 77 Vol.1 Proceeding of the Fourth International Conference on Fracture. University of Waterloo Press, Waterloo. 61-92.

Knott, J. F. 1983. Yield, Flow and Fracture of Polycrystals. ed. T. N. Baker. Applied Science Publishers. 87-.

Knott, J. F. 1983. Atomistics of Fracture. ed. R.M. Latanision and J.R. Pickeus, Plenum Publishing Corp., New York, 209-234.

Konishi, M., N. Ohashi and H. Yoshida. 1974. Kawasaki Steel Technical Report 6, no. 3, 305-323.

Konishi, M., Nishida and N. Ohashi. 1974. "Brittle Fracture of Steel Sheets After Press Forming". 8th Biennial Congress of the International Deep Drawing Research Group, Gothenburg, Sweden.

Konishi, M., T. Kohara and T. Tanaka. 1977. Tetsu-To-Hagane 63, no. 11, S874.

Krielaart, G., M. Baetens, S. Claessens, D. Vanderschueren and Y. Houbaert. 1998. Materials Science Forum 284-286, 209-217.

Kumar, A. and B. L. Eyre. 1980. Proceedings of the Royal Society A370, 431.

Kunishige, K., M. Fukada and S. Sugisawa. 1979. Transactions ISIJ 19, 324-331.

Lange, K. and L. Bruckner. 1990. Transactions of NAMR/SME. 71-75.

Langmuir, I. 1918. Journal of the American Chemical Society 40, 1361.

Lau, Y. H., B. C. DeCooman and M. Vermeulen. 1998. 39th MWSP Conference Proceedings Vol. 35, ISS, Warrendale, PA, 139-148.

Lawn, B. 1993. Fracture of Brittle Solids. Cambridge University Press, Cambridge.

Lejcek, P. 1994. Materials Science and Engineering A185, 109-114.

Lejcek, P., and S. Hofmann. 1991. Acta Metallurgica and Materialia 39, no. 10, 2469-2476.

Leslie, W. C., J. T. Michalak and F. W. Aul. 1963. Iron and its Dilute Solid Solutions. Interscience Publisher, New York. 119.

Lewis, S. G. 1998. Cold Work Embrittlement in Strip Steels. Ph. D. Thesis. University of Wales, Swansea.

Lewis, G., S. R. Daniel, M. P. Sidey and J. D. Parker. 1998. Modern LC and ULC Sheet Steels for Cold Forming: Processing and Properties, Vol. 2. ed. W. Bleck. Verlag Mainz, Aachen. 603-614.

Lewis, G., S. R. Daniel, J. D. Parker, D. T. Llewellyn and M. P. Sidey. 1998. Ironmaking and Steelmaking 25, no.1, 163-73.

Li, Daoming, G. Heßling and W. Bleck. 1999. Steel Research 70, no. 4&5, 155-161.

Lim, L. C. and T. Watanabe. 1990. Acta Metallurgica et Materialia 38, no. 12, 2507-2516.

Lo, K. K. 1978. Journal of Applied Mechanics 45, 797-802.

Low, J. R. 1954. Relation of Properties to Microstructures. ASM, 163.

Low, J. R., and R. G. Feustel. 1953. Acta Metallurgica 1. 185-192.

Lücke, K. and H. P. Stüwe. 1971. Acta Metallurgica 19, 1087-1099

Maehara, Y., N. Mizui and M. Arai. 1991. Interstitial Free Steel Sheet: Processing, Fabrication and Properties. ed. L.E. Collins and D.L. Barager. CIM, Montreal. 135-144.

Maîtrejean, S. 2000. Fragilité des Tôles D'Acier Sans Interstitiel: Influence du Changement du Chemin De Déformation. Ph. D. Thesis. Institute National Polytechnique de Grenoble, Grenoble.

Malis, T., S. Cheng and R. F. Egerton. 1988. Journal Electron Microscopy Techniques 8, 193.

Marciniak, Z. and J. L. Duncan. 1992. The Mechanics of Sheet Metal Forming. Edward Arnold, London.

Marder, A. 1990. Zinc-Based Steel Coating Systems: Metallurgy and Performance. ed. G. Krauss and D. K. Matlock, TMS, Warrendale, PA. 55-82.

Marder, A. 1991. Interstitial Free Steel Sheet: Processing , Fabrication and Properties. ed. L.E. Collins and D.L. Barager. CIM, Montreal., 157-174.

Martin, P., S. Dionne, O. Dremailova, J. Brown, B. Voyzelle, J. Bowker and D. Linkletter. 2000. 42nd MWSP Conference Proceedings Vol. 38., ISS, Warrendale, PA. 631-644.

Matsui, H., S. Moriya, S. Takaki and H. Kimura. 1978. Transactions JIM 19, 163.

Matsudo, K., K. Osawa, M. Yoshida and M. Sakoh. 1977. Nippon Kokan Technical Report -Overseas, no. 23, 15-24.

May, O. 1938. German Patent Number 658898.

McLean, D. 1956. Grain Boundaries in Metals. Clarendon Press, Oxford. 116-149.

McLean, M. 1971. Acta Metallurgica 19, 387.

McMahon Jr., C. J. and V. Vitek, 1979. Acta Metallurgica 27, 507.

McMahon Jr., C. J., C. L. Briant and S. K. Banerji. 1977. Proceedings of the Fourth International Conference on Fracture 1, ed. D.M.R. Taplin. University of Waterloo Press, Waterloo. 363-385.

Mecking, H. 1985. Preferred Orientation in Deformed Metals and Rocks: An Introduction to Modern Texture Analysis. ed. H.-R. Wenk. Academic Press, Orlando. 267-306.

Mega, T., J. Shimomura and K. Seto. 1996. Materials Transactions, JIM 37, no. 3, 323-329.

Mehta, S. C. and D. A. Smith. 1991. Grain Boundary Engineering. CIM, Montreal. 1-33.

Menyhard, M., B. Rothman, C. J. McMahon Jr. , P. Lejcek and V. Paidar. 1991. Acta Metallurgica and Materialia 39, no. 6, 1289-1295.

Meyer, L., W. Bleck and W. Muschenborn. 1994. International Forum for Physical Metallurgy of IF Sheet Steel, The Iron and Steel Institute of Japan,Tokyo, 203-222.

Militzer, M. and J. Wieting. 1987. Acta Metallurgica. 35, no. 2, 2765-2777.

Mintz, B., Ke Han and G. D. W. Smith. 1992. Materials Science and Technology 8, no. 6, 537-540.

Murr, L.E. 1975. Interfacial Phenomena in Metals and Alloys. Addison-Wesley, Reading, MA.

Nakamura, T. and T. Sakaki. 1970. Transactions of ISIJ 10, no. 4, 229-231.

Neutjens, J., J. C. Herman and V. Leroy. 1998. Modern LC and ULC Sheet Steels for Cold Forming: Processing and Properties, Vol. 2. ed. W. Bleck, Verlag Mainz, Aachen, 591-602.

Neutjens, J., H. Mathy and J. C. Herman. 1997. Revue de Metallurgie 94, no. 4, 551-561.

Oehler, G. 1963. Engineers Digest 24, no. 1, 81-83.

Ohfuji, T., S. Suzuki, S. Takaki and H. Kimura. 1992. Materials Transactions-JIM 33, no. 2, 138-142.

Oka, M. and H. Takechi. 1987. Formability and Metallurgical Structure. ed. A. K. Sachdev and J. D. Embury. The Metallurgical Society, Warrendale. 83-99.

Orientation Imaging Microscopy - User Manual. 1996. TexSEM Laboratories Inc. Utah.

Orowan, E. 1948. Reports on Progress in Physics, Vol. XII, 185.

Palumbo, G. P. J. King, K. T. Aust, U. Erb and P. C. Lichtenberg. 1991. Scripta Metallurgica et Materialia 25, 1775-1780.

Perovic, A., K. P. Boyle, J. D. Embury and G. C. Weatherly. 2001. unpublished research.

Petch, N. J. 1958. Philosophical Magazine 3, 1089-1097.

Piehler, H. R. and G. W. Jarvis. 1998. Constitutive and Damage Modelling of Inelastic Deformation and Phase Transformations. Neat Press, Maryland. 827-834.

Pradhan, R. 1994. International Forum for Physical Metallurgy of IF Sheet Steel, The Iron and Steel Institute of Japan,Tokyo. 165-178.

Priestner, R. 1964. Deformation Twinning. Metallurgical Society of AIME. Gordon and Breach Science Publishers. New York. 321-355.

Ragab, M. S., and H. Z. Orban. 2000. Journal of Materials Processing Technology 99, 54-61.

Randle, V. 1992. Microtexture Determination and Its Applications. The Institute of Materials, London.

Randle, V. 1999. Material Science Forum 294-296, 51-58.

Randle, V. and O. Engler. 2000. Introduction to Texture Analysis : Macrotexture, Microtexture and Orientation Mapping, Gordon and Breach Science Publishers, Amsterdam.

Ray, R. K., J. J. Jonas and R. E. Hook. 1994. International Materials Review 39, no. 4, 129-172.

Reidel, H. 1993. Materials Science and Technology - A Comprehensive Treatment, Vol. 6 -Plastic Deformation and Fracture of Metals, ed. R. W. Cahn, P. Haasen and E. J. Kramer. VCH, Weihman, 581.

Rege, J. S. 1997. The Role of Phosphorus in Cold Work Embrittlement in Ti and Ti-Nb Stabilized High Strength Ultra Low Carbon Steels. Ph.D. Thesis. University of Pittsburgh, Pittsburgh.

Rice, J. R. 1966. Proceedings of the 1st International Conference on Fracture. Sendai, Japan. ed. T. Yokobori, T. Kawasaki and J. L. Swedlow. 309-340.

Rice, J. R. 1992. Journal of Mechanics and Physics of Solids 40, 239.

Rice, J. R. and R. M. Thomson. 1973. Philosophical Magazine 29, 73.

Richards, C. E., C. N. Reid and R. E. Smallman. 1969. Transactions of the Japan Institute of Metals 9, supplement, 960-969.

Saada, G. 1995. Materials Science Forum 189-190. 149-154.

Saada, G. 1998. Diffusion and Defect Data Pt. B: Solid State Phenomena 59-60. 77-98.

Sachs, G. and G. Espey. 1942. Transactions of the American Institute of Mining and Metallurgical Engineers 147, 348-360.

Sadovskiy, V. D, G. N. Bogacheva and V. M. Umova. 1972. Physics of Metals and Metallography 34, no.1, 67-73.

Saindrenan, G., D. Roptin, J. M. Maufras and B. Bauche. 1989. Scripta Metallurgica 23, 1163-1168.

Saito, K. and Y. Shimahashi. 1978. Metal Forming Plasticity. ed. H. Lippman. Springer-Verlag. 53-65.

Saito, Y., H. Utsunomiya, N. Tsuji and T. Sakai. 1999. Acta Materialia 47, no. 2, 579-583.

Sakata, K., K. Hashiguchi, S. Okano, T. Higashino, M. Inoue and S. Sata. 1988. Kawasaki Steel Technical Report no. 18, 52-60.

Samajdar, I., B. Verlinden, P. Van Houtte and D. Vanderschueren. 1997. Scripta Materialia 37, no. 6. 869-874.

Satoh, S.,T. Obara and K. Tsunoyama. 1986. Transactions ISIJ 26, 737-744.

Schwarzer, R. A. 1993. Textures and Microstructures 20, 7-27.

Seah, M. P. 1983. Practical Surface Analysis by Auger and X-ray Photoelectron Spectroscopy. ed. D. Briggs and M. P. Seah. Wiley, Chichester.

Seibel, E. and W. Mühlhäuser. 1954. Mitt. Forschungsgesellschaft 21, 241-244.

Semiatin, S. L. and J. J. Jonas. 1984. Formability and Workability of Metals. American Society for Metals. Ohio.

Seto, K, D. J. Larson, D. J. Warren and G. D. W. Smith. 1999. Scripta Materialia 40, no. 9, 1209-1034.

Shaw, M.C. 1966. Mechanical Behaviour of Materials. eds. F.A. McClintock and A. S. Argon. Addison-Wesley, Reading , Mass. 443.

Sheridan, P. J. 1989. Journal of Electron Microscopy Techniques 11, 41.

Shi, M. F. and D. J. Meuleman. 1995. Journal of Materials Engineering and Performance 4, no. 3, 321-333.

Sih, G. C. and H. Liebowitz. 1968. Mathematical Theory of Brittle Fracture. Fracture, An Advanced Treatise Volume II. ed. H. Liebowitz. Academic Press, New York. 67-190.

Sklad, M. P. 1990. Winter Annual Meeting of the ASME. ASME, New York. 75-83.

Skogsmo, J. and A. Atrens. 1994. Acta Metallurgical et Materialia 42, no. 4, 1139-1146.

Small, M. B., D. A. Smith and A. J. Garratt-Reed. 1994. Scripta Metallurgica et Materialia 30, no. 12. 1531-1534.

Sowerby, R. 1985. Metal Forming and Impact Mechanics. ed. S. R. Reid. Pergamon Press, New York. 123-134.

Sowerby, R., D. K. Uko and Y. Tomita. 1979. Materials Science and Engineering 41, 43-58.

Sowerby, R., E. Chu. and J. L. Duncan. 1982. Journal of Strain Analysis 17, no. 2, 95-101.

Spalek, A., G. Reisner, E. A. Werner, A. Pickler and P. Stiaszny. 2000. 42nd MWSP Conference Proceedings Vol 38, ISS, Warrendale, PA. 621-629.

Stroh, A. H. 1954. Proceedings of the Royal Society (London) A223, 404-414.

Subramanian, S. V., M. Prikryl, A. Ulabhaje and K. Balasubramanian. 1991. Interstitial Free Steel Sheet: Processing, Fabrication and Properties. ed. L. E. Collins, D. S. Baragar. CIM, Montreal. 15-38.

Sudo, M., I. Tsukatani and Z. Shibata. 1982. Metallurgy of Continuous-Annealed Sheet Steel. ed. B. L. Bramfitt and P. L. Mangonon, Jr., The Metallurgical Society of the AIME, Warrendale, PA. 301-319.

Sutton, A. P. and R. W. Balluffi. 1987. Acta Metallurgica 35, no. 9. 2177-2201.

Sutton, A. P. and R. W. Balluffi. 1995. Interfaces in Crystalline Materials. Clarendon Press, Oxford.

Suzuki, S., M. Obata, K. Aiko and H. Kimura. 1983. Scripta Metallurgica 17, 1325-1328.

Tabor, D. 1991. Gases, Liquids and Solids and Other States of Matter. 3rd Edition. Cambridge University Press.

Takahashi, N., M. Shibata, Y. Furuno, H. Hayakawa, K. Kakuta and K. Yamamoto. 1982. Metallurgy of Continuous-Annealed Sheet Steel. ed. B. L. Bramfitt and P. L. Mangonon, Jr. The Metallurgical Society of the AIME, Warrendale, PA. 133-153.

Takahashi, A. and H. Sumitomo. 1998. CAMP-ISIJ 11, 1148.

Teshima, S. and M. Shimizu. 1965. Mechanical Working of Steel II. Metallurgical Society of AIME Vol 26, Gordon and Breach Science Publishers, New York. 279-320.

Timbres, D. H. 1970. Fracture in Low Carbon Steel. Ph.D. Thesis. McMaster University, Hamilton.

Tokunaga, Y. and H. Kata. 1990. Metallurgy of Vacuum-Degassed Steel Products, ed. R. Pradhan, TMS,Warrendale. PA. 91-108.

Tokunaga, Y., M. Yamada and T. Hada. 1986. Tetsu-To-Hagane. 72, no. 8, 997-1004.

Tsujimura, K., M. Sudo, T. Ohki and K. Kawanoto. 1974. Kobelco Technical Report 24-4, 59.

Tsurekawa,S., T. Ueda, K. Ichikawa, J. Nakashima, Y. Yoshitomi and H. Yoshinaga. 1996. Materials Science Forum 204-206, 221-226.

Tyson, W. R. 1978. Acta Metallurgica. 26, 1471-1478.

Watanabe, T. 1984. Res Mechanica. 11, no. 1, 47-84.

Wenk, H. R. and U. F. Kocks. 1987. Metallurgical Transactions A 18A, 1083-1092.

White, C. L. and W. A. Coghlan. 1977. Metallurgical Transactions A 8A, 1403-1412.

White, C. L. and D. F. Stein. 1978. Metallurgical Transactions A 9A, 13-22.

Wilson, D. V. 1967. Metal Science Journal 1, 40-47.

Wolf, D. 1992. Materials Interfaces, Atomic-Level Structure and Properties. ed. D. Wolf and S. Yip. Chapman and Hall, London. 1-57.

Yahya, O. M. L., F. Borit, R. Piques and A. Pineau. 1998. Fatigue and Fracture of Engineering Materials and Structures 21, 1485-1502.

Yan, B. and I. Gupta. 1996. 38th MWSP Conference Proceedings Vol. 34, ISS-AIME, Cleveland, 417-424.

Yan, B. and I. Gupta. 1998. Proceedings International Symposium on Modern LC and ULC Sheet Steels for Cold Forming: Processing and Properties,Vol. 2. ed. W. Bleck. Verlag Mainz, Aachen. 249-263.

Yasuhara, E., K. Sakata, T. Kato and O. Hashimoto. 1994. ISIJ International 34, no. 1, 99-107.

Yu-Qing, W. and C. J. McMahon, Jr. 1987. Materials Science and Technology 3, 207-216.

Zener, C. 1949. Fracturing of Metals. ASM, Cleveland, 3-31.

Zok, F. 1988. The Influence of Hydrostatic Pressure on Fracture. Ph.D. Thesis. McMaster University, Hamilton. 303-327.

Zok, F. and J. D. Embury. 1990. Metallurgical Transactions A 21A, 2565-2575.